

**ENERGETICS OF DYNAMIC PLASMA
IN THE SOLAR TRANSITION REGION**

by

AMY RENÉE WINEBARGER

A DISSERTATION

**Submitted in partial fulfillment of the requirements
for the degree of Doctor of Philosophy in
The Department of Physics
of
The School of Graduate Studies
of
The University of Alabama in Huntsville**

HUNTSVILLE, ALABAMA

1999

Copyright by
Amy Renée Winebarger
All Rights Reserved
1999

DISSERTATION APPROVAL FORM

Submitted by Amy Renée Winebarger in partial fulfillment of the requirements for the degree of Doctor of Philosophy with a major in Physics.

Accepted on behalf of the Faculty of the School of Graduate Studies by the dissertation committee:

_____ Committee Chair
(Date)

_____ Department Chair

_____ College Dean

_____ Graduate Dean

ABSTRACT

School of Graduate Studies
The University of Alabama in Huntsville

Degree Doctor of Philosophy College/Dept. Science / Physics
Name of Candidate Amy Renée Winebarger
Title Energetics of Dynamic Plasma in the Solar Transition Region

Observations of solar chromosphere-corona transition region plasma show evidence of small-scale, short-lived dynamic phenomena characterized by extreme nonthermal broadening and asymmetry in the wings of spectral line profiles. These impulsive mass motions (“explosive events”) are thought to be the product of magnetic reconnection and to be similar in driving mechanism (though larger in size) to *nanoflares*, the small-scale events proposed by Parker (1988) to heat the corona.

The nonthermal broadening and asymmetry associated with explosive events led to speculation that they were significant to the energy balance of the solar atmosphere, yet initial estimates of the energy flux contribution of these events suggested that the energy released was *not* sufficient to heat the corona and chromosphere. However, these previous estimates were based on characteristic velocities of the plasma (found from the average shift and width of the spectral line profile) and so did not adequately describe the energy flux.

To further establish the energetic significance of explosive events, the differential distribution of the number of events as a function of their energy, $\frac{dN}{dE} \sim E^{-\alpha}$, must be evaluated. If the index, α , of this distribution is greater than 2, the total power released by the events is dominated by the smallest events. Hence, if such a distribution continued to small enough energies, these small events (e.g., nanoflares) would be significant in coronal and chromospheric heating.

This dissertation addresses 1) whether explosive events are significant in the energy balance of the solar atmosphere and 2) if the distribution of the number of explosive events as a function of their energy implies that smaller releases of energy may be significant in coronal and chromospheric heating.

High spectral, spatial, and temporal resolution spectra of the C III 977 Å line, N IV 765 Å line, O VI 1032 Å line, and Ne VIII 770 Å line were observed with Solar Ultraviolet Measurements of Emitted Radiation (SUMER) telescope and spectrometer. Each line profile exhibiting explosive event characteristics was analyzed using the Velocity Differential Emission Measure (VDEM). A VDEM is a measure of the emitting power of the plasma as a function of its line-of-sight velocity. It characterizes the bulk flows of the plasma, and hence provides a method of accurately measuring the energy flux associated with an event.

The average global contribution of the energy flux released in these events toward both the corona and chromosphere is $\sim 4 \times 10^4$ ergs cm^{-2} s^{-1} . Though this value falls short of the atmospheric heating requirements (viz. 3×10^5 ergs cm^{-2} s^{-1} for the corona and 4×10^6 ergs cm^{-2} s^{-1} for the chromosphere), the distribution of events as a function of energy has an index of $\alpha = 2.9 \pm 0.1$. If this distribution is representative of the size distribution at lower event energies ($\sim 10^{21}$ ergs), these small, undetectable events would release enough energy to heat the solar atmosphere.

ACKNOWLEDGEMENTS

Throughout my education, I have been supported by many generous and gifted individuals. For the past four years, I have had the privilege of working with Dr. A. Gordon Emslie. Gordon's ability to reduce complicated solar phenomena into basic physics has greatly increased my appreciation and love of the science. I am also deeply indebted to Dr. John T. Mariska who has provided access to the SUMER data and has hosted my visits to NRL and Goddard. John is also the premier source of wisdom on transition region phenomena and was always willing to answer my many questions. I am profoundly grateful to Dr. Elizabeth Newton who has served as my mentor and who has provided invaluable personal and professional support throughout my time at UAH. I would like to acknowledge and thank the rest of my committee, Dr. Hugh Comfort, Dr. Jim Miller, and Dr. Ron Moore, for their careful criticisms of this research.

I would like to thank my high school physics teacher, Ms. Nancy Wagner. Without her encouragement, I would most likely be (unhappily) pursuing a degree in chemistry. I am also grateful to Dr. Ed DeLuca who served as my advisor and mentor for a summer program in 1994. He encouraged me to come to UAH to work with Gordon and has been generous enough to offer me a job to motivate me to graduate.

Finally, I would like to thank my sister, Mary Kidd, brother, Lynn Winebarger, and friends (especially the UAH physics graduate students) who have greatly enriched my life outside of the office. I am deeply appreciative of my fiancé, Michael Martin, who has been my constant companion and supporter for the last four years and who has suffered the most through the dissertation process. Most importantly, my mother, Linda Kidd, has always encouraged me to pursue higher education. This dissertation is the result of her gentle encouragement, love, and support.

TABLE OF CONTENTS

	Page
List of Figures	vii
List of Tables	xi
List of Symbols	xiii
1 INTRODUCTION	1
1.1 The Sun	1
1.2 Energy Requirements for the Quiet Solar Atmosphere	3
1.3 Nanoflares	8
1.4 Roadmap to the Dissertation	11
2 EXPLOSIVE EVENTS IN THE SOLAR TRANSITION REGION	13
2.1 The Transition Region	13
2.2 Explosive Event Characteristics	16
2.3 The Acceleration Mechanism	20
2.4 Energy Release	24
2.5 The Need for a Better Method	24
3 MEASURING THE ENERGETICS OF EXPLOSIVE EVENTS	26
3.1 The Energy Flux of a Transition Region Plasma	26
3.2 Measuring the Energy Flux of an Explosive Event	29
3.3 The Velocity Differential Emission Measure	32
3.4 Limitations of the VDEM Approximation	37
3.5 Data Restrictions	52
4 THE SUMER INSTRUMENT AND SPECTRAL DATA	55
4.1 Solar Ultraviolet Measurements of Emitted Radiation	55
4.2 Defining the Wavelength Array from Reference Lines	57
4.3 SUMER Spectral Data	59
4.4 Selecting Dynamic Profiles	71
4.5 Analyzing Event Line Profiles Observed by SUMER	76
5 EXPLOSIVE EVENT CHARACTERISTICS	80
5.1 The Analysis Technique: An Example	80
5.2 Explosive Event Characteristics	86
5.3 Characteristics of the Energy Flux of Explosive Events	88
5.4 Discussion of Event Characteristics	106
6 GLOBAL ENERGETICS	112
6.1 Global Energy Contribution	112
6.2 The Global Distribution Functions	116
6.3 Discussion of the Global Energetics of Explosive Events	122
7 SUMMARY AND CONCLUSIONS	130
APPENDIX	
Simulating Line Profiles	134
REFERENCES	186

LIST OF FIGURES

Figure	Page
1.1 The temperature (solid) and mass density (dotted) as a function of height for a one-dimensional model of the quiet solar atmosphere. (This figure is courtesy of Mariska 1992.)	4
1.2 The conductive flux of the solar atmosphere based on a simple empirical model (Mariska 1992).....	6
1.3 The radiative loss function of the solar atmospheric plasma (Mariska 1992).....	7
2.1 Examples of sequential spectra (a-f) of the C III 977 Å line exhibiting explosive event characteristics around spatial pixel 10. These observation were taken with the SUMER instrument on 1996 May 10.	18
2.2 Corresponding line profiles (solid) of the C III 977 Å line spectra in Figure 2.1 associated with spatial pixel 10 along with a thermally and nonthermally broadened Gaussian function (dashed) that would be considered a normal, non-event line profile.	19
2.3 Reconnection scenario based on Dere et al. (1991).....	22
3.1 (a) A SUMER spectrum of O VI 1032 Å line taken on 1996 May 10 at sun center. The horizontal axis is the dispersion pixel number and the vertical axis the spatial pixel along the slit. The arrow points out spatial pixel 26 that exhibits explosive event characteristics. The line profile associated with this pixel is shown in (b). The VDEM function recovered from this line profile is shown in (c).	36
3.2 (a) The emissivity function, $G(T)$, associated with the O IV 790 Å line and (b) the emission associated with constant pressure, $n_e^2 G(T)$	39
3.3 Assumed parallel bulk velocity distribution at $10^{5.2}$ K.	40
3.4 Examples of simulated line profiles of the O IV 790 Å line are shown in (a), (c), and (e), each defined by 500, 1,000, and 3,000 total counts, respectively. The normalized, deconvolved VDEM for each profile is shown in (b), (d), and (f) as a solid line. The assumed parallel bulk velocity distribution is shown as a dashed line.	41
3.5 A comparison of the net energy flux (a) energy flux toward the observer (b), and energy flux away from the observer (c) measured from the VDEM function deconvolved from simulated line profiles. The error bars in the energy fluxes are the standard deviations in the measurements. The true energy fluxes are the solid lines and the approximate uncertainties in the energy fluxes are the dotted lines.	44
3.6 An example of how heating the plasma in the high-speed volume elements while maintaining uniform density would affect the bulk velocity distribution (solid) and the theoretical VDEM function (dash-dot).	46
3.7 An example of how heating the plasma in the high-speed volume elements while maintaining constant pressure would affect the bulk velocity distribution (solid) and the theoretical VDEM function (dash-dot). The original bulk velocity function is shown as a dashed line.	48
3.8 An example of how cooling the plasma in the high-speed volume elements while maintaining uniform density would affect the bulk velocity distribution (solid) and the theoretical VDEM function (dash-dot).	49
3.9 An example of how cooling the plasma in the high-speed volume elements while maintaining constant pressure would affect the bulk velocity distribution (solid) and the theoretical VDEM function (dash-dot). The original bulk velocity distribution is shown as a dashed line.	50

3.10	The deprojected length of a single pixel as a function of the radial angle.....	53
4.1	The main components of the SUMER optical design (figure courtesy of Dietmar Germerott).....	56
4.2	This $H\alpha$ image was observed by Big Bear Solar Observatory on 1996 May 10. The dark line near sun center shows the average position of the SUMER slit.....	61
4.3	Examples of high cadence spectra observed around the C III 977 Å line (a) and O VI 1032 Å line (b).....	62
4.4	A spectrum around the C III 977 Å line along with the corresponding line profile averaged along the slit.....	63
4.5	A spectrum around the O VI 1032 Å line along with the corresponding line profile averaged along the slit.....	66
4.6	This $H\alpha$ image was observed by Big Bear Solar Observatory on 1996 October 18, the first day of observations for the N IV and Ne VIII data set. The dark line at sun center shows the position of the SUMER slit.....	68
4.7	An example spectrum around the N IV 765 Å line and Ne VIII 770 Å line along with the corresponding line profile averaged along the slit.....	69
4.8	Histograms (solid) of width of the C III profiles (a), N IV profiles (b), O VI profiles (c), and Ne VIII profiles (d). The lower half of each histogram was fit with a Gaussian function (dashed) and the number of excess events (dotted) above this Gaussian was found. The cutoff value (dash-dot) for each line was then taken to be the width where the number of events was larger than the number of non-events.....	73
4.9	Histograms (solid) of the skewness for the C III profiles (a), the N IV profiles (b), the O VI profiles (c), and the Ne VIII profiles (d). Ninety percent of the profiles with the skewness closest to the mean value were fit to find the Gaussian function (dashed). This function is assumed to represent the distribution of non-event profiles, hence by subtracting this function from the original histogram, the number of event profiles (dotted) can be found. The skewness cutoff (dash-dot) was then taken to be the value where the number of events was larger than the number of non-events.....	73
4.10	(a) Thirty-six profiles from this high-cadence C III spectra met the event criteria. An example of an event profile (solid) associated with spatial pixel 25 is shown in (b) along with a “normal” C III line profile (dashed). This profile exhibits both extreme broadening and skewness.....	77
5.1	This figure illustrates the preparations that occur before a profile can be analyzed. Figure (a) shows a high-cadence C III spectrum taken 1996 May 10. The line profile associated with spatial pixel 25 is shown in (b) with the pixels that define the boundaries on either side of the centroid highlighted. This line profile is background subtracted and calibrated to units of flux (c).....	81
5.2	The flux found in Figure 5.1 is shown again in (a) and the VDEM found by deconvolving the flux with a thermally and instrumentally broadened kernel function is shown in (b).....	83
5.3	The magnitude of the net energy flux, along with its constituents, is shown above as a function of the peak temperature of the emitting ions’ emissivity function. The uncertainty in these values are given in Table 5.7.....	92
5.4	Histograms of the net energy flux (solid) and thermal enthalpy flux (dashed) for the events observed in the C III spectral line (a), the N IV spectral line (b), the O VI spectral line (c), and the Ne VIII spectral line (d).....	93
5.5	Scatter plots of the net energy flux associated with a line profile as a function of the	

total intensity of the profile for the events observed in the C III spectral line (a), the N IV spectral line (b), the O VI spectral line (c), and the Ne VIII spectral line (d).....	94
5.6 The average values of the energy flux toward the observer and its constituents are shown as a function of the peak temperature of each ion's emissivity function. The uncertainties at each point are given in Table 5.8.	95
5.7 Histograms of the energy flux toward the observer (solid) and thermal enthalpy flux toward the observer (dashed) measured from the C III events (a) N IV events (b), O VI events (c), and Ne VIII events (d).....	99
5.8 Scatter plots of the energy flux toward the observer as a function of total intensity for the events observed in the C III spectral line (a), N IV spectral line (b), O VI (c), and Ne VIII (d).....	100
5.9 The energy flux away from the observer is shown as a function of the peak temperature of each ion's emissivity function. The uncertainties of these points are given in Table 5.10.	103
5.10 Histograms of the energy flux away from the observer (solid) and the thermal enthalpy flux away from the observer (dashed) for the events observed in the C III spectral line (a), N IV spectral line (b), O VI spectral line (c), and Ne VIII spectral line (d).....	104
5.11 Scatter plots of the energy flux away from the observer as a function of the total intensity of the event line profiles observed in the C III line (a), N IV line (b), O VI line (c), and Ne VIII line (d).....	105
5.12 The specific energy release rate, as well as the magnitudes of the energy flux toward and away from the observer. The uncertainties in these values are given in Table 5.12.	106
6.1 This simple model is assumed to represent the energy flows in the solar atmosphere associated with explosive events. The event plasma is driven away from the reconnection site either toward the corona or chromosphere. The plasma then deposits its energy through collisions with the ambient plasma in the volumes marked V_+ and V_-	114
6.2 The magnitudes of the global energy flux toward the observer and away from the observer, as well as the total global energy flux, are shown as a function of the peak temperature of each ion's emissivity function. The uncertainty associated with each point is given in Table 6.1.	116
6.3 The distribution of events observed in the C III spectral line as a function of their energy released toward the corona.....	117
6.4 The cutoff value for this distribution of events was found by fitting the high energy points, then adding a single low energy point until the fit deteriorated. The cutoff value determined for the above distribution was $\log E_+ = 22.7$	119
6.5 Distributions of events observed in the C III line (a), N IV line (b), O VI line (c), and Ne VIII line (d) as a function of their energy released toward the corona. The results of the fits of these distributions are given in Table 6.2. A composite plot of the fits is shown in Figure 6.6.....	120
6.6 A composite of the distribution of energy released toward the corona by the observed events [cf. Figure 6.5].....	121
6.7 Distributions of the events observed in the C III line (a), N IV line (b), O VI line (c), and Ne VIII line (d) as a function of their energy released toward the chromosphere. The results of the fits of these distributions are given in Table 6.3. A composite plot of	

	these fits is shown in Figure 6.8.....	123
6.8	A composite of the distributions of the number of events as a function of energy released toward the chromosphere [cf. Figure 6.7].	124
6.9	These two C III spectra show different groups of profiles selected as events. The profiles in spectrum (a) show similar shifts and velocity distributions, while the profiles in spectrum (b) are not convincingly similar.....	127
A.1	A simple bulk velocity distribution is shown in (a) and the corresponding velocity distribution of 10,000 volume elements shown in (b). The resulting intensity from this distribution of volume elements is shown as a function of wavelength in (c).	135

LIST OF TABLES

Table	Page
1.1 Energy flux losses of the corona and chromosphere in the quiet sun (Withbroe & Noyes 1977).....	5
2.1 Explosive event characteristics as observed by HRTS (Dere 1994).....	21
3.1 Summary of physical quantities associated with the energy flux.....	30
3.2 A comparison of the moments of the velocity found from an assumed bulk velocity distribution (“True”) and from the VDEM functions of three simulated line profiles [cf. Figure 3.4].....	42
3.3 A comparison of the energy flux measured from an assumed bulk velocity distribution and from a theoretical VDEM function when the plasma in the high-speed volume elements is heated and constant density is maintained.	47
3.4 A comparison of the energy flux measured from an assumed bulk velocity distribution and from a theoretical VDEM function when the plasma in the high-speed volume elements is heated and constant pressure is maintained.	48
3.5 A comparison of the energy flux measured from an assumed bulk velocity distribution and from a theoretical VDEM function when the plasma in the high-speed volume elements is cooled and constant density is maintained.	50
3.6 A comparison of the energy flux measured from an assumed bulk velocity distribution and from a theoretical VDEM function when the plasma in the high-speed volume elements is cooled and constant pressure is maintained.	52
3.7 A prioritized list of data restrictions.....	54
4.1 Characteristics of the data sets used for this study.....	59
4.2 Spectral lines in the wavelength range of 970 - 987 Å and their corresponding transitions. The O I lines used as reference lines are marked with an ‘R’.....	64
4.3 Spectral lines in the wavelength range of 1021 - 1043 Å and their corresponding transitions. The O I lines used as reference lines are marked with an ‘R’.....	67
4.4 Spectral lines in the wavelength range of 758 - 797 Å and their corresponding transitions. The transition region lines used as reference lines are marked with an ‘R’.....	70
4.5 The spectral lines used as reference lines to determine the dispersion coefficients for the Ne VIII and N IV spectra.....	71
4.6 Width and skewness cutoff values used to ascertain if a profile exhibits extreme nonthermal broadening or skewness and hence is an explosive event.....	74
5.1 Velocity moments of the example C III event line profile.....	84
5.2 Energy flux measurements for the example event line profile observed in the C III 977 Å line.....	85
5.3 The number of profiles and fraction of profiles that were selected as events, as well as general characteristics of the selected profiles.....	87
5.4 The global birthrate, lifetime, and steady-state number of the events observed in the four spectral lines.....	88
5.5 The temperature, density, mass density, area, scale height, and average filling factor for events observed in each spectral line.....	89
5.6 Values of the mean width of the non-event profiles, $(\sqrt{(\lambda - \bar{\lambda})^2})$, the instrumental width (σ_{instr}), the “normal” nonthermal width (σ), and the nonthermal velocity (ξ).....	89
5.7 The average values (\pm standard error) of the net energy flux and its components...	91

5.8	Average values for the energy flux towards the observer and its components.....	96
5.9	The average percentage magnitude and maximum percentage magnitudes of the components of the energy flux toward the observer for the event profiles observed in each spectral line.	97
5.10	The average values of the energy flux away from the observer and its components.....	101
5.11	The average and maximum percentage magnitudes of the components of the energy flux away from the observer for the event profiles observed in each spectral line. ...	102
5.12	The average values for the specific energy release rate for the events observed in each spectral line.	107
5.13	A comparison of the values for the most probable nonthermal velocity, ζ , and corresponding r.m.s. nonthermal velocity, ξ_{Chae} presented in Chae, Schühle, & Lemaire (1998) with the r.m.s. velocity, ξ , measured here [cf. Table 5.6].	110
6.1	These values are the global energy flux contribution toward the corona and toward the chromosphere, as well as the total energy flux associated with the explosive events.	115
6.2	The power law index and coefficient, A , for the fits to the distribution of events as a function of their energy released toward the corona observed in each ion, as well as the applicable range and the nanoflare energy and number implied by each distribution.....	121
6.3	The power law index and coefficient, A , for the fits to the distribution of events observed in each ion as a function of their energy released toward the chromosphere, as well as the applicable range and the nanoflare energy and number implied by each distribution.....	122

LIST OF SYMBOLS

Symbol	Definition
\mathbf{A}	Kernel function in matrix equation
A	Coefficient of power law
A_0, A_1	Coefficients of dispersion relation
A_E	Area of explosive event
A_{slit}	Deprojected area of the slit on the solar surface
A_{sun}	Solar surface area
\mathbf{B}	Magnetic field
B_0	Magnitude of constant magnetic field
\mathbf{b}_1	Perturbation in the magnetic field
b_x, b_y, b_z	Perturbation in the components of the magnetic field
C	Constant between 0.01 and 0.1
c	Speed of light
\mathbf{D}	Smoothing operator
D	Sun-satellite distance
E	Energy
E_{\pm}	Energy released into volumes above or below reconnection zone
$E_{\text{min}\pm}$	Nanoflare energy
ΔE	Difference between two bound energy states
F_c	Conductive flux
F_g	Gravitational potential energy flux
F_{kin}	Kinetic energy flux
F_R	Radiative energy flux
F_S	Energy flux associated with solar wind
F_{th}	Thermal enthalpy flux
\mathbf{f}	VDEM function in matrix equation
$f_{\text{bulk}}(\vec{v})$	Bulk velocity distribution
$f_{\text{instr}}(\lambda)$	Instrumental broadening function
$f_{\text{particle}}(\vec{v})$	Particle velocity distribution
$f_{\text{th}}(\vec{v})$	Thermal velocity distribution
$f_{\parallel}(v_{\parallel})$	Velocity distribution along the direction of motion
$f_{\perp}(v_{\perp})$	Velocity distribution perpendicular to the direction of motion
$G(T)$	Line emissivity function
$\text{GCV}(q)$	Generalized Cross-Validation function
\mathbf{g}	Line profile in matrix equation
\mathbf{H}	$\mathbf{D}^T \mathbf{D}$
H	Heating term
H_0	Scale height of a plasma
h	Planck's constant
\mathbf{I}	Identity matrix
$I(\lambda)$	Intensity function
$I_{\text{emitted}}(\lambda)$	Emitted intensity function
$I_{\text{obs}}(\lambda)$	Observed intensity function
\mathbf{J}	Current density
j_E	Net energy flux
j_{E+}	Energy flux toward the observer

$j_{\text{E-}}$	Energy flux away from the observer
j_{enthalpy}	Total enthalpy (thermal and nonthermal)
$j_{\text{global}\pm}$	Global energy flux contribution toward the corona or chromosphere
j_{globalT}	Total global energy flux contribution of explosive events
j_{kin}	Kinetic energy flux
j_{nth}	Nonthermal enthalpy flux
j_{skew}	Energy flux associated with the skewness in the distribution
j_{specific}	Specific energy release rate
j_{th}	Thermal enthalpy flux
$K(\lambda, v_{\text{los}})$	Kernel function
k	Boltzmann's constant
$k_{\text{skew}\pm}$	Cutoff value for the skewness of event profiles
k_{wid}	Cutoff value for the width of event profiles
L	Characteristic length of reconnection
l	Scale length
l_0	Oscillator strength
m	Mass
m_{e}	Electron mass
m_{H}	Hydrogen mass
m_{He}	Helium mass
m_{i}	Ion mass
N	Number of events occurring globally per second
N_0	Total number of events observed
N_{global}	Steady-state number of events
n	Number density
n_{e}	Electron density
n_{H}	Hydrogen density
n_{He}	Helium density
$P(T)$	Radiative loss function
P_{T}	Total power
p	Particle pressure of a plasma
p_0	Initial uniform particle pressure
p_1	Perturbation in particle pressure
Q	Function of bulk flows
q	Smoothing parameter
R	Global birthrate
R_{m}	Magnetic Reynolds number
R_{n}	Predicted number of nanoflares
\mathbf{r}	Position in a volume
r	Radial distance from cylindrical axis
\hat{r}	Radial unit vector
r_{sun}	Solar radius
r_0	Constant
s	Path length in the solar atmosphere
T	Plasma temperature
T_{eff}	Effective temperature
T_{nth}	Effective “nonthermal” temperature
T_{th}	Effective “thermal” temperature

t	Time
t_0, t_1	Observation times of two long exposure spectra
t_E	Lifetime of an explosive event
Δt	Cooling time
\mathbf{U}	Velocity of a plasma element
u	Mean speed of the fluid
V	Volume
V_{\pm}	Volume above (+) or below (-) reconnection zone
V_A	Alfvén speed
VDEM	Velocity Differential Emission Measure
v	Velocity
v_{los}	Line-of-sight velocity
v_{th}	Thermal velocity
v_{\parallel}	Velocity along the direction of motion
$v_{\parallel\pm}$	Velocity along the direction of motion toward and away from the observer
v_{\perp}	Velocity perpendicular to the direction of motion
Δv	Width of velocity bin
\hat{x}	Cartesian unit vector
\hat{y}	Cartesian unit vector
Z	Net charge on an ion
z	Distance along cylindrical axis
\hat{z}	Unit vector along cylindrical axis or Cartesian unit vector
α	Index of power-law
β	Ratio of particle pressure to magnetic field pressure
γ	Volumetric filling factor
δ	Width of energy bin
ϵ	Uncertainty in intensity
ϵ_{VDEM}	Uncertainty in VDEM
ϵ_v	Uncertainty in velocity
ϵ_v^{-k}	Uncertainty in the moments of velocity
ε	Energy density
ε_R	Energy density loss due to radiation
ε_{kin}	Kinetic energy density
ζ	Most probable nonthermal velocity
η	Plasma resistivity
κ	Coefficient of thermal conductivity
λ	Wavelength
$\bar{\lambda}$	Average solar wavelength
λ_0	Rest (laboratory) wavelength
$\Delta\lambda$	Width of spectral bin
μ	Pixel number
ξ	Root mean square nonthermal velocity
ρ	Mass density
Σ	Area under observation
σ	Width of line profile
σ_K	Width of Kernel function
σ_{instr}	Width (in Å) associated with the instrumental function
σ_{th}	Width (in Å) associated with the thermal velocity

τ	Total observation time
τ_0	Optical Depth
τ_R	Characteristic reconnection time
τ_T^e	Electron isotropization time
τ_T^i	Ion isotropization time
$\tau_\epsilon^{\alpha/\beta}$	Thermal equilibration time
ϕ	Potential magnetic field function
$\hat{\phi}$	Unit vector in azimuthal direction
ω	Non-potential magnetic field coefficient

CHAPTER 1

INTRODUCTION

This dissertation investigates the energetics of small-scale dynamic processes occurring in the solar chromosphere-corona transition region. These events, thought to be associated with magnetic reconnection, are observed as skewed or broadened spectral lines. Their energies have been found by analysis of the latest UV and EUV spectral data with a new inversion technique to find the bulk velocity distribution function (and hence the energy flux) associated with the emitting plasma. This introductory chapter develops the complexity of the problem of heating the solar atmosphere and introduces the heating mechanism that is investigated.

1.1 The Sun

The Sun is the closest star to Earth. Not only does it offer the radiation necessary for life to exist in the solar system, it also conveniently supplies a large scale physics laboratory to test constructs of plasma and stellar physics. It is a massive nuclear reactor containing 10^{27} tons of very hot, ionized gas. At its core, where energy is released through “hydrogen burning” (fusing four hydrogen nuclei to create an alpha particle), temperatures exceed 10 million degrees. The energy is radiated and convected outward through the solar interior to the solar surface, commonly referred to as the *photosphere*. The photosphere is where most visible light originates and has a characteristic temperature of 5,800 K.

One of the most intriguing aspects of solar structure is the solar atmosphere. First observed as large white light plumes during solar eclipses, its outer structure was determined in the early 1900’s with the onset of solar spectroscopy. If the energy transport in the solar atmosphere was purely radiative and convective, the temperature would decrease as the distance from the solar surface increased. However, when scientists first observed the emission lines during an eclipse, they found a temperature much higher than that of the photosphere. Just above the photosphere, the emission is dominated by the hydrogen emission lines formed around 10^4 K, an order of magnitude hotter than the photosphere. Because of the reddish color associated with $H\alpha$ emission, this layer of the solar atmosphere was called the *chromosphere*. Much later, the emission lines observed from the outer layers of the solar atmosphere, called the *corona*, were determined to be from ions that only exist at temperatures on the order of millions of degrees. These scientific discoveries uncovered a fundamental mystery of the solar atmosphere which still remains unsolved today. Why is the plasma in the solar atmosphere so hot? Where does the energy come from to heat this plasma? Energy cannot be radiated or convected through the photosphere to heat the solar atmosphere to temperatures above photospheric temperatures. Therefore, another method of energy transfer must be responsible for the heating of the chromosphere and corona.

An obvious possible accomplice for this energy transfer is the magnetic field that dominates the geometry of the solar upper atmosphere. The strength of these fields, measured at their footpoints in the photosphere, ranges from 10 to 1,000 G. These footpoints are moved

by the convective motions underneath the solar surface into the lanes between convective cells, commonly referred to as the *magnetic network*. The magnetic fields provide a general way to classify the atmospheric structure. Areas where the magnetic field lines are open are called *coronal holes*. Coronal holes are not observed to emit radiation from ions formed at high temperatures, hence they must be relatively cool areas of the solar atmosphere. These areas are also the source of high speed solar particles (called the *solar wind*) that flow into space along the open field lines. If the magnetic field lines are closed, large arching loops (*coronal loops*) are formed as observed by X-ray observations of the solar corona. An area containing intense magnetic field with large amounts of high temperature emission is called an *active region*. Active regions are associated with intense photospheric field, or *sunspots*, and large eruptions and releases of magnetic energy, *flares*. Regions where high temperature emission and magnetic fields are moderate are called, simply, the *quiet sun*. For simplicity, this dissertation deals mainly with the quiet solar atmosphere.

The shape of the field lines can be deduced from the equation of motion for hydromagnetic equilibrium, or

$$\nabla p = \mathbf{J} \times \mathbf{B}, \quad (1.1)$$

where p is the particle pressure in the plasma, \mathbf{B} is the magnetic field, and \mathbf{J} is the current density associated with plasma motions within the field or with the curl of the field itself. In the low β plasma of the solar upper atmosphere (meaning the magnetic field pressure is much larger than the particle pressure), this can be approximated as

$$\mathbf{J} \times \mathbf{B} = (\nabla \times \mathbf{B}) \times \mathbf{B} = 0, \quad (1.2)$$

which is known as the force-free condition. One solution to this equation (other than the trivial $\mathbf{B} = \mathbf{0}$ solution) is a potential (non-current-carrying) field such that $\nabla \times \mathbf{B} = \mathbf{0}$, or $\mathbf{B} = \nabla \phi$. A second solution is a nonpotential (current-carrying) field, or $\nabla \times \mathbf{B} = \omega \mathbf{B}$, where ω may or may not be constant in space. An example of a cylindrical, nonpotential field with nonconstant ω is a uniform twist field,

$$\mathbf{B} = B_0 \left[\frac{\frac{r}{r_0}}{1 + \left(\frac{r}{r_0}\right)^2} \hat{\phi} + \frac{1}{1 + \left(\frac{r}{r_0}\right)^2} \hat{z} \right] \quad (1.3)$$

(Tandberg-Hanssen & Emslie 1988), where $\hat{\phi}$ is the azimuthal unit vector, \hat{z} is the unit vector along the axis of the cylinder, r is the radial distance from the axis, r_0 is a constant, and B_0 is the magnetic field strength along the axis of the cylinder where $r = 0$. [Note that in the above example, there is no component of the magnetic field in the radial (\hat{r}) direction.] These stressed, current-carrying fields contain the free energy that, in principle, could be harnessed to heat the solar atmosphere. An illustration of that energy is seen as often as several times a day during solar maximum, when the coronal loops erupt, or “flare,” releasing as much as 10^{32} ergs over a timescale of seconds to hours. As spectacular as these large solar flares remain, they do not happen often enough to heat the global ambient atmosphere. Yet their presence demonstrates the energy stored in the (current-carrying) field lines.

The relationship between the magnetic field and the emitting plasma can be derived from the induction or magnetic diffusion equation (e.g., Mariska 1992),

$$\frac{\partial \mathbf{B}}{\partial t} = \nabla \times (\mathbf{U} \times \mathbf{B}) + \frac{\eta c^2}{4\pi} \nabla^2 \mathbf{B}, \quad (1.4)$$

where t is time, \mathbf{U} is the plasma velocity, η is the plasma resistivity, and c is the speed of light. The first term on the right hand side is the advection term and describes how the motions of the plasma convect the magnetic field. The second term is the diffusive term, describing how the magnetic field is destroyed by the resistivity of the plasma. The relative importance of the two terms can be found from their ratio which is called the *magnetic Reynolds number*,

$$R_m = \frac{4\pi U l}{\eta c^2}, \quad (1.5)$$

where l is the scale length of the plasma. For typical atmospheric plasmas,

$$\eta \approx 8 \times 10^8 \ln \Lambda T^{-\frac{3}{2}} \quad [\text{esu}], \quad (1.6)$$

where $\ln \Lambda \approx 10$ is the Coulomb logarithm and T is the plasma temperature. The characteristic velocity, U , in Equation (1.5) is simply the Alfvén speed, $V_A = \frac{B}{(4\pi\rho)^{\frac{1}{2}}}$ (where ρ is the mass density). Substituting these quantities into Equation (1.5) and assuming a temperature, $T = 10^5$ K, and a mass density $\rho = 2 \times 10^{-14}$ g cm $^{-3}$, the magnetic Reynolds number becomes

$$R_m = 12.5 B l \quad (1.7)$$

(Mariska 1992). For typical structure scales ($\sim 10^8$ cm – Mariska 1992) and magnetic field strengths ($\sim 10^2$ G), the magnetic Reynolds number is approximately 10^{11} , very much larger than unity. This implies that the advective term overwhelmingly dominates the induction equation, or that only plasma motions change the magnetic field content of a plasma. To put it another way, a plasma element that is initially located on a given magnetic field line must continue to remain on that same field line. This is referred to as “frozen-in” field.

Taken together, these two magnetic field qualities (“force-free” and “frozen-in”) demonstrate the importance of the magnetic field in the quiet solar atmosphere. The structure is defined by the geometry of the magnetic field and the atmospheric plasma is constrained to move along the magnetic field lines. It is within this complex geometry that the energy equation must be solved.

1.2 Energy Requirements for the Quiet Solar Atmosphere

The energy requirements to heat the solar atmosphere are not easily established. They rely heavily on the temperature and density structures, which, in turn, are very dependent on this complex geometry of the field lines mentioned in the previous section. Models of the temperature and density that assume a one-dimensional atmosphere and hence neglect the horizontal structure are overly simplistic, yet physically realizable models of a true three-dimensional atmosphere have yet to be developed. This section will introduce the heating needs of the chromosphere and corona, noting that the temperature and density structures assumed may not be accurate.

A one-dimensional model for the temperature and mass density structure of the quiet sun is shown in Figure 1.1. The chromosphere is the relatively thin layer (on the order of a few thousand kilometers) that is generally defined from the temperature minimum at approximately 4,000 K to approximately 25,000 K. The corona begins around 10^6 K and extends several million kilometers into space. The temperatures in the corona are quite high, yet the density of this region is low ($n \sim 10^9$ cm $^{-3}$). The region between the chromosphere and corona is called the *transition region*. In this layer of the solar atmosphere, the

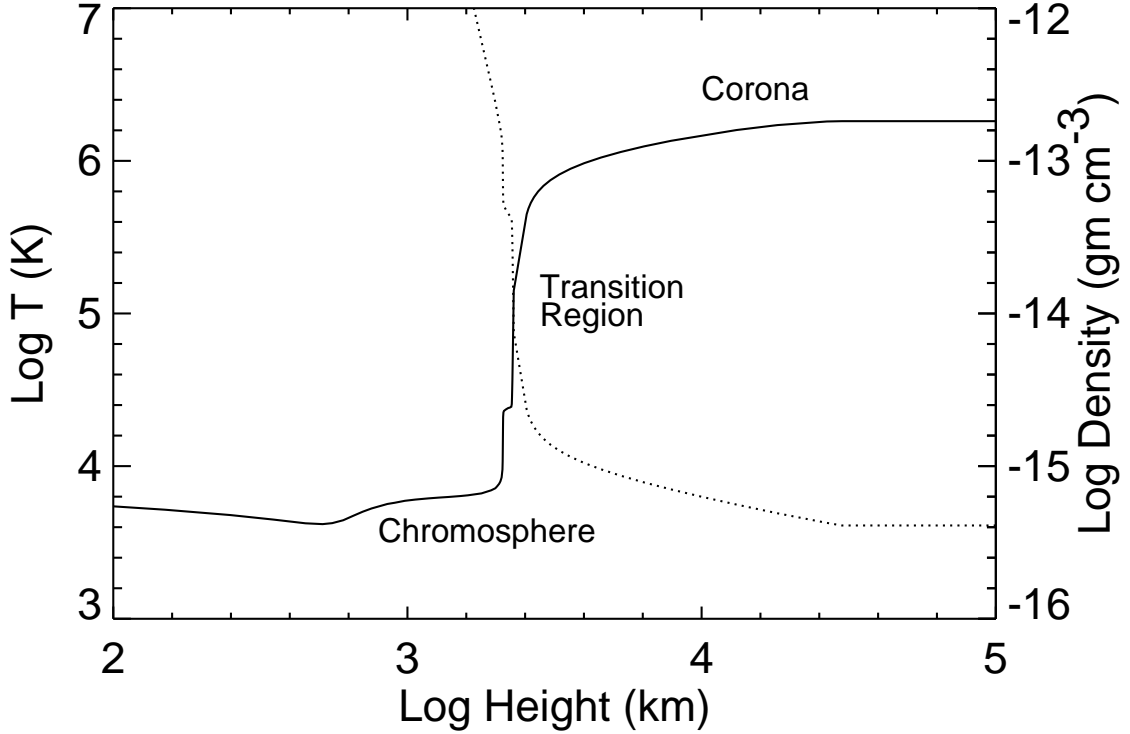


Figure 1.1: The temperature (solid) and mass density (dotted) as a function of height for a one-dimensional model of the quiet solar atmosphere. (This figure is courtesy of Mariska 1992.)

temperature increases two orders of magnitude while the density decreases two orders of magnitude over a relatively small change in atmospheric height (tens of kilometers). It is, then, generally assumed that the pressure ($\sim n_e T$, where n_e is the electron number density and Boltzmann's constant, k , is omitted for simplicity) is constant at $\sim 1 \times 10^{15} \text{ K cm}^{-3}$ (e.g., Mariska 1992). Because the temperature associated with an emission line is relatively easy to define, the temperature, instead of height, is often used as a scale for the solar atmosphere.

The volumetric energy rate equation can be approximated as

$$\frac{d\varepsilon}{dt} = \nabla \cdot (F_c + F_R + F_g + F_{\text{kin}} + F_{\text{th}} + F_S) + H \quad [\text{ergs cm}^{-3} \text{ s}^{-1}] \quad (1.8)$$

(Withbroe & Noyes 1977), where ε (ergs cm^{-3}) is the energy density, F_c is the conductive flux, F_R is the radiative energy flux, F_g is the gravitational potential energy flux, F_{kin} is the kinetic energy flux associated with the general bulk flows of the plasma, F_{th} is the thermal enthalpy flow associated with the general bulk flows of the plasma, F_S is the energy flux associated with the solar wind, and H is the enigmatic heating term. The conductive flux and radiative flux are the dominant energy loss terms for the corona and chromosphere of the quiet sun and other values (for instance, the energy flux associated with the solar wind) are assumed negligible. Approximate values for these terms derived from empirical models

Table 1.1: Energy flux losses of the corona and chromosphere in the quiet sun (Withbroe & Noyes 1977).

Coronal losses:	(ergs cm ⁻² s ⁻¹)
Conductive Flux	2×10^5
Radiative Flux	1×10^5
Total Coronal Loss	3×10^5
Total Chromospheric Loss (Radiation)	4×10^6

of the corona and chromosphere are given in Table 1.1 (from Withbroe & Noyes 1977). In the chromosphere, energy loss is dominated by radiation, while in the corona, both terms are significant. Each term will be discussed below.

The thermal conductive flux, F_c , is the thermal energy that travels along the temperature gradient from hot to cold. It is found by

$$F_c = -\kappa T^{\frac{5}{2}} \frac{\partial T}{\partial s} \quad [\text{ergs cm}^{-2} \text{ s}^{-1}] \quad (1.9)$$

(Mariska 1992), where κ is the coefficient of thermal conductivity (for solar atmospheric plasma, $\kappa = 1.1 \times 10^{-6}$ – Ulmschneider 1970) and s is the path length in the solar atmosphere. Empirically, it has been found that the conductive flux is a constant ($\sim 1 - 2 \times 10^6$ ergs cm⁻² s⁻¹) above $\sim 10^{5.2}$ K (see Mariska 1992 for details). Below this temperature, the conductive flux falls off steeply, dropping four orders of magnitude between 10^4 and 10^5 K. Figure 1.2 shows the conductive flux found from a simple empirical model (Mariska 1992). Knowledge of the conductive flux offers a method to estimate the scale height of the atmosphere by rewriting Equation (1.9), i.e.,

$$H_0 = \int_{T_{\min}}^{T_{\max}} \frac{\kappa}{F_c} T^{\frac{5}{2}} dT. \quad (1.10)$$

(This integral can be evaluated analytically for temperatures where the conductive flux is constant and numerically integrated where it is not.) Typical values for this scale height range from tens of kilometers at chromospheric temperatures to tens of thousands of kilometers at coronal temperatures.

The energy density loss rate due to radiation is given by

$$\frac{d\varepsilon_R}{dt} = \nabla \cdot F_R = n_e n_H P(T) \quad [\text{ergs cm}^{-3} \text{ s}^{-1}], \quad (1.11)$$

where n_H is the hydrogen density and $P(T)$ (ergs cm³ s⁻¹) is the radiative loss function. The magnitude of the radiative loss function in the solar atmosphere is $10^{-22} - 10^{-23}$ ergs cm³ s⁻¹

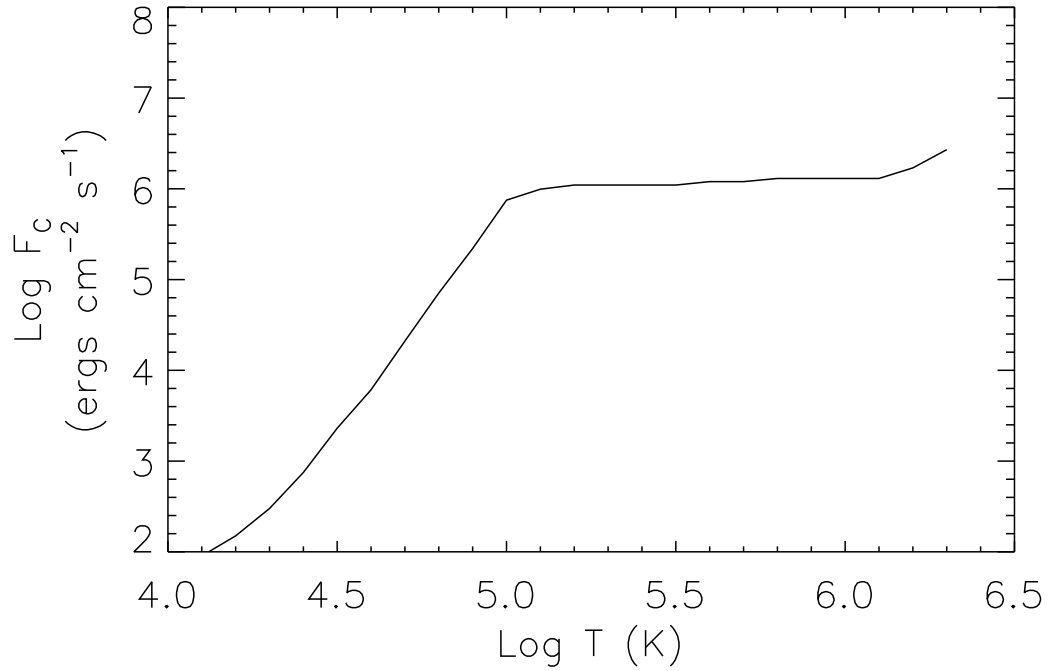


Figure 1.2: The conductive flux of the solar atmosphere based on a simple empirical model (Mariska 1992).

and is shown in Figure 1.3 (e.g., Mariska 1992). The shape of the radiative loss curve is determined by the type of emission produced by the plasma and the abundances of ions at different temperatures. The peak in the curve at $\sim 10^{4.2}$ K is due to Lyman α emission from the hydrogen atom. In this area of the curve ($\sim 10^4 - 10^5$ K) the radiation is dominated by bound-bound transitions of electrons. As the temperature increases ($\sim 10^5 - 10^{7.4}$ K), more ions become completely ionized. The radiation from this hot plasma, then, becomes dominated by bound-free transitions of the electrons. This is a less efficient process than the bound-bound transitions, so as the temperature increases (i.e., more ions become fully ionized), the radiative loss curve decreases. Above $10^{7.4}$ K, all particles in the plasma are essentially fully ionized and hence the radiation is dominated by free-free emission. (For more information on the radiative loss curve, see Cox & Tucker 1969.) Because the energy loss due to radiation is proportional to density squared (due to the predominance of collisional processes), radiative losses are the main energy sink in the relatively high density chromosphere.

In the quiet sun, approximately 3×10^5 ergs cm⁻² s⁻¹ are required to heat the solar corona and 4×10^6 ergs cm⁻² s⁻¹ to heat the chromosphere (Withbroe & Noyes 1977). Multiplied by the solar surface area, the power required is 3×10^{28} and 2×10^{29} ergs s⁻¹ for the corona and chromosphere, respectively. This is an enormous amount of energy. Compare it to the electrical power consumed on Earth, $\sim 10^{19}$ ergs s⁻¹ (estimated from power usage of several U.S. cities). The same energy that is required to sustain the solar atmosphere for

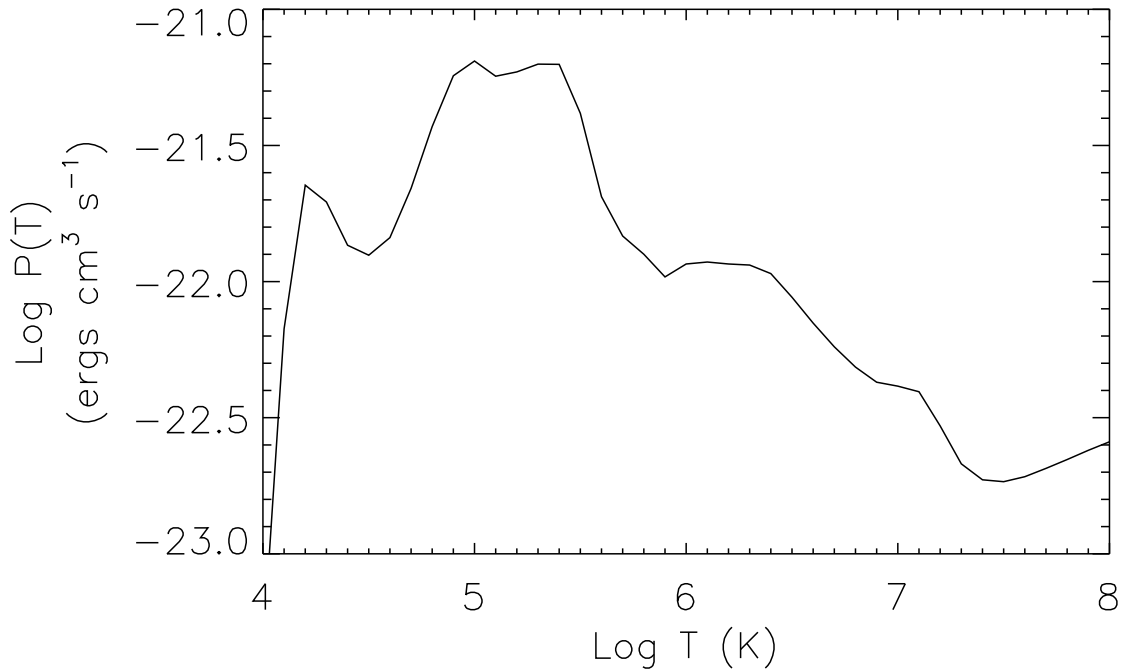


Figure 1.3: The radiative loss function of the solar atmospheric plasma (Mariska 1992).

1 s would supply Earth with enough energy for 10^{10} s, over 300 years. This energy must be somehow passed to the solar atmosphere through the low temperature photosphere, yet no observation has confirmed the transfer of this energy.

There has been considerable debate over the mechanism that is responsible for the energy transfer in the solar atmosphere. Two main mechanisms, Alfvén wave heating and dissipation of current in thin sheets, have emerged as the most viable candidates and will be discussed briefly below. (For a review, see Zirker 1993 and references therein.) Both these theories rely on the convective motions beneath the solar surface to store free energy in the magnetic field which can be dissipated in the solar atmosphere. The primal energy source, then, remains the hydrogen burning occurring in the solar core.

Originally it was thought that waves created by the convective motions of the plasma beneath the solar surface propagated into the solar atmosphere where they dissipated and deposited their energy (e.g., Whitaker 1963). More recently, however, it has been shown that only Alfvén waves (low frequency waves caused by small perturbations in the magnetic field perpendicular to the direction of the field) reach the solar atmosphere before dissipating (e.g., Priest 1982). Alfvén waves make a questionable coronal heating mechanism because of difficulties in both exciting these waves with photospheric motions and dissipating them at coronal heights. The excitation must occur on faster timescales than that of the convective motions (Zirker 1993) and, due to the incompressibility of the waves, the dissipation must be facilitated (by, for instance, turbulence) and occur within one period (Hollweg 1991). Attempted observations of Alfvén waves are summarized by Tsubaki

(1988). No observations currently clarify the role of Alfvén waves in coronal heating.

As an alternative, Parker (1979, 1988) has suggested that dissipation of magnetic current sheets created by tangential discontinuities in the magnetic field heats the ambient solar atmosphere. He called the energy released in this dissipation process a *nanoflare*. The following section will review nanoflare theories and observations.

1.3 Nanoflares

Parker (1972) first proposed that the flux tubes in the solar corona are in nonequilibrium and that this absence of equilibrium will result in small, intermittent releases of free energy. His theory, simplified here, considers a flux tube with an initial uniform magnetic field, $B_0\hat{z}$, and particle pressure, p_0 . The footpoints of this flux tube are rooted in the photosphere where the convective motions will randomly move the magnetic field lines. These motions result in distortions of the flux tube such that

$$\mathbf{B} = B_0\hat{z} + \mathbf{b}_1 \quad (1.12)$$

$$p = p_0 + p_1, \quad (1.13)$$

where $\mathbf{b}_1 = b_x\hat{x} + b_y\hat{y} + b_z\hat{z}$ and $p_1 = p_1(x, y, z)$ are the perturbations in the magnetic field and pressure, respectively. Substituting these values into the equation for magnetostatic equilibrium, $(\nabla \times \mathbf{B}) \times \mathbf{B} = \nabla p$, and reducing gives the condition

$$\nabla(p_1 + B_0b_z) = B_0\frac{\partial \mathbf{b}_1}{\partial z}. \quad (1.14)$$

Taking the divergence of Equation (1.14) gives

$$\nabla^2(p_1 + B_0b_z) = 0 \quad (1.15)$$

(noting that $\nabla \cdot \mathbf{b}_1 = 0$), which implies that $p_1 + B_0b_z$ is a constant except near boundary layers at either footpoint (see Parker 1972 for full discussion). Also, from the \hat{z} -component of Equation (1.14), it can be found that $\frac{\partial p_1}{\partial z} = 0$. Applying this result to the result obtained from Equation (1.15) demonstrates that b_z must also be independent of z .

This result illustrates that for magnetostatic equilibrium to be maintained, the perturbations of the magnetic field in the \hat{z} direction must be invariant. In general, however, the random asymmetric motions of the footpoints will braid the field into a complex, highly variant pattern. Therefore, the field must be in dynamic nonequilibrium, developing tangential discontinuities (current sheets) between areas of dissimilar twisting. Dissipation of these current sheets through fast reconnection (Petschek 1964; and reviewed by Priest 1985) should intermittently release the free energy which Parker has called a *nanoflare*. Because each flux tube is composed of smaller flux tubes called filaments and each filament can be independently driven by the photospheric motions, each flux tube is quite possibly a swarm of nanoflares.

Parker's model of coronal heating by dissipation of current sheets has been carefully scrutinized. Critics suggest that an initially uniform field suffering only small, slow displacements will maintain equilibrium. Supporters, however, have argued that tangential discontinuities must, in fact, occur in various explicit configurations, such as when the field contains a neutral point or when a given field is twisted while the neighboring field is not (for a review of the debate, see Browning 1991). Though it is certain that some

specific configurations will result in current sheet formation, it is not clear that the degree of nonequilibrium will create a sufficient number of current sheets (and hence nanoflares) to be significant in the energy balance of the solar atmosphere.

An alternative interpretation of the dissipation process has been suggested by van Ballegooijen (1986). He hypothesizes that the braiding of an initially uniform field will drive large gradients in the field and plasma. The field remains close to equilibrium (so current sheets do not form), but energy flows “cascade” from large scale lengths to small scale lengths. The resulting turbulence releases the stored magnetic energy.

The energetic significance of nanoflares (if, in fact, they do occur) depends on their rate of occurrence as a function of energy. If they are similar to solar flare hard X-ray bursts (e.g., Dennis 1985), the number of events falls off as a power law with index, α , or

$$\frac{dN}{dE} = AE^{-\alpha} \quad [\text{events erg}^{-1} \text{ s}^{-1}], \quad (1.16)$$

where E (ergs) is the energy of an event and N (events s^{-1}) is the number of events occurring globally per second. The total power due to all events can then be found from

$$\begin{aligned} P_T &= \int_{E_{\min}}^{E_{\max}} E \frac{dN}{dE} dE \\ &= A \int_{E_{\min}}^{E_{\max}} E^{1-\alpha} dE. \end{aligned} \quad (1.17)$$

The result of this integration is

$$P_T = \frac{A}{(2-\alpha)} (E_{\max}^{2-\alpha} - E_{\min}^{2-\alpha}) \quad (1.18)$$

for $\alpha < 2$ and

$$P_T = \frac{A}{(\alpha-2)} \left[\left(\frac{1}{E_{\min}} \right)^{\alpha-2} - \left(\frac{1}{E_{\max}} \right)^{\alpha-2} \right] \quad (1.19)$$

for $\alpha > 2$. This is written in both ranges to show which events limit the total power. For $\alpha < 2$, the total power is determined by the energy of the largest events [Equation (1.18)], but for $\alpha > 2$, the total power is determined by the energy of the smallest events [Equation (1.19)]. For the dissipation process associated with nanoflares to release the energy necessary to account for atmospheric heating, α must be greater than 2 (Hudson 1991). Such a distribution would be softer than that observed for solar flare hard X-ray bursts, viz. $\alpha = 1.8$ (e.g., Dennis 1985).

Determining this distribution through observations of nanoflares, however, is virtually impossible. The lifetime of each event compared to the frequency with which they must occur implies that one nanoflare would begin before the previous one could end; hence, they would be indistinguishable from background noise (Hudson 1991). Furthermore, these events occur on the spatial scale of a filament (~ 200 km). If an individual nanoflare could be observed, it would require a four-fold increase over current instruments' resolving capabilities. It would also require that the line-of-sight of the instrument intercept only the emission from a single filament, a highly improbable situation. The only remaining hope of determining the distribution of nanoflares as a function of energy is to determine the distribution of small-scale, *yet detectable*, energy releases, and assume the observed distribution can be extrapolated to nanoflare energies.

Observations of detectable, small-scale, short-lived releases of energy are plentiful. Extreme ultraviolet (EUV) bursts were observed by *Skylab* as early as 1978 (Emslie & Noyes 1978). Lin et al. (1984) reported short-lived (1-2 s), intermittent spikes in X-ray data. In general, these events have been divided into two classes of phenomena, “explosive events” and “microflares.” In 1983, Brueckner & Bartoe reported small-scale, short-lived distortions in transition region spectral lines observed with the Naval Research Laboratory’s High Resolution Telescope and Spectrograph (HRTS) instrument. These events, characterized by large Doppler shifted and skewed lines profiles, were later dubbed *explosive events* (Dere, Bartoe, & Brueckner 1984, 1989). Microflares were first observed by Porter, Toomre, & Gebbie (1984; Porter et al. 1987) as brightenings throughout the magnetic network present in the Ultraviolet Spectrometer and Polarimeter, an imaging instrument aboard the *Solar Maximum Mission*. It was originally thought that an explosive event was simply the spectral signature of a microflare, but it is not currently clear if these two phenomena are the same process observed with a different instrument type, or two related, yet different phenomena (see the discussion in Porter & Dere 1991). Throughout this dissertation, the term “transition region dynamics” will refer to all dynamic events observed in wavelengths associated with photons emitted by ions at transition region temperatures, while the term “explosive event” will imply a dynamic event observed in spectral data and “microflare” will imply an event observed in image data.

Both microflares and explosive events indicate energy release in the solar atmosphere. Their associated energies are thought to be larger than the theoretical nanoflare energies and smaller than the large energy release associated with typical solar flares. The distribution determined for this “median” energy range may or may not be representative of the distribution at smaller (nanoflare) energies. Recall that the hard X-ray bursts associated with solar flares have a power-law index of 1.8 (e.g., Dennis 1985). If the power index, α , of the distribution of microflares or explosive events as a function of energy is greater than 2, it would demonstrate a steepening of the event size distribution as one progresses from high energy to medium energy events. Such a steepening could continue to lower energies, or the distribution could again flatten.

The distribution of events as a function of energy has previously been estimated for some microflare events. For instance, Krucker & Benz (1998) found this distribution to have an index between 2.3 and 2.6 for the range of energy between 8×10^{24} and 1.6×10^{26} ergs by interpreting changes in the emission measure as heating in the atmospheric plasma. These results depend heavily upon the assumed efficiency of the process to convert the released energy into thermal energy and hence to be observable in the emission measure. This efficiency may be energy dependent and so may dramatically influence the distribution function and its index. Porter, Fontenla, & Simnett (1995) attempted to correct the distribution by assuming an energy dependent efficiency function, but found that the distribution (and index) could not unambiguously be obtained. Furthermore, estimating the energy of these events from an emission measure does not take into account the nonthermal energy associated with bulk flows in the plasma or streaming of high-energy particles. The energy associated with these flows could be a significant portion of the released energy.

The nonthermal energy release is, however, observable in spectral data where the nonthermal velocities of the plasma can be deduced from the Doppler shifts of the spectral line. Therefore measuring the energies related to explosive events would be a more accurate way to find the distribution of events as a function of energy. To measure the energies associated with these events, however, is complex. Even though a general idea of the velocities of the emitting plasma can be deduced from the spectral line, the line profile is weighted by

the emission function of the emitting ion. Also, some part of the observed Doppler shifted velocities are due to the thermal motion of the emitting ion, and so do not apply to the plasma as a whole.

This dissertation will tackle the issue of finding the coronal and chromospheric energy flows associated with these explosive events. After the energy fluxes associated with these events are found, the distribution of events as a function of energy will be compiled to find whether the best-fit power law distribution has an index greater or less than 2. The dissertation, then, will address the questions of 1) whether explosive events themselves are energetically significant and 2) if the distribution of events as a function of energy implies that smaller, undetectable events (nanoflares) may have an effect on the energy balance of the solar atmosphere.

1.4 Roadmap to the Dissertation

Chapter 2 will begin by reviewing general transition region structure and steady-state phenomena. The previously known characteristics of transition region dynamics (or explosive events) will also be reviewed in Chapter 2. The accepted model of magnetic reconnection will be discussed, as well as the previous methods of estimating the energies associated with these events. The need for a better method will be argued.

Chapter 3 will review the physics of measuring the energy flux of a plasma given a velocity distribution function. The energy flux expression will be reduced into four fundamental terms: the kinetic energy flux, the thermal enthalpy flux, the nonthermal enthalpy flux, and the “high-energy component” associated with the skewness of the velocity distribution function. The VDEM function will then be presented as a way to determine the velocity distribution function of the emitting plasma. This approximation has been tested using data simulations and the results of these tests, and hence the robustness of VDEM method, will be discussed. Finally, the data requirements that are necessary to find accurately the energy flux will be stated.

The data used in this study of transition region dynamics were taken with the Solar Ultraviolet Measurements of Emitted Radiation (SUMER) instrument flown aboard the *Solar and Heliospheric Observatory (SOHO)*. This instrument provides the highest resolution available for UV and EUV spectral lines with near continuous coverage. The instrument specifications, as well as a method to find the wavelength array associated with an observed spectrum from reference lines will be discussed in Chapter 4. The spectral lines used in this study will also be introduced and the technique of selecting event profiles from the raw data will be discussed. Finally, the method of preparing event line profiles for VDEM analysis will be reviewed.

The analysis technique introduced in Chapters 3 and 4 will be illustrated in Chapter 5 with an event line profile. The general results and event characteristics will be shown for all profiles selected as events. Chapter 5 will also compare the event characteristics derived from this study to the previous results and explain the possible sources of any discrepancy.

The global energetics extrapolated from the data used in this study are discussed in Chapter 6. The distribution of events as a function of energy for coronal and chromospheric flows is shown for the events observed in each analyzed spectral line. The necessary nanoflare energy (and number of nanoflares at this energy required to heat the solar atmosphere) is predicted from the distribution. These findings will be compared to previous results and the possible sources of systematic errors will also be discussed.

Chapter 7 will summarize the results of the dissertation. The implications of these results will be reviewed, as well as the needs for future study.

CHAPTER 2

EXPLOSIVE EVENTS IN THE SOLAR TRANSITION REGION

Explosive events involve highly dynamic plasmas in the solar transition region. Before discussing them, it is first appropriate to describe the conditions of the “quiet” transition region. This chapter begins with an overview of its properties including structure, relevant timescales, and static phenomena. The characteristics of explosive events will then be reviewed along with the current model explaining them. Previous estimates of the energy flux associated with these events will be discussed in Section 2.4, along with the reasons why these estimates do not fully address the energetics of explosive events. Finally, the need for a better method of analyzing explosive events will be argued in Section 2.5.

2.1 The Transition Region

The transition region of the solar atmosphere, defined roughly by the temperature range from $10^{4.4}$ to 10^6 K, has been discussed in detail by Mariska (1992). It is generally accepted to consist of gas at a uniform pressure, $n_e T \approx 1 \times 10^{15}$ K cm $^{-3}$. The main constituents of the atmospheric plasma are electrons and hydrogen and helium nuclei. The density of hydrogen, n_H , and helium, n_{He} , can be found from their abundances relative to the electron density, viz. $n_H = 0.83n_e$ and $n_{He} = 0.083n_e$ (based on abundances in Mariska 1992).

There has been an ongoing debate concerning the magnetic structure of the solar transition region. The classical view of the transition region has been of a one-dimensional interface between the cool ($\leq 10^4$ K) chromospheric plasma and the hot ($\geq 10^6$) coronal plasma confined to a large scale flux tube. However, images taken in UV and EUV wavelengths show that small scale structure (similar to chromospheric fine structure) persists at transition region temperatures. Dowdy, Rabin, & Moore (1986) suggested that the solar atmosphere is a magnetic “junkyard” – a combination of short, low-lying loops (with a spatial scale of ~ 1000 km and a maximum temperature of $\sim 10^5$ K) and tall coronal loops that indeed contain a classical interface-type transition region. The percentage of the observed emission that originates from the shorter loops has been suggested to be as high as 85% (Dere, Bartoe, & Brueckner 1984). Such a possible complex structure obviously complicates the discussion of the energy transfer in the solar atmosphere. Yet, because the spatial scale of the fine structure is the same as current instrumental resolution limits, it is difficult to assess the true magnetic structure in the transition region.

The filamentary structure of the transition region is described by a volumetric filling factor, γ . The filling factor is the ratio between the true volume of the emitting plasma and an assumed volume (usually related to the resolution of the instrument and the scale height of the atmosphere). Values for the filling factor range from 1 (implying the assumed volume is entirely filled with emitting plasma) to $\ll 1$ (implying only a small fraction of the assumed volume is filled with the emitting plasma). To find the true volume, the density must be accurately measured using *density sensitive line ratios*. This method is based on the ratio of the emission between two lines formed by the same ion by transitions between two

separate energy states. If one state is always populated by collisions and deexcited through spontaneous decay and another state is populated by collisions but deexcited through both collisions and spontaneous decay, the ratio of the two lines is density sensitive. (For full discussion, see Mariska 1992.) This accurate density can then be used in conjunction with the emission measure, $\int n_e^2 dV$, to find the true volume of the emitting plasma, i.e.,

$$V_{\text{true}} = \frac{\int n_e^2 dV}{n_e^2}. \quad (2.1)$$

Typically, the true volume of emitting plasma is much smaller than the assumed volume. Values for the volumetric filling factor for the transition region are generally 10% or less (e.g., Mariska 1992).

Static plasma in the solar transition region is generally assumed to be in thermal equilibrium and at a uniform pressure. The validity of these approximations depends upon the relevant timescales of the emitting plasma. These timescales will be discussed in terms of a plasma with an initial temperature of 10^5 K, electron density of 10^{10} cm^{-3} and hydrogen and helium densities from the abundances given above.

If a plasma is anisotropically heated (for instance, parallel to the direction of the magnetic field), the time for the plasma to re-establish thermal equilibrium, or isotropize, can be found by

$$\tau_T^e \approx 9.6 \times 10^{-2} \frac{T^{\frac{3}{2}}}{n_e} \quad \tau_T^i \approx 3.3 \times 10^{10} \frac{(m_i T^3)^{\frac{1}{2}}}{n_i Z^2} \quad (2.2)$$

(Huba 1994), where m_i is the mass of the ion, Z is the charge of the ion, and τ_T^e and τ_T^i are the isotropization times for the electrons and ions, respectively. For the plasma described above, the electrons would reach equilibrium on the order of 10^{-4} s, the hydrogen on the order of 10^{-2} s and the helium on the order of 10^{-1} s.

If a single species (α) is preferentially heated over the background species (β), the time for both species in the plasma to re-establish equilibrium is given by

$$\tau_e^{\alpha/\beta} \approx 5.6 \times 10^{17} \frac{(m_\alpha T_\beta + m_\beta T_\alpha)^{\frac{3}{2}}}{(m_\alpha m_\beta)^{\frac{1}{2}} Z_\alpha^2 Z_\beta^2 n_\beta} \quad (2.3)$$

(Huba 1994). If electrons are preferentially heated, equilibrium would be re-established between the heated electrons and the background plasma (consisting of electrons and hydrogen and helium nuclei) on the order of 10^{-5} s, hydrogen on the order of 10^{-2} s, and helium on the order of 10^{-3} s. Note that any preferentially accelerated helium will reach equilibrium with hydrogen long before it isotropizes, so the time for the plasma to reach thermal equilibrium is limited by the time for preferentially heated hydrogen to establish equilibrium with the background plasma, or 10^{-2} s.

If a change in the pressure of a plasma (for instance, through sudden heating) occurs at a given point within a magnetic structure, the plasma within that structure can no longer be considered at constant pressure. The time it would take for the perturbation to propagate throughout the structure (and hence for uniform pressure to be re-established) is related to the time for an ion pressure wave (traveling at the ion sound speed, $\sqrt{\frac{kT}{m_i}}$) to traverse the length of the plasma structure. At a temperature of 10^5 K, the ion sound speed is approximately 40 km s^{-1} . Assuming the structure of the emitting plasma is 1,000 km in length, constant pressure would be re-established on the order of 25 s. The plasma, then, can be considered at thermal equilibrium for time scales on the order of a hundredth of a

second, but the uniform pressure assumption is not valid except for timescales greater than ~ 25 s.

Although the search for an energy source in the solar atmosphere centers around the heating of the solar chromosphere and corona, the plasma in the transition region also requires energy input to sustain radiation. The time for a typical transition region plasma to lose its thermal energy through radiation is found by

$$\begin{aligned} \frac{\frac{3}{2}nkT}{\Delta t} &= n_e n_H P(T) \\ \Delta t &= \frac{\frac{3}{2}nkT}{n_e n_H P(T)}, \end{aligned} \quad (2.4)$$

where n is the total number density of the plasma. For a plasma at 10^5 K with a density characteristic of a constant pressure of 10^{15} K cm $^{-3}$, the cooling time is approximately 2 s. Therefore, energy input must be on a timescale of seconds to maintain observed transition region temperatures.

Transition region plasma emits radiation primarily in the form of emission lines formed by bound-bound transitions in highly ionized species. These spectral lines are often redshifted away from their expected laboratory wavelengths. Due to the difficulty in defining the absolute wavelength associated with an observed spectral line, the absolute Doppler shifts of the line centroids are not well known. There have been several studies, however, that have found the relative Doppler shifts between transition region emission lines and chromospheric emission lines. (It is believed that lines emitted by neutral, chromospheric ions suffer no or very small shifts from their laboratory wavelengths, e.g., Brekke, Hassler, & Wilhelm 1997.) Chae, Yun & Poland (1998) have determined the Doppler shift velocities as a function of temperature with reference to the coolest chromospheric lines. They found that the magnitude of the Doppler redshift increases as a function of temperature to approximately 11 km s $^{-1}$ at $10^{5.4}$ K and then decreases toward coronal temperatures. (Throughout this dissertation, the term “solar wavelength” will refer to the typical redshifted wavelength associated with a spectral line observed from a solar plasma.)

The redshift observed in transition region spectral lines implies that mass is flowing from the corona downward through the transition region. To maintain mass continuity, there must also be mass injected into the corona. The injected mass is believed to be linked to the upflows associated with spicules (cool plasma jets approximately 1,000 km in cross-sectional diameter). Initially the spicule plasma is at chromospheric temperatures, and so it is not observed in transition region spectral lines. The matter flows into the corona, is heated, and falls back toward the solar surface. As this matter cools to transition region temperatures, it emits photons associated with redshifted wavelengths.

All spectral line profiles emitted in the transition region are also broadened well beyond their expected thermal width; however, most are still well represented by a Gaussian function, i.e.,

$$I(\lambda) \sim e^{-\frac{(\lambda-\bar{\lambda})^2}{2\sigma^2}}, \quad (2.5)$$

where $I(\lambda)$ is the intensity of the line profile as a function of wavelength, λ , and $\bar{\lambda}$ is the wavelength associated with the centroid of the line profile. (As mentioned above, transition region lines are typically redshifted from their laboratory wavelengths, thus $\bar{\lambda}$ is the wavelength associated with that redshift, or the average “solar wavelength.”) Traditionally, the

width of the line profile, σ , has been expressed as

$$\sigma = \frac{\lambda_0}{c} \sqrt{\frac{kT}{m_i} + \frac{\zeta^2}{2}}, \quad (2.6)$$

where λ_0 is the rest wavelength of the spectral line, $\sqrt{\frac{kT}{m_i}}$ is the thermal velocity of the emitting ion with mass, m_i , and ζ is the most probable nonthermal velocity. The magnitude of this nonthermal velocity begins at approximately 10 km s^{-1} for a plasma at $2 \times 10^4 \text{ K}$ and increases to a maximum of approximately 30 km s^{-1} for a plasma with a temperature of $3 \times 10^5 \text{ K}$. The most probable nonthermal velocity then decreases to approximately 20 km s^{-1} for plasma at coronal temperatures (Chae, Schühle, & Lemaire 1998). No center-to-limb dependence of these values has been found. Explanations for this excess broadening are varied, but these motions are typically explained as being due to turbulent motions in the emitting plasma.

(Throughout the remainder of this dissertation, a slightly different definition of nonthermal velocity has been adopted. The width of the Gaussian describing the line intensity is re-defined as

$$\sigma = \frac{\lambda_0}{c} \sqrt{\frac{kT}{m} + \xi^2}, \quad (2.7)$$

where ξ is the nonthermal root mean square (r.m.s.) velocity. This would imply that $\xi = \frac{\zeta}{\sqrt{2}}$, i.e., that the r.m.s. nonthermal velocity is $\frac{1}{\sqrt{2}}$ times the most probable speed.)

2.2 Explosive Event Characteristics

One of the most significant results from the 1975 High Resolution Telescope and Spectrograph (HRTS) rocket flight was the discovery of highly time- and space-dependent brightenings in chromosphere-corona transition region spectral lines. The observed events were small-scale ($\sim 1,500 \text{ km}$ or 2 HRTS pixels), short-lived ($\sim 60 \text{ s}$) phenomena characterized by enhanced nonthermal broadening and/or asymmetry in the wings of the spectra. They were mainly observed in transition region emission lines, most often in lines with a formation temperature around 10^5 K , and were the first unambiguous observation of nonthermal releases of energy in the solar transition region. Brueckner & Bartoe (1983) originally classified these events into *turbulent events* (with maximum Doppler shifted velocities of $\pm 250 \text{ km s}^{-1}$) and *jets* (with maximum observed velocities of $\pm 400 \text{ km s}^{-1}$). Their classification did not depend on the asymmetry of the line profile, but in general, one wing of the profile was dominant for both turbulent events and jets. In later HRTS flights, however, the “turbulent” events were observed to have their red and blue wings separated along the slit (meaning the emission of each wing originated in spatially distinct regions), hence the motions could not be explained through turbulence alone. The classification was dropped and the name “explosive events” was adopted (Dere, Bartoe, & Brueckner 1984, 1989).

Figure 2.1 shows an example of a typical explosive event in the C III 977 Å spectral line. [These sample spectra were taken with the Solar Ultraviolet Measurements of Emitted Radiation (SUMER) telescope and spectrometer (discussed fully in Section 4.1) on 1996 May 10. The spatial and temporal resolution of this instrument is very similar to that of the HRTS instrument, thus these observations are similar to the original observations made by HRTS.] The exposures are shown sequentially (a-f), each with an exposure time of 48 s. The horizontal axis is the dispersion direction and the vertical axis is the spatial pixel

number measured along the slit. The arrow highlights the onset and decline of enhanced emission in the wings of the profile around spatial pixel 10. This type of emission, first observed by HRTS, is referred to as an explosive event.

The loose definition of the spectral signature of explosive events introduces a wide variety of line profile shapes that can be included in the explosive event category. A sample of these line profiles (solid) is shown in Figure 2.2 along with a thermally and nonthermally broadened Gaussian function (dashed) that would be considered a normal (non-event) line profile. These are the line profiles associated with spatial pixel 10 of the spectra shown in Figure 2.1. Profile (a) is not notably broadened or skewed, and so would not immediately be considered an explosive event. The remaining profiles, however, are both broadened and skewed to varying degrees. They illustrate the different line profile shapes that might be associated with explosive events. From the HRTS data, it was noted that some events showed very symmetric, yet extremely broadened line profiles, while others showed asymmetric profiles with one wing clearly dominant (the blue wing dominant 60% of the time – Porter & Dere 1991) or excess emission in one wing completely absent (Dere, Bartoe, & Brueckner 1989).

The location of these explosive events were observed to be randomly distributed over the solar surface, yet the shape of the line profiles (for instance, the degree of broadening) was not dependent on the observing angle, as one would expect if the flows had a preferred direction (such as radial). Hence the events were said to be “statistically isotropic” (Dere, Bartoe, & Brueckner 1989). Explosive events were mainly observed in the edges of the magnetic network lanes but were not generally associated with the strongest magnetic field unlike most energetic phenomena (Porter & Dere 1991). Instead they most often occurred in areas of mixed polarity near magnetic neutral lines (Chae et al. 1998). They did not exhibit any proper motion along the slit (e.g., Brueckner & Bartoe 1983) which would indicate no motion transverse to the line-of-sight.

The spatial and temporal scales associated with explosive events ($\sim 1,500$ km and 60 s) are similar to the spatial and temporal resolution of the HRTS spectrograph (~ 750 km and 20 s). Significant changes in the line profiles were observed between two sequential exposures. Also, explosive events were observed to recur in the same location repeatedly. It is not clear, then, if the events were resolved by the HRTS instrument or if several events with temporal and spatial scales much less than the spectrograph resolution were being interpreted as a single event.

The global birthrate of the events, R (events s^{-1}), describes the number of new events occurring per second. It is defined as

$$R = \frac{N_0 A_{\text{sun}}}{\tau A_{\text{slit}}}, \quad (2.8)$$

where N_0 is the total number of events counted in the observation time τ , A_{sun} is the total solar surface area ($4\pi r_{\text{sun}}^2$ where r_{sun} is the solar radius), and A_{slit} is the deprojected area of the slit. Basically, it multiplies the number of events observed per second during the observation time by a “spatial coverage factor.” Brueckner and Bartoe (1983) first found a global birthrate of 753 events s^{-1} estimated from the data of the first three HRTS flights. Dere, Bartoe, & Brueckner (1989) found a similar birthrate of 600 events s^{-1} using the same method. Cook et al. (1988) reported a birthrate significantly lower than these two values (44 events s^{-1}) but used an incorrect definition of birthrate in their estimate. Note that the total number of events observed, N_0 , is influenced by the event detection technique. For HRTS data, events were identified by visual inspection of the photographic prints (e.g.,

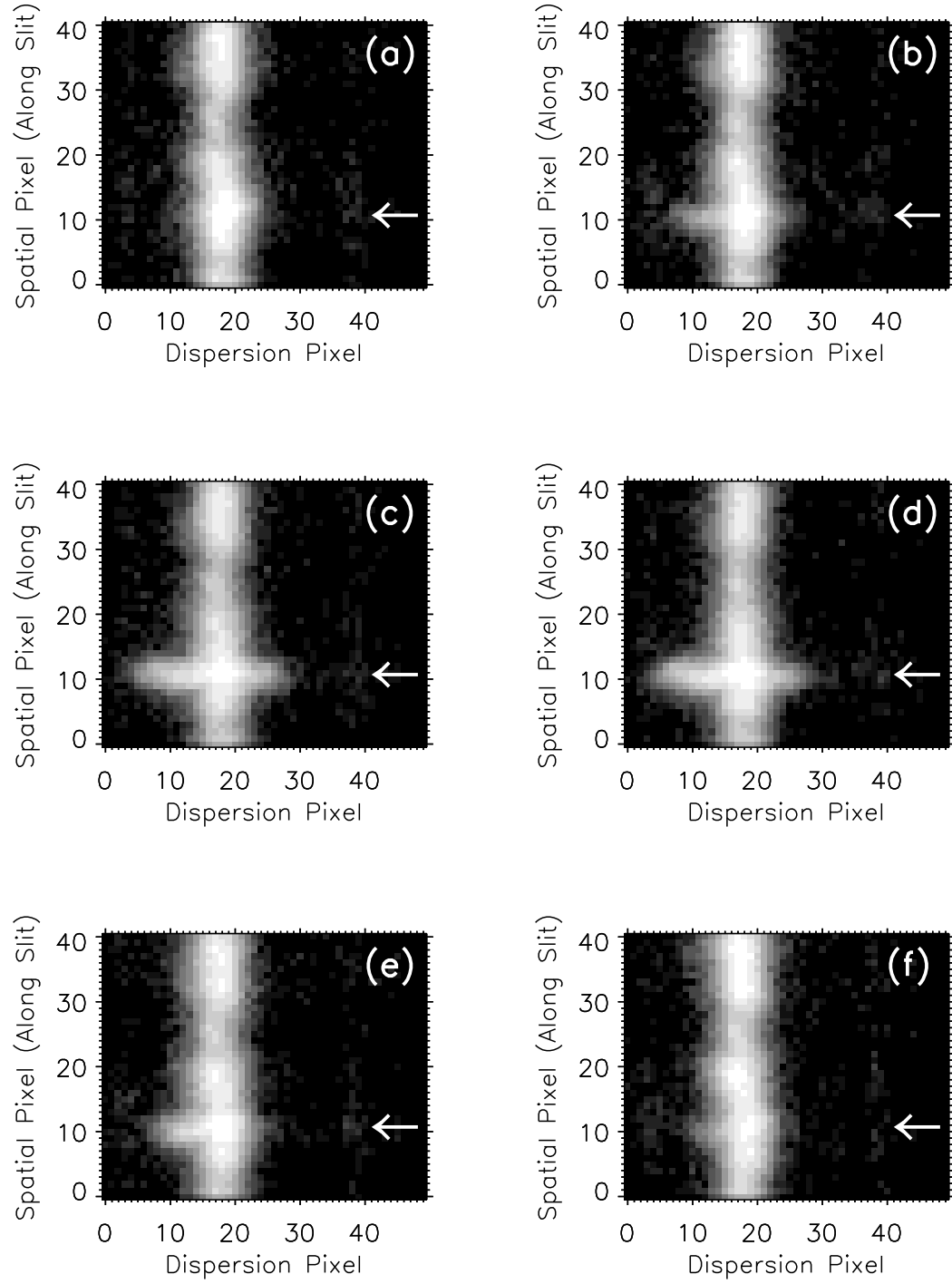


Figure 2.1: Examples of sequential spectra (a-f) of the C III 977 Å line exhibiting explosive event characteristics around spatial pixel 10. These observation were taken with the SUMER instrument on 1996 May 10.

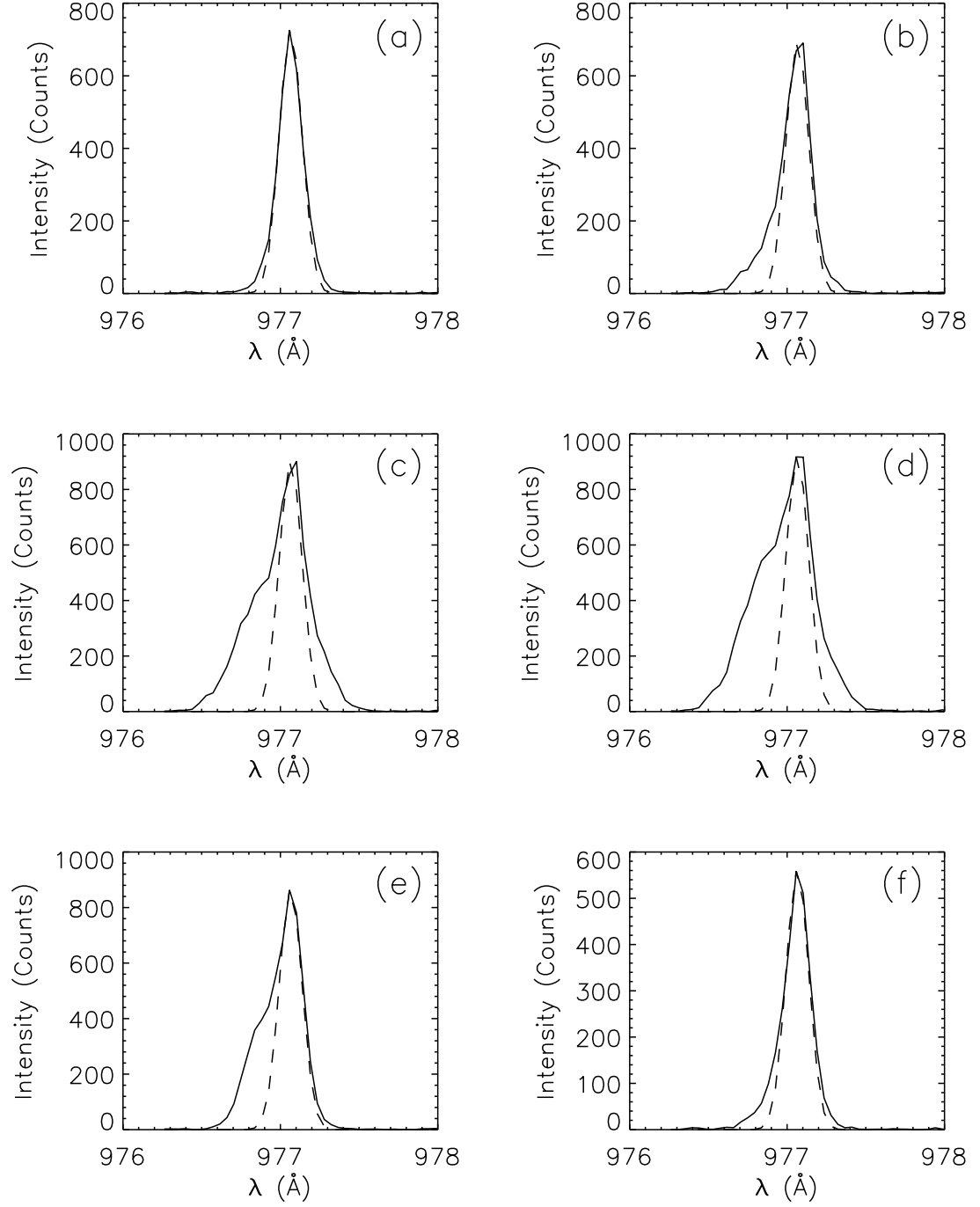


Figure 2.2: Corresponding line profiles (solid) of the C III 977 Å line spectra in Figure 2.1 associated with spatial pixel 10 along with a thermally and nonthermally broadened Gaussian function (dashed) that would be considered a normal, non-event line profile.

Cook et al. 1988). [Brueckner & Bartoe (1983) and other references did not explicitly state the event selection method, but it is assumed that it was also by direct examination of the photographic prints.] This implies that only large, easily distinguishable events were selected. Hence, the birthrate reported from these studies represents only a lower limit on the true birthrate.

The density of the explosive event plasma has only been measured twice using the density sensitive line ratio method. Dere et al. (1991) examined a single explosive event line profile in lines of O IV at approximately 1.7×10^5 K. They found a density of $7 \times 10^{10} \text{ cm}^{-3}$, an order of magnitude greater than would be implied by a constant pressure transition region, $7 \times 10^9 \text{ cm}^{-3}$. More recently, Doschek et al. (1998) have measured the density in a single O IV event profile emitted from an active region. They, again, found a very high density $1 \times 10^{12} \text{ cm}^{-3}$ (implying a pressure of $2 \times 10^{17} \text{ K cm}^{-3}$), but they felt this one explosive event profile was atypical and the result should not imply that all explosive event plasmas have such a high density.

A large volume of literature has been published detailing the explosive event characteristics observed by HRTS (Brueckner & Bartoe 1983; Dere, Bartoe, & Brueckner 1986, 1989; Cook et al. 1988; Dere et al. 1991). Dere (1994) reviewed these previous works and published the average (or median) values for typical characteristics such as length, lifetime, birthrate, and global “steady-state” number, N_{global} . The steady state number is found by multiplying the global birthrate by the average lifetime of the events, $\overline{t_E}$, i.e.,

$$N_{\text{global}} = R\overline{t_E}. \quad (2.9)$$

Table 2.1 summarizes these characteristics. Though other UV and EUV spectrometers have observed explosive events (most notably, the Solar Ultraviolet Measurements of Emitted Radiation (SUMER) telescope and spectrometer), the HRTS results remain the most complete characterization of explosive events.

2.3 The Acceleration Mechanism

Explosive events are most often observed to occur in the magnetic network lanes at the boundaries of supergranular cells near magnetic neutral lines during times of magnetic cancellation (Porter & Dere 1991; Chae et al. 1998). They have also been associated with the emergence of new magnetic flux (e.g., Dere et al. 1991). Because of these associations, explosive events are thought to be the products of magnetic reconnection, specifically magnetic cancellation of the photospheric fields with either emerging flux (Dere et al. 1991) or dissipating active region flux (Porter & Dere 1991).

This reconnection mechanism is very similar to the one discussed in Chapter 1 for nanoflares with the main difference being one of magnitude. The reconnection that is thought to drive nanoflares takes place between two filaments with a spatial scale of 10^2 km, while the reconnection that accelerates explosive event plasma occurs between flux tubes with a spatial scale of 10^4 km. A possible reconnection scenario is shown in Figure 2.3 (based on a hypothesis by Dere et al. 1991). The new magnetic flux emerging from the supergranular cells is driven toward the stationary field in the network lanes by supergranular flows. If the driven flux is of opposite polarity to the stationary flux, the fields reconnect driving a bi-directional jet of plasma away from the reconnection point. This type of bi-directional jet would explain observations of simultaneous offsets of the red and blue wings

Table 2.1: Explosive event characteristics as observed by HRTS (Dere 1994).

Profiles	<p>Average Doppler shift velocities of 100 km s^{-1}</p> <p>Asymmetric profiles</p> <p>Motions along slit rarely detected</p> <p>No center-to-limb variation: statistically isotropic</p>
Spatial Scales	<p>$1,500 \text{ km}$</p> <p>Evidence for smaller scales</p>
Time Scales	<p>Average lifetime = 60 s</p> <p>Evidence for repeatability</p>
Temperature	<p>Maximum brightness at 10^5 K</p> <p>Rarely seen in chromospheric lines</p> <p>Occasionally seen in coronal lines</p>
Birthrate	<p>$600 \text{ events s}^{-1}$</p> <p>Quiet Sun and Coronal Holes</p>
Steady-State Number	<p>$36,000 \text{ events}$</p>

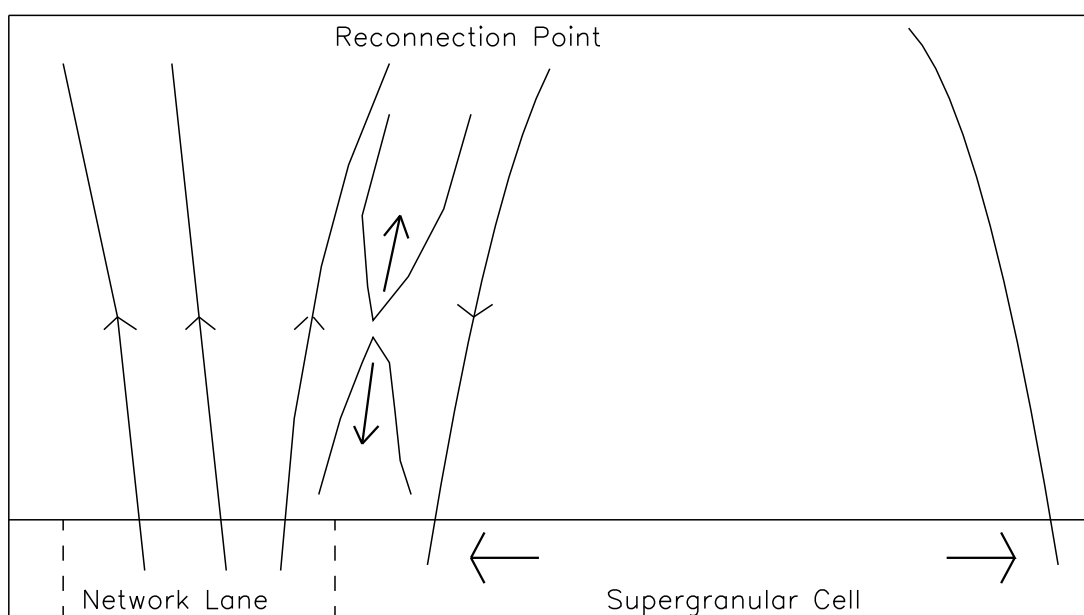
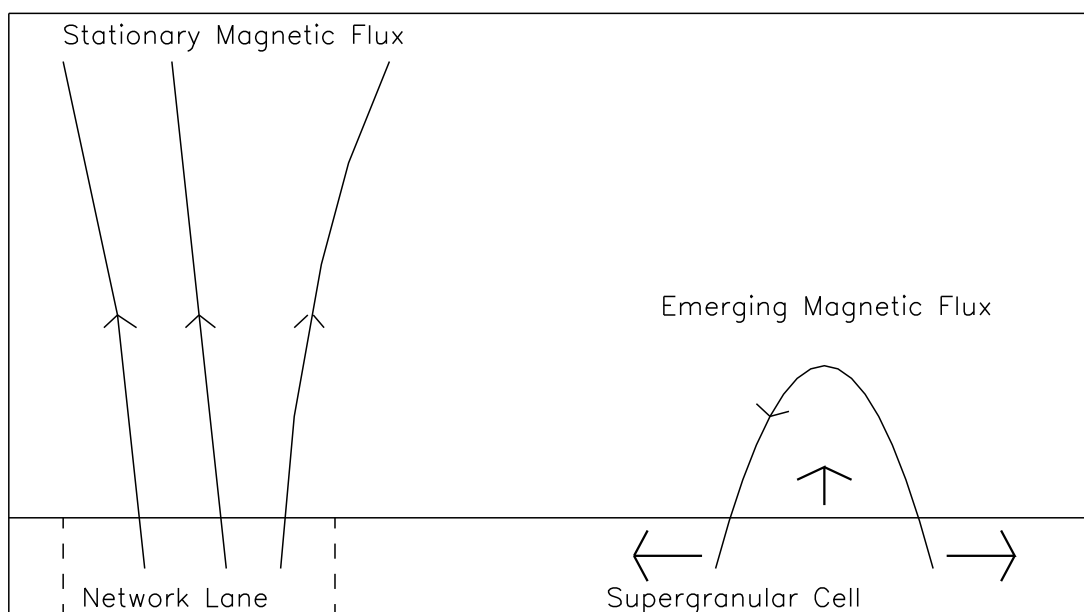


Figure 2.3: Reconnection scenario based on Dere et al. (1991).

of explosive events along the spectrograph slit (Dere, Bartoe, & Brueckner 1989; Innes et al. 1997).

Though it is generally agreed that changes in the magnetic field must be somehow connected to the energy release in the solar atmosphere, it is not clear that a simple magnetic reconnection scenario can explain all the observational elements associated with explosive events. For instance, events occur on the time scale of 60 s and spatial scale of 1,500 km, while photospheric cancellation occurs on time scales of hours and spatial scales of 5,000–10,000 km (Livi, Wang, & Martin 1985). These scales have been reconciled by assuming that the reconnection occurs in a bursty manner in intervals along the neutral line of cancellation (Dere et al. 1991). This is consistent with the fast reconnection model suggested by Petschek (1964; Priest 1982). In this model, the reconnection time is found by

$$\tau_R = \frac{L}{CV_A}, \quad (2.10)$$

where L is the characteristic length of the reconnection, C is a constant between 0.01 and 0.1, and V_A is the local Alfvén speed. With a characteristic length of 1,500 km and Alfvén speed of 100 km s^{-1} , the reconnection time would be 150–1,500 s.

Another difficult observational element to explain using a simple reconnection scenario is the lack of center-to-limb dependence of the explosive event profiles. If most coronal loops have a similar geometry (such as the uniform twist field), then the bi-directional jet product of magnetic reconnection would have a preferred direction (such as radial). However, Karpen et al. (1998) have shown through MHD modeling that the direction of these flows is determined by the shear and geometry of the reconnecting field. The flows need not have a preferred direction, but instead depend only on the unique structure of the local magnetic field.

One puzzling observation is the absence of motion of an event along the spectral slit (i.e., transverse to the line-of-sight). An average explosive event with a maximum velocity of 100 km s^{-1} should traverse $6 \times 10^3 \text{ km}$ (or $8''$ at sun center) in its lifetime of 60 s. If even a small component of the velocity was directed along the slit, the propagation of the explosive events would be detected with the spatial resolution of the HRTS spectrograph ($1''$). However, only rarely has motion along the slit been detected (Brueckner & Bartoe 1983; Dere, Bartoe, & Brueckner 1989). One explanation commonly accepted is that the accelerated material is being heated or cooled and is no longer visible in the original spectral line (Dere, Bartoe, & Brueckner 1989). The cooling timescale of a transition region plasma at 10^5 K (2 s) is much less than the temporal resolution of the HRTS instrument (20 s); therefore, this hypothesis is plausible.

Accepting the hypothesis that explosive events are caused by magnetic reconnection, the local magnetic field strength can then be found. Most models suggest that during reconnection, plasma is ejected at approximately the local Alfvén speed,

$$V_A = \frac{B}{(4\pi\rho)^{\frac{1}{2}}}, \quad (2.11)$$

where B is the local magnetic field strength and ρ is the mass density of the plasma (Dere et al. 1991). This is a useful tool to find the local magnetic field strength associated with the reconnection. For a mass density typical of that in the solar transition region and Alfvén speed of 100 km s^{-1} , the local magnetic field annihilated to accelerate the explosive event would be approximately 5 G. The magnetic field strength measured at the photosphere is 10–1,000 G, so this amount of field is physically realizable.

2.4 Energy Release

The large nonthermal broadening and asymmetries exhibited by explosive events led to speculation that they are associated with significant mass and energy flows and perhaps could be the elusive coronal heating source. Brueckner & Bartoe (1983) first estimated the turbulent energy flux associated with typical events from the line widths observed during the first three HRTS rocket flights. They found an average energy flux contribution to the global solar atmosphere using

$$j_{\text{global}} = \frac{\varepsilon_{\text{kin}} V R}{A_{\text{sun}}}, \quad (2.12)$$

where V was their estimate for the total volume of the plasma element (related to the resolution of the spectrograph) and R was the global birthrate. The average kinetic energy density of the events, ε_{kin} (ergs cm⁻³), in Equation (2.12) was found by $\varepsilon_{\text{kin}} = \frac{1}{2} \rho \overline{v^2}$, with $\overline{v^2}$ found from the average width, σ , of the event line profiles [cf. Equation (2.6)]. (Note that they used this definition of the width to find the average velocity even though the intensity of the explosive event line profiles was non-Gaussian.) They assumed a mass density typical of that in a constant pressure transition region and a filling factor of unity. Based on this method, they determined that explosive events represented an energy flux into the corona of 9×10^3 ergs cm⁻² s⁻¹, insufficient by at least an order of magnitude to meet coronal heating requirements, viz. 3×10^5 ergs cm⁻² s⁻¹ (Withbroe & Noyes 1977).

A second estimate of the energy associated with explosive events was done by Cook et al. (1988) from a spectral survey using the HRTS instrument aboard *Spacelab 2*. They calculated the energy flux contribution of a single explosive event to the global solar atmosphere and multiplied it by the steady-state number of events, N_{global} , i.e.,

$$j_{\text{global}} = N_{\text{global}} \left\{ \frac{n_e n_H P(T) V}{A_{\text{sun}}} + \frac{\frac{5}{2} n k T \bar{v} A_E}{A_{\text{sun}}} + \frac{\frac{1}{2} \rho \bar{v}^3 A_E}{A_{\text{sun}}} \right\}, \quad (2.13)$$

where A_E is the area of the event and the first term in the bracket on the right hand side is the radiation term, the second term is the thermal enthalpy flux, and the final term is the kinetic energy flux. In Equation (2.13), $P(T)$ is the radiative loss function around 10^5 K ($\sim 10^{-21}$ ergs cm³ s⁻¹). The average velocity, \bar{v} , was again derived from the width of the distribution [cf. Equation (2.6)]. They found the energy flux to be 2.5×10^4 ergs cm⁻² s⁻¹, still ~ 10 times too small to be significant for coronal heating.

Both of the above estimates of the energy flux associated with explosive events are inadequate approximations. Both have assumed the energy flux depends solely on the velocity associated with the width of the line profile, $\overline{v^2}$. Yet, as will be shown in this dissertation, the true measurement of energy flux scales with $\overline{v^3}$.

2.5 The Need for a Better Method

The majority of information known about explosive events originates from the ten HRTS data sets. Though this information is invaluable to the present understanding of explosive events, several advances can be made using a more complete data set and improved analysis techniques. This dissertation endeavors to improve upon several areas of analysis concerning explosive events and address 1) whether explosive events are important to the global energetics of the solar atmosphere and 2) if their distribution as a function of energy

implies that smaller, undetectable events may have an effect on the energy balance of the solar atmosphere.

A correct estimate of the energy flux carried by individual events requires a more careful consideration of the energetics than the first-order approximation based on the characteristic velocities used by Brueckner & Bartoe (1983) and Cook et al. (1988). As will be derived in Chapter 3, the energy flux can only be accurately calculated from the bulk velocity distribution function of the plasma. Using a new analysis technique previously developed for the analysis of soft X-ray line profiles, the Velocity Differential Emission Measure (VDEM) (Newton, Emslie, & Mariska 1995), the bulk velocity distribution can be found. With an accurate measurement of the energy flux, the importance of explosive events to the energy balance of the solar atmosphere can be addressed.

A complete evaluation of the global energetics associated with reconnection events must consider the distribution of event sizes, $\frac{dN}{dE}$ (events $\text{erg}^{-1} \text{s}^{-1}$), and in particular whether this distribution has a power-law index, α [$\frac{dN}{dE} \sim E^{-\alpha}$], greater or less than 2 (Hudson 1991). As discussed in Chapter 1, an index greater than 2 could imply that small, undetectable events (nanoflares) are the source of atmospheric heating. The HRTS data set was not extensive enough for a statistical number of events to be observed and hence this index has yet to be determined. Moreover, the method of selecting events utilized with the HRTS data is inadequate to develop an accurate distribution of events as a function of energy. If only the large, easily distinguishable events are analyzed, the distribution would not well represent the low energy events. A new method of selecting events based on comparing a line profile's measured width and skewness to statistically significant cutoff values will be introduced in Chapter 4.

To complete these goals, the most recent spectral data from the Solar Ultraviolet Measurements of Emitted Radiation (SUMER) telescope and spectrometer will be used. The SUMER instrument has spatial and temporal resolution similar to that of the HRTS instrument, but it provides an extensive data set so that a statistically significant number of events can be analyzed.

CHAPTER 3

MEASURING THE ENERGETICS OF EXPLOSIVE EVENTS

This chapter introduces a new method for measuring the energy flux of a dynamic transition region plasma from an explosive event line profile. The first section reviews how to measure the energy flux from the bulk velocity distribution of the plasma, a function that describes the fraction of fluid flowing with a given velocity. Also in this section, the four components of energy flux (the kinetic energy flux, the thermal enthalpy flux, the nonthermal enthalpy flux, and the “high-energy” component) are derived from the general definition of energy flux and their physical interpretations are discussed. To accurately evaluate the energy flux, the temperature, density, filling factor, and bulk velocity distribution of the plasma must be known. In Sections 3.2 and 3.3, the procedures for determining or approximating these values from an explosive event line profile are introduced including a method of approximating the bulk velocity distribution with the Velocity Differential Emission Measure (VDEM) function. The robustness of using these approximations to find the energy flux will be characterized in Section 3.4 and the resulting data restrictions on useful data sets will be summarized in Section 3.5.

3.1 The Energy Flux of a Transition Region Plasma

As discussed in the last chapter, a more complete analysis is needed to address the importance of transition region dynamics on the energy balance of the solar atmosphere. To calculate the energy deposited in the corona or chromosphere by reconnection events in the solar transition region, the energy flux of the events must first be accurately measured. It is important to measure the energy *flux* of the events (proportional to $\overline{v^3}$), as opposed to simply the energy of the events (proportional to $\overline{v^2}$), because the interest lies in how much energy travels out of the transition region and into the other areas of the solar atmosphere. It is this dependence on the third moment of the velocity that makes the energy flux a difficult quantity to measure. Furthermore, classical (and commonly accepted) approximations for the energy flux are no longer valid when treating the highly dynamic (non-Maxwell-Boltzmann) plasmas associated with explosive events. Therefore, a full treatment of the energy flux equation is required.

Before discussing the specific methods of measuring the energy flux associated with explosive events, it is appropriate to review the energy flux equations derived from a given particle’s velocity distribution function, $f_{\text{particle}}(\vec{v})$ ($(\text{cm s}^{-1})^{-3}$). Formally, the energy flux associated with particle species, i , in a given volume can be written as

$$\vec{j}_{E,i} = \overline{\frac{1}{2}\rho_i(\vec{v} \cdot \vec{v})\vec{v}} = \int \frac{1}{2}\rho_i(\vec{v} \cdot \vec{v})\vec{v}f_{\text{particle},i}(\vec{v})d\vec{v} \quad (3.1)$$

(Krall & Trivelpiece 1986), where ρ_i (g cm^{-3}) is the mass density of the particles. In Equation (3.1), $f_{\text{particle},i}(\vec{v})d\vec{v}$ describes the fraction of particles with a velocity between \vec{v} and $\vec{v} + d\vec{v}$ where, assuming cylindrical symmetry, $\vec{v} = v_{\perp}\hat{r} + v_{\parallel}\hat{z}$. If there are several species

of particles in the plasma, the energy flux must be found for each species individually. The total energy flux of the plasma would then be the sum of these constituent energy fluxes. As a way to concisely describe the energy flux associated with a multi-species plasma in thermal equilibrium, we introduce the *bulk velocity distribution*. The bulk velocity distribution function, $f_{\text{bulk}}(\vec{v})$ ($(\text{cm s}^{-1})^{-3}$), represents bulk, fluid flows in the plasma but contains no information on the thermal motions of the constituent ions. It is related to a constituent particle's velocity distribution function through the convolution

$$f_{\text{particle},i}(\vec{v}) = \int f_{\text{bulk}}(\vec{v}') f_{\text{th},i}(\vec{v} - \vec{v}') d\vec{v}', \quad (3.2)$$

where $f_{\text{th},i}$ ($(\text{cm s}^{-1})^{-3}$) is the distribution of particles' velocity that arises from the temperature of the ion in question as opposed to the bulk fluid motion. The thermal velocity distribution can simply be considered a thermally broadened Gaussian function,

$$f_{\text{th},i} = \frac{1}{\sqrt{(2\pi v_{\text{th},i}^2)^3}} e^{-\frac{(\vec{v}-\vec{v}')^2}{2v_{\text{th},i}^2}}, \quad (3.3)$$

where $v_{\text{th},i} = \sqrt{\frac{kT}{m_i}}$ is the thermal velocity and m_i is the mass of the particle. The dependence of this thermal function on the mass of the particle results in a different particle velocity distribution for each constituent particle in the plasma. However, the bulk distribution function is the same for all components of the plasma. Assuming the bulk flows in the plasma are confined to be along a single “parallel” direction (i.e., aligned to the magnetic field such as in a bi-directional jet scenario introduced in Chapter 2), the bulk velocity distribution is cylindrically symmetric and separable, i.e., $f_{\text{bulk}}(v_{\perp}, v_{\parallel}) = f_{\perp}(v_{\perp}) f_{\parallel}(v_{\parallel})$ where $f_{\perp}(v_{\perp})$ ($(\text{cm s}^{-1})^{-2}$) is the perpendicular bulk velocity distribution and $f_{\parallel}(v_{\parallel})$ ($(\text{cm s}^{-1})^{-1}$) is the parallel bulk velocity distribution. The average of any function of the bulk flows, Q , can then be found by

$$\overline{Q(v_{\perp})} = \int_0^{+\infty} Q(v_{\perp}) f_{\perp}(v_{\perp}) 2\pi v_{\perp} dv_{\perp}; \quad \overline{Q(v_{\parallel})} = \int_{-\infty}^{+\infty} Q(v_{\parallel}) f_{\parallel}(v_{\parallel}) dv_{\parallel}. \quad (3.4)$$

Substituting Equations (3.2) and (3.3) into Equation (3.1) and reversing the order of the integration, the average energy flux carried by a plasma can then be written as

$$\vec{j}_{\text{E}} = \overline{\frac{5}{2} \gamma n k T \vec{v} + \frac{1}{2} \gamma \rho (\vec{v} \cdot \vec{v}) \vec{v}} \quad [\text{ergs cm}^{-2} \text{ s}^{-1}], \quad (3.5)$$

where the average represented by the bar is now over the bulk velocity distribution, f_{bulk} , of the fluid. In Equation (3.5), \vec{v} is the bulk velocity, T is the plasma temperature, n (cm^{-3}) is the number density of the constituent particles, and ρ (gm cm^{-3}) is the mass density of the plasma (as opposed to that of the constituent particle, ρ_i). In the case of a transition region plasma, $n = n_e + n_H + n_{\text{He}}$ and $\rho = m_e n_e + m_H n_H + m_{\text{He}} n_{\text{He}}$, where n_e is the electron density and m_e is the electron mass, n_H is the hydrogen density and m_H is the mass of a hydrogen atom, and n_{He} is the helium density and m_{He} is the mass of a helium atom. A volumetric filling factor, γ , has been empirically added to Equation (3.5) to account for the filamentary structure of the solar atmosphere.

The first term in Equation (3.5) is the thermal enthalpy flux and the second is the total nonthermal energy flux. If, for instance, the particles of the plasma were in a Maxwell-Boltzmann velocity distribution moving with a mean speed, u , then the energy flux in

the direction of the motion would reduce to the classical kinetic energy flux of the fluid, $\frac{1}{2}\gamma\rho u^3$, plus the thermal enthalpy flux, $\frac{5}{2}nkTu$. These two terms constitute the classical approximation for the energy flux of a fluid. However, when a plasma is associated with a line profile that is nonthermally broadened and non-Gaussian (implying that the velocity distribution of the emitting plasma is not Maxwell-Boltzmann), the final term in Equation (3.5) cannot be simplified to $\frac{1}{2}\gamma\rho u^3$.

Applying the assumption that the plasma is confined to move along a single “parallel” direction (i.e., the bi-directional jet scenario), Equation (3.5) simplifies to

$$\begin{aligned} j_E &= \int_{v_{\parallel}=-\infty}^{+\infty} \frac{5}{2}\gamma nkTv_{\parallel} + \frac{1}{2}\gamma\rho(\overline{v_{\perp}^2}v_{\parallel} + v_{\parallel}^3) dv_{\parallel} \\ &= \frac{5}{2}\gamma nkT\overline{v_{\parallel}} + \frac{1}{2}\gamma\rho(\overline{v_{\perp}^2}\overline{v_{\parallel}} + \overline{v_{\parallel}^3}), \end{aligned} \quad (3.6)$$

where j_E is the energy flux along the direction of motion, $\overline{v_{\perp}^2} = \int_0^{+\infty} v_{\perp}^2 f_{\perp}(v_{\perp}) 2\pi v_{\perp} dv_{\perp}$, and the filling factor, density, and temperature are taken to be essentially constant (an assumption that will be critically analyzed in Section 3.4). Now employing the equation for mean skewness,

$$\overline{(v_{\parallel} - \overline{v_{\parallel}})^3} = \overline{v_{\parallel}^3} - 3\overline{v_{\parallel}}(\overline{v_{\parallel}^2} - \overline{v_{\parallel}}^2) - \overline{v_{\parallel}}^3, \quad (3.7)$$

and substituting into Equation (3.6), the energy flux can be reduced to four components:

$$\begin{aligned} j_E &= \frac{5}{2}\gamma nkT\overline{v_{\parallel}} + \frac{1}{2}\gamma\rho(\overline{v_{\perp}^2})\overline{v_{\parallel}} + \frac{1}{2}\gamma\rho\left\{\overline{v_{\parallel}^3} + 3\overline{v_{\parallel}}(\overline{v_{\parallel}^2} - \overline{v_{\parallel}}^2) + \overline{(v_{\parallel} - \overline{v_{\parallel}})^3}\right\} \\ &= \underbrace{\frac{1}{2}\gamma\rho\overline{v_{\parallel}^3}}_{\mathbf{A}} + \underbrace{\frac{5}{2}\gamma nkT\overline{v_{\parallel}}}_{\mathbf{B}} + \underbrace{\left[\frac{1}{2}\gamma\rho\overline{v_{\perp}^2} + \frac{3}{2}\gamma\rho(\overline{v_{\parallel}^2} - \overline{v_{\parallel}}^2)\right]}_{\mathbf{C}} \overline{v_{\parallel}} \\ &\quad + \underbrace{\frac{1}{2}\gamma\rho\overline{(v_{\parallel} - \overline{v_{\parallel}})^3}}_{\mathbf{D}} \end{aligned} \quad (3.8)$$

(Winebarger et al. 1999). These four terms will be discussed in detail below.

Term **A** in Equation (3.8) represents the kinetic energy flow of the plasma in the direction of motion. It is associated with the mean bulk velocity of the plasma, $\overline{v_{\parallel}}$. Term **B** is the thermal (internal) enthalpy flow (the advection of the thermal energy in the plasma, $\frac{3}{2}nkT\overline{v_{\parallel}}$, and the work required to move this energy, $nkT\overline{v_{\parallel}}$). As stated above, these two terms together comprise the classical approximation for energy flow in a fluid. Term **C** is here termed the nonthermal enthalpy; it contains both parallel and perpendicular terms. It is the advection of the the energy associated with the plasma’s nonthermal velocities. Finally, Term **D** in Equation (3.8) is the “skewness” in the velocity distribution and is here termed the “high-energy” component. A large contribution from this term implies that particles in the tail of the distribution are carrying disproportionately more energy than the particles in the bulk of the distribution. For an extremely broadened or skewed distribution (thus for dynamic transition region plasma), the last two terms are significant, thus the energy flux cannot be accurately estimated with the classical approximation.

To find the energy flux and its components, the first three moments of the velocity must be known. These moments can be found from the bulk velocity distributions [cf. Equations

tion (3.4)], i.e.,

$$\overline{v_{\perp}^k} = \int_0^{+\infty} v_{\perp}^k f_{\perp}(v_{\perp}) 2\pi v_{\perp} dv_{\perp}; \quad \overline{v_{\parallel}^k} = \int_{-\infty}^{+\infty} v_{\parallel}^k f_{\parallel}(v_{\parallel}) dv_{\parallel}. \quad (3.9)$$

Because the limits on the integral of the parallel moments in Equation (3.9) are from $-\infty$ to $+\infty$, the quantity j_E found through Equation (3.6) represents the *net* energy flux flowing through the region under observation. It is also desirable to measure the energy flux traveling in a single direction, either toward or away from the observer. This is accomplished by separating the parallel moments of the velocity into the positive and negative parts, i.e.,

$$\overline{v_{\parallel}^k} = \int_0^{\infty} v_{\parallel}^k f_{\parallel}(v_{\parallel}) dv_{\parallel} + \int_{-\infty}^0 v_{\parallel}^k f_{\parallel}(v_{\parallel}) dv_{\parallel} = \overline{v_{\parallel+}^k} + \overline{v_{\parallel-}^k}, \quad (3.10)$$

where (+) represents the velocity component moving toward the observer and (−) represents the component moving away from the observer. The directional energy fluxes, j_{E+} and j_{E-} , can then be found from

$$j_{E\pm} = \frac{5}{2} \gamma n k T \overline{v_{\parallel\pm}} + \frac{1}{2} \gamma \rho (\overline{v_{\perp}^2 v_{\parallel\pm}} + \overline{v_{\parallel\pm}^3}). \quad (3.11)$$

This separation into positive and negative energy fluxes further allows us to measure the specific energy release rate associated with the explosive events: $j_{\text{specific}} = |j_{E+}| + |j_{E-}|$ (ergs cm^{−2} s^{−1}). If the area under observation contains the original site of the explosive reconnection, this quantity, when multiplied by the area of the event, gives the total power created by the event. Otherwise, it is a measure of the rate of energy supply, in both upward and downward directions, to that area. Table 3.1 summarizes the various energy flux measurements. In this dissertation, Equation (3.6) and Equation (3.11) are used to obtain the desired energy fluxes. The magnitude of the various terms in Equation (3.8) are also computed for analysis. The kinetic energy flux, thermal and nonthermal enthalpy flux, and skewed energy flux components can also be evaluated for the energy flux moving toward or away from the observer by substituting $\overline{v_{\parallel+}^k}$ or $\overline{v_{\parallel-}^k}$ for $\overline{v_{\parallel}^k}$ in Equation (3.8).

3.2 Measuring the Energy Flux of an Explosive Event

To measure the energy flux associated with an explosive event, several quantities, such as density, temperature, and the moments of the velocity distribution, must be known or estimated from the available data. Because explosive events are observed as broadened or skewed spectral lines, this section begins with a brief review of the fundamentals of spectral line emission and observation. Then, the method of finding the density, temperature, and filling factor of the emitting plasma, and the velocity distribution perpendicular to the direction of motion, $f_{\perp}(\overline{v_{\perp}})$, will be discussed. The technique to estimate the first, second, and third moments of the parallel velocity distribution using the Velocity Differential Emission Measure will be introduced in the next section.

When a bound electron of an excited ion decays to a lower energy state, a photon is emitted. The wavelength associated with the photon emitted from a ion at rest, which is called the rest or laboratory wavelength, is found by $\lambda_0 = \frac{hc}{\Delta E}$, where ΔE is the difference in energy between the energy states of the electron, h is Planck's constant, and c is the speed of light. Observations of this type of emission from a volume of plasma form a given spectral line. The intensity of the emission from a volume element at position, \mathbf{r} , in the plasma

Table 3.1: Summary of physical quantities associated with the energy flux.

Quantity	Description
Parallel Moments of Velocity	$\overline{v_{\parallel}^k} = \int_{-\infty}^{+\infty} v_{\parallel}^k f_{\parallel}(v_{\parallel}) dv_{\parallel}$
Upward Moments of Velocity	$\overline{v_{\parallel+}^k} = \int_0^{+\infty} v_{\parallel}^k f_{\parallel}(v_{\parallel}) dv_{\parallel}$
Downward Moments of Velocity	$\overline{v_{\parallel-}^k} = \int_{-\infty}^0 v_{\parallel}^k f_{\parallel}(v_{\parallel}) dv_{\parallel}$
Energy Flux	$j_E = \frac{5}{2}\gamma nkT\overline{v_{\parallel}} + \frac{1}{2}\gamma\rho(\overline{v_{\perp}^2}\overline{v_{\parallel}} + \overline{v_{\parallel}^3})$
Upward/Downward Energy Flux	$j_{E\pm} = \frac{5}{2}\gamma nkT\overline{v_{\parallel\pm}} + \frac{1}{2}\gamma\rho(\overline{v_{\perp}^2}\overline{v_{\parallel\pm}} + \overline{v_{\parallel\pm}^3})$
Kinetic Energy Flux	$j_{\text{kin}} = \frac{1}{2}\gamma\rho\overline{v_{\parallel}^3}$
Thermal Enthalpy Flux	$j_{\text{th}} = \frac{5}{2}\gamma nkT\overline{v_{\parallel}}$
Nonthermal Enthalpy Flux	$j_{\text{nth}} = \left\{ \frac{1}{2}\gamma\rho\overline{v_{\perp}^2} + \frac{3}{2}\gamma\rho(\overline{v_{\parallel}^2} - \overline{v_{\parallel}}^2) \right\} \overline{v_{\parallel}}$
Skewed (“High-Energy”) Energy Flux	$j_{\text{skew}} = \frac{1}{2}\gamma\rho\overline{(v_{\parallel} - \overline{v_{\parallel}})^3}$
Specific Energy Release Rate	$j_{\text{specific}} = j_{E+} + j_{E-} $

source depends upon the square of the electron density, $n_e^2(\mathbf{r})$ (due to the predominance of collisional excitation) and the line emissivity function, $G(T(\mathbf{r}))$ (photons $\text{cm}^3 \text{s}^{-1}$). The emissivity function takes into account both the abundance of the emitting ion as a function of the plasma temperature and the likelihood that the transition between the two energy states will occur. For typical transition region species, $G(T)$ is a narrow function of temperature with a well-defined maximum. (For an example, see Figure 3.2 on page 39.)

An observed spectral line can be thought of as the convolution of the emission from many different volume elements in the plasma. Some elements will be moving toward the observer, others moving away from the observer, while some will have no line-of-sight velocity. If the volume element of plasma is moving toward or away from the observer with a given line-of-sight velocity, v_{los} , the emitted wavelength is shifted by an amount $\lambda - \lambda_0 = -\frac{v_{\text{los}}}{c}\lambda_0$, where a velocity toward the observer is defined as positive and results in negative shift in the wavelength (i.e., the wavelength emitted by a volume element traveling towards the observer is blueshifted). The resulting intensity, $I(\lambda)$ (photons $\text{cm}^{-2} \text{s}^{-1} \text{\AA}^{-1}$), can then be expressed as

$$I(\lambda) = \frac{1}{4\pi D^2} \iiint_V n_e(\mathbf{r})^2 G(T(\mathbf{r})) K(\lambda, v_{\text{los}}) d^3\mathbf{r}(v_{\text{los}}) \quad (3.12)$$

(Newton 1996), where D is the distance between the Sun and the observer. The kernel function, $K(\lambda, v_{\text{los}})$, describes the shape of the emission from each volume element as a function of its line-of-sight velocity. An appropriate kernel might be simply a thermally broadened Gaussian function centered on the line-of-sight velocity in question. (The kernel function assumed in this dissertation will be fully discussed in Section 3.3 in terms of its role in VDEM analysis.)

For transition region species, the temperature of the emitting plasma can be roughly established through the emissivity function of the observed spectral line. As stated above, the emissivity function is generally a narrow function of temperature. It is assumed, then, that the temperature of the emitting plasma is the temperature where the emissivity function of a spectral line peaks. The electron density of the plasma can then be estimated from the constant pressure assumption, i.e., $n_e = \frac{p}{T}$ where $p = 1 \times 10^{15} \text{ K cm}^{-3}$ (Mariska 1992). The density of hydrogen and helium are then found from their relative abundances, i.e., $n_{\text{H}} = 0.83n_e$ and $n_{\text{He}} = 0.083n_e$ (Mariska 1992).

The filling factor, γ , is again the ratio of the true volume of the emitting plasma to the assumed volume based on the resolution of the instrument and scale height of the atmosphere. The true volume of the emitting plasma can be estimated from the total flux of the spectral line,

$$\begin{aligned} \int I(\lambda) d\lambda &= \frac{1}{4\pi D^2} \overline{n_e^2 G(T)} V_{\text{true}} \\ V_{\text{true}} &= \frac{4\pi D^2}{\overline{n_e^2 G(T)}} \int I(\lambda) d\lambda, \end{aligned} \quad (3.13)$$

where $\overline{G(T)}$ is the average emissivity of the ion ($\overline{G(T)} \approx 0.7[G(T)]_{\text{max}}$ – Mariska 1992). The true volume is proportional to $\frac{1}{n_e^2}$, so having an accurate measure of the average density of the emitting plasma is essential to achieving an accurate estimate of the true volume. Yet, for explosive events, it is very difficult to estimate the density of the emitting plasma. For this study, the average density is simply assumed to be associated with constant pressure; hence, the resulting measurement of the true volume of the emitting plasma is extremely

prone to unavoidable systematic errors. The assumed volume is generally taken to be $V_{\text{assumed}} = \Sigma H_0$, where Σ is the area under observation (typically the resolution of the spectrometer) and H_0 is the scale height of the plasma. (For this study, the scale height was found from the constant conductive flux assumption discussed in Chapter 1 [cf. Equation (1.10)].) Therefore, the filling factor is further dependent on an assumed scale height of the atmosphere. Combining Equation (3.13) and the assumed volume, density, and average emissivity function, the filling factor is

$$\gamma = \frac{\frac{4\pi D^2}{n_e^2 0.7 [G(T)]_{\text{max}}} \int I(\lambda) d\lambda}{\Sigma H_0}. \quad (3.14)$$

Assuming a scale height or density that is much less than the true value would result in a (physically unrealistic) filling factor greater than 1. The implications on the results of the possible systematic errors associated with this measurement of the filling factor will be addressed in Chapters 5 and 6.

One advantage of using spectral data is that the shifts in the spectral lines provide information on the bulk flows present in the emitting plasma. However, the Doppler shift velocities are only representative of the motion along the line-of-sight and, hence, provide no information about motion perpendicular to the line-of-sight. For simplicity, then, the direction of motion (“parallel” as discussed in Section 3.1) is assumed to coincide with the line-of-sight. Perpendicular to the line-of-sight, only “normal”, turbulent transition region motions are assumed to occur. This would imply that the perpendicular bulk velocity distribution is a Gaussian function with the width associated with the “normal” turbulent velocity, ξ [cf. Section 2.1], i.e.,

$$f_{\perp}(v_{\perp}) = \frac{1}{2\pi\xi^2} e^{-\frac{v_{\perp}^2}{2\xi^2}}. \quad (3.15)$$

(The method of determining this nonthermal velocity from non-event profiles is discussed in Chapter 5.) To evaluate the energy flux [cf. Equation (3.6)], the average width of the perpendicular velocity distribution, $\overline{v_{\perp}^2}$, must be known. Integrating this quantity over the perpendicular velocity distribution given in Equation (3.15) gives

$$\begin{aligned} \overline{v_{\perp}^2} &= \frac{1}{2\pi\xi^2} \int_{v_{\perp}=0}^{+\infty} v_{\perp}^2 e^{-\frac{v_{\perp}^2}{2\xi^2}} 2\pi v_{\perp} dv_{\perp} d\phi \\ &= 2\xi^2. \end{aligned} \quad (3.16)$$

Hence, the width of the perpendicular velocity distribution is directly related to the velocity of the turbulent motions in the transition region plasma.

3.3 The Velocity Differential Emission Measure

Establishing accurate values for the density, temperature, and filling factor of the emitting plasma, and the width of its perpendicular bulk velocity distribution is important for estimating the energy flux of a dynamic plasma. However, the energy flux is essentially defined by the moments of the parallel bulk velocity distribution. Hence, the accuracy of the measured energy flux depends upon the ability to measure these moments. One way of doing this is by examining the spectral lines emitted by ions in the plasma. If the plasma

is moving toward (away) from the observer, the spectral line will be blueshifted (redshifted). By examining these shifts in the spectral lines, it is possible to glean information on the bulk flows of the emitting plasma.

The spectral lines emitted at transition region temperatures come from highly ionized trace elements, such as oxygen, carbon, nitrogen, and neon. These elements make up less than 0.1% of the particles in the solar atmosphere, and hence do not constitute a large percentage of the total energy flux associated with explosive events. Instead, hydrogen, helium, and electrons, which make up 99.9% of the particles in the solar atmosphere, are responsible for most of the energy flux, yet there is no way of directly observing these fully-ionized particles. It is therefore necessary to derive the bulk motions of the plasma from the spectral lines of trace elements and assume they apply to the bulk motions of all the ions in the plasma. However, the observed spectral lines of the trace elements are not only broadened by bulk flows in the plasma, but also by thermal motions of the emitting ion. These thermal motions do not reflect the general velocities of the plasma. A function that removes the thermal information and quantifies the bulk motions in the spectral line is the Velocity Differential Emission Measure (Newton, Emslie, & Mariska 1995; Newton 1996).

Previous attempts to describe the motions of the plasma emitting non-Gaussian profiles have usually employed techniques such as double-Gaussian fitting (e.g., Antonucci et al. 1982, in an analysis of soft X-ray line profiles). This six-parameter (position, amplitude and width of each component) technique essentially assumes that the plasma is composed of two fluid elements, each consisting of particles with a Gaussian velocity distribution of parametric width. One fluid element (corresponding to the emission centered near the rest wavelength of the line) is considered to represent the near-stationary bulk of the emitting plasma, and the other is considered to be moving at a mean speed, given by the Doppler wavelength shift between the centroids of the components. The excess width of each component (over the thermal Doppler width) is dealt with by parametrically invoking a “nonthermal turbulent velocity,” which could represent either microturbulence within the emitting element or velocity gradients across the volume observed.

Such parametric fitting techniques can only approximate the characteristics of the emitting plasma (especially quantities, such as the energy flux, which are functions of higher order moments of the velocity distribution) when significant line asymmetries are present. To overcome this limitation, Newton, Emslie, & Mariska (1995) introduced a new diagnostic, the Velocity Differential Emission Measure (VDEM), which admits a *continuum* of fluid elements, each a shifted Gaussian distribution of thermal width (or other appropriate kernel function).

A VDEM function is a measure of the emitting power of a portion of the atmosphere traveling with a given line-of-sight velocity. Formally, it is defined by

$$\text{VDEM}(v_{\text{los}}) = n_e^2 G(T) \frac{ds}{dv_{\text{los}}} \quad [\text{photons s}^{-1} \text{ cm}^{-2} (\text{cm s}^{-1})^{-1}]. \quad (3.17)$$

(For a more general definition of VDEM, see Newton, Emslie, & Mariska 1995.) The VDEM function is related to the observed intensity [cf. Equation (3.12)] of the emitted line through

$$I(\lambda) = \frac{\Sigma \gamma}{4\pi D^2} \int \text{VDEM}(v_{\text{los}}) K(\lambda, v_{\text{los}}) dv_{\text{los}}. \quad (3.18)$$

In the case of the transition region species analyzed in this dissertation, the kernel function, $K(\lambda, v_{\text{los}})$, is assumed to be a thermally-broadened Gaussian function centered on the

wavelength corresponding to the line-of-sight velocity in question, i.e.,

$$K(\lambda, v_{\text{los}}) = \frac{1}{\sqrt{2\pi\sigma_K^2}} \exp \left[-\frac{(\lambda - \lambda_0[1 - \frac{v_{\text{los}}}{c}])^2}{2\sigma_K^2} \right] \quad (3.19)$$

(Newton 1996), where

$$\sigma_K = \sigma_{\text{th}} = \frac{\lambda_0}{c} \sqrt{\frac{kT}{m_i}}, \quad (3.20)$$

k is Boltzmann's constant and m_i is the mass of the emitting ion. The kernel function could also be expanded to include the nonthermal velocity, ξ [cf. Equation (2.7)], associated with the turbulence typical to transition region plasmas. (See Newton 1996 for details on including a nonthermal velocity term in the kernel function.) The plasma in the transition region, however, exhibits a range of nonthermal velocities; hence, assuming a single value for the nonthermal velocity could introduce systematic errors into the energy flux measurement. For this reason, the kernel function is chosen to simply be a thermally broadened Gaussian function (Equation (3.19)). This implies that any turbulent velocity information will be contained in the VDEM function.

Deconvolving the kernel function, $K(\lambda, v_{\text{los}})$, from an observed line profile, $I(\lambda)$, produces the corresponding VDEM function. The deconvolution procedure was thoroughly discussed by Newton, Emslie, & Mariska (1995) and Newton (1996) in the context of X-ray spectra observed during solar flares. For the reader's benefit, it will briefly be reviewed here.

In Equation (3.18), $I(\lambda)$ is the line profile, $\text{VDEM}(v_{\text{los}})$ is the source function, and $K(\lambda, v_{\text{los}})$ is the kernel function. Properly discretized, Equation (3.18) can be written as the matrix equation $\mathbf{A} \cdot \mathbf{f} = \mathbf{g}$, where \mathbf{f} represents the VDEM, \mathbf{g} represents the observed line profile, $4\pi D^2 I$, and \mathbf{A} represents the kernel function, K . The inversions of such equations are generally unstable; however, several techniques exist to overcome the instability.

One such technique is a linear regularization method. This technique optimizes the trade-off between reducing χ^2 errors and constraining the source function with a smoothing parameter. The source function, \mathbf{f} , is found by minimizing

$$\| \mathbf{A} \cdot \mathbf{f} - \mathbf{g} \|^2 + q \| \mathbf{D} \cdot \mathbf{f} \|^2, \quad (3.21)$$

where the first term in Equation (3.21) is the squared residual, q is a smoothing parameter, and \mathbf{D} is a smoothing operator. By including a smoothing parameter and operator, some additional constraints are incorporated into the inversion process. Incorporating these constraints is necessary to stabilize the results, yet careful consideration must go into choosing these parameters to minimize their effects, discussed below.

Taking the derivative of Equation (3.21) with respect to \mathbf{f} , the inversion reduces to

$$(\mathbf{A}^T \cdot \mathbf{A} + q\mathbf{H}) \cdot \mathbf{f} = \mathbf{A}^T \cdot \mathbf{g}, \quad (3.22)$$

where $\mathbf{H} = \mathbf{D}^T \mathbf{D}$. This can be solved for \mathbf{f} , i.e.,

$$\mathbf{f} = (\mathbf{A}^T \cdot \mathbf{A} + q\mathbf{H})^{-1} \mathbf{A}^T \cdot \mathbf{g}. \quad (3.23)$$

The uncertainties in the resulting VDEM can be found from

$$\epsilon_{\text{VDEM } i} = \sqrt{[(\mathbf{A}^T \cdot \mathbf{A} + q\mathbf{H})^{-1} \mathbf{A}^T \cdot \mathbf{A} (\mathbf{A}^T \cdot \mathbf{A} + q\mathbf{H})^{-1}]_{ii} \epsilon_i}, \quad (3.24)$$

where ϵ_i is the uncertainty in the data associated with bin, i . (For more information on the derivation of uncertainties, see Newton 1996.)

The smoothing operator, \mathbf{D} , is chosen so that, if \mathbf{f} follows an expected functional form, $\mathbf{D} \cdot \mathbf{f}$ vanishes. Because it is believed \mathbf{f} (i.e., VDEM) is well-represented by a piecewise quadratic function, \mathbf{D} is chosen to be the third derivative operator, i.e. $\mathbf{D} \cdot \mathbf{f} = \mathbf{f}'''$, or, using the central difference formula:

$$(\mathbf{D} \cdot \mathbf{f})_m = f'''(v_m) = \frac{-f(v_{m-\frac{3}{2}}) + 3f(v_{m-\frac{1}{2}}) - 3f(v_{m+\frac{1}{2}}) + f(v_{m+\frac{3}{2}})}{(\Delta v)^3}. \quad (3.25)$$

Use of such a smoothing operator essentially forces the solution toward a piecewise quadratic function. The degree of this forcing is determined by the magnitude of the smoothing parameter. (Note that the width of a velocity bin, Δv , in Equation (3.25) is dictated by the width of the spectral bin, $\Delta\lambda$, in the original data, i.e., $\Delta v = c \frac{\Delta\lambda}{\lambda_0}$.)

The smoothing parameter, q , controls the degree of forced smoothing in the solution. If the parameter is too large, the returned VDEM function would be overly smooth and information present in the original data would be lost. If q is too small, artifacts from the inversion process could permeate the resulting VDEM. An optimal value for the smoothing parameter would highlight real, interesting structure, while suppressing artificial structure. One method of determining this optimal value is by minimizing the generalized cross-validation (GCV) function. This function has been approximated (Golub, Heath, & Wahba 1979) by

$$\text{GCV}(q) = \frac{\|\mathbf{g} - \mathbf{A} \cdot \mathbf{f}\|_i^2}{\text{Tr}[\mathbf{I} - \mathbf{A}(\mathbf{A}^T \cdot \mathbf{A} + q\mathbf{H})^{-1} \mathbf{A}^T]^2}, \quad (3.26)$$

where \mathbf{I} is the identity matrix. The numerator in Equation (3.26) is the χ^2 residual between the original intensity, \mathbf{g} , and the forwardly-convolved intensity found from the VDEM function, $\mathbf{A} \cdot \mathbf{f}$, while the denominator is known as the *equivalent degrees of freedom for error*, which is related to the degrees of freedom in the actual data and the inversion techniques. (For more information, see Golub, Heath, & Wahba 1979; Newton, Emslie, & Mariska 1996.) This function basically measures the difference between the original data and the data predicted by the VDEM function given the degrees of freedom admitted by the data. Minimizing this function will ensure that the VDEM accurately reflects the original data. The merits and performance of the GCV function in inverse problems were explored by Barrett (1996). This technique for finding the optimal smoothing parameter was utilized for this investigation.

Deconvolving the kernel from an observed line profile produces the corresponding VDEM function. Figure 3.1 (a) displays a sample spectrum of the O VI 1032 Å line. The arrow notes a spatial pixel exhibiting nonthermal broadenings and a strong blue-wing asymmetry. The intensity of this spatial pixel is shown in Figure 3.1 (b), while Figure 3.1 (c) shows the VDEM returned from deconvolving the line profile using this discretized inversion procedure. (Note the velocity axis of the VDEM function has been reversed so that positive (upward) flows corresponds to the blueshifts observed in the line profile in the plot above it.)

A line profile is broadened by both thermal and nonthermal motions of the emitting plasma. By deconvolving the line profile using a thermally broadened kernel function, the thermal information is removed. Therefore, as stressed earlier, a VDEM function does not contain any information on thermal velocities, only on bulk flows of the fluid along the line-of-sight. By assuming the line-of-sight coincides with the direction of motion (an assumption that will be tested in Section 3.4), a normalized VDEM function is related to

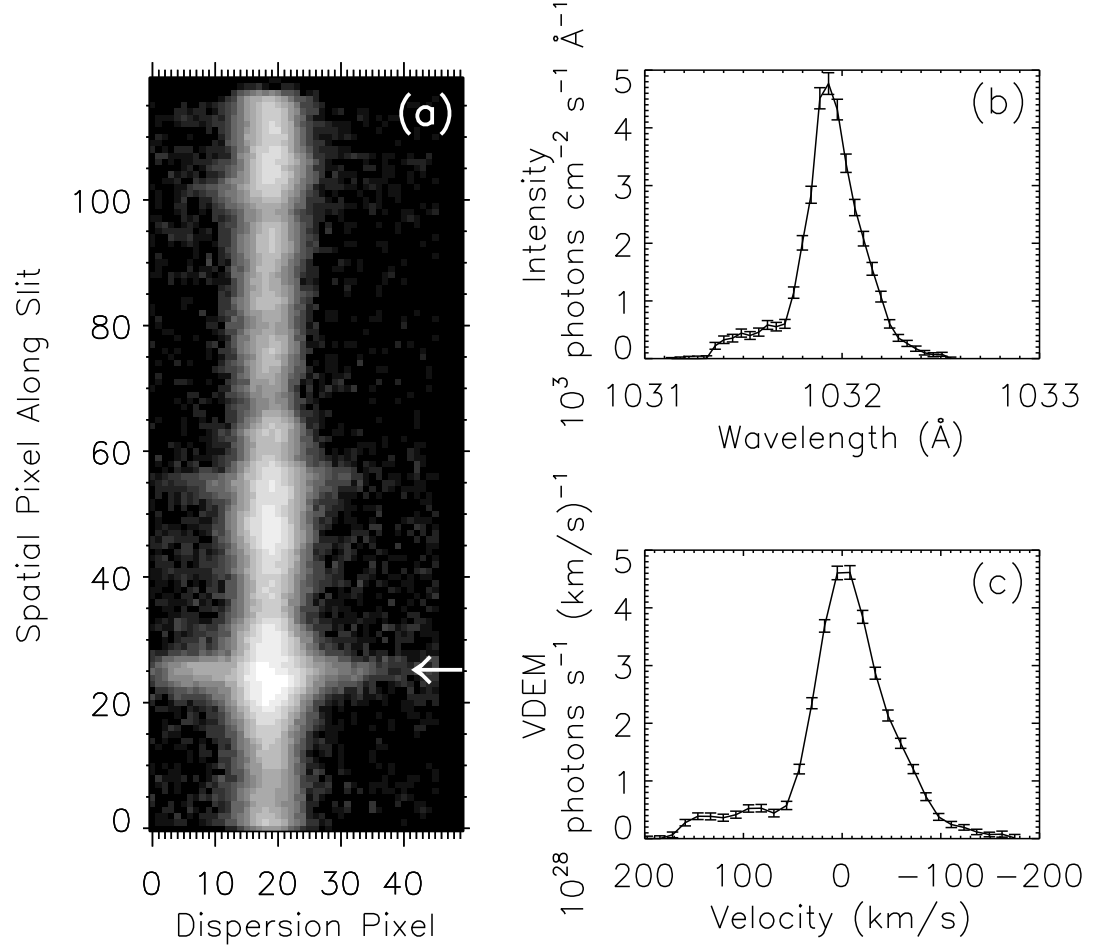


Figure 3.1: (a) A SUMER spectrum of O VI 1032 Å line taken on 1996 May 10 at sun center. The horizontal axis is the dispersion pixel number and the vertical axis the spatial pixel along the slit. The arrow points out spatial pixel 26 that exhibits explosive event characteristics. The line profile associated with this pixel is shown in (b). The VDEM function recovered from this line profile is shown in (c).

the parallel component of the bulk velocity distribution such as in Equation (3.9). However, the returned VDEM is proportional to the emission of the ion which scales not as n (which weights the bulk velocity distribution), but as $n^2 G(T)$. Thus, if the ion exists over a large range of densities and temperatures (such as for soft X-ray lines formed in the corona), the averages represented in Equation (3.9) are not easily translated into moments of the VDEM function. However, the emission from a given transition region line is over a relatively narrow range of temperature and hence density. Therefore, it is assumed that the parallel moments of the velocity can be calculated by weighting with the normalized VDEM function instead of $f_{||}$:

$$\overline{v_{||}^k} = \frac{\int v_{||}^k \text{VDEM}(v_{||}) dv_{||}}{\int \text{VDEM}(v_{||}) dv_{||}}. \quad (3.27)$$

Uncertainties in the VDEM function (which are proportional to the uncertainties in the line intensity) and in the velocity array associated with the VDEM function (which are related to the uncertainties in the wavelength associated with each spectrum) contribute to the uncertainties in the moments of the velocity distribution, and hence, in the energy flux. The magnitude of possible systematic errors associated with approximating the parallel bulk velocity distribution with the VDEM function will be addressed in Section 3.4.

3.4 Limitations of the VDEM Approximation

Considerable systematic error may be associated with using a normalized VDEM function in lieu of the actual parallel velocity distribution to find the moments of the velocity [cf. Equation (3.27)]. These errors restrict the data that are suitable to be analyzed using the VDEM method.

Let us first deal with two relatively trivial examples where the VDEM function fails to give an adequate representation of the bulk velocity distribution. Often two spectral lines are blended to the point that they are indistinguishable from one another. A VDEM function deconvolved from a blended line profile would then not represent the motions of the plasma at the temperature of interest. In fact, Equation (3.12) is no longer representative of the line intensity. This simple example implies a clear restriction: for a returned VDEM function to be a measure of the bulk motions of the plasma, the spectral line under study must not be blended with any other spectral line. [The exception to this argument occurs when the emission of both spectral lines originates from a single volume of plasma, and hence are both well-described by a single VDEM function. In this situation, a modified kernel function can be used and a single VDEM can be deconvolved from the two blended lines (Newton 1996).]

Also, because VDEM only returns information about the velocity distribution along the line-of-sight, the assumption that the line-of-sight direction coincides with the direction of motion of the reconnection event is necessary. This idealized geometry implies the absence of a deprojection factor (which would always be greater than 1) in the resulting energy flux. As a result, the energy flux thus determined is a lower limit to the true value. Note, however, that this unknown deprojection factor would not change the *sign* of the energy flux, except in cases where, for example, an upward flow direction constitutes a motion away from the observer (such as motion near the limb along a field line which is angled significantly away from the local vertical.) To ensure that a positive value for the energy flux implies motion toward the observer and into the corona, it is necessary that the measurements be taken near sun center.

The magnitudes of two other systematic errors are not easily quantified and must be addressed through numerical simulations of line profiles and theoretical predictions of the VDEM function given an initial temperature and density structure of the emitting plasma. Each will be discussed in detail below in the context of the O IV 790 Å line which is formed at $10^{5.2}$ K. The emissivity function associated with this line is shown in Figure 3.2 (a). The emission of the line ($n_e^2 G(T)$) as a function of temperature is shown in Figure 3.2 (b), assuming the line is formed at constant pressure, i.e., $n_e = \frac{p}{T}$ where $p = 1 \times 10^{15}$ K cm³.

3.4.1 Systematic Errors Due to a Low Number of Counts

Explosive events are short-lived, small-scale phenomena; observing them requires high-cadence, high-resolution spectral data. A line profile taken from a high-cadence, high-resolution spectrum is likely to consist of a low number of total counts (on the order of 10^2 counts per profile). Such a line profile may not well represent the emitting plasma. It may have a spurious peak or wings that are indistinguishable from the background distribution. If an intensity is not well-defined, the deconvolved VDEM may not adequately represent the line-of-sight velocity distribution. This implies that some minimum number of counts must define a line profile before the deconvolved VDEM can be trusted. This minimum count number will be established in this section using numerical modeling of line profiles.

One problem with using low count data is the inability to define accurately the boundaries of the spectral line. The bulk velocity distribution of the emitting plasma is essentially defined from $-\infty$ to $+\infty$. An observation of a spectral line emitted by this plasma, however, will have specific wavelength values on either side of the rest wavelength that define where the emission of spectral line becomes indistinguishable from the background continuum emission. These border wavelengths imply that a deconvolved VDEM would be significant only for a limited velocity range (as compared to the infinite velocity range of the bulk velocity distribution). If a spectral line has a low number of total counts, its wings may be well-blended with the background emission implying more severe limits on its deconvolved VDEM function than a line formed by higher number of total counts.

Consider the parallel bulk velocity distribution function shown in Figure 3.3. Assume this distribution is representative of the bulk velocities in a volume element in the solar transition region with a uniform temperature of $10^{5.2}$ K. Some emission from this element will be from the O IV ion, which is the dominant oxygen species at this temperature. Figure 3.4 (a, c, & e) shows simulations of how O IV 790 Å line profiles might appear with no assumed background emission and 500, 1,000, and 3,000 counts defining them, respectively. (The method of simulating these profiles is given in the Appendix.) The edges of these simulated lines were taken to be the first spectral bin with no counts. [In real data, the edges are generally taken to be where the intensity of the spectral line falls to the average background intensity (for more information, see Section 4.5).] Figure 3.4 (b, d, & f) shows the normalized VDEM functions deconvolved from each simulated line profile (solid) along with the original velocity distribution (dashed). First, notice that the velocities for which VDEM is defined increase as the number of counts increase. This is a function of the wings of the profile being distinguishable above background as count statistics improve. Also, note that the VDEM function for the 3,000 count line profile more closely matches the original bulk velocity distribution than the VDEM function for the 500 count line profile. These examples demonstrate that the normalized VDEM function is a better estimate for the parallel bulk velocity distribution as the counts defining the line increase. These differences

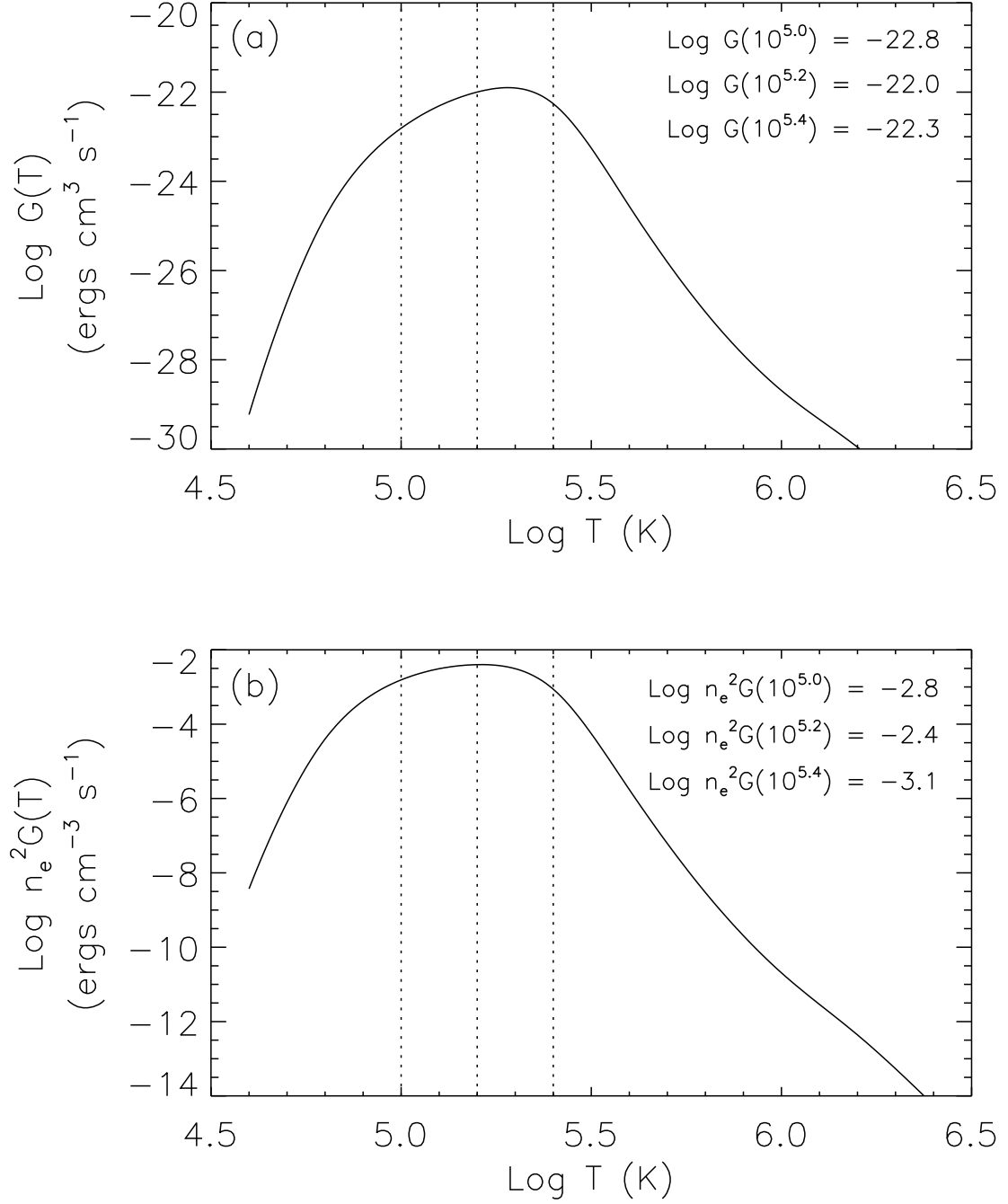


Figure 3.2: (a) The emissivity function, $G(T)$, associated with the O IV 790 Å line and (b) the emission associated with constant pressure, $n_e^2 G(T)$.

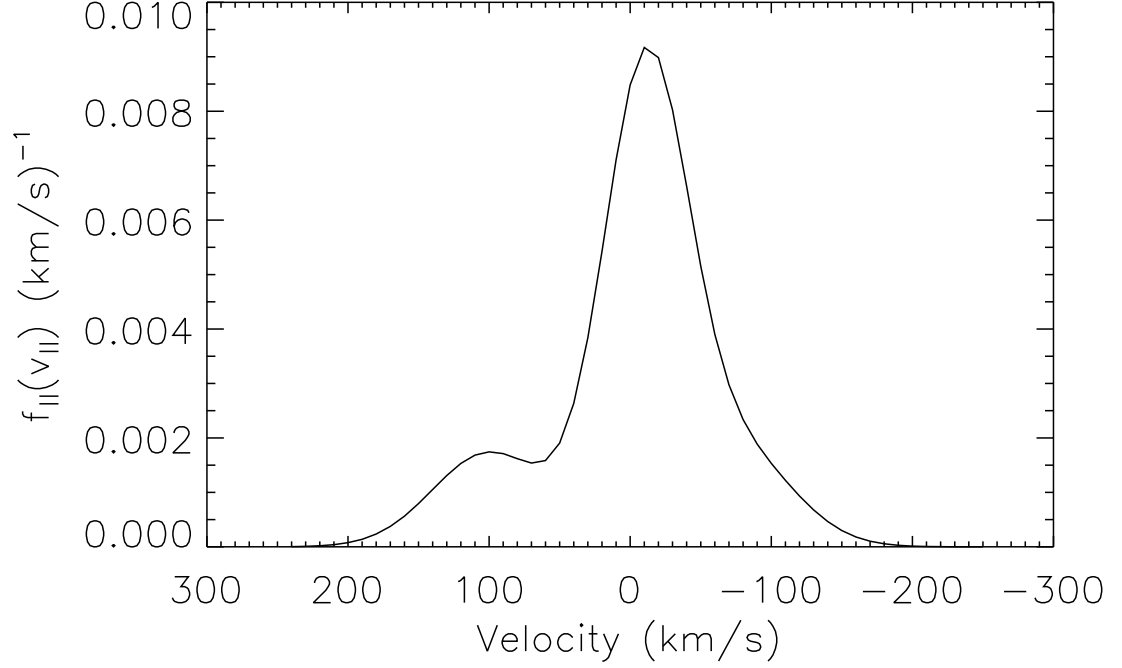


Figure 3.3: Assumed parallel bulk velocity distribution at $10^{5.2}$ K.

Table 3.2: A comparison of the moments of the velocity found from an assumed bulk velocity distribution (“True”) and from the VDEM functions of three simulated line profiles [cf. Figure 3.4].

Velocity Moments (km s ⁻¹)	True	500 counts	1,000 counts	3,000 counts
$\overline{v_{\parallel}}$	-3×10^5	-9×10^5	-7×10^5	-4×10^5
$\sqrt{v_{\parallel}^2}$	6×10^6	5×10^6	6×10^6	6×10^6
$\sqrt[3]{v_{\parallel}^3}$	5×10^6	-3×10^6	-1×10^6	4×10^6

are obvious when comparing the moments of the velocity from the VDEM deconvolved from these examples with the moments of the original distribution given in Table 3.2.

To find the minimum number of counts required to measure adequately the energy flux from the VDEM function, many more simulations were needed. Still assuming the parallel

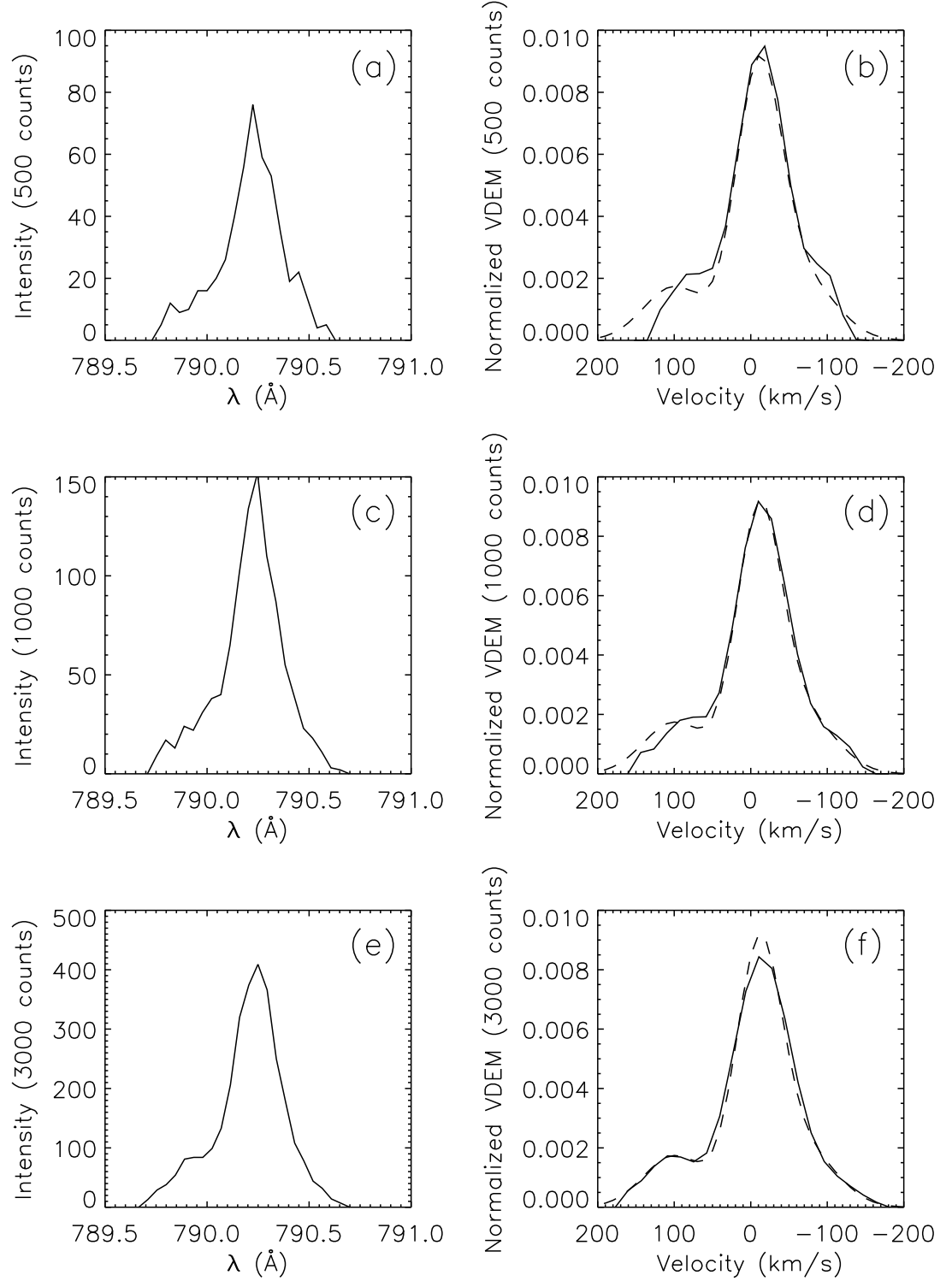


Figure 3.4: Examples of simulated line profiles of the O IV 790 Å line are shown in (a), (c), and (e), each defined by 500, 1,000, and 3,000 total counts, respectively. The normalized, deconvolved VDEM for each profile is shown in (b), (d), and (f) as a solid line. The assumed parallel bulk velocity distribution is shown as a dashed line.

bulk velocity distribution shown in Figure 3.3, 100 profiles were simulated with 500 counts each, 100 with 1,000 counts each, etc., up to 100 profiles with 3,000 counts each. A VDEM function was then deconvolved from each simulated profile and the velocity moments were found, as well as the net energy flux (j_E) and energy flux toward (j_{E+}) and away (j_{E-}) from the observer. The results are shown graphically in Figure 3.5 (a,b, & c). The points on each graph represent the average j_E (a), j_{E+} (b), or j_{E-} (c) measured for each number of defining counts, while the error bars are the standard deviation in the energy fluxes at these counts. The solid lines are the true energy fluxes found from the assumed bulk distribution function. The dotted lines show an uncertainty in this value (derived from assumed uncertainties in the velocity array $\sim 10 \text{ km s}^{-1}$) that reflects a good estimate for the probable uncertainty of the energy fluxes measured from a VDEM function. Above 1,000 counts, the true energy flux is fairly well approximated by the energy flux found using the normalized VDEM function and the systematic errors are approximately the same or less than the assumed uncertainty in the energy flux values.

3.4.2 Density and Temperature Gradients

It is naive to think that the temperature and density assumptions mentioned in Section 3.3 truly describe the physical conditions of the emitting plasma. During a reconnection event, particles moving into the acceleration region may be “pinched” by the field lines into a confined volume, increasing the temperature and density of the plasma. This will lead to convection of energy along the temperature gradient and acceleration of the particles as they exit the reconnection site. Attempts to model numerically this situation including realistic energy transfer and temperature structure have been unsuccessful (Karpen 1998). Because there is no way to deduce this temperature or density structure, several scenarios will be examined to determine the effects of various temperature and density structures on the accuracy of the VDEM method.

The plasma that is being accelerated in these reconnection events is also believed to be heated or cooled as indicated by the observations that the events “disappear” instead of propagating along the slit. A simple model would be that the volume elements traveling at speeds greater than 50 km s^{-1} contain hotter or cooler plasma than the volume elements traveling at speeds less than 50 km s^{-1} . The density of the plasma in these accelerated volumes is uncertain. The plasma in the transition region is generally assumed to be at constant pressure; therefore, an increase (decrease) in temperature would imply a decrease (increase) in density. However, because the plasma is being heated or cooled quickly in the reconnection event, is it not clear if the constant pressure approximation is valid. The timescale for constant pressure to re-establish after a sudden change in temperature is $\sim 25 \text{ s}$ (Chapter 2). This is on the order of the typical lifetime of an explosive events, so at least a portion of the emitting plasma can be assumed to not be at a constant pressure.

Based on these arguments, four different scenarios are presented here: (1) the plasma in volume elements with speed greater than 50 km s^{-1} is heated and a uniform, pre-event density is maintained, (2) the plasma in volume elements with speed greater than 50 km s^{-1} is heated and constant pressure is maintained, (3) the plasma in volume elements with speed greater than 50 km s^{-1} is cooled and a uniform, pre-event density is maintained, and (4) the plasma in volume elements with speed greater than 50 km s^{-1} is cooled and constant pressure is maintained. Each of these scenarios is addressed using the emissivity function, $G(T)$, of the O IV 790 Å line (shown in Figure 3.2 a). This function peaks at approximately $10^{5.2} \text{ K}$; this temperature will be assumed to represent the temperature of the plasma in

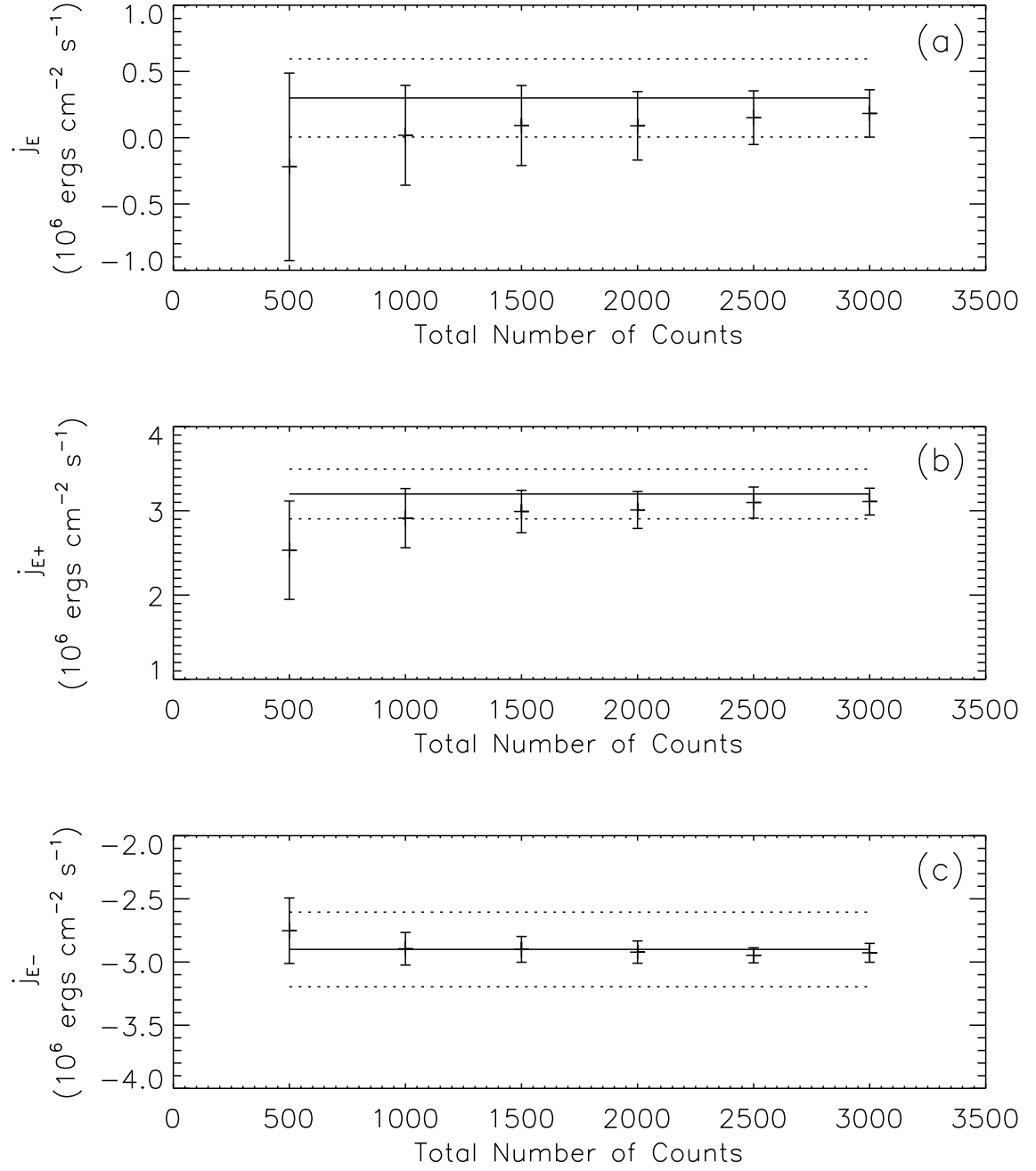


Figure 3.5: A comparison of the net energy flux (a) energy flux toward the observer (b), and energy flux away from the observer (c) measured from the VDEM function deconvolved from simulated line profiles. The error bars in the energy fluxes are the standard deviations in the measurements. The true energy fluxes are the solid lines and the approximate uncertainties in the energy fluxes are the dotted lines.

the volume elements with flow speed less than 50 km s^{-1} . The temperature of the plasma in the high-speed volume elements will be assumed to be at $10^{5.0} \text{ K}$ for the cooled plasma scenarios and $10^{5.4} \text{ K}$ for the heated plasma scenarios. Emission from a constant density plasma will scale as $G(T)$, shown in Figure 3.2 (a). If the emission is from a constant pressure plasma, it will scale with $n_e^2 G(T)$, shown in Figure 3.2 (b). The values for the emissivity and emission are given in the figure at the temperatures of interest.

The validity of the assumption that this emissivity function, which generally reflects a plasma in equilibrium, represents the rapidly changing conditions of dynamic plasma depends on the recombination and ionization rates of the plasma. Ionization times tend to keep pace with the heating, even if the heating is nearly instantaneous. For instance, if a volume element of plasma at $10^{5.2} \text{ K}$ containing the O IV ion is instantaneously heated to the temperature of $10^{5.4} \text{ K}$, a temperature where O V is the dominant species, the ionization time is less than 1 s (Mariska 1992). However, the recombination rates are much slower for some ions, implying that there may be highly ionized species existing at much lower temperatures than implied by the emissivity function for a period of time after the cooling occurs. Many factors affect these ion-dependent rates (for review, see Mariska 1992), and their influences are difficult to assess. For the following scenarios, the emissivity function at a given temperature will be assumed to characterize the emission from the plasma at that temperature.

Heated, High-Speed Plasma with Uniform, Pre-Event Density

This scenario addresses a volume of plasma with uniform pre-event density. The temperature of the plasma in the high-speed (greater than 50 km s^{-1}) volume elements is assumed to be $10^{5.4} \text{ K}$. The temperature of the plasma in the remaining volumes elements is assumed to be $10^{5.2} \text{ K}$. The bulk velocity distribution (which scales as density and is not affected by a change in temperature) will remain unchanged. However, the emission from the heated plasma, which scales with $G(T)$ and, hence, decreases rapidly at high temperatures [Figure 3.2 (a)], will consequently be reduced ($G(10^{5.2}) = 10^{-22} \text{ ergs cm}^3 \text{ s}^{-1}$ while $G(10^{5.4}) = 10^{-22.3} \text{ ergs cm}^3 \text{ s}^{-1}$ resulting in a reduction in emission from the high-speed volume elements of 0.5). This implies that the observed line profile, and hence inferred VDEM function, will be suppressed in the wings of the profile (where the emission originates from the plasma in the high-speed volume elements). Figure 3.6 displays an assumed bulk velocity distribution (solid), along with the normalized theoretical VDEM function. This is how a “perfect” VDEM would appear and is calculated by weighting the bulk velocity distribution with the emission function at each temperature. The magnitude of this normalized VDEM function in the wings of the distribution is lower than the bulk velocity distribution. The energy flux measured from this VDEM function will then be less than the true energy flux, as the values given in Table 3.3 verify. (The percentage difference given in this table is defined as the difference in the two values divided by the true value.) The values given for the energy fluxes measured from the bulk velocity distribution are the true values found from the assumed temperature and density structure of the emitting plasma, while those measured from the VDEM function assume that the temperature of the plasma is $10^{5.2} \text{ K}$ and electron density is $\frac{p}{T}$, where p is the constant pressure of $1 \times 10^{15} \text{ K cm}^{-3}$. The net energy flux is the quantity most affected by this increase in temperature (the net energy flux measured from the VDEM function is not even the correct sign). Both the positive and negative energy fluxes are lower than the true values.

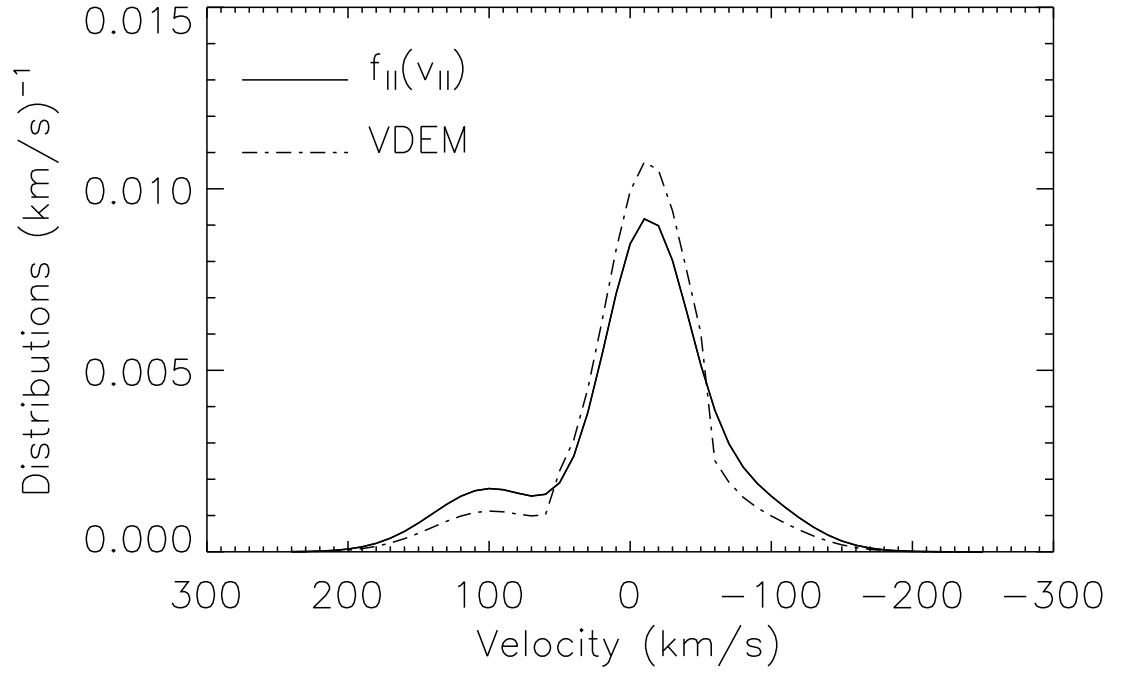


Figure 3.6: An example of how heating the plasma in the high-speed volume elements while maintaining uniform density would affect the bulk velocity distribution (solid) and the theoretical VDEM function (dash-dot).

Table 3.3: A comparison of the energy flux measured from an assumed bulk velocity distribution and from a theoretical VDEM function when the plasma in the high-speed volume elements is heated and constant density is maintained.

Energy Flux (ergs cm ⁻² s ⁻¹)	From $f_{ }(v_{ })$	From VDEM	Percentage Difference
j_E	3.4×10^5	-2.7×10^4	108 %
j_{E+}	3.2×10^6	2.3×10^6	28 %
j_{E-}	-2.9×10^6	-2.3×10^6	21 %

Heated, High-Speed Plasma at Constant Pressure

Figure 3.7 illustrates how the bulk velocity distribution and inferred VDEM function are affected when the plasma in the high-speed volume elements is heated to $10^{5.4}$ K and

constant pressure is maintained throughout the entire volume (hence the density in the plasma in the high-speed volume elements drops). The original bulk velocity distribution is shown as the dashed line, while the bulk velocity distribution with lower density in the high-speed region is shown as the solid line. The dash-dot line shows the theoretical VDEM function. In this scenario, both the bulk velocity distribution and VDEM function are suppressed at high-speeds, but, because the VDEM function scales as $n_e^2 G(T)$, it is reduced by a greater amount than the bulk velocity distribution, which just falls off as n_e . The electron densities at these temperatures implied by constant pressure are $n_e(10^{5.2}) = 10^{9.8} \text{ cm}^{-3}$ and $n_e(10^{5.4}) = 10^{9.6} \text{ cm}^{-3}$ (a factor of 1.6 difference), while the emission at these temperatures are $n_e^2 G(10^{5.2}) = 10^{-2.4} \text{ ergs cm}^{-3} \text{ s}^{-1}$ and $n_e^2 G(10^{5.4}) = 10^{-3.1} \text{ ergs cm}^{-3} \text{ s}^{-1}$ (a factor of 5.0 difference). The true energy flux along with the energy flux measured from this VDEM function is given in Table 3.4. The comparison between the two values is very similar to that of the previous scenario. Again, the sign of the net energy flux is changed, while the measured positive and negative energy fluxes are smaller than their true values.

Cooled, High-Speed Plasma with Uniform, Pre-Event Density

As in the scenario with heated, high-speed plasma with uniform, pre-event density, the bulk velocity distribution for cooled ($10^{5.0} \text{ K}$) plasma in the high-speed volume elements does not change (see Figure 3.8). The VDEM function is again suppressed in the wings of the distribution as a result of the drop in the emissivity function, $G(T)$, for this cooler plasma. The emissivity function decreases by a factor of 6.3 ($G(10^{5.0}) = 10^{-22.8} \text{ ergs cm}^3 \text{ s}^{-1}$ and $G(10^{5.2}) = 10^{-22.0} \text{ ergs cm}^3 \text{ s}^{-1}$). The energy flux measured from the VDEM function is compared to the true energy flux in Table 3.5. The magnitudes of the measured energy fluxes flowing towards and away from the observer are lower than the true value and the net energy flux is considerably different from the true value.

Cooled, High-Speed Plasma at a Constant Pressure

Figure 3.9 illustrates how the original bulk velocity distribution (dashed) is changed when the temperature of the plasma in the high-speed volume elements is reduced to $10^{5.0} \text{ K}$ and constant pressure is maintained (solid). Because of the temperature drop in the high-

Table 3.4: A comparison of the energy flux measured from an assumed bulk velocity distribution and from a theoretical VDEM function when the plasma in the high-speed volume elements is heated and constant pressure is maintained.

Energy Flux ($\text{ergs cm}^{-2} \text{ s}^{-1}$)	From $f_{\parallel}(v_{\parallel})$	From VDEM	Percentage Difference
j_E	4.8×10^4	-3.9×10^5	912 %
j_{E+}	2.5×10^6	1.4×10^6	44 %
j_{E-}	-2.4×10^6	-1.8×10^6	25 %

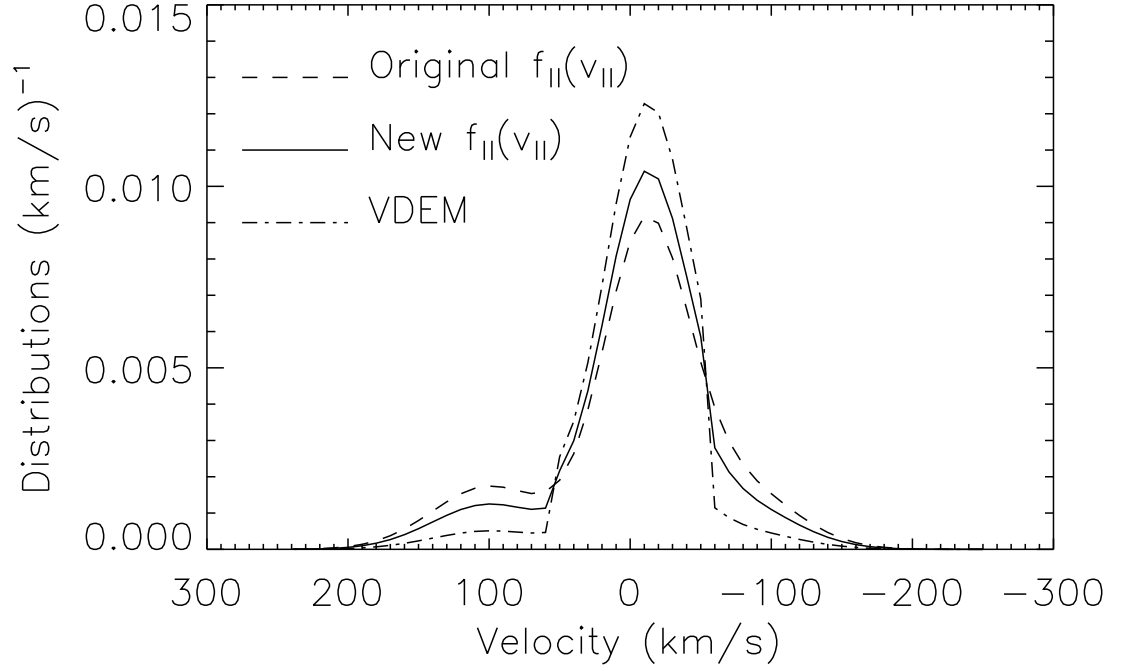


Figure 3.7: An example of how heating the plasma in the high-speed volume elements while maintaining constant pressure would affect the bulk velocity distribution (solid) and VDEM function (dash-dot). The original bulk velocity function is shown as a dashed line.

Table 3.5: A comparison of the energy flux measured from an assumed bulk velocity distribution and from a theoretical VDEM function when the plasma in the high-speed volume elements is cooled and constant density is maintained.

Energy Flux (ergs cm ⁻² s ⁻¹)	From $f_{ }(v_{ })$	From VDEM	Percentage Difference
j_E	3.4×10^5	-4.7×10^5	238 %
j_{E+}	3.2×10^6	1.2×10^6	62 %
j_{E-}	-2.9×10^6	-1.7×10^6	41 %

speed volume elements and the constraint of constant pressure, the density in these elements increases, which in turn, increases the bulk velocity distribution. The VDEM function, however, is still suppressed. Even though the density increases (which scales up the VDEM by n_e^2), the drop in the emissivity function at the lower temperature dominates. (The densities at these temperatures are $n_e(10^{5.0}) = 10^{10} \text{ cm}^{-3}$ and $n_e(10^{5.2}) = 10^{9.8} \text{ cm}^{-3}$, a factor of 1.6 increase for the lower temperature plasma. The emissions at these temperatures are $n_e^2 G(10^{5.0}) = 10^{-2.8} \text{ ergs cm}^{-3} \text{ s}^{-1}$ and $n_e^2 G(10^{5.2}) = 10^{-2.4} \text{ ergs cm}^{-3} \text{ s}^{-1}$, a factor of 2.5 decrease for the lower temperature emission.) In this scenario, the true energy flux measurements are expected to increase from those of the original distribution, while the energy flux measured from the VDEM function will again decrease. The results are given in Table 3.6.

3.4.3 Summary of the Validity of the VDEM Approximation

Finding the energy flux with the moments of the VDEM function assumes that the temperature and density are essentially constant, that the line-of-sight coincides with the direction of motion, and that the line profile well-represents the emitting plasma. Even in the idealized situation when the line-of-sight does correspond with the direction of motion and there are no temperature or density gradients, the line profile must still be defined by more than 1,000 counts for the deconvolved VDEM function to well represent the parallel bulk velocity distribution of the emitting plasma. If there are density or temperature

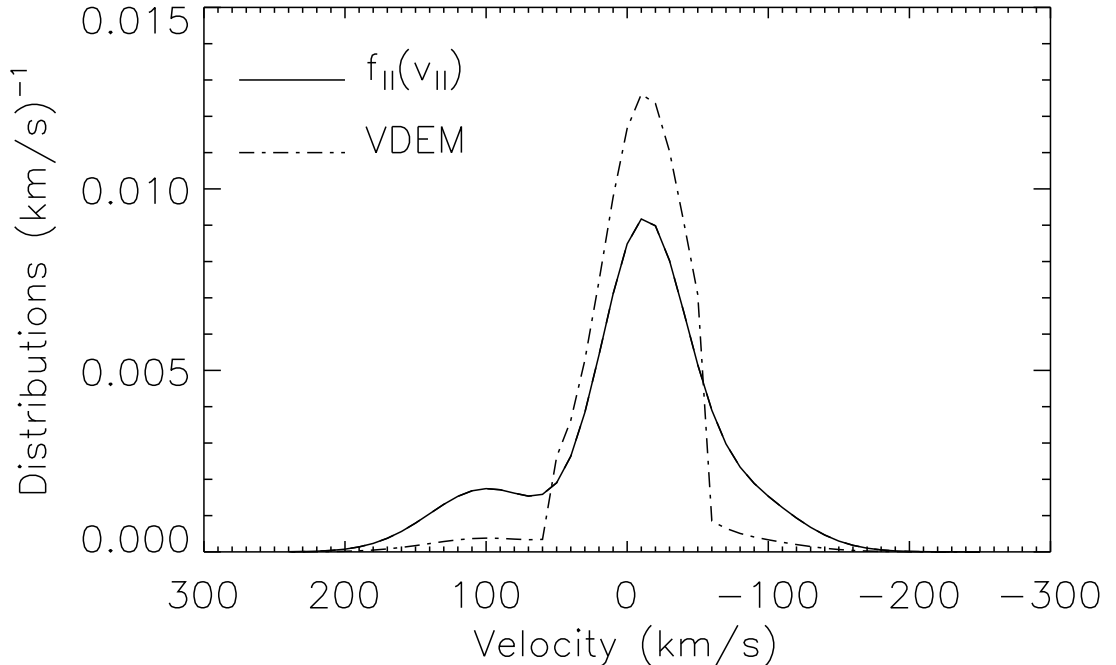


Figure 3.8: An example of how cooling the plasma in the high-speed volume elements while maintaining uniform density would affect the bulk velocity distribution (solid) and VDEM function (dash-dot).

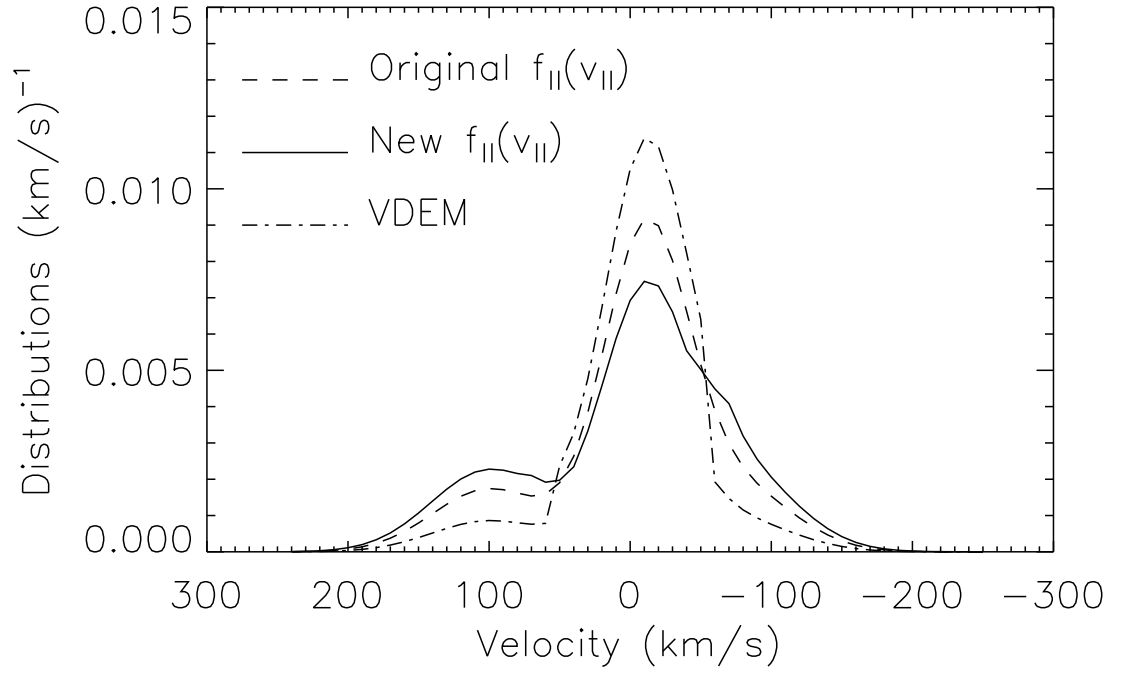


Figure 3.9: An example of how cooling the plasma in the high-speed volume elements while maintaining constant pressure would affect the bulk velocity distribution (solid) and VDEM function (dash-dot). The original bulk velocity distribution is shown as a dashed line.

Table 3.6: A comparison of the energy flux measured from an assumed bulk velocity distribution and from a theoretical VDEM function when the plasma in the high-speed volume elements is cooled and constant pressure is maintained.

Energy Flux (ergs cm ⁻² s ⁻¹)	From $f_{ }(v_{ })$	From VDEM	Percentage Difference
j_E	6.8×10^5	-1.8×10^5	126 %
j_{E+}	4.1×10^6	1.9×10^6	54 %
j_{E-}	-3.4×10^6	-2.1×10^6	38 %

gradients in the emitting plasma associated with the acceleration or if the line-of-sight does not correspond to the direction of motion, the energy flux measured from the VDEM function will always be less than the true energy flux. Note that regardless of the direction of

the temperature or density gradients, the returned VDEM will always be suppressed at high velocities. (The degree that VDEM will be suppressed is dependent upon the temperature and density of the emitting plasma and the emissivity function of the spectral line.) This is mainly due to the narrowness of the emissivity function for transition region ions, and supports the initial assumption that density in the bulk of the emitting region can, for present purposes, be assumed constant. The value for the net energy flux in particular is much less reliable if there are temperature or density gradients present in the emitting plasma.

The simulations and discussions in this sections have shown that, with minimal data requirements (discussed in the following section), the energy flux measured with the VDEM function gives a *lower limit* to the true energy flux of the emitting plasma.

3.5 Data Restrictions

There are several restrictions that need to be placed on the data used for this study. Some restrictions are present because of the subject (explosive events), others to reduce systematic errors in finding the energy flux using the VDEM approximation.

The spatial scale of a typical explosive event is on the order of 1,500 km, with evidence that events have yet to be fully resolved. To spatially resolve an event, the deprojected length of a single pixel along the slit onto the sun must be significantly less than this value. The deprojected length of a 1'' pixel as a function of radial angle (the angle between the line-of-sight direction and the local normal) is shown in Figure 3.10. For this length to be

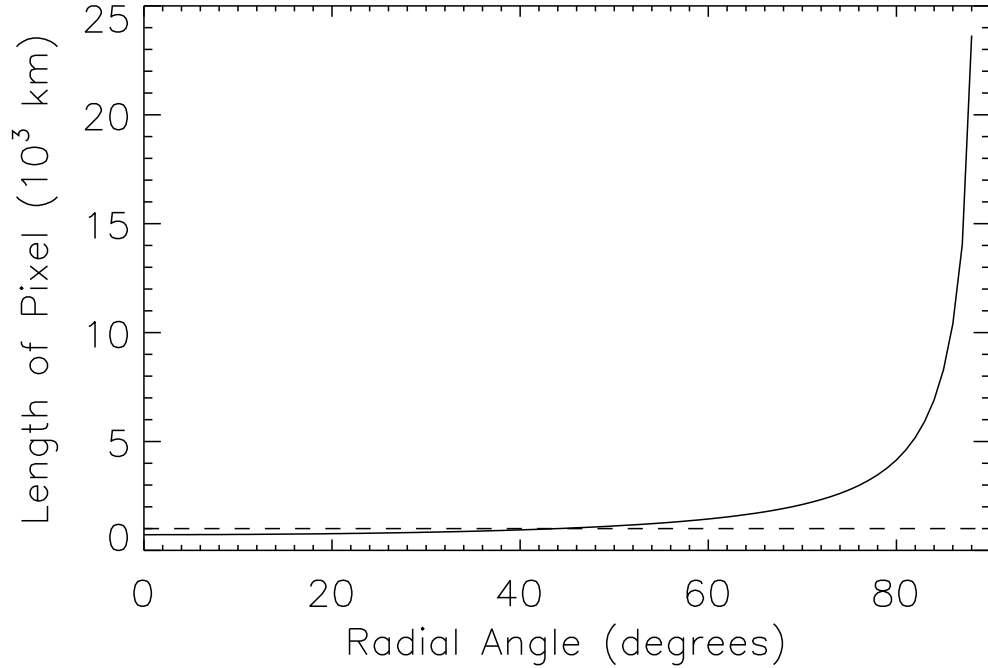


Figure 3.10: The deprojected length of a single pixel as a function of the radial angle.

Table 3.7: A prioritized list of data restrictions.

Priority	Restriction
1	Number of Counts defining a line above 1,000 Non-blended lines Adequate method to determine wavelength array
2	Line formed at different temperatures observed simultaneously Spectra observed at or very near sun center Long observation times with large quantities of spectra
3	High spatial and temporal resolution

less than 1,000 km, the data must be taken within 40° of sun center. Also, observing events near sun center further assures that the energy flux measured moving toward the observer is also moving into the corona. The data, then, will be restricted to spectra taken at or very close to sun center.

The lifetime of a typical event is on the order of tens of seconds with evidence for significant change in the event profile within 20 s. To capture the energetics of these events, the exposure time (the lower limit of the lifetime) must be on the order of tens of seconds or less. Furthermore, to find the distribution of events as a function of energy, a statistically significant number of events must be observed. This implies the data must contain many spectra taken over long observation times.

As presented in Section 3.4, it is necessary to maintain a high number of counts defining a line profile to ensure that the deconvolved VDEM function will accurately describe the velocities in the emitting plasma. To have systematic errors on the order of data uncertainties, at least 1,000 counts must define a spectral line before energy flux from a normalized VDEM function can be thought of as accurate. It is also necessary to have unblended lines and an adequate method of establishing a wavelength array that is associated with the spectrum to reduce the uncertainties in the returned energy flux.

Finally, it is desirable to observe these explosive events in lines formed at different temperatures simultaneously. This would provide an unambiguous idea of how event characteristics change with temperature since all lines would presumably be formed in the same solar structure.

With so many restrictions placed on the data, it is difficult to imagine that *any* data set

will meet these standards. Therefore, priorities have been assigned each data restriction, shown in Table 3.7. Priority 1 restrictions are the minimal requirements every line profile must meet before a deconvolved VDEM function can adequately describe the bulk velocity distribution. Priority 2 and 3 restrictions are less necessary and oftentimes will be sacrificed to meet the first priority restrictions. For instance, the resolution of the spectra may be sacrificed to ensure that the number of counts defining a line is acceptable, or to observe lines formed at different temperatures simultaneously.

The only current instrument that observes in the UV and EUV wavelength range with high spatial and temporal resolution is the Solar Ultraviolet Measurements of Emitted Radiation (SUMER) telescope and spectrometer. This instrument has been recording solar spectra for over 3 years and has observed large quantities of high cadence data, perfect for the study of explosive events. The SUMER instrument will be introduced in the next chapter along with the data sets that were analyzed in this study.

CHAPTER 4

THE SUMER INSTRUMENT AND SPECTRAL DATA

This chapter introduces the Solar Ultraviolet Measurements of Emitted Radiation Telescope and Spectrometer and the spectral data selected for this study. It begins by reviewing the specifications of the SUMER optical design, pointing out limitations of the instrument and detectors, while emphasizing the improvements SUMER has made over past instruments. One of the limitations of the SUMER instrument is its poor wavelength calibration. To correct for this problem, a method of determining the wavelength associated with SUMER spectra is discussed in Section 4.2. The SUMER data sets used in this study are then reviewed in Section 4.3. Finally, the criteria for selecting explosive event profiles from the spectral data are introduced in Section 4.4 and the method of preparing these profiles for VDEM analysis is discussed in Section 4.5.

4.1 Solar Ultraviolet Measurements of Emitted Radiation

In 1995, the Solar Ultraviolet Measurements of Emitted Radiation (SUMER) Telescope and Spectrometer was launched aboard the *Solar and Heliospheric Observatory (SOHO)* to orbit around the first Sun-Earth Lagrange point providing an uninterrupted view of the sun. Its scientific objectives included studying solar coronal heating, solar wind acceleration, and the structure of the solar upper atmosphere, while expanding the knowledge of stellar physics, plasma physics, and the Sun-Earth relationship. To meet these scientific objectives, the SUMER telescope and spectrometer were built to make high spatial, spectral, and temporal resolution measurements of UV and EUV emission lines from 600 Å to 1,610 Å. The instrument has been thoroughly discussed in several papers (Wilhelm et al. 1995, 1997; Lemaire et al. 1997), but will be reviewed briefly here.

The main optical components of the SUMER instrument consist of two parabolic mirrors, a plane mirror, and a spherical concave grating mounted in an aluminum housing that serves as an optical bench (see Figure 4.1). The first parabolic (telescope) mirror has capabilities to move ± 38 arcmin in two perpendicular directions and serves as the pointing and scanning mirror. It images the sun onto the spectral slit and through the rear slit camera, which assists in pointing. The light is then focused by the second parabolic mirror, and imaged onto a spherical grating by the plane mirror. The wavelength range is adjusted by rotating the plane mirror from 8.3° to 17.6° . The point spread function of the telescope has a full width at half-maximum (FWHM) of less than $1''$ and suffers a sharp decrease at $3.5''$.

Two two-dimensional detectors (referred to as A and B) are located in the focal plane of the spherical grating and are used alternately. Detector A is centered on the grating normal and detector B is offset by approximately 70 mm. They are both 1,024 pixels in the dispersion (wavelength) direction and 360 pixels in the spatial direction. For observations in first order, a pixel width in the dispersion direction is approximately 45 mÅ, implying the wavelength range of a full detector observation is 46 Å. The pixel width in the spatial direction is $1''$. The center portion of each detector is coated with potassium bromide (KBr)

which enhances the quantum detection efficiency, while the rest of the detector is left bare. Very intense lines must be observed with attenuators which are located over a portion of the bare wings of each detector. In-flight sensitivity tests show detector non-uniformities on a scale of 20 pixels and a geometrical distortion across the edge of the detectors caused by fringe field. To correct both problems, each spectrum must be flat-field corrected and destretched. Instrumental broadening has been derived from chromospheric lines to be a Gaussian function with a FWHM of 2 pixels ($\sim 88 \text{ m}\text{\AA}$) for Detector A and 3 pixels ($\sim 132 \text{ m}\text{\AA}$) for Detector B. (This dependence of the instrumental function on the detector was documented by Chae, Schühle, & Lemaire 1998.)

The SUMER instrument provides 4 spectral slits, as well as a $1'' \times 1''$ “pin-hole” for focusing. Slit 1 is a $4'' \times 300''$ slit for use off the limb. Slit 2 is a $1'' \times 300''$ slit for normal intensity lines or low-continuum. Slit 4 is $1'' \times 120''$ and slit 7 is $0.3'' \times 120''$ for high intensity lines. The smallest structure measured along the slit has been 2 pixels ($2''$). The smallest structure width (measured using the $0.3'' \times 120''$ slit and a mirror step size of $0.38''$) was $1.2''$. The slits are oriented parallel to the solar central meridian. Coordinates for SUMER spectral data refer to the position of the center of the slit and are given in arcsecs from the sun center, i.e., a coordinate of $500''$ North and $200''$ East would imply that the center of the slit was $500''$ to the north of sun center and $200''$ to the east of the central meridian.

The spectral response of the SUMER instrument was determined pre-flight from its response to the known radiation of a calibrated light source. The derived calibrations have an uncertainty of 10% in absolute flux. In-flight tests show that the calibrations have

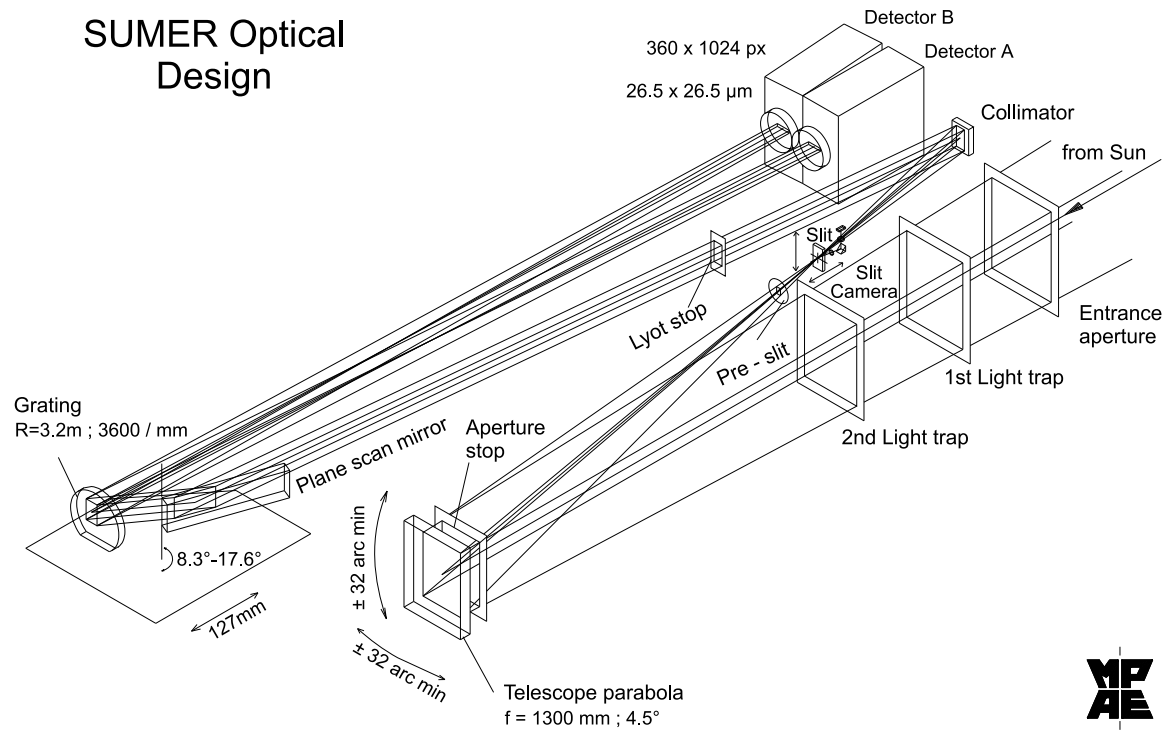


Figure 4.1: The main components of the SUMER optical design (figure courtesy of Dietmar Germerott).

not degraded (Wilhelm et al. 1997). The SUMER software package includes a radiometry program that calculates the conversion of count rate (counts s^{-1}) to specific intensity ($\text{photons cm}^{-2} \text{s}^{-1} \text{\AA}^{-1} \text{sr}^{-1}$). Due to the accuracy of the radiometric calibration, good measurements for intensity and emission measure are expected.

Unfortunately, the wavelength calibration performed pre-flight was substantially changed during in-flight operations. The instrument has been recalibrated in-flight and can now place a given wavelength within a 25 pixel window, implying that an average first order dispersion of $45 \text{ m\AA pixel}^{-1}$ could lead to a systematic error in wavelength of 1 \AA (300 km s^{-1} at 1000 \AA) (Wilhelm et al. 1997). Because SUMER was specifically designed to study wavelength-sensitive transition region phenomena, such as redshifts, this inaccuracy severely limits analysis. An alternate method of determining the wavelength array associated with a SUMER spectrum using reference lines will be discussed in Section 4.2.

Despite this loss in wavelength accuracy, the SUMER telescope and spectrometer has greatly improved the quality and quantity of the available spectra at UV and EUV wavelengths. The spatial and spectral resolution is comparable to that of the HRTS instrument ($\sim 1''$ and 45 m\AA for SUMER and $\sim 1''$ and 50 m\AA for HRTS), but the wavelength coverage is nearly double that of HRTS. (The SUMER instrument can observe between $600\text{--}1,610 \text{ \AA}$, while HRTS spectral coverage was only $1,175\text{--}1,710 \text{ \AA}$.) The most significant advantage of the SUMER instrument is the amount of data it produces and the versatility it offers in observation programs. Because SUMER is flown on a satellite (as opposed to sounding rockets), the only limit to the amount of data observed is the lifetime of the detector. Observations of a single solar structure can go on for hours or days, providing time coverage of solar events that no other instrument has been able to match. Observations can be taken with long exposures or short exposures, partial spectra or full spectra. A single structure can be observed in the entire wavelength range, or the entire sun can be scanned in a single wavelength.

4.2 Defining the Wavelength Array from Reference Lines

As mentioned above, the SUMER on-board wavelength calibration is a poor estimate for the true dispersion of an observed spectrum. To improve the wavelength calibration, some spectral lines present in the spectrum, along with their solar wavelengths, can be used to calculate the spectral dispersion. The choice of these spectral lines, referred to as reference lines, affects the accuracy of the resulting wavelength array and must be made carefully. A reference line must be a non-blended line with a well-defined centroid. To avoid detector non-linearity problems, it is better to choose reference lines in the center of the detector (where the dispersion is assumed to be “locally linear”—Chae, Yun, & Poland 1998). Lines formed by neutral or singly ionized chromospheric ions are preferred as reference lines because they tend to exhibit relatively small absolute shifts (e.g., Brekke, Hassler, & Wilhelm 1997) and their laboratory wavelengths are known to high precision. For the wavelength ranges where no non-blended chromospheric lines are emitted, transition region or coronal lines can be used as reference lines. To account for the redshifts that are often observed in transition region and coronal lines, the laboratory wavelength must be shifted by the typical redshifted velocity (e.g., Chae, Yun, & Poland 1998). Not only do these velocities have rather large uncertainties ($\pm 2 \text{ km s}^{-1}$), they are also temperature dependent and may be dependent on the emitting solar structure. Using the shifted wavelengths, then, as reference lines introduces a possibility for significant systematic error in the established

wavelength array.

Each reference line is averaged along the slit, background subtracted, and fit with a single Gaussian function. The Gaussian centroids and solar wavelengths of the reference lines are then fit to a first degree polynomial function using a weighted least squares method. The resulting dispersion relationship is:

$$\lambda(\mu) = A_0 + A_1 \mu, \quad (4.1)$$

where A_0 and A_1 are the coefficients returned from the fit, and $\lambda(\mu)$ is the wavelength associated with the center of each spectral pixel, μ . The uncertainty in the wavelength array is found from the uncertainties in the solar wavelengths and from the uncertainty in the fit of the solar wavelengths and centroids to a first degree polynomial function. If the reference lines are chromospheric lines, their solar wavelengths are simply their laboratory wavelengths and the uncertainty in the dispersion is dominated by the deviation of the points from the straight line. If the reference lines are transition region lines, the uncertainty in the wavelength array is dominated by the uncertainty in the redshifted wavelengths.

Temperature variations of the detector cause the parameters A_0 and A_1 in the dispersion relation (4.1) to oscillate on a time scale of 30 minutes, which results in fluctuations in the wavelength array of ± 10 mÅ. To avoid additional uncertainty in the wavelength array, it is desirable to update the dispersion relation for every spectrum observed. However, for the high cadence data typically needed to observe explosive events, only small spectral windows around single spectral lines (approximately 2 Å) are retrieved. Such spectral windows are too narrow to include observations of reference lines which are generally observed only when a full detector image is taken.

To ensure an accurate wavelength array over the entire observation time, a full detector image should be observed every 30 minutes to update the dispersion coefficients. Assuming that the dispersion coefficients change linearly with time, the time dependence of the wavelength array can be found from the coefficients of each full spectrum, i.e.,

$$\lambda(\mu, t) = A_0(t) + A_1(t) \mu, \quad (4.2)$$

where, for instance,

$$A_0(t) = A_0(t_0) + \left[\frac{A_0(t_1) - A_0(t_0)}{t_1 - t_0} \right] (t - t_0), \quad (4.3)$$

and t_0 and t_1 are the times that the two full spectra were observed. If full detector images are not taken periodically during a high cadence observing sequence, it is necessary to assume an additional ± 10 mÅ uncertainty in the wavelength array. (This uncertainty was established by determining the wavelength fluctuations over time for the Ne VIII and N IV data set discussed below.)

4.3 SUMER Spectral Data

The SUMER data archives were scanned for data that closely met the guidelines and restrictions given in Section 3.5 and wavelength calibration needs discussed in Section 4.2. Only observations of the quiet sun were considered. Two data sets were selected for analysis. The first data set was taken over 5 hours on 1996 May 10. It contains observations of the C III 977 Å line and the O VI 1032 Å line observed sequentially with high spatial and spectral

Table 4.1: Characteristics of the data sets used for this study.

	C III	O VI	Ne VIII & N IV
Date(s) Observed	1996 May 10	1996 May 10	1996 Oct 18-Nov 2
Slit	0.3'' \times 120''	1'' \times 120''	1'' \times 120''
Detector	A	A	B
Average Solar Position	200'' W, 150'' N	200'' W, 150'' N	0'', 0''
Spatial Resolution	740 km	740 km	2170 km
Temporal Resolution	48 s	36 s	120 s
Number of Profiles	17,520	39,360	43,560
Chromospheric Lines	Yes	Yes	No
Multiple Full Exposures	No	No	Yes

resolution. The second data set included 36 hours of observations taken over 9 days in the period between 1996 October 18 - November 2. It contains observations of two spectral lines simultaneously (N IV 765 Å line and Ne VIII 770 Å line), but with poor spatial and temporal resolution. These spectral lines are formed in the temperature range of $10^{4.8}$ to $10^{5.9}$ K. The characteristics of each data set, presented below, are summarized in Table 4.1.

4.3.1 The C III & O VI Data Sets

The C III 977 Å and O VI 1032 Å lines were sequentially observed over 5 hours on 1996 May 10. The O VI line was observed over the first 3 hours, while the C III line was observed over the remaining 2 hours. These quiet sun observations were taken as a set of rasters centered at approximately 200'' West and 150'' North of sun center, resulting in a spatial resolution (along the slit) of 740 km. An H α image taken on the same day is shown in Figure 4.2 with the average position of the slit marked.

C III 977 Å line

The emissivity function of the C III line peaks at a temperature of $10^{4.8}$ K with a value of $10^{-21.9}$ ergs cm³ s⁻¹ (Landini & Monsignori Fossi 1990). This strong resonance line was observed with a narrow slit (0.3'' \times 120'') and fast exposure time (6 s). Only 50 pixels (~ 2 Å) around the C III line were retrieved during these high cadence exposures.

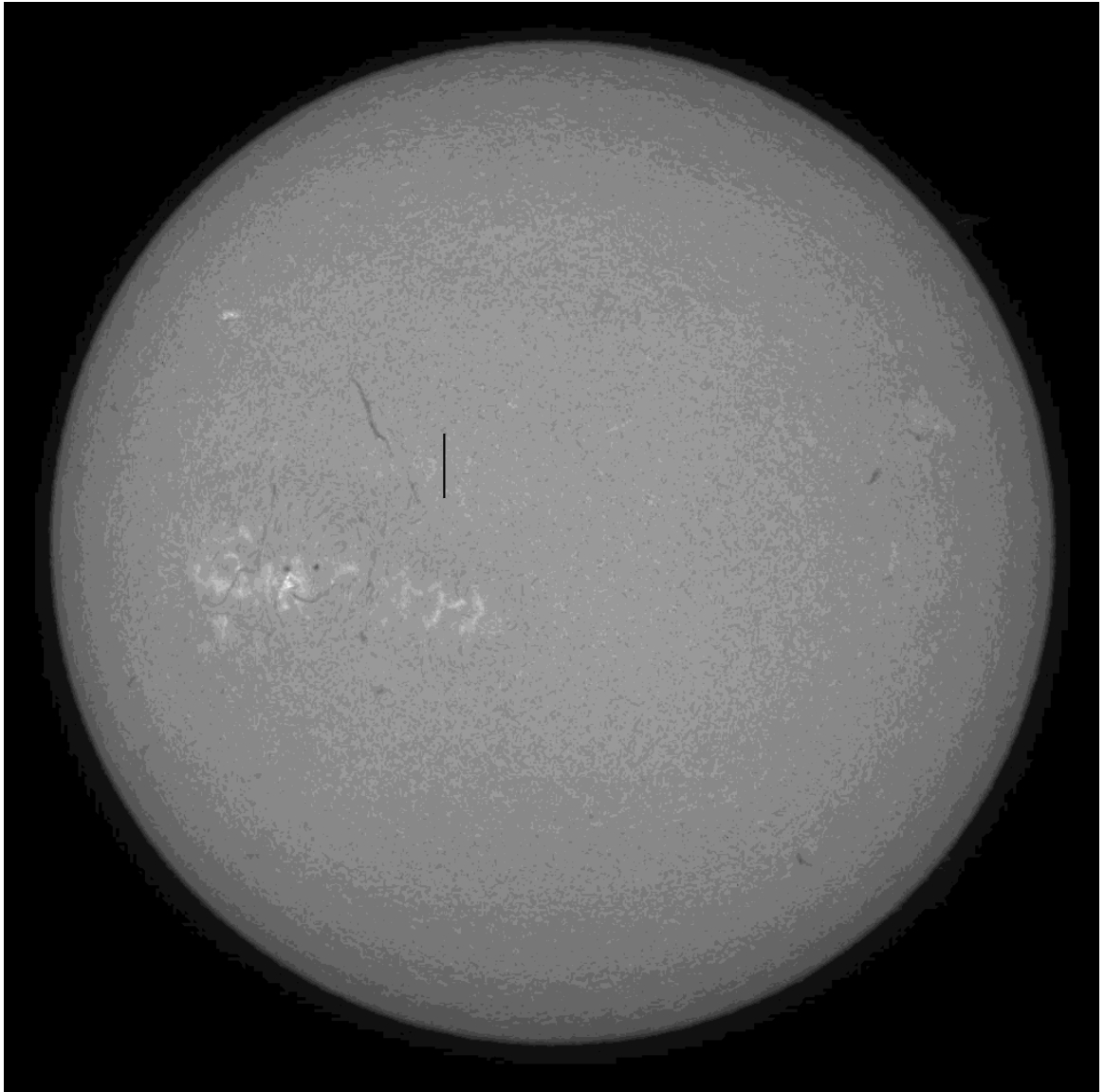


Figure 4.2: This $H\alpha$ image was observed by Big Bear Solar Observatory on 1996 May 10. The dark line near sun center shows the average position of the SUMER slit.

Each spatial pixel along the slit constitutes a line profile. The average number of counts per profile was approximately 200 counts. To increase this average number of counts to an acceptable amount (1,500 counts per profile) eight consecutive spectra were summed to form a single spectrum with an exposure time of 48 s. An example of a resulting spectrum is shown in Figure 4.3 (a). This produced 17,520 line profiles with a temporal resolution of 48 s and spatial resolution of 740 km.

Because C III is a strong resonance line, it may suffer from broadening due to opacity. The optical depth for a volume of plasma with a scale height, H_0 , is found by

$$\tau_0 = nH_0l_0, \quad (4.4)$$

where n is the number density of the emitting ion and l_0 is proportional to the oscillator strength for the transition and inversely proportional to the Doppler width of the spectral line. (For full definition, see Mariska 1992.) Assuming an oscillator strength of the C III line of 0.8 (Landini & Monsignori Fossi 1990) and a Doppler velocity width of 22 km s^{-1} , the optical depth is

$$\tau_0 \approx 5.2 \times 10^{-8} H_0, \quad (4.5)$$

where H_0 is expressed in centimeters. This implies an optical thickness of unity will be obtained when the thickness of the emitting plasma reaches $\sim 200 \text{ km}$. The scale height for the lower transition region found from the constant conductive flux approximation is $\sim 10 \text{ km}$, so broadening due to opacity near sun center may be ignored. (Note, however, that if the observations were taken off the solar limb, the depth of the volume of emitting plasma would be significantly increased and hence the spectral line may reflect additional broadening due to opacity.)

In the middle of the high cadence observing sequence, a single long exposure (100 s) spectrum observing half the detector (approximately 20 \AA) was taken. Figure 4.4 shows this long exposure along with the flux of the spectrum found by averaging over the spatial pixels. Spectral lines emitted in this wavelength range ($\sim 967 - 987 \text{ \AA}$) were identified using the catalog of spectral lines appearing in Feldman et al. (1997) and Curdt et al. (1997). They are labeled along the right hand side of the plot and listed, along with their corresponding transitions, in Table 4.2. Four unblended O I lines were used to determine the wavelength array associated with the C III spectra. The resulting dispersion relation was

$$\lambda(\mu) = 966.055 + 0.0442\mu. \quad (4.6)$$

The uncertainty in the returned wavelength array from the fit of the 4 reference line wavelengths and centroids to a first degree polynomial was 12 m\AA . An additional uncertainty of 10 m\AA must be assumed due to the lack of multiple observations of reference lines. The total uncertainty in the wavelength array is then 16 m\AA , corresponding to a velocity uncertainty of 5 km s^{-1} .

O VI 1032 Å line

The emissivity function of the O VI 1032 Å line peaks at a temperature of $10^{5.45} \text{ K}$ with a value of $10^{-22.4} \text{ ergs cm}^3 \text{ s}^{-1}$ (Landini & Monsignori Fossi 1990). In the May 10 data set, this line was observed with the $1'' \times 120''$ slit. Only partial spectra (50 pixels or approximately 2 \AA around the line) were retrieved, each with an exposure time of 6 s. Each spatial pixel along the slit constituted a line profile. The average number of counts per line profile was 250. To achieve a more acceptable average, every 6 exposures were added to

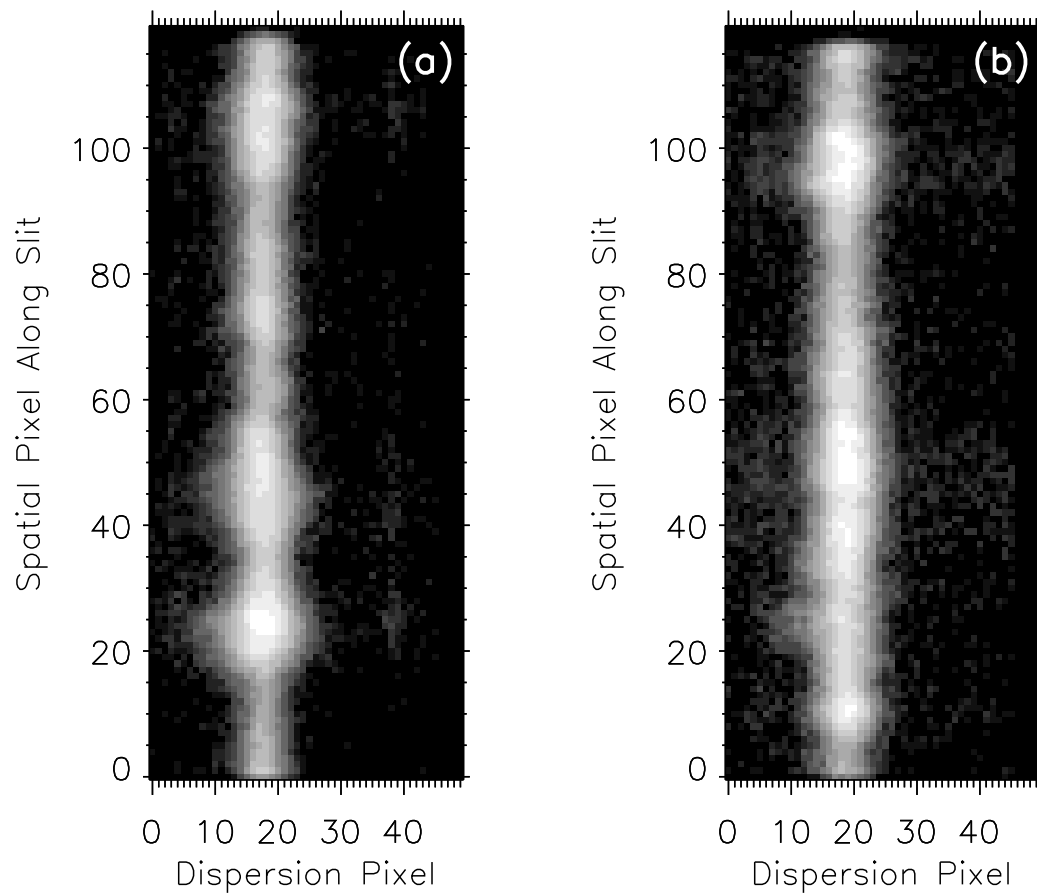


Figure 4.3: Examples of high cadence spectra observed around the C III 977 Å line (a) and O VI 1032 Å line (b).

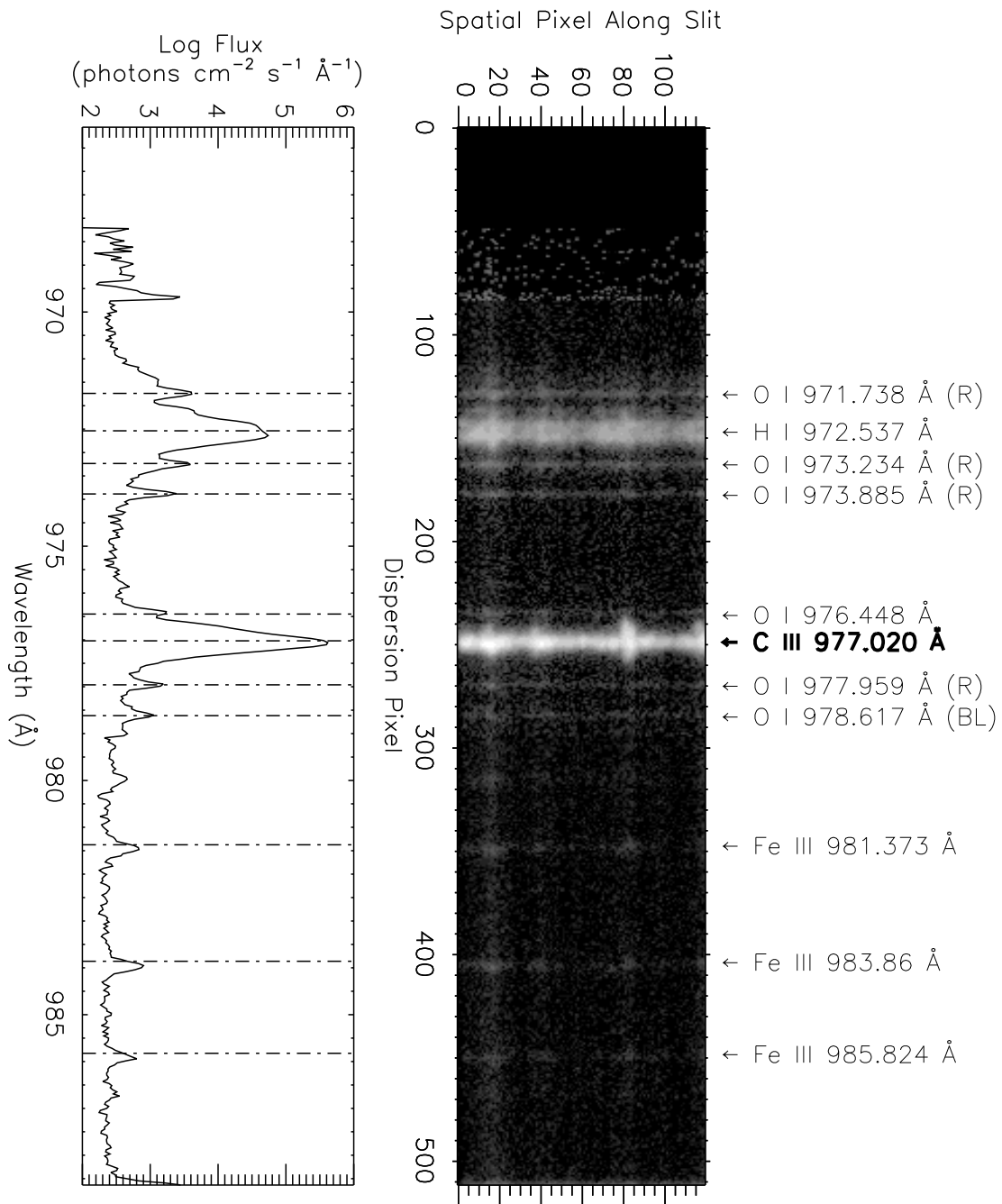


Figure 4.4: A spectrum around the C III 977 Å line along with the corresponding line profile averaged along the slit.

Table 4.2: Spectral lines in the wavelength range of 970 - 987 Å and their corresponding transitions. The O I lines used as reference lines are marked with an ‘R’.

Ion	Laboratory Wavelength (Å)	Transition	Reference
O I	971.7381	$2s^2 2p^4 \ ^3P_2 - 2s^2 2p^3 4d \ ^3D_3$	R
H I	972.537	$1s \ ^2S - 4p \ ^2P$	
O I	973.2343	$2s^2 2p^4 \ ^3P_1 - 2s^2 2p^3 4d \ ^3D_2$	R
O I	973.8852	$2s^2 2p^4 \ ^3P_0 - 2s^2 2p^3 4d \ ^3D_1$	R
O I	976.4481	$2s^2 2p^4 \ ^3P_2 - 2s^2 2p^3 5s \ ^3S_1$	
C III	977.020	$2s^2 \ ^1S_0 - 2s 2p \ ^1P_1$	
O I	977.9594	$2s^2 2p^4 \ ^3P_1 - 2s^2 2p^3 5s \ ^3S_1$	R
O I	978.6170	$2s^2 2p^4 \ ^3P_0 - 2s^2 2p^3 5s \ ^3S_1$	
Fe III	981.373	$3d^5(a^4P)4s \ ^5P_2 - 3d^5(a^6S)5p \ ^5P_2$	
Fe III	983.860	$3d^6 \ ^3H_5 - 3d^5(a^4G)4p \ ^3G_4$	
Fe III	985.824	$3d^6 \ ^3H_4 - 3d^5(a^4G)4p \ ^3G_3$	

create a single spectrum with an exposure time of 36 s. Figure 4.3 (b) shows an example of a resulting spectrum. This created a total of 39,360 line profiles with a temporal resolution of 36 s and spatial resolution of 740 km.

In the middle of the observing sequence, a single long exposure (100 s) spectrum was taken where 512 pixels in the dispersion direction were retrieved. This exposure is shown in Figure 4.5. Table 4.3 lists the lines emitted in this wavelength range, $\sim 1,021 - 1,043 \text{ \AA}$ with their corresponding transitions. Five O I lines are emitted in this range and were used for finding the wavelength array of the O VI spectra. The resulting dispersion relation was

$$\lambda(\mu) = 1021.006 + 0.0437\mu. \quad (4.7)$$

The total uncertainty in the wavelength array is 17 m\AA (5 km s^{-1}), including uncertainty due to the poor fit of the five reference wavelengths and centroids to a first degree polynomial and the lack of multiple observations of reference lines.

Table 4.3: Spectral lines in the wavelength range of 1021 - 1043 \AA and their corresponding transitions. The O I lines used as reference lines are marked with an ‘R’.

Ion	Laboratory Wavelength (\AA)	Transition	Reference
H I	1025.722	$1s \text{ } ^2S - 3p \text{ } ^2P$	
O I	1027.4307	$2s^2 2p^4 \text{ } ^3P_1 - 2s^2 2p^3 3d \text{ } ^3D_2$	R
O I	1028.1571	$2s^2 2p^4 \text{ } ^3P_0 - 2s^2 2p^3 3d \text{ } ^3D_1$	R
O VI	1032.9261	$2s \text{ } ^2S_{\frac{1}{2}} - 2p \text{ } ^2P_{\frac{3}{2}}$	
C II	1036.3367	$2s^2 2p \text{ } ^2P_{\frac{1}{2}} - 2s 2p^2 \text{ } ^2S_{\frac{1}{2}}$	
C II	1037.0182	$2s^2 2p \text{ } ^2P_{\frac{3}{2}} - 2s 2p^2 \text{ } ^2S_{\frac{1}{2}}$	
O VI	1037.614	$2s \text{ } ^2S_{\frac{1}{2}} - 2p \text{ } ^2P_{\frac{1}{2}}$	
O I	1039.2304	$2s^2 2p^4 \text{ } ^3P_2 - 2s^2 2p^3 4s \text{ } ^3S_1$	R
O I	1040.9425	$2s^2 2p^4 \text{ } ^3P_1 - 2s^2 2p^3 4s \text{ } ^3S_1$	R
O I	1041.6876	$2s^2 2p^4 \text{ } ^3P_0 - 2s^2 2p^3 4s \text{ } ^3S_1$	R

4.3.2 The N IV & Ne VIII Data Set

The N IV 765 \AA line and Ne VIII 770 \AA line were observed simultaneously for more than 36 hours over 9 days from 1996 October 18 to 1996 November 2. The observations

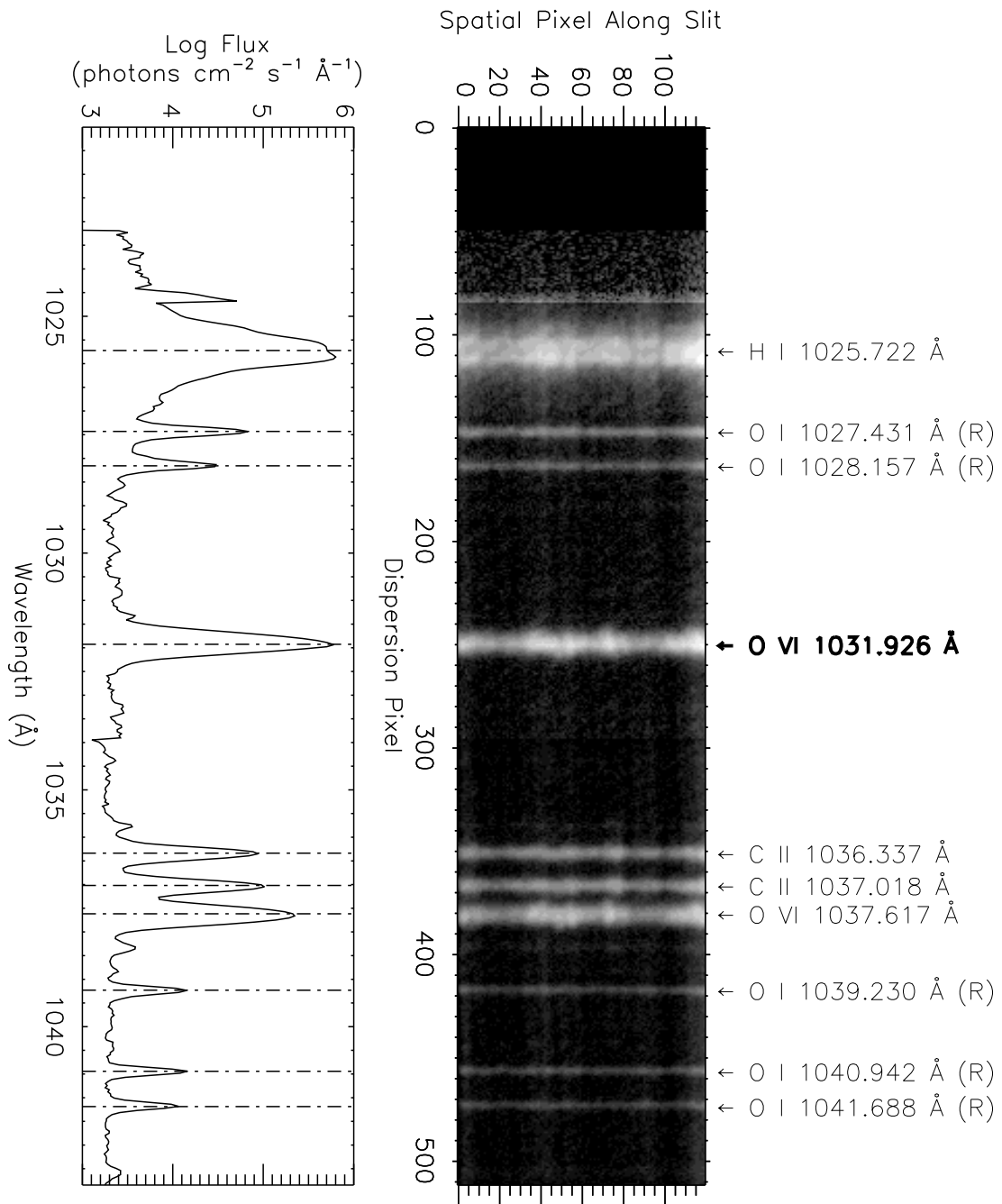


Figure 4.5: A spectrum around the O VI 1032 \AA line along with the corresponding line profile averaged along the slit.

were taken with the $1'' \times 120''$ slit at or near sun center. Figure 4.6 shows the quiet sun on the first day of observation with a deprojection of the slit image at sun center.

Over the 36 hours of observations, 53 exposures of the full detector were made, approximately one full exposure every 40 minutes. These long exposures include observations of several spectral lines other than the two spectral lines observed at high cadence. An example of a full exposure spectrum observed on 1996 October 18 is shown in Figure 4.7. The lines emitted in this wavelength range are shown along the right hand side of the spectrum and given in Table 4.4 with their corresponding transitions. No chromospheric lines are emitted in this wavelength range, so the coefficients of the dispersion relation were found using the four transition region lines given in Table 4.5. The temperature associated with the emitting ion was used to estimate the redshift velocities from Chae, Yun, & Poland (1998). The uncertainty in the velocities was assumed to be 2 km s^{-1} . [This uncertainty is twice the uncertainty of the velocity found by Chae, Yun, & Poland (1998). The additional uncertainty was assumed due to the error in the extrapolating the redshifted velocities to the temperature of the transition region reference lines.] The time-dependent dispersion relation was then evaluated [cf. Equation (4.2)]. A typical dispersion relation was

$$\lambda(\mu) = 754.837 + 0.0447\mu, \quad (4.8)$$

with an uncertainty of between 10 and 20 mÅ, or 4 - 8 km s^{-1} . This uncertainty was mainly due to the uncertainty in the wavelengths of the transition region reference lines.

The original high cadence spectra were taken with 20 s exposure times. The average number of counts defining each profile at a single spatial pixel in the original data was approximately 80 counts. To increase this average to a more acceptable 1,500 counts per profile, every 6 exposures and every 3 pixels along the slit were summed to create 43,560 profiles with spatial resolution of 2,170 km and exposure time of 120 s.

4.4 Selecting Dynamic Profiles

Each data set contains between 17,000 and 45,000 profiles, but only a fraction of those profiles can be considered explosive event profiles. A method must be implemented to select the dynamic profiles for VDEM analysis. The effectiveness of the selection criteria will have a direct effect on the accuracy of the distribution of events as a function of energy, $\frac{dN}{dE}$. If the selection criteria are too broad and non-event (low energy) profiles are mistakenly included, the distribution will be skewed toward lower energies. However, if the criteria are too specific, only the extremely dynamic profiles will be selected and the distribution will be skewed toward the higher energies.

One problem is the ambiguity in the definition of an explosive event. Explosive event profiles are defined as exhibiting extreme nonthermal broadening or skewness that imply bulk motions in the emitting plasma. The first question, then, is what is the normal width or skewness expected in a non-event transition region line profile? Transition region line profiles are generally well fit by Gaussian functions. The widths of typical profiles, however, are broadened far beyond the expected thermal widths, a phenomenon generally associated with microturbulence (e.g., Mariska 1992). The magnitude of the nonthermal broadening varies with temperature (e.g., Chae, Schühle, & Lemaire 1998); therefore, each ion studied here will have a different “normal” nonthermal width. Previous measurements of the nonthermal width summed all spectra along the slit without first excluding the explosive event profiles, and thus do not reflect solely non-event profiles. To find the “normal” nonthermal width of

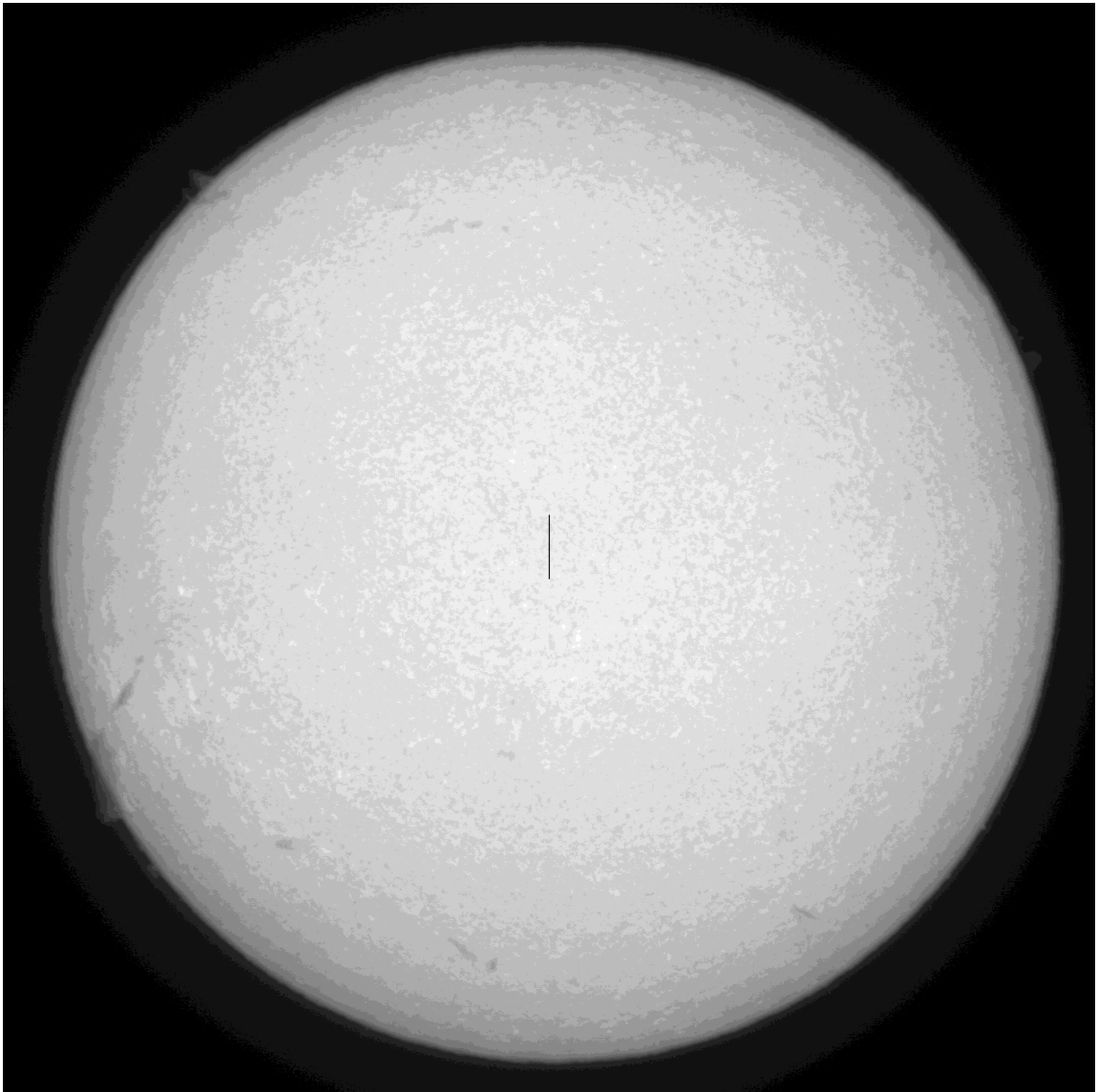


Figure 4.6: This $H\alpha$ image was observed by Big Bear Solar Observatory on 1996 October 18, the first day of observations for the N IV and Ne VIII data set. The dark line at sun center shows the position of the SUMER slit.

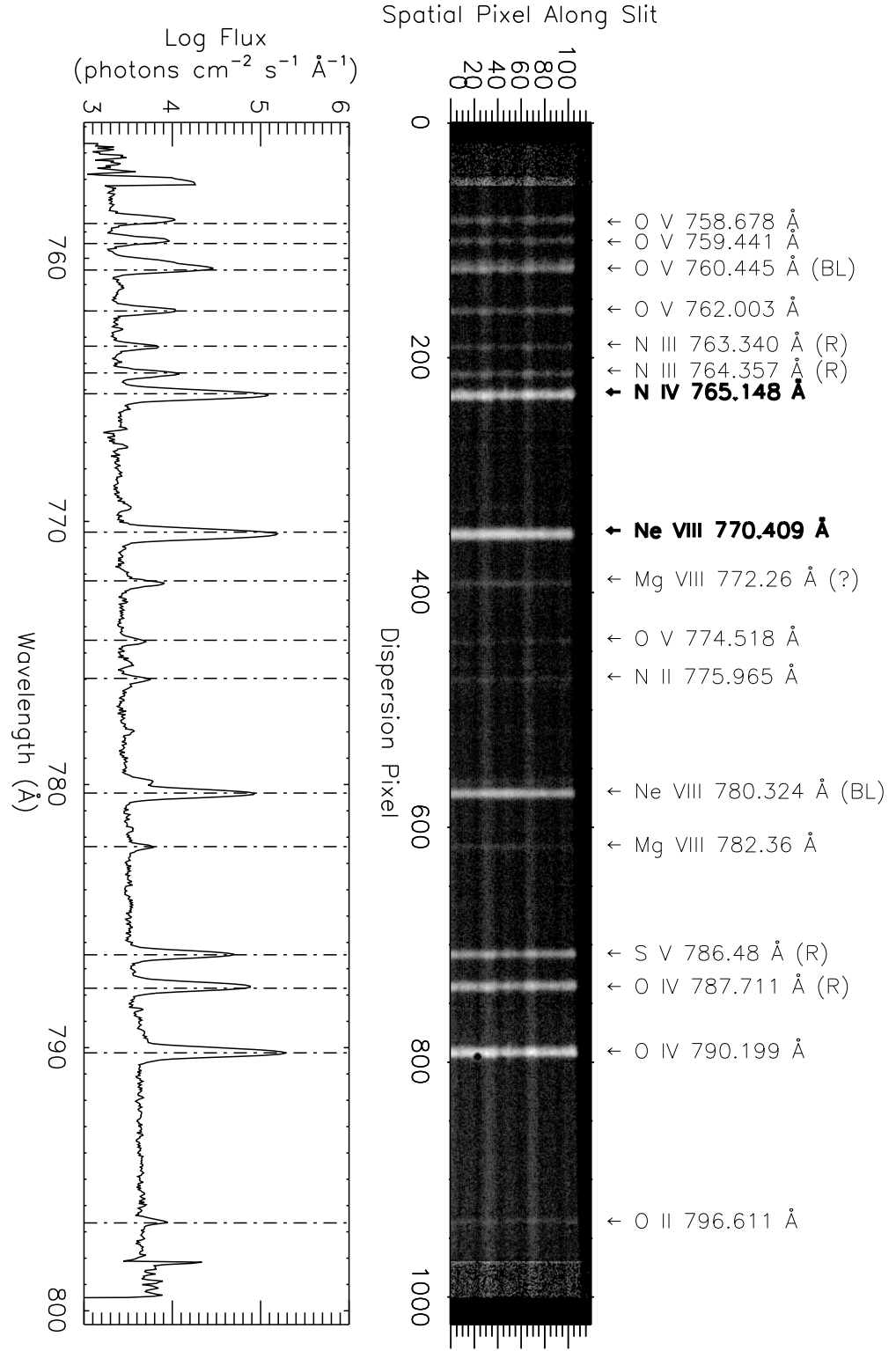


Figure 4.7: An example spectrum around the N IV 765 \AA line and Ne VIII 770 \AA line along with the corresponding line profile averaged along the slit.

Table 4.4: Spectral lines in the wavelength range of 758 - 797 Å and their corresponding transitions. The transition region lines used as reference lines are marked with an ‘R’.

Ion	Laboratory Wavelength (Å)	Transition	Reference
O V	758.678	$2s2p\ ^3P_1 - 2p^2\ ^3P_2$	
O V	759.441	$2s2p\ ^3P_0 - 2p^2\ ^3P_1$	
O V	760.445	$2s2p\ ^3P_2 - 2p^2\ ^3P_2$	
O V	762.003	$2s2p\ ^3P_2 - 2p^2\ ^3P_1$	
N III	763.340	$2s2p\ ^2P_{\frac{1}{2}} - 2s2p^2\ ^2S_{\frac{1}{2}}$	R
N III	764.357	$2s2p\ ^2P_{\frac{3}{2}} - 2s2p^2\ ^2S_{\frac{1}{2}}$	R
N IV	765.148	$2s^2\ ^1S_0 - 2s2p\ ^1P_1$	
Ne VIII	770.409	$2s\ ^2S_{\frac{1}{2}} - 2p\ ^2P_{\frac{1}{2}}$	
Mg VIII	772.26	$2s^22p\ ^2P_{\frac{3}{2}} - 2s2p^2\ ^5P_{\frac{5}{2}}$	
O V	774.518	$2s2p\ ^1P_1 - 2p^2\ ^1S_0$	
N II	775.965	$2s^22p^2\ ^1D_2 - 2s2p^2\ ^1D_2$	
Ne VIII	780.324	$2s\ ^2S_{\frac{1}{2}} - 2p\ ^2P_{\frac{1}{2}}$	
Mg VIII	782.36	$2s^22p\ ^2P_{\frac{3}{2}} - 2s2p^2\ ^4P_{\frac{3}{2}}$	(?)
S V	786.48	$3s^2\ ^1S_0 - 3s3p\ ^1P_1$	R
O IV	787.711	$2s^22p\ ^2P_{\frac{1}{2}} - 2s2p^2\ ^2D_{\frac{3}{2}}$	R
O IV	790.199	$2s^22p\ ^2P_{\frac{3}{2}} - 2s2p^2\ ^2D_{\frac{5}{2}}$	
O II	796.661	$2s^22p^3\ ^2P_{\frac{3}{2}} - 2s2p^4\ ^2D_{\frac{5}{2}}$	

Table 4.5: The spectral lines used as reference lines to determine the dispersion coefficients for the Ne VIII and N IV spectra.

Ion	Laboratory Wavelength (Å)	Temperature (K)	Redshifted Velocity (km s⁻¹)	Solar Wavelength (Å)
N III	763.340	10 ^{4.85}	7.7	763.360
N III	764.357	10 ^{4.85}	7.7	764.377
S V	786.47	10 ^{5.2}	11.1	786.50
O IV	787.741	10 ^{5.24}	11.1	787.740

non-event profiles, the event profiles must first be identified and excluded from the average flux, but to remove the event profiles, the nonthermal width must be known. This “chicken and egg” problem greatly increases the difficulty in defining the “normal” width of a spectral line. Furthermore, the plasma in the transition region exhibits a distribution of nonthermal widths, not simply a single value. The width of this distribution will affect the definition of what constitutes an extremely broadened profile.

If all transition region lines exhibit extra-thermal motions, then why are they all not considered dynamic events and analyzed? The difference between an explosive event profile and normal, nonthermally broadened profile is the model of the driving mechanism that creates the excess broadening. Normal nonthermal broadening is believed to be the result of turbulent, churning motions in the plasma. These motions do not imply bulk flows of the plasma or energy flux out of the volume element. Explosive events, however, are thought to be the product of magnetic reconnection. Enhanced broadening in an explosive event line profile does imply bulk flows in the emitting plasma and can produce significant energy flux.

Previous techniques of selecting event profiles include direct analysis of the spectra (e.g., Cook et al. 1988) and fitting each profile with a Gaussian function to see if it is excessively broadened (e.g., Chae et al. 1998). The first method is biased toward larger, more easily distinguishable events which would skew the distribution of events toward large energies. The second method requires fitting a profile that is intrinsically non-Gaussian with a Gaussian function. The fitting procedure often fails and the widths that are retrieved are poor representations of the profile’s true width.

A more straightforward method of selecting explosive event profiles is to measure the width, $\overline{(\lambda - \bar{\lambda})^2}$, and the skewness, $\overline{(\lambda - \bar{\lambda})^3}$, of each profile directly from the line intensity, i.e.,

$$\overline{(\lambda - \bar{\lambda})^2} = \frac{\int I(\lambda)(\lambda - \bar{\lambda})^2 d\lambda}{\int I(\lambda) d\lambda}, \quad (4.9)$$

and compare them to acceptable cutoff values, k_{wid} and k_{skew} . If the measured width or

Table 4.6: Width and skewness cutoff values used to ascertain if a profile exhibits extreme nonthermal broadening or skewness and hence is an explosive event.

	C III	N IV	O VI	Ne VIII
k_{wid}	7.8×10^{-3}	1.2×10^{-2}	1.2×10^{-2}	1.4×10^{-2}
$k_{\text{skew}+}$	2.7×10^{-4}	2.8×10^{-4}	3.7×10^{-4}	3.2×10^{-4}
$k_{\text{skew}-}$	-2.7×10^{-4}	5.3×10^{-4}	-4.4×10^{-4}	-5.6×10^{-4}

skewness of a profile is larger than the cutoff value, the profile is selected as an event. Although this scheme is simple, careful consideration must go into defining these cutoff values for width and skewness. Because the plasma in the transition region exhibits a distribution of “normal” nonthermal velocities, there will be similar distributions of acceptable widths and skewnesses. The cutoff values, then, must be defined in terms of these distributions of widths and skewnesses for each data set.

Figure 4.8 shows histograms (solid) of the measured widths for the 17,520 line profiles of the C III 977 Å line (a), the 43,560 line profiles of the N IV 765 Å line (b), the 39,360 line profiles of the O VI 790 Å line (c), and the 43,560 line profiles of the Ne VIII 770 Å line (d). Each distribution of widths is really the convolution of two separate distributions: the distribution of the “normal” widths associated with non-event profiles and the distribution of the extremely broadened widths associated with event profiles. Non-event profiles will definitely dominate the convolved distribution at low widths and the event profiles will dominate at high widths. The width at which the dominance changes from non-event profiles to event profiles, was taken to be the cutoff value. Assuming that the distribution of widths associated with non-event profiles is well-represented by a Gaussian function, it can be estimated by fitting only the low-width portion of the histograms. The Gaussian fits are shown in Figure 4.8 as dashed lines. The number of events (dotted) can then be found by subtracting the Gaussian curve from the original histogram. The cutoff value (dash-dot) is then assumed to be the width where the number of events becomes larger than the number of non-events. The width cutoff values found from each distribution are given in Table 4.6.

It is more difficult to establish the cutoff values for the expected skewness of the distribution. Figure 4.9 shows histograms (solid) of the measured skewnesses for the C III profiles (a), the N IV profiles (b), the O VI profiles (c), and the Ne VIII profiles (d). Again, these distributions represent both non-event (low skewness) and event (high skewness) profiles. However, in these distributions, it is more difficult to assess where the boundary between event and non-event profiles lies because there is not a range of skewness where the non-event profiles are clearly dominant (such as they were at the low end of the width distributions). To estimate the distribution of non-event profiles, the deviation from the mean skewness, $(\lambda - \bar{\lambda})^3 - (\lambda - \bar{\lambda})^3$, was measured for each profile. Then, ninety-percent

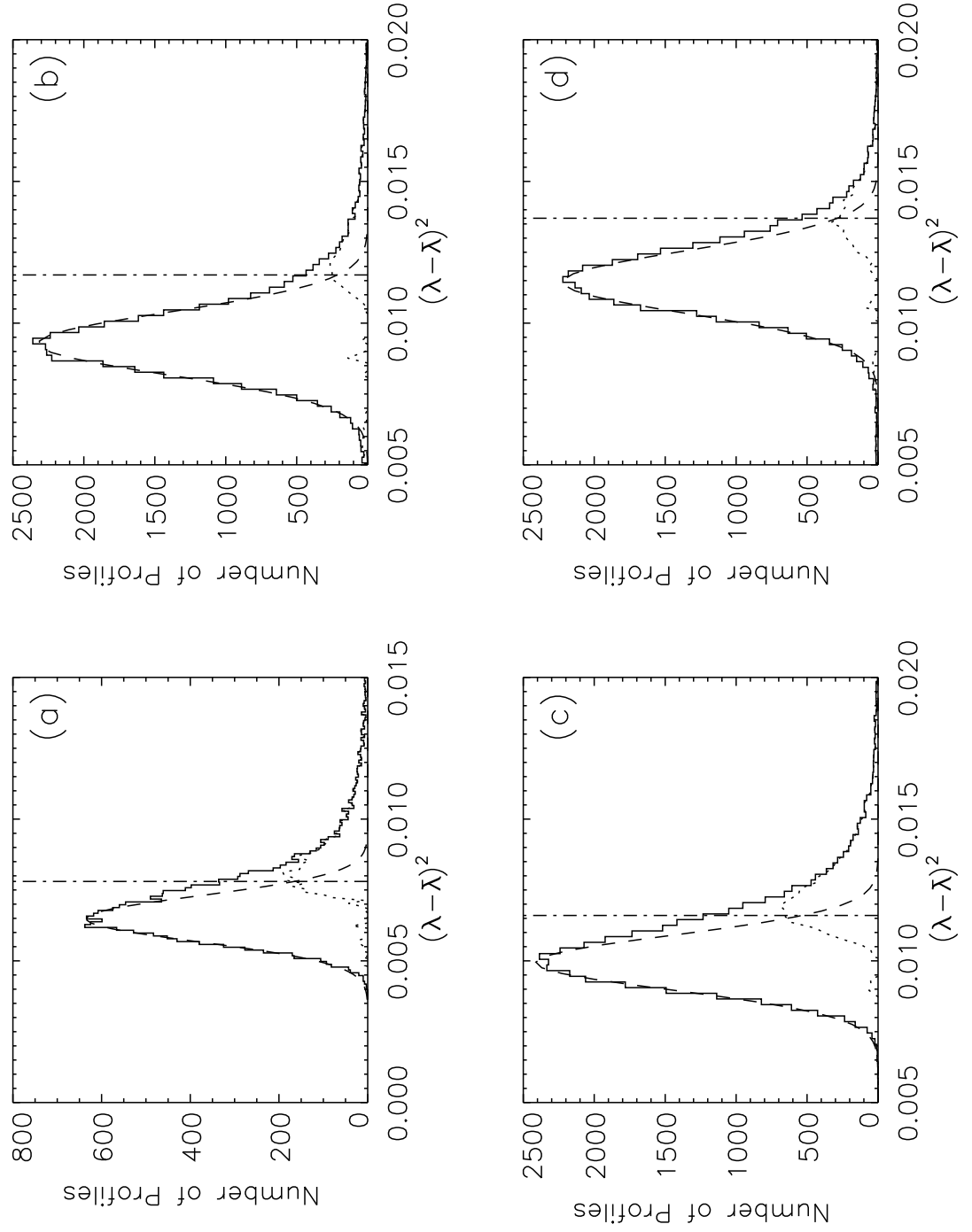


Figure 4.8: Histograms (solid) of width of the C III profiles (a), N IV profiles (b), O VI profiles (c), and Ne VIII profiles (d). The lower half of each histogram was fit with a Gaussian function (dashed) and the number of excess events (dotted) above this Gaussian was found. The cutoff value (dash-dot) for each line was then taken to be the width where the number of events was larger than the number of non-events.

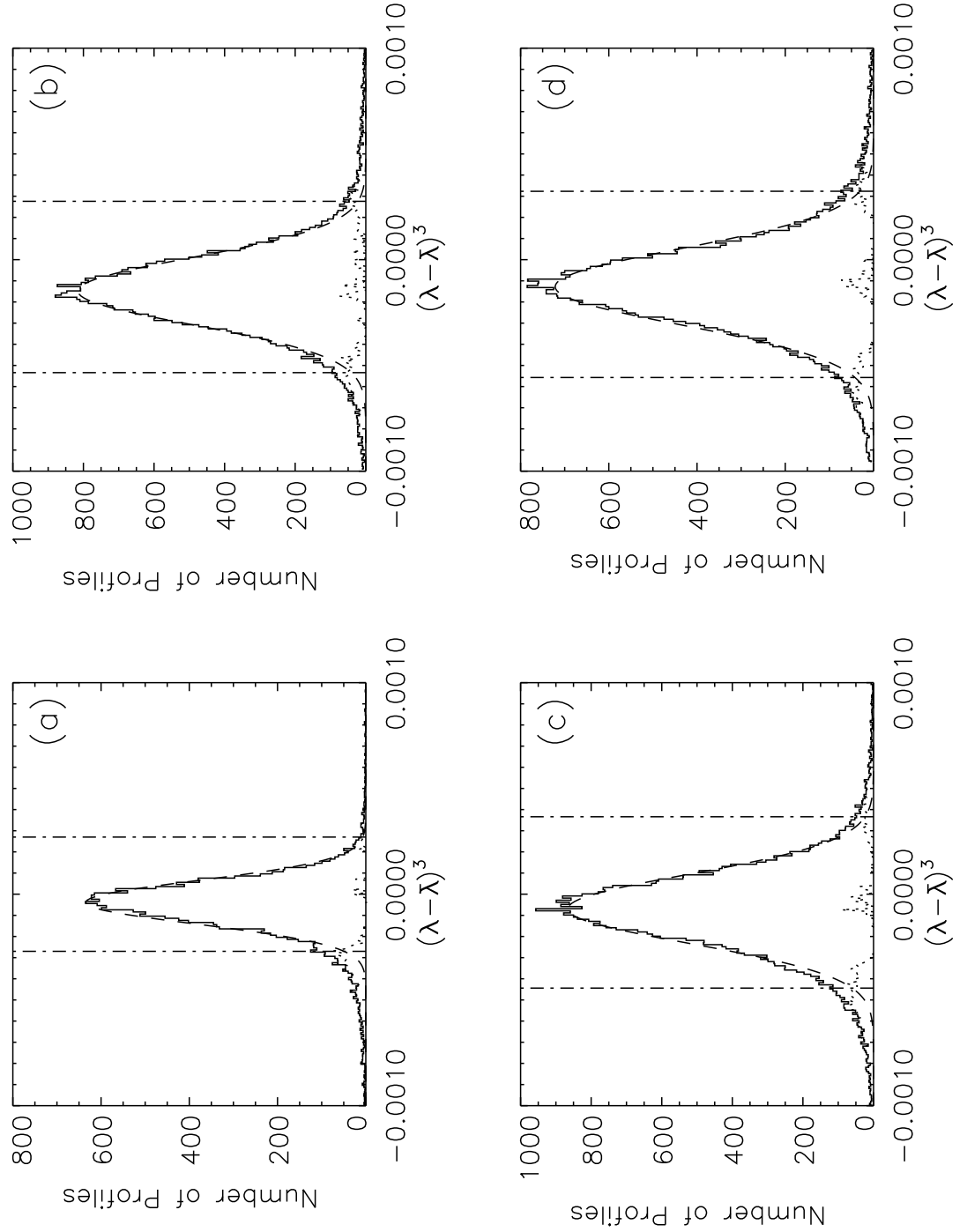


Figure 4.9: Histograms (solid) of the skewness for the C III profiles (a), the N IV profiles (b), the O VI profiles (c), and the Ne VIII profiles (d). Ninety percent of the profiles with the skewness closest to the mean value were fit to find the Gaussian function (dashed). This function is assumed to represent the distribution of non-event profiles, hence by subtracting this function from the original histogram, the number of event profiles (dotted) can be found. The skewness cutoff (dash-dot) was then taken to be the value where the number of events was larger than the number of non-events.

of the total number of profiles with the smallest deviations from the mean skewness were taken to be non-event profiles. These profiles represented the central portion of each histogram. A histogram of only these profiles were fit with a Gaussian function (dashed). The number of events (dotted) was then found from the difference in the distribution of skewnesses and the Gaussian curve. The cutoff value (dash-dot) is again assumed to be the skewness value where the number of events becomes larger than the number of non-events. Note that because the center of the distributions are offset to negative values, the cutoff values are different for profiles with negative or positive skewnesses. Both skewness cutoff values, denoted with $k_{\text{skew}+}$ for the positive cutoff and $k_{\text{skew}-}$ for negative cutoff, are given in Table 4.6.

If a profile exhibits *either* width *or* skewness larger than these cutoff values, the profile is selected as an event. By choosing the cutoff values as the width and skewness where the number of events dominates the number of non-events (as opposed to simply taking 3σ above the mean of the non-event distributions), some non-events will be selected and included in the event distribution. Similarly, some event profiles will not be identified and hence not included in the event distribution. Implications of this method of selecting event profiles on the results will be discussed in Chapter 6.

Figure 4.10 (a) shows the high cadence C III spectra originally shown in Figure 4.3 (a). From the 120 profiles present in this spectra, 36 met the event criteria; these are marked by the brackets on the right-hand side of the spectrum. An example of one such profile associated with spatial pixel 25 is shown in Figure 4.10 (b) along with a Gaussian function that would be considered a normal, non-event profile for C III. The width and skewness measured from this line profile are

$$\overline{(\lambda - \bar{\lambda})^2} = 0.012 = 1.5k_{\text{wid}}; \quad \overline{(\lambda - \bar{\lambda})^3} = -4.5 \times 10^{-4} = 1.7k_{\text{skew-}}, \quad (4.10)$$

where k_{wid} and $k_{\text{skew-}}$ are the cutoff values for C III [cf. Table 4.6]. Thus, this profile exhibits both excess broadening and skewness. (This profile will be used as an example to illustrate the analysis technique in Section 5.1.)

There are two ways to proceed with the analysis after the event profiles have been selected. Much of the analysis depends on the average size of the event, i.e., the area and lifetime of each individual event. It becomes important, then, to consider how the profiles are grouped into events. The method utilized for the HRTS data involves grouping event profiles together as a single event if they occurred in adjacent spatial pixels in a single spectrum, or occurred in the same spatial pixel in consecutive spectra. The area of the event would be the (average length along the slit)², the event's lifetime would be the number of consecutive spectra multiplied by the exposure time of the spectra. If this grouping method were implemented, all the profiles from, for instance, spatial pixel 17 to 30 in Figure 4.10 would be considered a single event representative of the area $14'' \times 14''$.

The HRTS observations show, however, that different events tend to occur in the same area of the disk over time, and that individual events may not be resolved spatially along the slit. Because the resolution of the spectra used in this study is of comparable or worse resolution than that of the HRTS spectra, this dissertation will assume that each individual pixel exhibiting event characteristics is a single event with area equal to the (width of the pixel)² and lifetime equal to the exposure time of the spectrum. This treatment implies that each profile is a “snapshot” of the dynamics occurring in the observed volume of plasma and is not physically connected to the surrounding volume elements. The effects of this assumption on the results will be discussed in Chapters 5 and 6.

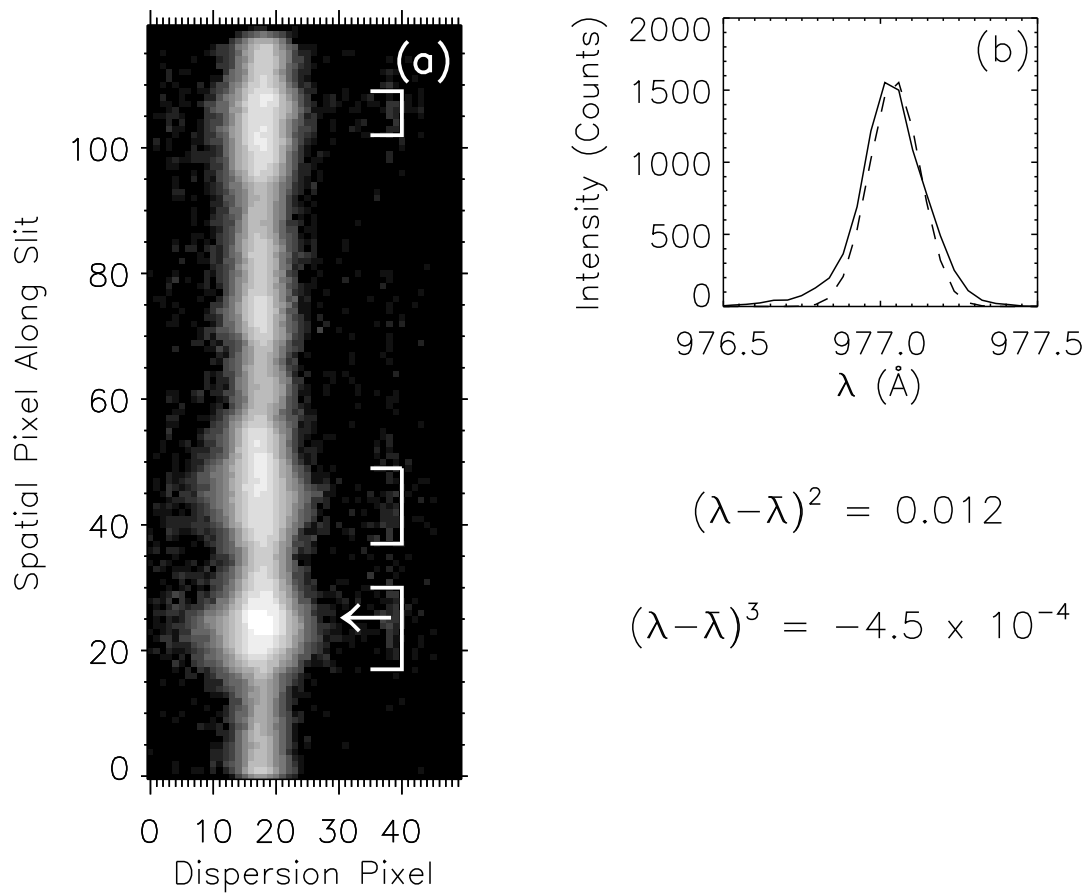


Figure 4.10: (a) Thirty-six profiles from this high-cadence C III spectra met the event criteria. An example of an event profile (solid) associated with spatial pixel 25 is shown in (b) along with a “normal” C III line profile (dashed). This profile exhibits both extreme broadening and skewness.

4.5 Analyzing Event Line Profiles Observed by SUMER

Each line profile that meets the event criteria must be calibrated to the units of flux (photons $\text{cm}^{-2} \text{s}^{-1} \text{\AA}^{-1}$) and background subtracted. Also, the spectral pixels defining the boundaries of the profile (the pixels on either side of the line profile that define where the emission from the spectral line is indistinguishable from the background emission) must be identified before it can be deconvolved to find its corresponding VDEM. This section will review the analysis technique specific to the SUMER data. An example of this analysis technique will be given in Section 5.1.

From the raw SUMER data, an event line profile is initially the number of counts received by the detector in a spectral bin. The counts in each bin are assumed to obey Poisson statistics, hence the uncertainty in the counts in a given bin is proportional to the square root of the number of counts in that bin. The SUMER radiometry program provides the conversion factor to change the count rate (counts s^{-1}) to specific intensity (photons $\text{cm}^{-2} \text{s}^{-1} \text{\AA}^{-1} \text{sr}^{-1}$) for each data set. The flux, $I(\lambda)$ (photons $\text{cm}^{-2} \text{s}^{-1} \text{\AA}^{-1}$), is then found by multiplying the specific intensity by the area of the pixel under observation and dividing by the sun-satellite distance squared. The uncertainty in the flux is then found by simply propagating the uncertainty in the counts.

The background of each profile is found by fitting the counts in the bins on either side of the spectral line with a linear function. To find the background, then, it is first necessary to define the boundary pixels of the spectral line. In cases where the background is much less than the peak emission for the spectral line, the boundary pixels can be defined as where the flux drops to 1% of the peak flux. If the line profile was well-represented by a Gaussian function, this reduction in flux would signify a 3σ width. If the peak line intensity is not 100 times that of the background, the background must be defined first by spectral pixels that are significantly far away from the line centroid. After the background is calculated, the boundary pixels of the line can be defined by the first spectral pixels with average background flux bordering either side of the line centroid. Empirically, it was established that subtracting only seventy percent of the calculated background would prevent the counts in any bin from being negative.

A line profile observed by SUMER is broadened not only by the motions in the plasma, but also by the SUMER instrument. Before a VDEM deconvolved from a line profile can represent the bulk velocity distribution, the excess width of the line due to instrumental broadening must be removed. The observed line profile, $I_{\text{obs}}(\lambda)$, is the convolution of the emitted intensity, $I_{\text{emitted}}(\lambda)$, with a function that describes the instrumental broadening, f_{instr} , i.e.,

$$I_{\text{obs}}(\lambda) = \int I_{\text{emitted}}(\lambda') f_{\text{instr}}(\lambda - \lambda') d\lambda'. \quad (4.11)$$

The instrumental function of the SUMER detectors is a Gaussian function with a width, σ_{instr} , related to the FWHM of the detectors (2 pixels or $\sim 90 \text{ m\AA}$ for Detector A and 3 pixels or $\sim 135 \text{ m\AA}$ for Detector B). The emitted intensity in Equation (4.11) can be written in terms of the VDEM function [cf. Equation (3.18)], i.e.,

$$I_{\text{obs}}(\lambda) = \int \left[\int VDEM(v_{\text{los}}) K(v_{\text{los}}, \lambda') dv_{\text{los}} \right] f_{\text{instr}}(\lambda - \lambda') d\lambda'. \quad (4.12)$$

By reversing the order of integration,

$$I_{\text{obs}}(\lambda) = \int VDEM(v_{\text{los}}) \left[\int K(v_{\text{los}}, \lambda') f_{\text{instr}}(\lambda - \lambda') d\lambda' \right] dv_{\text{los}}, \quad (4.13)$$

the quantity in the brackets can be evaluated:

$$K'(v_{\text{los}}, \lambda) = \int K(v_{\text{los}}, \lambda') f_{\text{instr}}(\lambda - \lambda') d\lambda'. \quad (4.14)$$

Convolving the existing kernel function (which is a thermally broadened Gaussian function) with the instrument function (an instrumentally broadened Gaussian function), results in a modified kernel function, K' , which is also a Gaussian function with a width of

$$\sigma_K = \sqrt{\sigma_{\text{th}}^2 + \sigma_{\text{instr}}^2}. \quad (4.15)$$

Thus, the effects of the instrumental broadening can be removed by deconvolving the observed intensity with a thermally and instrumentally broadened kernel function (For simplicity, the primes are dropped and this modified kernel function is assumed for the rest of the dissertation.)

CHAPTER 5

EXPLOSIVE EVENT CHARACTERISTICS

This chapter examines the characteristics of explosive events derived from our analysis. The first section will illustrate the analysis technique on a single explosive event line profile observed in the C III 977 Å line. In Section 5.2, the general characteristics of explosive events (such as birthrate and steady-state number) and the specific characteristics that are needed to calculate the energy flux (e.g., the filling factor) will be reviewed. Section 5.3 will address the average energy flux characteristics associated with these events. Finally, Section 5.4 will discuss these event characteristics and compare them to previous results.

5.1 The Analysis Technique: An Example

This section illustrates the analysis procedure introduced in Chapter 3 and discussed further in Chapter 4 by calculating the energy flux associated with a single event profile observed in the C III spectral line. This event is highlighted in Figure 4.10 (a) and shown again in Figure 5.1 (a). The calculations to be completed include not only the net energy flux, but also the energy flux toward and away from the observer, the components of each energy flux (kinetic energy flux, thermal and nonthermal enthalpy flux, and the “high-energy” component) and the specific energy release rate.

Recall that the net energy flux is found by

$$j_E = \frac{5}{2}\gamma nkT\overline{v_{\parallel}} + \frac{1}{2}\gamma\rho(\overline{v_{\perp}^2 v_{\parallel}} + \overline{v_{\parallel}^3}) \quad (5.1)$$

[cf. Equation (3.6)], and the energy fluxes toward and away from the observer are

$$j_{E\pm} = \frac{5}{2}\gamma nkT\overline{v_{\parallel\pm}} + \frac{1}{2}\gamma\rho(\overline{v_{\perp}^2 v_{\parallel\pm}} + \overline{v_{\parallel\pm}^3}) \quad (5.2)$$

[cf. Equation (3.11)]. The components of each energy flux are reviewed in Table 3.1. The terms that must be determined to evaluate these quantities are the temperature, T , density, n , mass density, ρ , and filling factor, γ , of the plasma, the width of the perpendicular velocity distribution, $\overline{v_{\perp}^2}$, and the first three moments of the parallel velocity distribution (normalized VDEM function).

The temperature of the explosive event plasma is assumed to be where the emissivity function is at a maximum. For the C III 977 Å line, this temperature is $10^{4.8}$ K. The electron density is then found through the constant pressure assumption, i.e., $n_e = \frac{10^{15} \text{ K cm}^{-3}}{10^{4.8} \text{ K}} = 10^{10.2} \text{ cm}^{-3}$. The density of hydrogen and helium, the two other main constituents in the atmospheric plasma, are found from the abundances relative to the electron density, i.e., $n_H = 0.83n_e = 10^{10.1} \text{ cm}^{-3}$ and $n_{He} = 0.083n_e = 10^{9.1} \text{ cm}^{-3}$. The total density is then $n = n_e + n_H + n_{He} = 10^{10.5} \text{ cm}^{-3}$. The mass density for the C III explosive event is $\rho = m_e n_e + m_H n_H + m_{He} n_{He} = 10^{-13.5} \text{ g cm}^{-3}$.

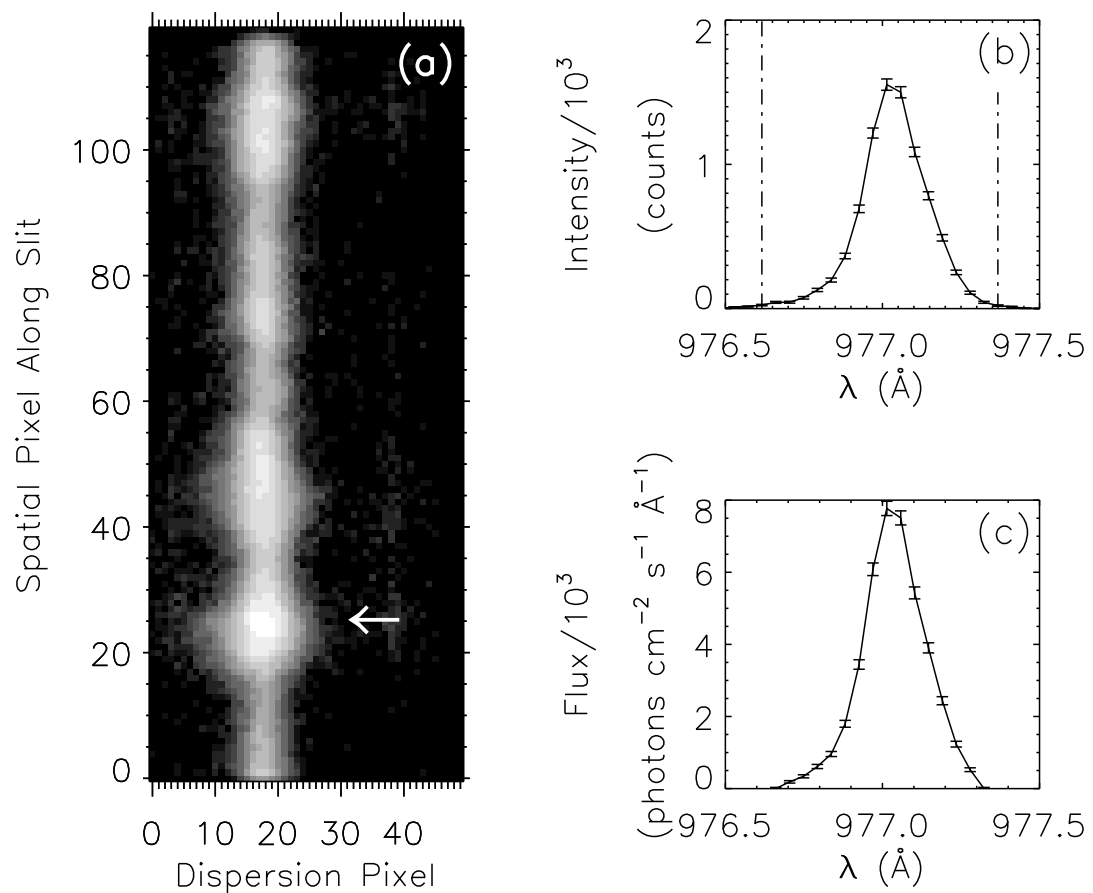


Figure 5.1: This figure illustrates the preparations that occur before a profile can be analyzed. Figure (a) shows a high-cadence C III spectrum taken 1996 May 10. The line profile associated with spatial pixel 25 is shown in (b) with the pixels that define the boundaries on either side of the centroid highlighted. This line profile is background subtracted and calibrated to units of flux (c).

The filling factor of the plasma is found from

$$\gamma = \frac{\frac{4\pi D^2}{n_e^2 0.7[G(T)]_{\max}} \int I(\lambda) d\lambda}{\Sigma H_0} \quad (5.3)$$

[cf. Equation (3.14)], where D is the distance between the Sun and observer ($\sim 1.5 \times 10^{13}$ cm for the SUMER instrument), Σ is the area under observation ($\sim 5.5 \times 10^{15}$ cm² for the C III pixels), H_0 is the scale height in the line profile region, and $[G(T)]_{\max}$ is the maximum value of the emissivity function. The maximum value of the emissivity function for C III is 1.4×10^{-22} ergs cm³ s⁻¹. The total flux, $\int I(\lambda) d\lambda$, for the event line profile is 3.8×10^{-8} ergs cm⁻² s⁻¹. (Note that this flux is given in ergs instead of photons, which is more commonly used in this dissertation. The flux must be given in ergs to match the units of the emissivity function.)

To find the filling factor, it is first necessary to find the scale height, H_0 , by evaluating Equation (1.10). For the C III temperature range, this equation must be integrated numerically. The minimum and maximum temperatures for this integral are taken to be $\frac{1}{\sqrt{2}}T$ and $\sqrt{2}T$, respectively, where T is the temperature where the emissivity function of the ion peaks. For the C III temperature ($10^{4.8}$ K), the scale height must be integrated from $10^{4.6}$ K to $10^{5.0}$ K. The scale height found for C III is 9.3×10^5 cm. Substituting the scale height into Equation (5.3), along with the Sun-satellite distance, pixel area, total flux, electron density and maximum emissivity function, the filling factor for the C III explosive event line profile is 86%. This filling factor is much larger than normally estimated for transition region plasmas (10%). The possible reasons for this inflation and the impact on the results will be discussed in Section 5.4.

Recall from Equation (3.17) that the width of the perpendicular velocity distribution is defined by the “normal” nonthermal r.m.s. velocity, ξ , i.e.,

$$\overline{v_{\perp}^2} = 2\xi^2. \quad (5.4)$$

The r.m.s. velocity is associated with the excess broadening in the typical non-event width, σ , of transition region spectral lines, i.e.,

$$\sigma = \frac{\lambda_0}{c} \sqrt{\frac{kT}{m} + \xi^2} \quad (5.5)$$

[restated from Equation (2.7)]. Therefore, to find the width of the perpendicular velocity distribution, the the typical width of non-event spectral lines must be first be determined. Its best approximation is the mean of the distribution of the measured widths, $(\lambda - \bar{\lambda})^2$, of non-event profiles [cf. Figure 4.8]. Because this measurement is taken directly from the initial intensity [cf. Equation (4.9)], it also reflects the excess width due to instrumental broadening. However, the instrumental effects are easily removed, i.e., $\sigma = \sqrt{(\lambda - \bar{\lambda})^2 - \sigma_{\text{instr}}^2}$ where σ_{instr} is the width of the Gaussian function and σ represents the average width of a typical non-event profile from Equation (5.5), which can now be solved for the nonthermal velocity, ξ . For the C III line, the mean of the Gaussian distribution of measured widths is $\sqrt{(\lambda - \bar{\lambda})^2} = 80.5$ mÅ. Because this C III event profile was observed with Detector A, the FWHM of the instrumental function is 2 pixels, or 88.4 mÅ. This corresponds to a Gaussian width of $\sigma_{\text{instr}} = 37.8$ mÅ. The average width of a non-event profile is then $\sigma = 71.1$ mÅ, which corresponds to a nonthermal velocity of $\xi = 21.1$ km s⁻¹. The width of the perpendicular velocity distribution is thus $\overline{v_{\perp}^2} = 2\xi^2 = 890$ (km s⁻¹)².

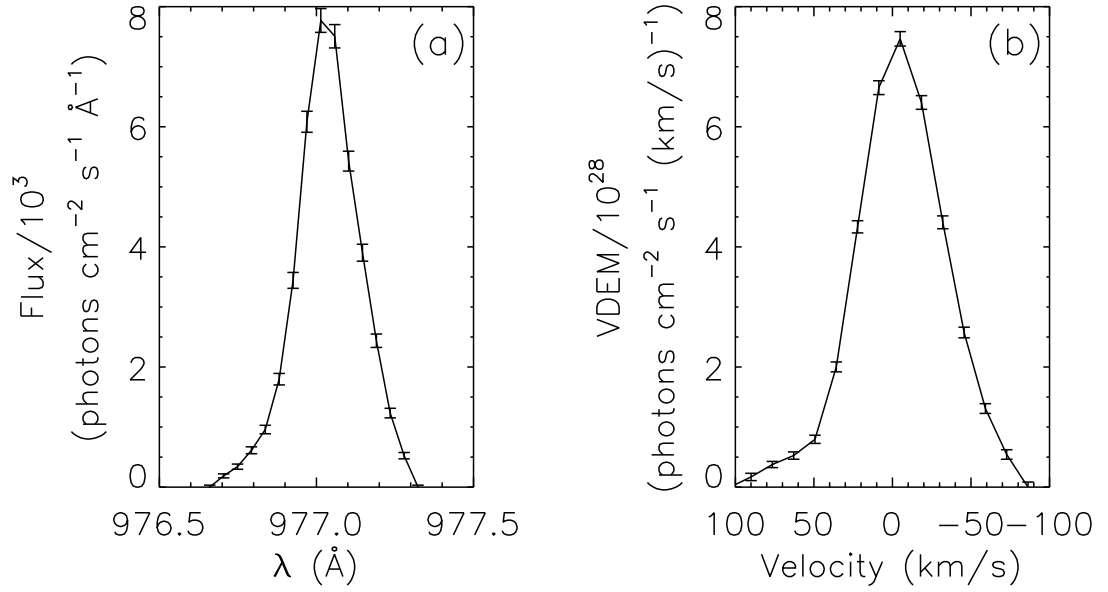


Figure 5.2: The flux found in Figure 5.1 is shown again in (a) and the VDEM found by deconvolving the flux with a thermally and instrumentally broadened kernel function is shown in (b).

Finally, the moments of the normalized VDEM function must be analyzed. Before the line profile can be deconvolved with the kernel function to retrieve the corresponding VDEM, it is background subtracted and the bins that define the line profile on either side of the centroid are identified. The line profile is also converted from the original units of counts to the units of flux ($\text{photons cm}^{-2} \text{s}^{-1} \text{\AA}^{-1}$). This is illustrated in Figure 5.1. The C III spectrum is shown in Figure 5.1 (a), while the event line profile associated with spatial pixel 25 is shown in Figure 5.1 (b). The vertical lines demonstrate the bins that define the boundary pixels on either side of the centroid of the line profile. The background in this area of the solar spectrum is very low and so is not observable in this figure. The resulting flux derived from the initial profile is shown in Figure 5.1 (c).

Once the profile is in units of flux, the associated VDEM function can be found by deconvolving the profile with a thermally and instrumentally broadened kernel function. For C III, the thermal width (21.5 m\AA) and the instrumental width (37.8 m\AA) correspond to a width of the kernel function of 43.5 m\AA . The resulting VDEM is shown in Figure 5.2.

From the normalized VDEM it is then possible to measure the moments of the parallel velocity distribution. The moments are given in Table 5.1. The uncertainties in the velocity moments are due to uncertainties in both the deconvolved VDEM function and its associated velocity array. They are found through

$$\epsilon_{v^k} = \sqrt{\sum_{i=0}^N \left(\frac{\partial v^k}{\partial \text{VDEM}_i} \right)^2 \epsilon_{\text{VDEM}_i}^2 + \left(\frac{\partial v^k}{\partial v} \right)^2 \epsilon_v^2}, \quad (5.6)$$

where ϵ_{VDEM_i} is the uncertainty in the VDEM function at a given bin i , ϵ_v is the uncertainty

Table 5.1: Velocity moments of the example C III event line profile.

Net moments:

$$\bar{v} = (-6 \pm 2) \times 10^5 \text{ (cm s}^{-1}\text{)}$$

$$\overline{v^2} = (9.1 \pm 0.8) \times 10^{12} \text{ (cm s}^{-1}\text{)}^2$$

$$\overline{v^3} = (-1.0 \pm 0.5) \times 10^{19} \text{ (cm s}^{-1}\text{)}^3$$

Moments Toward Observer:

$$\overline{v_+} = (9 \pm 1) \times 10^5 \text{ (cm s}^{-1}\text{)}$$

$$\overline{v_+^2} = (3.4 \pm .5) \times 10^{11} \text{ (cm s}^{-1}\text{)}^2$$

$$\overline{v_+^3} = (1.8 \pm 0.3) \times 10^{19} \text{ (cm s}^{-1}\text{)}^3$$

Moments Away From Observer:

$$\overline{v_-} = (-1.5 \pm 0.1) \times 10^6 \text{ (cm s}^{-1}\text{)}$$

$$\overline{v_-^2} = (5.7 \pm 0.6) \times 10^{12} \text{ (cm s}^{-1}\text{)}^2$$

$$\overline{v_-^3} = (-2.8 \pm 0.4) \times 10^{19} \text{ (cm s}^{-1}\text{)}^3$$

in the velocity array due to the uncertainty in the initial wavelength array. For the C III spectrum, the uncertainty in the wavelength array is 16 mÅ, or 5 km s⁻¹.

Finally, using the temperature, density, mass density, filling factor, width of the perpendicular velocity distribution, and moments of the parallel velocity, it is possible to evaluate the equations for net energy flux, energy flux toward the observer, and energy flux away from the observer as well as their components: kinetic energy flux, thermal and nonthermal enthalpy flux, and the “high-energy” component [cf. Table 3.1]. The resulting values for energy flux are given in Table 5.2. The uncertainty in the energy flux is assumed to be from the uncertainty in the parallel moments of the velocity distribution. All other quantities in the energy flux equation are taken to be exact.

The net energy flux and its components are the most uncertain of the energy flux measurements. The net energy flux is negative which implies that it is flowing away from the observer. However, not all the components have the same sign; the skewed energy flux is toward the observer, while the other components are away from the observer. Because the net energy flux and its components are directional quantities, it is difficult to discuss what percentage of the net energy flux is carried by a single component. In this example profile, the percentage magnitude of the kinetic term is negligible, $\frac{|j_{kin}|}{|j_E|} = 5 \times 10^{-4}$ or 0.05%.

Table 5.2: Energy flux measurements for the example event line profile observed in the C III 977 Å line.

Net Energy Flux

$$\dot{j}_{\text{E}} = (-6 \pm 2) \times 10^5 \text{ ergs cm}^{-2} \text{ s}^{-1}$$

$$\dot{j}_{\text{kin}} = (-3 \pm 3) \times 10^2 \text{ ergs cm}^{-2} \text{ s}^{-1}$$

$$\dot{j}_{\text{th}} = (-4 \pm 2) \times 10^5 \text{ ergs cm}^{-2} \text{ s}^{-1}$$

$$\dot{j}_{\text{nth}} = (-3 \pm 2) \times 10^5 \text{ ergs cm}^{-2} \text{ s}^{-1}$$

$$\dot{j}_{\text{skew}} = (7 \pm 8) \times 10^4 \text{ ergs cm}^{-2} \text{ s}^{-1}$$

Energy Flux Toward Observer

$$\dot{j}_{\text{E}+} = (1.0 \pm 0.1) \times 10^6 \text{ ergs cm}^{-2} \text{ s}^{-1}$$

$$\dot{j}_{\text{kin}+} = (1.2 \pm 0.4) \times 10^4 \text{ ergs cm}^{-2} \text{ s}^{-1}$$

$$\dot{j}_{\text{th}+} = (6 \pm 1) \times 10^5 \text{ ergs cm}^{-2} \text{ s}^{-1}$$

$$\dot{j}_{\text{nth}+} = (2 \pm 1) \times 10^5 \text{ ergs cm}^{-2} \text{ s}^{-1}$$

$$\dot{j}_{\text{skew}+} = (1.5 \pm 0.3) \times 10^5 \text{ ergs cm}^{-2} \text{ s}^{-1}$$

Energy Flux Away From Observer

$$\dot{j}_{\text{E}-} = (-1.6 \pm 0.2) \times 10^6 \text{ ergs cm}^{-2} \text{ s}^{-1}$$

$$\dot{j}_{\text{kin}-} = (-5 \pm 1) \times 10^4 \text{ ergs cm}^{-2} \text{ s}^{-1}$$

$$\dot{j}_{\text{th}-} = (-1.0 \pm 0.1) \times 10^6 \text{ ergs cm}^{-2} \text{ s}^{-1}$$

$$\dot{j}_{\text{nth}-} = (-4 \pm 1) \times 10^5 \text{ ergs cm}^{-2} \text{ s}^{-1}$$

$$\dot{j}_{\text{skew}-} = (-1.5 \pm 0.3) \times 10^5 \text{ ergs cm}^{-2} \text{ s}^{-1}$$

Specific Energy Release Rate

$$\dot{j}_{\text{specific}} = (2.6 \pm 0.2) \times 10^6 \text{ ergs cm}^{-2} \text{ s}^{-1}$$

However, when comparing the percentage magnitudes of the other three terms, $\frac{|j_{th}|}{|j_E|} = 0.67$ (67%), $\frac{|j_{nth}|}{|j_E|} = 0.50$ (50%), and $\frac{|j_{skew}|}{|j_E|} = 0.12$ (12%), the sum of the percentages is more than 100%. Therefore, it is not meaningful to assess what percentage of the net energy flux is carried by a single component although it is meaningful to compare the magnitudes of each component to assess which is the dominant component for the net energy flux.

The same is not true for the directional energy fluxes (j_{E+} and j_{E-}) and their constituents. Each component of the positive flux is pointing toward the observer, while each component of the negative flux is pointing away from the observer. It is then very meaningful to discuss what percentage of the directional energy flux is carried by a single component. For this example, the kinetic energy flux is 1% of the positive energy flux, the thermal enthalpy flux constitutes 62%, while the nonthermal enthalpy and “high-energy” component constitute 21% and 16%, respectively. The breakdown of the energy flux away from the observer is 3% kinetic, 63% thermal, 25% nonthermal, and 9% high-energy. The specific energy release rate of this event is 2.6×10^6 ergs cm⁻² s⁻¹.

5.2 Explosive Event Characteristics

The calculations illustrated in the previous section must be carried out for every line profile selected as an event. Applying the selection technique introduced in Chapter 4 to the profiles of the four spectral lines identify all profiles that have extreme width or skewness. The resulting numbers of event profiles selected from each data set are given in Table 5.3. Approximately 12% of all profiles were selected as events. Of these selected profiles, many ($\sim 24\%$) exhibit both statistically significant width and skewness. Of the profiles exhibiting significant skewness, an average of 71% have dominant blue wings, i.e., $(\lambda - \bar{\lambda})^3 < 0$. This dominance is very evident in the C III and O VI profiles, while the N IV and Ne VIII data have an equal number of events with dominant blue and red wings. Possible reasons for this observation will be discussed in Section 5.4.

After selecting the event profiles, the global birthrate, R (events s⁻¹), can be found from

$$R = \frac{N_0 A_{\text{sun}}}{\tau A_{\text{slit}}} \quad (5.7)$$

[restated from Equation (2.8)], where N_0 is the number of event profiles from Table 5.3, A_{sun} is the solar surface area, τ is the total observation time of the data, and A_{slit} is the projected area of the slit onto the solar surface. The steady-state number of events that are occurring globally, N_{global} , can then be calculated by multiplying the global birthrate by the average lifetime of the event, \bar{t}_E , or $N_{\text{global}} = R \bar{t}_E$. (The average lifetime is taken to be the exposure time of the spectra.) The results for each line are given in Table 5.4. The global birthrate is between 10^3 and 10^4 events s⁻¹, while the steady-state number is 10^5 - 10^6 events. These numbers are one to two orders of magnitude larger than the birthrate and steady-state numbers predicted by the HRTS data.

The peak temperature of each ion’s emissivity function is given in Table 5.5, along with the density and mass density for each line observed. The scale height of the atmosphere was evaluated from the conductive flux model given in Chapter 1. It was evaluated analytically for the O VI and Ne VIII lines and numerically for the C III and N IV lines. The scale height increased dramatically from 9 km for the C III plasma to 14,000 km for the Ne VIII plasma. These values, along with the area of the pixels, were used to evaluate the filling factor in each profile. The average filling factor for the event profiles in each line, as well as

Table 5.3: The number of profiles and fraction of profiles that were selected as events, as well as general characteristics of the selected profiles.

	C III	N IV	O VI	Ne VIII
Number of Event Profiles	3,403	2,505	5,531	2,907
Percentage of Total Profiles	20%	6.4%	14%	7.5%
Percentage of Event Profiles:				
Exhibiting Enhanced Width	97%	79%	96%	70%
Exhibiting Enhanced Skewness	29%	45%	28%	51%
Exhibiting Both	26%	24%	25%	21%
Percentage of Skewed Event Profiles:				
With Dominant Blue-Wing Asymmetry	96%	57%	81%	51%
With Dominant Red-Wing Asymmetry	4%	43%	19%	49%

the scale height and area, are also given in Table 5.5. The filling factor varies significantly in each line observed, with an average of 23%.

The width of the perpendicular bulk velocity distribution is derived from the average nonthermal velocity of the non-event profiles. The nonthermal velocity is measured from the typical width of a non-event spectral line. The results are given for each ion in Table 5.6. The width of the perpendicular velocity distribution can then be found, i.e., $\overline{v_{\perp}^2} = 2\xi^2$. The values given here for typical nonthermal velocity are slightly greater than the values generally reported in the literature. The possible reasons and implications of these results will be discussed in Section 5.4.

5.3 Characteristics of the Energy Flux of Explosive Events

It is very difficult to make general statements about the energy flux associated with the explosive events analyzed in this study. The local conditions of each event plasma greatly influence the shape of the line profile and hence the VDEM function. Some profiles may exhibit extreme broadening with very little skewness while others may be highly skewed but with relatively little broadening. This diversity results in highly individual energy flux signatures for each event profile. Also, the data analyzed here includes four spectral lines formed at different temperatures and observed at different times. The degree to which these conditions influence the data is unknown. Therefore, the average energy flux characteristics presented here are truly an average over an ensemble of events and do not completely describe any one event. The uncertainties in the average energy flux are the standard error (standard deviation divided by the square root of the number of events).

5.3.1 Net Energy Flux

The average values for the net energy flux and its components are given in Table 5.7. The average magnitude of the net energy flux is 1.3×10^5 ergs cm⁻² s⁻¹. The direction of the average net energy flux is away from the observer in the C III, N IV, and Ne VIII lines, while it is toward the observer in the O VI line. The net energy flux is away from the observer in 89% of the C III event profiles, 89% of the N IV event profiles, 19% of the

Table 5.4: The global birthrate, lifetime, and steady-state number of the events observed in the four spectral lines.

	C III	N IV	O VI	Ne VIII
Global Birthrate (events s ⁻¹)	4.5×10^4	1.9×10^3	4.3×10^4	2.2×10^3
Lifetime (s)	48	120	36	120
Steady State Number	2.2×10^6	2.2×10^5	1.5×10^6	2.6×10^5

Table 5.5: The temperature, density, mass density, area, scale height, and average filling factor for events observed in each spectral line.

	C III	N IV	O VI	Ne VIII
Temperature (K)	$10^{4.8}$	$10^{5.15}$	$10^{5.45}$	$10^{5.9}$
Density (cm^{-3}) $n = n_e + n_H + n_{\text{He}}$	$10^{10.48}$	$10^{10.13}$	$10^{9.83}$	$10^{9.38}$
Mass Density (g cm^{-3}) $\rho = m_e n_e + m_H n_H + m_{\text{He}} n_{\text{He}}$	$10^{-13.51}$	$10^{-13.86}$	$10^{-14.16}$	$10^{-14.61}$
Area (cm^2)	5.5×10^{15}	5.0×10^{16}	5.5×10^{15}	5.0×10^{16}
Scale Height (cm)	9.3×10^5	9.6×10^5	4.1×10^7	1.4×10^9
Average Filling factor	30%	8.6%	52%	1.2%

Table 5.6: Values of the mean width of the non-event profiles, ($\sqrt{(\lambda - \bar{\lambda})^2}$), the instrumental width (σ_{instr}), the “normal” nonthermal width (σ), and the nonthermal velocity (ξ).

	C III	N IV	O VI	Ne VIII
$\sqrt{(\lambda - \bar{\lambda})^2} (\text{m}\text{\AA})$	80.5	96.3	99.7	107.0
$\sigma_{\text{instr}} (\text{m}\text{\AA})$	37.8	57.0	37.6	57.0
$\sigma (\text{m}\text{\AA})$	71.1	77.6	82.9	77.8
$\xi (\text{km s}^{-1})$	21.1	29.0	24.1	30.3

O VI event profiles, and 56% of the Ne VIII event profiles. The profound differences in the direction of the net energy flux may be attributed to the different observation times, and hence different plasma conditions. The net energy flux is also the most affected when plasma conditions are not in equilibrium and, hence, the most unreliable [cf. Section 3.4].

The average magnitude of the kinetic component is $2.2 \times 10^3 \text{ ergs cm}^{-2} \text{ s}^{-1}$. In general, the kinetic energy flux is insignificant when compared to the net energy flux, but this is not necessarily true for each event profile. In fact, the maximum percentage magnitude for the kinetic energy flux, $\frac{|j_{\text{kin}}|}{|j_{\text{E}}|}$, is 20%.

The average magnitude of the thermal enthalpy flux is $9.6 \times 10^4 \text{ ergs cm}^{-2} \text{ s}^{-1}$. The thermal component is the best estimate for the net energy flux. It is the dominant component in 93% of the event profiles. The net thermal enthalpy is directed away from the observer in 65% of the profiles. In the C III and N IV lines, the percentage of profiles with a negative thermal enthalpy flux is quite high ($\sim 90\%$) while in the O VI profiles, the percentage is amazingly low (18%).

The average magnitude of the nonthermal enthalpy flux is $4.1 \times 10^4 \text{ ergs cm}^{-2} \text{ s}^{-1}$ and the average magnitude of the “high-energy” component of the energy flux (associated with the skewed tail of the distribution) is $8.9 \times 10^3 \text{ ergs cm}^{-2} \text{ s}^{-1}$. In general, the nonthermal enthalpy is the second most significant component, but it is the dominant component in less than 1% of the event profiles. The skewed energy flux, however, is dominant in 6% of the profiles. This component is toward the observer in 73% of all the profiles.

The magnitude of the average values given in Table 5.7 are shown graphically in Figure 5.3. The values are given as a function of the peak temperature of each ion’s emissivity function. This graph illustrates that the thermal enthalpy is the best estimate for the net energy flux, especially at higher temperatures, while the nonthermal enthalpy flux and the “high-energy” component are also significant.

Figure 5.4 shows histograms (solid) of the net energy flux for the events observed in the C III spectral line (a), the N IV spectral line (b), the O VI spectral line (c), and the Ne VIII spectral line (d). Histograms of the thermal enthalpy flux (dashed) for the events observed in each spectral line are also shown. The distributions are very similar, especially in the events observed in the (high temperature) O VI and Ne VIII lines. The differences in the two distributions are due to the influence of the other terms in the energy flux equation.

A scatter plot of the net energy flux of an event as a function of the total intensity of the event profile, $\int I(\lambda) d\lambda$, is shown Figure 5.5. (Note that the scales of the four plots are all different.) These plots demonstrate that profiles with low intensities have relatively narrow range of net energy fluxes, while profiles with larger intensity have a larger range of net energy fluxes. These plots, however, are heavily influenced by the assumptions made in the filling factor measurement and will be discussed in section Section 5.4.

5.3.2 Energy Flux Towards the Observer

The average values for energy flux towards the observer and its constituents are given in Table 5.8. These average values are shown graphically in Figure 5.6. The average energy flux toward the observer over all event profiles is $2.3 \times 10^5 \text{ ergs cm}^{-2} \text{ s}^{-1}$. The average energy flux toward the observer and its constituents are shown as a function of peak temperature of each ion’s emissivity function. The energy flux towards the observer is very similar in the events observed in the C III, N IV and O VI lines, then drops significantly in the events observed in the Ne VIII line. At all temperatures, thermal energy flux is the most significant, followed by the nonthermal enthalpy and skewed energy flux. The significance

Table 5.7: The average values (\pm standard error) of the net energy flux and its components.

	C III ($10^{4.8}$ K)	N IV ($10^{5.15}$ K)	O VI ($10^{5.45}$ K)	Ne VIII ($10^{5.9}$ K)
\dot{j}_{E} (ergs cm $^{-2}$ s $^{-1}$)	(-2.11 ± 0.05) $\times 10^5$	(-1.10 ± 0.03) $\times 10^5$	(2.14 ± 0.05) $\times 10^5$	(6 ± 2) $\times 10^2$
\dot{j}_{kin} (ergs cm $^{-2}$ s $^{-1}$)	(-4.5 ± 0.2) $\times 10^3$	(-3.3 ± 0.1) $\times 10^3$	(1.0 ± 0.1) $\times 10^3$	(3 ± 1) $\times 10^0$
\dot{j}_{th} (ergs cm $^{-2}$ s $^{-1}$)	(-1.39 ± 0.02) $\times 10^5$	(-7.1 ± 0.2) $\times 10^4$	(1.74 ± 0.04) $\times 10^5$	(3 ± 1) $\times 10^2$
\dot{j}_{nth} (ergs cm $^{-2}$ s $^{-1}$)	(-8.8 ± 0.2) $\times 10^4$	(-4.5 ± 0.1) $\times 10^4$	(3.18 ± 0.09) $\times 10^4$	(7 ± 2) $\times 10^1$
\dot{j}_{skew} (ergs cm $^{-2}$ s $^{-1}$)	(1.9 ± 0.1) $\times 10^4$	(9.0 ± 0.4) $\times 10^3$	(7.2 ± 0.4) $\times 10^3$	(2.5 ± 0.1) $\times 10^2$

of each component is discussed below.

The average kinetic energy flux is $2.6 \times 10^3 \text{ ergs cm}^{-2} \text{ s}^{-1}$, an average contribution of $< 1 \%$ to the total energy flux over all profiles. The maximum contribution of the kinetic energy flux in a single event is 8%. The average thermal enthalpy flux is $1.7 \times 10^5 \text{ ergs cm}^{-2} \text{ s}^{-1}$. It is the dominant component of the energy flux toward the observer in all the event profiles. It represents an average of 78% of the total energy flux toward the observer. The average nonthermal enthalpy flux is $3.4 \times 10^4 \text{ ergs cm}^{-2} \text{ s}^{-1}$ and the average high energy component is $1.5 \times 10^4 \text{ ergs cm}^{-2} \text{ s}^{-1}$. They represent a average of 15% and 6% of the total energy flux in all event profiles, respectively. The average and maximum percentage magnitudes of each of these components for the events observed in each spectral line are given in Table 5.9. The thermal enthalpy becomes more significant at higher temperatures, while the kinetic energy flux, nonthermal enthalpy, and skewed energy flux lose significance.

Figure 5.7 shows histograms of the energy flux toward the observer (solid), as well as the thermal enthalpy flux (dashed), for the events observed in the C III spectral line (a), the N IV spectral line (b), the O VI spectral line (c), and the Ne VIII spectral line (d). The the distributions are very similar in the events observed in the (high temperature) ions (O VI and Ne VIII). Any differences in the distributions are the result of the other terms in the energy flux equation.

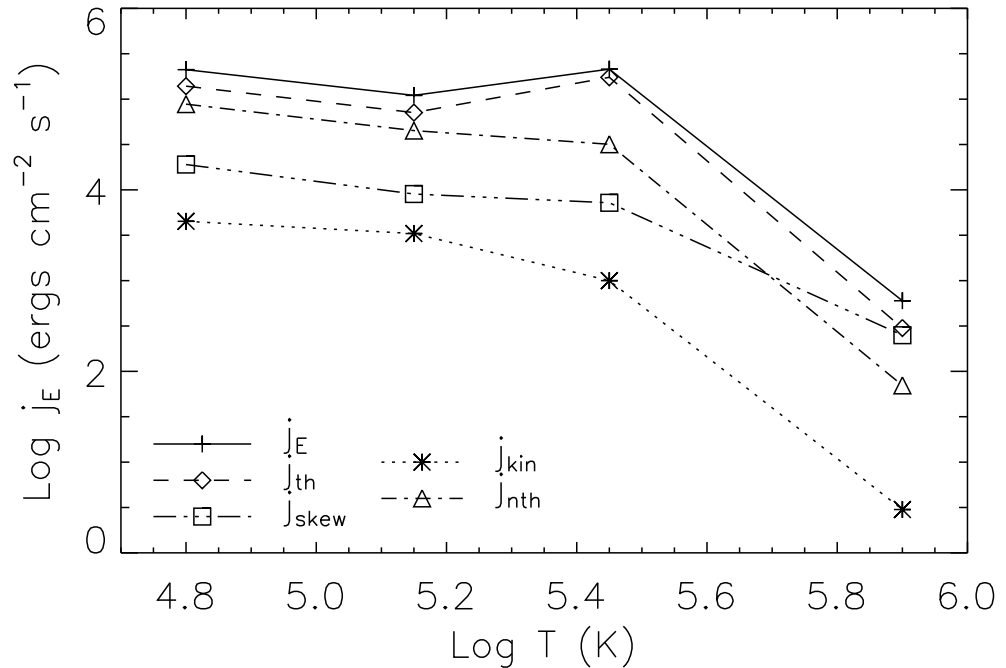


Figure 5.3: The magnitude of the net energy flux, along with its constituents, is shown above as a function of the peak temperature of the emitting ions' emissivity function. The uncertainty in these values are given in Table 5.7.

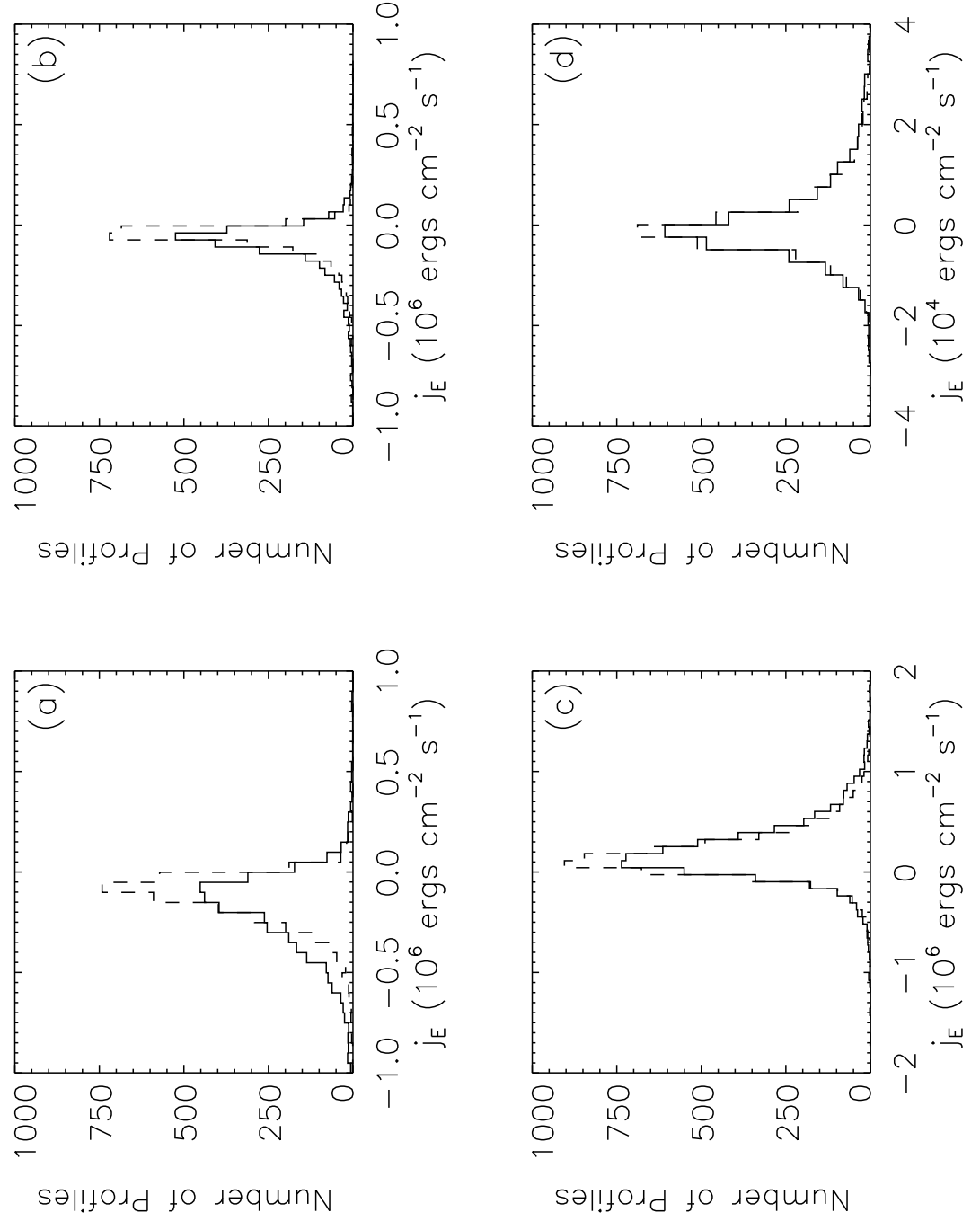


Figure 5.4: Histograms of the net energy flux (solid) and thermal enthalpy flux (dashed) for the events observed in the C III spectral line (a), the N IV spectral line (b), the O VI spectral line (c), and the Ne VIII spectral line (d).

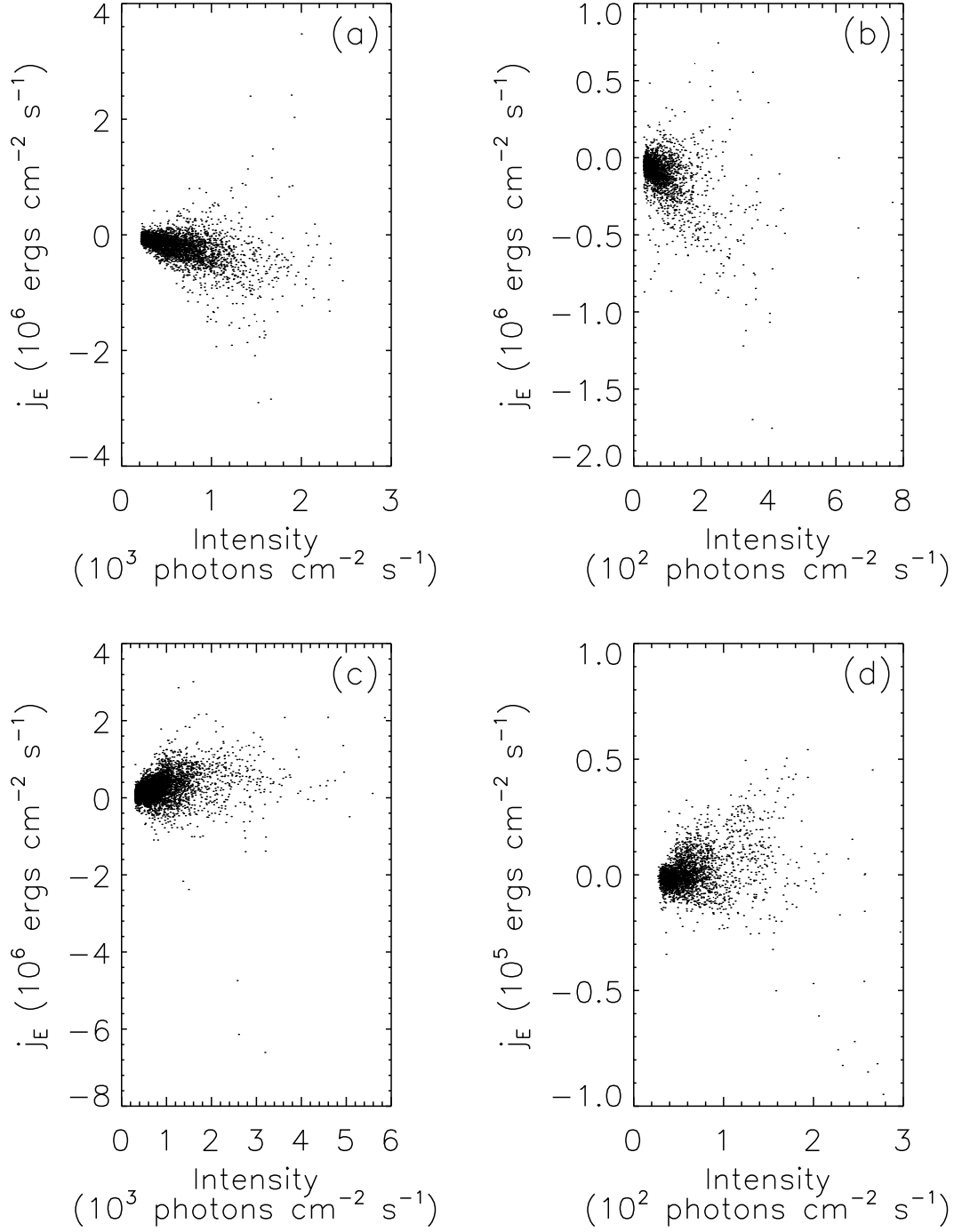


Figure 5.5: Scatter plots of the net energy flux associated with a line profile as a function of the total intensity of the profile for the events observed in the C III spectral line (a), the N IV spectral line (b), the O VI spectral line (c), and the Ne VIII spectral line (d).

Table 5.8: Average values for the energy flux towards the observer and its components.

	C III ($10^{4.8}$ K)	N IV ($10^{5.15}$ K)	O VI ($10^{5.45}$ K)	Ne VIII ($10^{5.9}$ K)
j_{E+} (ergs cm $^{-2}$ s $^{-1}$)	$(2.30 \pm 0.05) \times 10^5$	$(9.1 \pm 0.2) \times 10^4$	$(5.69 \pm 0.06) \times 10^5$	$(1.27 \pm 0.02) \times 10^4$
j_{kin+} (ergs cm $^{-2}$ s $^{-1}$)	$(3.0 \pm 0.2) \times 10^3$	$(1.15 \pm 0.06) \times 10^3$	$(6.0 \pm 0.1) \times 10^3$	$(6.3 \pm 0.2) \times 10^1$
j_{th+} (ergs cm $^{-2}$ s $^{-1}$)	$(1.42 \pm 0.02) \times 10^5$	$(5.9 \pm 0.1) \times 10^4$	$(4.85 \pm 0.05) \times 10^5$	$(1.15 \pm 0.02) \times 10^4$
j_{nth+} (ergs cm $^{-2}$ s $^{-1}$)	$(5.5 \pm 0.2) \times 10^4$	$(2.15 \pm 0.06) \times 10^4$	$(5.80 \pm 0.07) \times 10^4$	$(7.8 \pm 0.1) \times 10^2$
j_{skew+} (ergs cm $^{-2}$ s $^{-1}$)	$(2.9 \pm 0.1) \times 10^4$	$(9.8 \pm 0.3) \times 10^3$	$(1.92 \pm 0.04) \times 10^4$	$(3.7 \pm 0.1) \times 10^2$

Table 5.9: The average percentage magnitude and maximum percentage magnitude of the components of the energy flux toward the observer for the event profiles observed in each spectral line.

	C III ($10^{4.8}$ K)	N IV ($10^{5.15}$ K)	O VI ($10^{5.45}$ K)	Ne VIII ($10^{5.9}$ K)
$\frac{1}{N_0} \sum_i^{N_0} \frac{j_{\text{kin}+i}}{j_{\text{E}+i}}$	< 1%	< 1%	< 1%	< 1%
$\left(\frac{j_{\text{kin}+i}}{j_{\text{E}+i}} \right)_{\text{max}}$	8%	8%	5%	2%
$\frac{1}{N_0} \sum_i^{N_0} \frac{j_{\text{th}+i}}{j_{\text{E}+i}}$	67%	68%	86%	92%
$\left(\frac{j_{\text{th}+i}}{j_{\text{E}+i}} \right)_{\text{max}}$	79%	82%	92%	96%
$\frac{1}{N_0} \sum_i^{N_0} \frac{j_{\text{nth}+i}}{j_{\text{E}+i}}$	22%	22%	10%	6%
$\left(\frac{j_{\text{nth}+i}}{j_{\text{E}+i}} \right)_{\text{max}}$	41%	38%	25%	11%
$\frac{1}{N_0} \sum_i^{N_0} \frac{j_{\text{skew}+i}}{j_{\text{E}+i}}$	10%	9%	3%	3%
$\left(\frac{j_{\text{skew}+i}}{j_{\text{E}+i}} \right)_{\text{max}}$	40%	33%	24%	14%

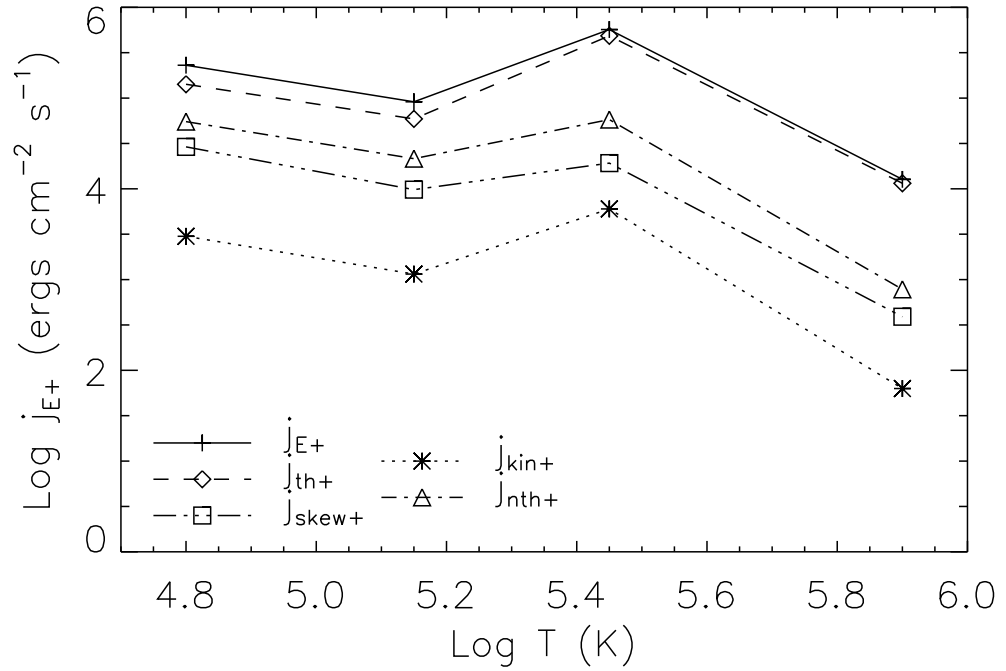


Figure 5.6: The average values of the energy flux toward the observer and its constituents are shown as a function of the peak temperature of each ion's emissivity function. The uncertainties at each point are given in Table 5.8.

Figure 5.8 shows scatter plots of the energy flux toward the observer as a function of total intensity for the events observed in the C III line (a), N IV line (b), O VI line (c), and Ne VIII line (d). (Note that the scale on each plot is different.) These plots show that there is a main distribution of the events exhibiting a positive correlation between energy flux and intensity. (This positive correlation is most likely due to the filling factor and will be discussed in Section 5.4.) There are also some high energy flux, high intensity events (for instance, in Figure 5.8 (a)) and some high intensity, but low energy flux events (for instance, Figure 5.8 (d)) that significantly deviate from the general distribution. There are also some high energy flux, low intensity events (for instance, in Figure 5.8 (b) and (d)), but because the uncertainty in energy flux is larger at lower intensities (and also because these events are observed in the poor spatial and temporal resolution N IV and Ne VIII data), it is questionable whether these events truly deviate from the general distribution.

5.3.3 Energy Flux Away from the Observer

The characteristics of the energy flows away from the observer are very similar to those of the energy flows toward the observer. The average values for the total energy flux away from the observer and its constituents are given in Table 5.10 and are shown graphically in Figure 5.9 as a function of the peak temperature of each ion's emissivity function. This figure illustrates that the thermal enthalpy is the most significant term in the energy flux

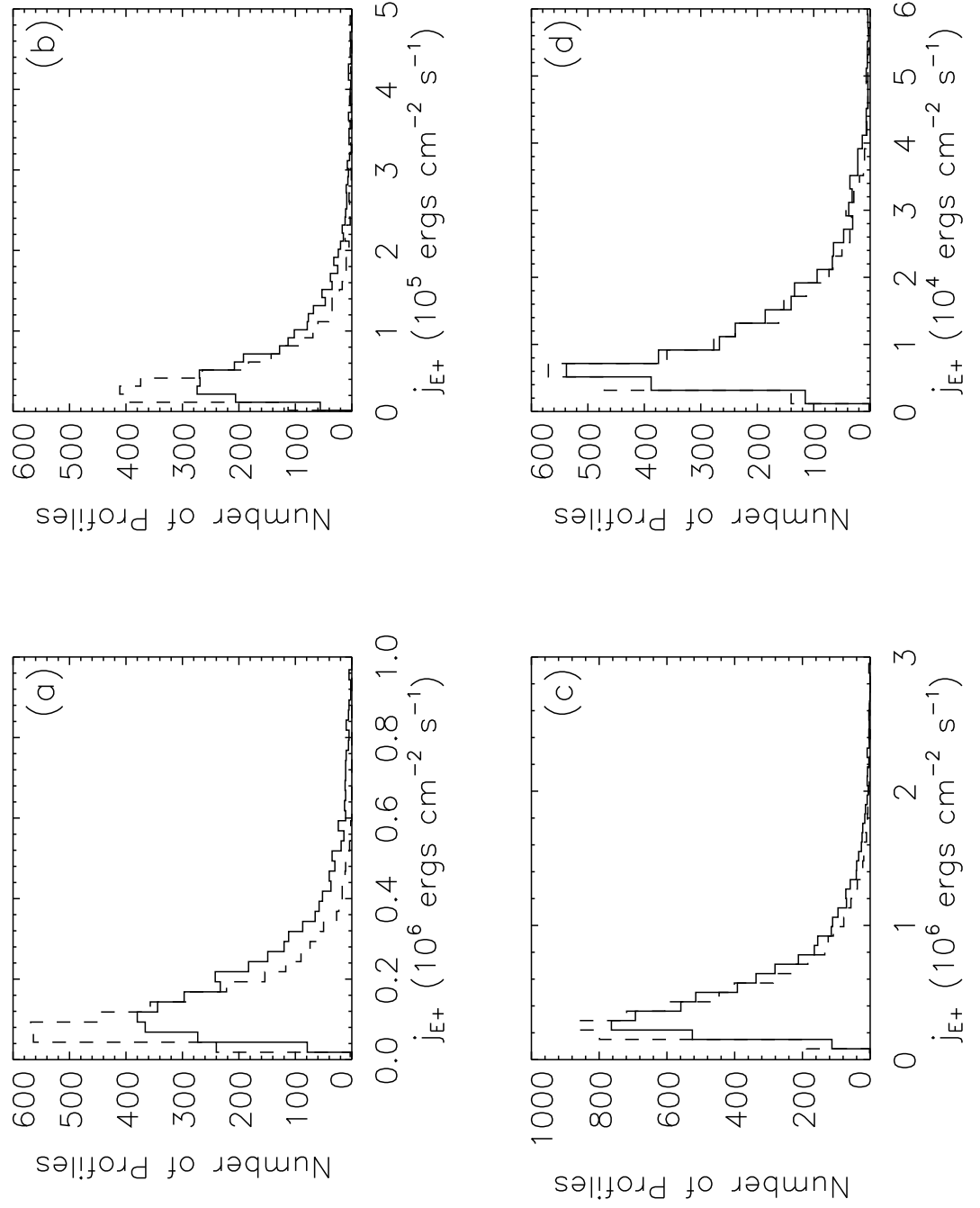


Figure 5.7: Histograms of the energy flux toward the observer (solid) and thermal enthalpy flux toward the observer (dashed) measured from the C III events (a) N IV events (b), O VI events (c), and Ne VIII events (d).

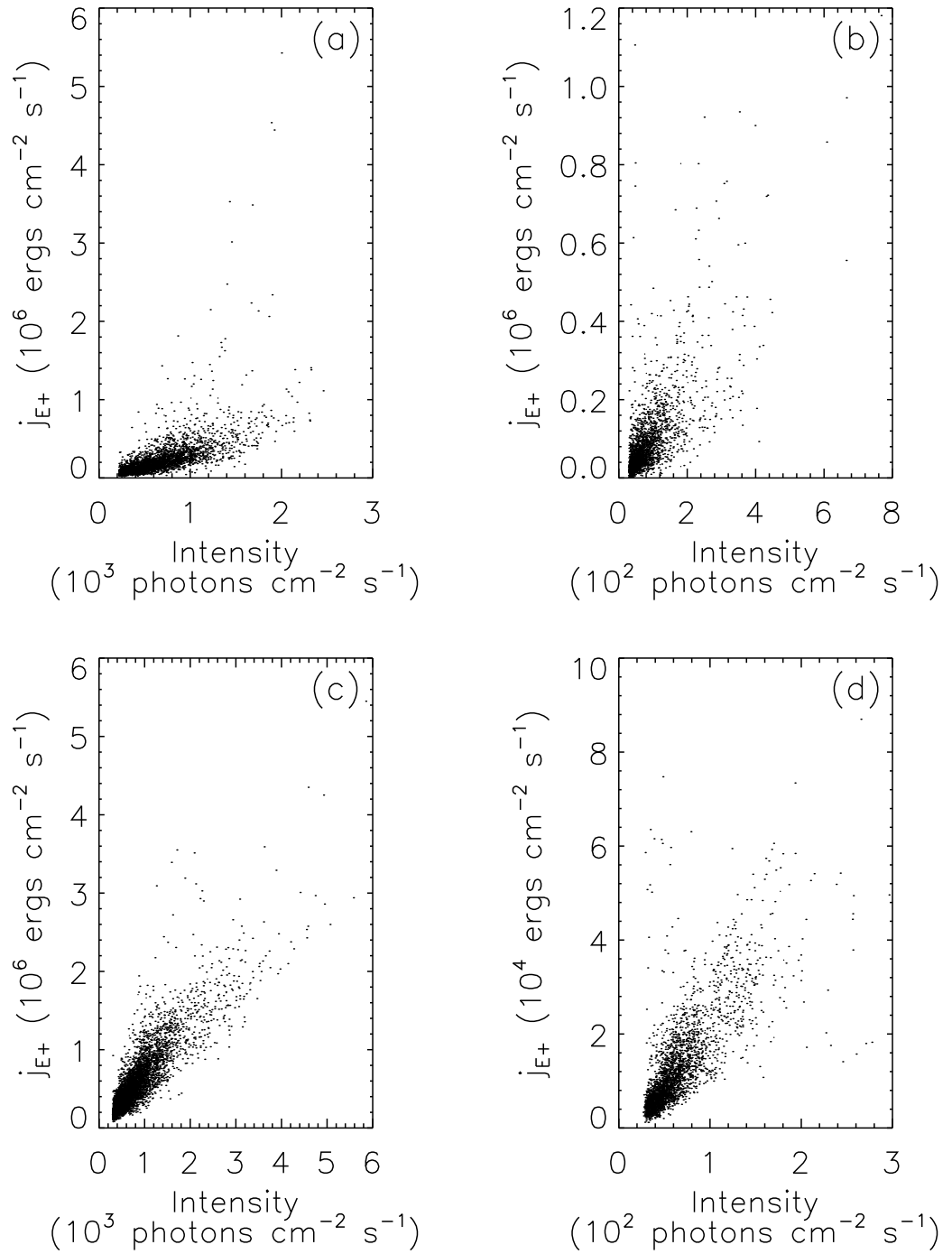


Figure 5.8: Scatter plots of the energy flux toward the observer as a function of total intensity for the events observed in the C III spectral line (a), N IV spectral line (b), O VI (c), and Ne VIII (d).

Table 5.10: The average values of the energy flux away from the observer and its components.

	C III ($10^{4.8}$ K)	N IV ($10^{5.15}$ K)	O VI ($10^{5.45}$ K)	Ne VIII ($10^{5.9}$ K)
\dot{j}_{E-} (ergs cm $^{-2}$ s $^{-1}$)	$(-4.41 \pm 0.05) \times 10^5$	$(-2.01 \pm 0.04) \times 10^5$	$(-3.54 \pm 0.05) \times 10^5$	$(-1.21 \pm 0.02) \times 10^4$
\dot{j}_{kin-} (ergs cm $^{-2}$ s $^{-1}$)	$(-1.60 \pm 0.03) \times 10^4$	$(-8.6 \pm 0.2) \times 10^3$	$(-2.0 \pm 0.2) \times 10^3$	$(-5.4 \pm 0.2) \times 10^1$
\dot{j}_{th-} (ergs cm $^{-2}$ s $^{-1}$)	$(-2.81 \pm 0.03) \times 10^5$	$(-1.30 \pm 0.02) \times 10^5$	$(-3.11 \pm 0.04) \times 10^5$	$(-1.12 \pm 0.01) \times 10^4$
\dot{j}_{nth-} (ergs cm $^{-2}$ s $^{-1}$)	$(-1.18 \pm 0.02) \times 10^5$	$(-5.4 \pm 0.1) \times 10^4$	$(-3.07 \pm 0.06) \times 10^4$	$(-6.5 \pm 0.1) \times 10^2$
\dot{j}_{skew-} (ergs cm $^{-2}$ s $^{-1}$)	$(-2.50 \pm 0.05) \times 10^4$	$(-8.2 \pm 0.2) \times 10^3$	$(-1.04 \pm 0.03) \times 10^4$	$(-1.80 \pm 0.05) \times 10^2$

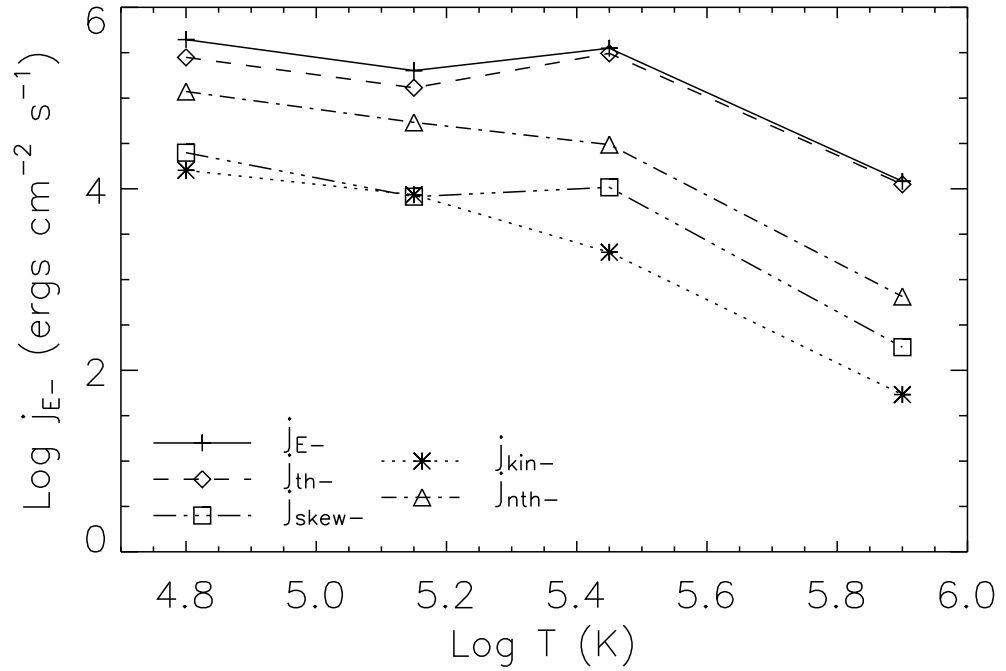


Figure 5.9: The energy flux away from the observer is shown as a function of the peak temperature of each ion's emissivity function. The uncertainties of these points are given in Table 5.10.

away from the observer, while the nonthermal enthalpy is the second most significant. The average energy flux away from the observer is 2.5×10^5 ergs cm⁻² s⁻¹. The magnitude of the energy flux away from the observer is of the same order of magnitude for the events observed in the C III line, N IV line, and O VI line, then drops an order of magnitude for the events observed in the Ne VIII line.

The average kinetic energy flux away from the observer is 6.7×10^3 ergs cm⁻² s⁻¹, $\sim 3\%$ of the total energy flux away from the observer. The maximum percentage of the total flux away from the observer carried by the kinetic flux is 13%. The average value of the thermal enthalpy flux is 1.8×10^5 ergs cm⁻² s⁻¹. Again, it is the best estimate for the total energy flux away from the observer. It is the largest component of the energy flux away from the observer in every event profile. In general, it represents $\sim 79\%$ of the total energy flux away from the observer.

The average value of the nonthermal enthalpy flux is 5.1×10^4 ergs cm⁻² s⁻¹ and the average value of the skewed energy flux is 1.1×10^4 ergs cm⁻² s⁻¹. The nonthermal enthalpy flux is more significant at lower temperatures, it represents 26% of the total energy flux away from the observer in C III profiles, but falls to 5% for Ne VIII profiles. The skewed energy flux follows the same pattern. It constitutes 5% of the energy flux away from the observer in the C III events, but only 1% of the Ne VIII events. Although, in general, it is less significant than the kinetic energy flux, in some events it can be more significant. The maximum percentage of the energy flux away from the observer constituted by the skewed

energy flux is 27%. The average and maximum percentage magnitudes of the components in each spectral line are given in Table 5.11.

Histograms of the energy flux away from the observer (solid), as well as the thermal enthalpy flux (dashed) are shown in Figure 5.10 for the events observed in the C III spectral line (a), the N IV spectral line (b), the O VI spectral line (c), and the Ne VIII spectral line (d). The two distributions are more similar in the events observed in the O VI and Ne VIII lines, yet remain markedly different for the events observed in the C III and N IV lines. The differences indicate that other energy components are also significant in the lower temperature events.

Figure 5.11 shows scatter plots of the energy flux away the observer as a function of total intensity for the events observed in the C III spectral line (a), N IV spectral line (b), O VI spectral line (c), and Ne VIII spectral line (d). (Note that the scales on the energy flux are different for each plot.) The correlation between energy flux away from the observer and intensity is similar to the correlation between energy flux toward the observer and intensity [cf. Figure 5.8]. These figures show that there are some events with high energy flux that deviate from the general distribution. Figures 5.11 (b) and (d) also show some low intensity, high energy flux events, but because of the high uncertainties associated with these events, it is difficult to assess if they truly deviate from the general distribution.

5.3.4 Specific Energy Release Rate

The average values for the specific energy release rate, along with the energy flux toward and away from the observer, are given in Table 5.12 and shown graphically as a function of the peak temperature of each ion's emissivity function in Figure 5.12. The average specific energy release rate is 4.8×10^5 ergs $\text{cm}^{-2} \text{s}^{-1}$. The energy flux away from the observer is dominant in the C III, N IV, and Ne VIII profiles, while the energy flux toward the observer is dominant in the O VI profiles.

5.4 Discussion of Event Characteristics

This chapter has demonstrated the analysis technique applied in this study and detailed the event characteristics found. This section will review these characteristics, comparing them to previous event characteristics observed by the HRTS instrument and explaining possible sources of error. The global birthrate and steady-state number predicted from the events observed in the SUMER data are $2 \times 10^3 - 5 \times 10^4$ events s^{-1} and $2 \times 10^5 - 2 \times 10^6$ events, respectively, one to two orders of magnitude greater than the global birthrate and steady-state number predicted by the HRTS analysis, approximately 6×10^2 events s^{-1} and 4×10^4 events [cf. Table 2.1], respectively. The substantial differences in these two sets of numbers can be explained by the different analysis techniques applied to the two data sets. Restated from Equations (2.8) and (2.9), the birthrate and steady-state number can be found through

$$R = \frac{N_0 A_{\text{sun}}}{\tau A_{\text{slit}}}; \quad N_{\text{global}} = R \overline{t_E}, \quad (5.8)$$

where N_0 is the number of events observed and $\overline{t_E}$ is the average lifetime of the events. The HRTS analysis and the analysis presented here have employed different methods to determine these two quantities.

Table 5.11: The average and maximum percentage magnitudes of the components of the energy flux away from the observer for the event profiles observed in each spectral line.

	C III ($10^{4.8}$ K)	N IV ($10^{5.15}$ K)	O VI ($10^{5.45}$ K)	Ne VIII ($10^{5.9}$ K)
$\frac{1}{N_0} \sum_i^{N_0} \frac{j_{\text{kin}-i}}{j_{\text{E}-i}}$	3%	4%	< 1%	< 1%
$\left(\frac{j_{\text{kin}-i}}{j_{\text{E}-i}} \right)_{\text{max}}$	13%	13%	8%	2%
$\frac{1}{N_0} \sum_i^{N_0} \frac{j_{\text{th}-i}}{j_{\text{E}-i}}$	66%	66%	89%	93%
$\left(\frac{j_{\text{th}-i}}{j_{\text{E}-i}} \right)_{\text{max}}$	76%	75%	93%	96%
$\frac{1}{N_0} \sum_i^{N_0} \frac{j_{\text{nth}-i}}{j_{\text{E}-i}}$	26%	26%	8%	5%
$\left(\frac{j_{\text{nth}-i}}{j_{\text{E}-i}} \right)_{\text{max}}$	40%	36%	20%	11%
$\frac{1}{N_0} \sum_i^{N_0} \frac{j_{\text{skew}-i}}{j_{\text{E}-i}}$	5%	4%	3%	1%
$\left(\frac{j_{\text{skew}-i}}{j_{\text{E}-i}} \right)_{\text{max}}$	24%	27%	25%	13%

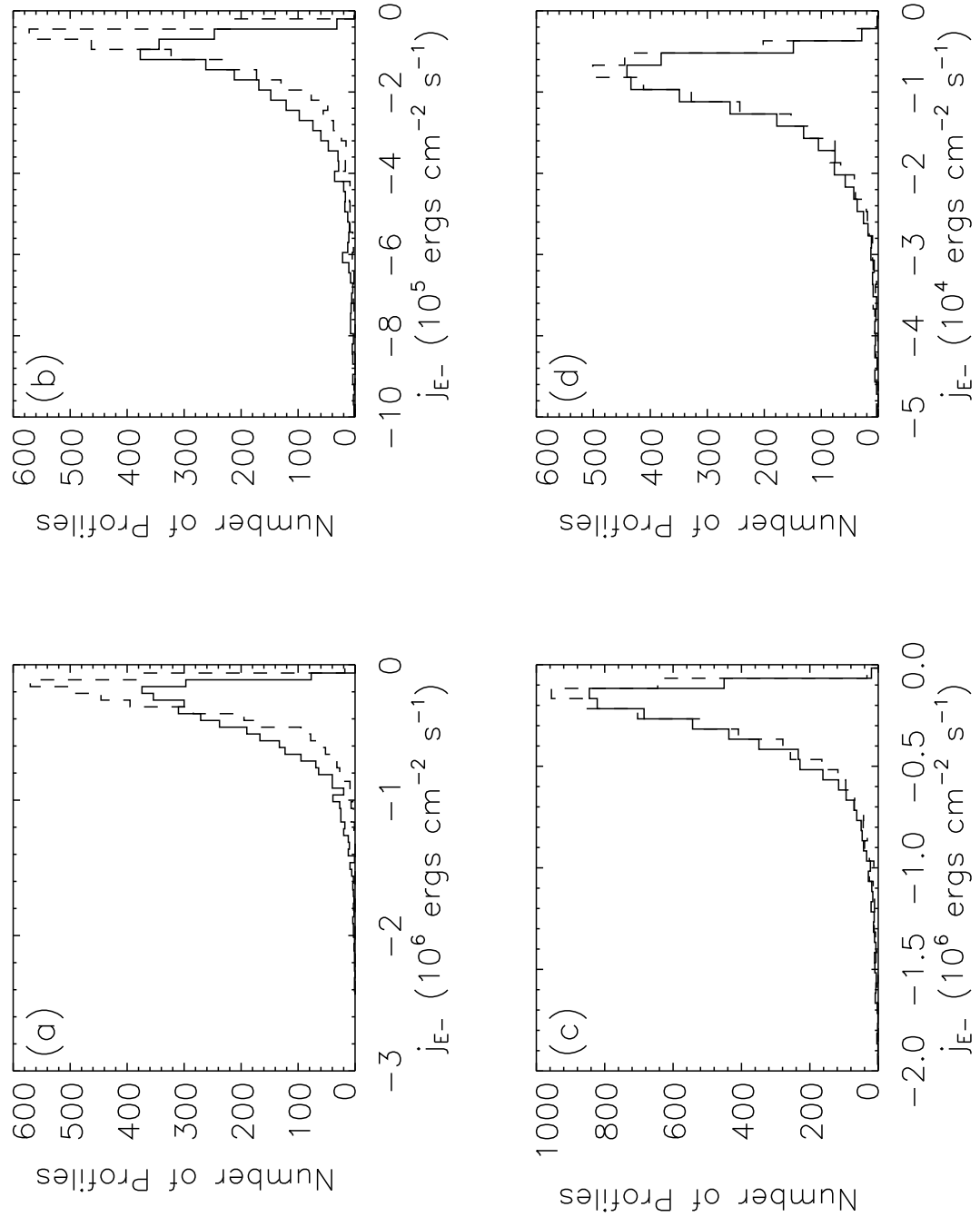


Figure 5.10: Histograms of the energy flux away from the observer (solid) and the thermal enthalpy flux away from the observer (dashed) for the events observed in the C III spectral line (a), N IV spectral line (b), O VI spectral line (c), and Ne VIII spectral line (d).

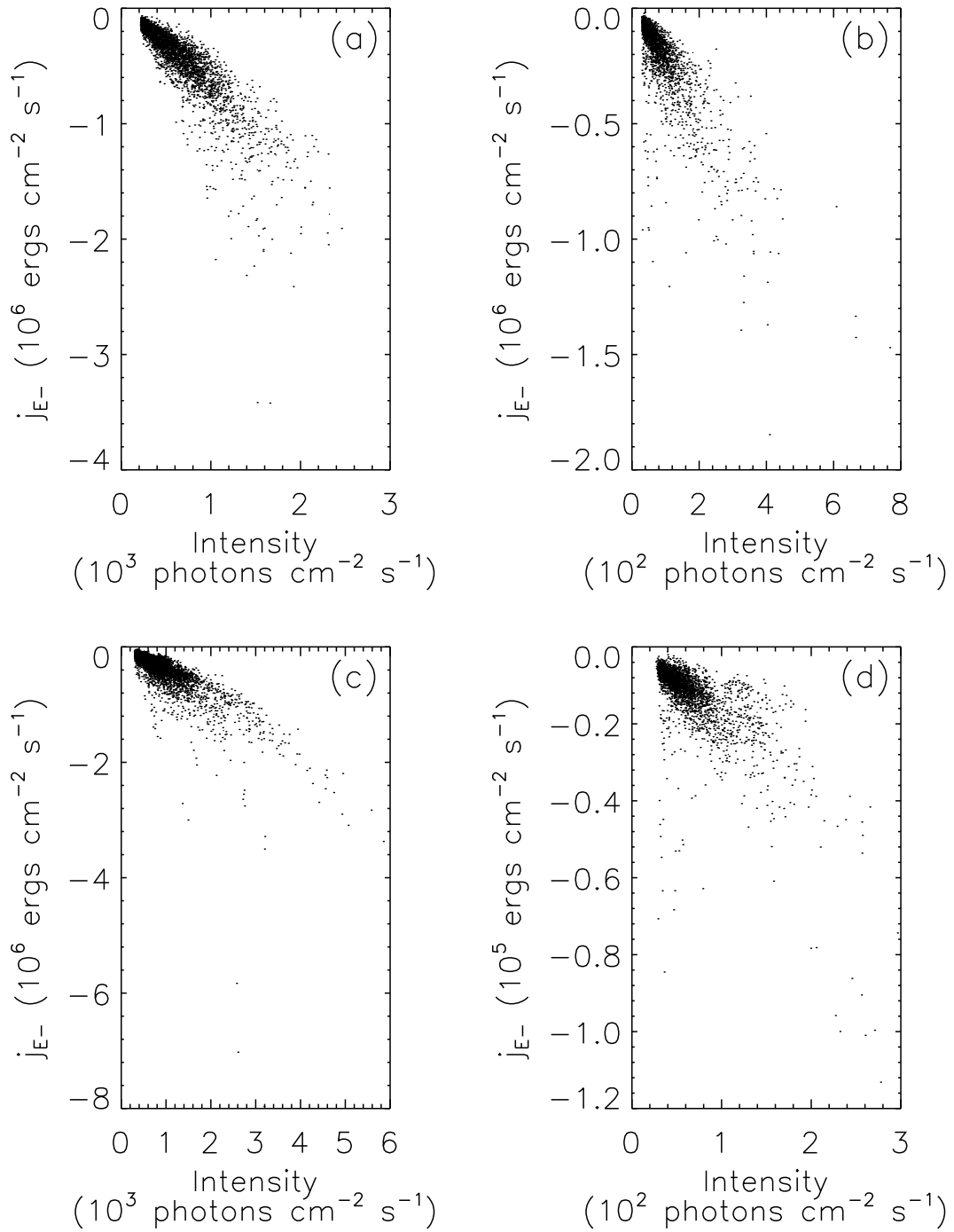


Figure 5.11: Scatter plots of the energy flux away from the observer as a function of the total intensity of the event line profiles observed in the C III line (a), N IV line (b), O VI line (c), and Ne VIII line (d).

The two main factors that affect the number of events observed, N_0 , are the event profile selection criteria and the methods implemented to group selected profiles into individual

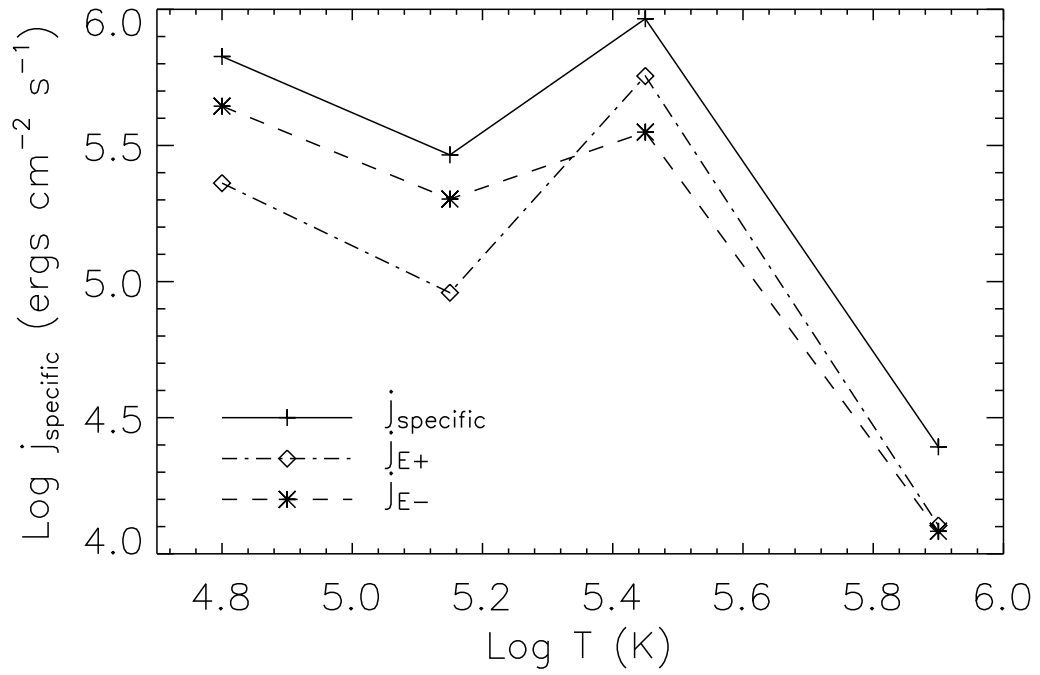


Figure 5.12: The specific energy release rate, as well as the magnitudes of the energy flux toward and away from the observer. The uncertainties in these values are given in Table 5.12.

Table 5.12: The average values for the specific energy release rate for the events observed in each spectral line.

	C III ($10^{4.8}$ K)	N IV ($10^{5.15}$ K)	O VI ($10^{5.45}$ K)	Ne VIII ($10^{5.9}$ K)
j_{specific} (ergs cm ⁻² s ⁻¹)	$(6.71 \pm 0.09) \times 10^5$	$(2.92 \pm 0.05) \times 10^5$	$(9.23 \pm 0.09) \times 10^5$	$(2.47 \pm 0.03) \times 10^4$
j_{E+} (ergs cm ⁻² s ⁻¹)	$(2.30 \pm 0.05) \times 10^5$	$(9.1 \pm 0.2) \times 10^4$	$(5.69 \pm 0.06) \times 10^5$	$(1.27 \pm 0.02) \times 10^4$
j_{E-} (ergs cm ⁻² s ⁻¹)	$(-4.41 \pm 0.05) \times 10^5$	$(-2.01 \pm 0.04) \times 10^5$	$(-3.54 \pm 0.05) \times 10^5$	$(-1.21 \pm 0.02) \times 10^4$

events. The HRTS events were selected based on direct examination of the photographic prints, thus only profiles that showed extreme nonthermal broadening or skewness were selected. A more careful, systematic approach was implemented in selecting the events from the SUMER data. Profiles were selected if their measured width and skewness were greater than those expected for normal non-event profiles. The HRTS event profiles were then grouped together into a single event if they occurred in adjacent spatial pixels in the same spectrum or the same spatial pixel in consecutive spectra. The average width of an event along the slit thus determined was 1,500 km, or $2''$. The SUMER event profiles were each treated individually. If the HRTS grouping method was implemented in the SUMER analysis, the number of event profiles would decrease approximately by a factor of 2 for the C III and O VI data sets where the resolution is $1''$. The difference in grouping methods can only account for a factor of 2 difference between the number of HRTS and SUMER events, and hence cannot be responsible for the order of magnitude increase in the global birthrate. The dominant reason for this increase is then believed to be the event selection criteria.

The steady-state number is not only dependent on the number of events observed, but also the average lifetime of the events. In the HRTS analysis, the lifetime was estimated by the number of consecutive spectra in which extremely broadened or skewed profiles in a given spatial pixel were observed. The average lifetime thus found was ~ 60 s. In the analysis presented here, the lifetime of these events is taken to simply be the exposure time of each spectrum. The exposure time of the C III and O VI spectra (48 s and 36 s, respectively) are approximately equal to the predicted HRTS lifetime, so no further inflation of the steady-state number is expected. However, the exposure time of the spectra in N IV and Ne VIII (120 s) is twice the lifetime of the HRTS events, which causes the steady-state number to possibly be inflated by a factor of 2. This cannot explain the two orders of magnitude difference between the steady-state number predicted by the SUMER events and that predicted by the HRTS events. Again, it is believed that the most significant cause of the increase in the global birthrate and steady-state number is the careful selection criteria.

Each of the global birthrates and steady-state numbers predicted by the events observed in the four spectral lines are greater than those predicted by HRTS data. However, there remains an order of magnitude variation in these four sets of quantities measured from the SUMER data. The global birthrate and steady-state number predicted by the events observed in the N IV and Ne VIII data are approximately 2×10^3 events s^{-1} and 2×10^5 events, respectively, while these quantities predicted from the events observed in the C III and O VI lines are 4×10^4 events s^{-1} and 2×10^6 events, respectively. These differences are again believed to be related to the selection criteria established in Section 4.4 and to the poor resolution of the N IV and Ne VIII data sets. The spatial and temporal resolution of this data (2,100 km and 120 s) was much greater than the typical event length and lifetime observed by the HRTS data (1,500 km and 60 s). This indicates that events observed in the N IV and Ne VIII lines were unresolved and that possibly more than one event was integrated in a single profile. This would lead to excess broadening in the profiles and make it more difficult to determine the distribution of non-event widths [cf. Figure 4.8]. Hence, a smaller percentage of profiles was identified to exhibit event characteristics ($\sim 6\%$ of the Ne VIII and N IV profiles were selected compared to $\sim 16\%$ of the C III and O VI – Table 5.3) and the global birthrate and steady-state number were suppressed.

The same reasoning can explain the differing characteristics concerning the dominance of the blue-wing in skewed events. The blue-wing was dominant in approximately 88% of the C III and O VI events, but in only $\sim 54\%$ of the N IV and Ne VIII profiles. For the

long exposure time profiles, however, it was more difficult to determine the skewness cutoff, and by integrating over longer time periods, the skewness could have been reduced. These differences are also observed when comparing the SUMER events with HRTS events. In the HRTS data, the blue-wing was estimated to be dominant in only 60% of the profiles. The difference in these numbers can be attributed to a more accurate way of measuring blue-wing dominance in the events presented here. Also there appears to be no temperature dependence on the events observed by SUMER (given the resolution is approximately the same), while the results from HRTS report that events most often occur in lines formed around 10^5 K. This discrepancy is probably due to the lack of lines observed at a variety of temperatures in the HRTS spectral range.

The average filling factors determined in this analysis from the C III, N IV, O VI, and Ne VIII profiles were 30%, 9%, 52%, and 1%, respectively. The filling factors found from the C III and O VI events were much greater than typical values for filling factors associated with the solar transition region (10% or less – e.g., Mariska 1992). Recall that the filling factor depends both on the density and the assumed scale height of the plasma. Typically when measuring the filling factor, the density of the plasma is known through density sensitive line ratios, and hence the only assumed quantity is the scale height (and hence geometry) of the emitting atmosphere. Although the assumption of a scale height can drastically affect the resulting filling factor, it is easily accounted for when comparing two different sets of filling factors. (For instance, if one filling factor was measured from a line profile assuming a one-dimensional atmosphere structure and another assuming a “magnetic junkyard” atmospheric structure, the differences in the two measurements could be easily remedied when comparing the scale height assumptions.) For the measurements made here, however, neither the density or the scale height are known; both are estimates. Given the estimated density and scale height, the filling factor was then used to account for how much volume would be filled if these estimates were correct. Thus the high estimates of the filling factor could be due to either an underestimation of the height of the volume element emitting the explosive event profile or of the density of the explosive event plasma. If either quantity was underestimated, the filling factor (and hence energy flux) would decrease. (The ratio of the energy flux to the energy flux components, however, would remain unchanged.) The effects of such an underestimation on the distribution of events as a function of energy will be discussed in Chapter 6.

By assuming the density and scale height to be the same for all event observed in a spectral line, the differences in intensity are assumed to be solely due to differences in the true volume of the emitting plasma. Basically, an intense spectral line implies a larger volume of plasma is filled, and hence, that plasma is associated with a larger energy flux. This assumption is the reason for the positive correlation between the energy flux and the intensity observed in Figures 5.8 and 5.11, as well as the larger distribution of net energy fluxes as higher intensities in Figure 5.5. However, if, for instance, larger events have a slightly higher density, their intensity would be drastically increased (due to the dependence of the intensity on the square of the density) but the energy flux would be reduced. This scenario demonstrates the possibly significant systematic (but unavoidable) error associated with finding the filling factor from an assumed density.

Comparing the average r.m.s. nonthermal velocity, ξ , presented in Table 5.6, to the generally reported value of most probable speed, ζ , requires an adjustment of $\sqrt{2}$ [cf. Section 2.1]. The values for the most probable nonthermal velocity found by Chae, Schühle, & Lemaire (1998) are given in Table 5.13, along with the corresponding r.m.s. velocities. The values measured from the SUMER data used in this study are from Table 5.6. The

values determined in this study are, without exception, greater than the previously reported values. The nonthermal velocities in C III and O VI are only $\sim 5 \text{ km s}^{-1}$ greater than the previously reported values. This discrepancy is probably due to the fact that Chae, Schöhle, & Lemaire assumed an instrumental broadening for Detector A of 2.3 pixels instead of the 2 pixels that was assumed here. Much larger discrepancies are in the N IV and Ne VIII nonthermal velocities, which were measured to be $\sim 13 \text{ km s}^{-1}$ greater than the previously reported values. This large discrepancy is probably because these lines were observed with Detector B which not only has a large instrumental broadening function (~ 3 pixels) but the instrumental function varies widely, ± 0.5 pixels compared to the ± 0.15 pixels for Detector A. Also, the widths of the N IV and Ne VIII lines were affected by the large spatial resolution and exposure time. This possible overestimate in the nonthermal velocity will not greatly affect the energy flux. As discussed above, the energy flux is most accurately estimated by the thermal enthalpy flux term. A small change in the nonthermal enthalpy, then, would not greatly influence the results.

The energy flux characteristics presented in the previous section provide reliable information on the energy flux associated with explosive events. It appears that the energy flux is best estimated by the thermal enthalpy flux, especially at high temperatures. The non-thermal enthalpy flux and “high-energy” component are also significant, while the kinetic energy flux ($\frac{1}{2}\rho\bar{v}^3$) is generally insignificant.

As stated in the example presented in Section 5.1, it is very difficult to assess what percentage of the net energy flux is carried by a single component. It is instead more meaningful to simply address the dominant component. For the net energy flux, the thermal enthalpy flux was the dominant component in 97% of the profiles, while the nonthermal enthalpy flux was dominant in less than 1% and the energy flux associated with the skewed tail of the distribution was dominant in 3% of the profiles. For the directional energy fluxes, it is possible to discuss what percentage of the energy flux is represented by the kinetic energy flux, thermal enthalpy flux, etc. For the energy flux toward the observer, the

Table 5.13: A comparison of the values for the most probable nonthermal velocity, ζ , and corresponding r.m.s. nonthermal velocity, ξ_{Chae} presented in Chae, Schöhle, & Lemaire (1998) with the r.m.s. velocity, ξ , measured here [cf. Table 5.6].

	C III	N IV	O VI	Ne VIII
$\zeta \text{ (km s}^{-1}\text{)}$ (Chae, Schöhle, & Lemaire 1998)	21.6	26.3	29.0	24.6
$\xi_{\text{Chae}} = \frac{\zeta}{\sqrt{2}} \text{ (km s}^{-1}\text{)}$	15.3	18.6	20.5	17.4
$\xi \text{ (km s}^{-1}\text{)}$	21.1	29.0	24.1	30.3

average contribution of thermal enthalpy flux was 80%, of nonthermal enthalpy flux was 14%, and of skewed energy flux 5%. The kinetic energy flux represented less than 1% of the energy flux toward the observer. For the energy flux away from the observer, the thermal enthalpy flux represented approximately 73% and the nonthermal enthalpy flux 20%. The skewed energy flux and kinetic energy flux each represent 3% of the energy flux away from the observer.

It might seem odd that the thermal enthalpy flux is larger than the nonthermal enthalpy flux, as it is for the events presented here. In general, a line profile emitted by a transition region ion has a nonthermal velocity much larger than its thermal velocity, e.g., the C III thermal velocity is $\sqrt{\frac{kT}{m}} = 7 \text{ km s}^{-1}$ while the nonthermal velocity width of the example event line profile shown in Section 5.1 is $\sqrt{(\overline{v^2} - \overline{v}^2)} = 29.5 \text{ km s}^{-1}$. Therefore it would be intuitive to think that the nonthermal enthalpy flux would always be greater than the thermal enthalpy flux. However, the energy flux given here is the energy flux of the electrons and hydrogen and helium nuclei. It is easier to understand the dominance of the thermal enthalpy when the total enthalpy is expressed in terms of an effective temperature, $j_{\text{enthalpy}} = j_{\text{th}} + j_{\text{nth}} = \frac{5}{2}nkT_{\text{eff}} = \frac{5}{2}nk(T_{\text{th}} + T_{\text{nth}})$, where

$$T_{\text{nth}} = \frac{\frac{1}{2}nm\overline{v_{\perp}^2} + \frac{3}{2}nm(\overline{v_{\parallel}^2} - \overline{v_{\parallel}}^2)}{\frac{5}{2}nk}. \quad (5.9)$$

The “nonthermal temperature” for the electron species is negligible (50 K) when compared to the true temperature of the plasma ($10^{4.8}$ K). The nonthermal temperature for the hydrogen species ($10^{4.9}$ K) is approximately equal to the true temperature of the plasma, while the nonthermal temperature for the helium species ($10^{5.5}$ K) dominates. Basically, each of these species contribute to the thermal enthalpy flux, but only the hydrogen and helium species contribute to the nonthermal enthalpy flux. In general, then, the advection of the thermal energy is more significant than advection of the nonthermal energy.

When examining the components of the directional energy flux compared to the components of the net energy flux, notice that the directional components do not sum to the net components, i.e., $j_{\text{kin}} \neq j_{\text{kin}+} + j_{\text{kin}-}$. The reason for this inequality is straightforward. Though it is true that $\overline{v} = \overline{v_+} + \overline{v_-}$, as shown in Equation (3.10), it is also true that $\overline{v^3} \neq \overline{v_+^3} + \overline{v_-^3}$, as would have to be the case for the kinetic energy fluxes to be equivalent. The relationship between the various values of energy flux is illustrated below. The net energy flux must equal the sum of its components, i.e., $j_{\text{E}} = j_{\text{kin}} + j_{\text{th}} + j_{\text{nth}} + j_{\text{skew}}$. Also, the net energy flux must equal the sum of the directional energy fluxes, $j_{\text{E}} = j_{\text{E}+} + j_{\text{E}-}$. However, the sum of the components to the net energy flux do not necessarily equal the net energy flux component, e.g., $j_{\text{kin}} \neq j_{\text{kin}+} + j_{\text{kin}-}$.

$$\left. \begin{array}{l} j_{\text{kin}+} \\ j_{\text{th}+} \\ j_{\text{nth}+} \\ j_{\text{skew}+} \end{array} \right\} j_{\text{E}+} \quad \left. \begin{array}{l} j_{\text{kin}-} \\ j_{\text{th}-} \\ j_{\text{nth}-} \\ j_{\text{skew}-} \end{array} \right\} j_{\text{E}-} \quad \left. \begin{array}{l} j_{\text{E}+} \\ j_{\text{E}-} \end{array} \right\} j_{\text{E}} \quad \left\{ \begin{array}{l} j_{\text{kin}} \\ j_{\text{th}} \\ j_{\text{nth}} \\ j_{\text{skew}} \end{array} \right.$$

CHAPTER 6

GLOBAL ENERGETICS

This chapter will derive the energy contribution of explosive events to the global solar atmosphere by assuming the characteristics of the events presented in Chapter 5 apply to the global distribution of events. The global contribution of energy flux toward and away from the observer will be calculated, as well as the total energy flux released by events. Also, this chapter will compile the distribution of events as a function of energy, $\frac{dN}{dE}$, to assess if smaller, undetectable events may be energetically significant. Finally, the results of this analysis will be discussed.

6.1 Global Energy Contribution

An estimate of the contribution of explosive events to the global energetics of the solar atmosphere relies on the ability to observe a statistically significant number of events as a sample distribution and then to apply the characteristics of the sample distribution to the entire sun. Events, taken individually, are markedly unique and dissimilar. They are highly dependent on the local conditions of the solar transition region, and because they are most likely linked to magnetic phenomena, their characteristics may change dramatically over the solar cycle. Furthermore, the size and lifetime of explosive events stretch the resolving capabilities of current instrumentation, even while applying the latest observational technologies. Also, in extrapolating event characteristics to a global scale, several (potentially drastic) assumptions must be made. In this section, the energetics of the events observed in the four spectral lines discussed in Chapter 5 will be used to estimate the global energetics.

The global contribution of energy flux, j_{global} (ergs cm⁻² s⁻¹), from explosive events can be constructed from the average of the total energy produced by a single event, \overline{E} (ergs event⁻¹), times the global birthrate, R (events s⁻¹), divided by the surface area of the sun, A_{sun} (cm²), or

$$j_{\text{global}} = \frac{\overline{E}R}{A_{\text{sun}}}. \quad (6.1)$$

The global birthrate has already been found in the last chapter [cf. Table 5.4], thus the only unknown in Equation (6.1) is the average energy per event released into the solar atmosphere.

To find the energy released into the solar atmosphere from an explosive event plasma, it is first necessary to develop a basic geometrical model of the energy flows associated with events. The model assumed for this dissertation is shown in Figure 6.1. In this simple model, the plasma is contained within a coronal loop in a classical one-dimensional transition region. The reconnection event drives plasma away from the reconnection point, either toward the corona or the chromosphere. (By only observing events near sun center, the energy flux toward the observer is assumed to represent the energy flux toward the corona and the energy flux away from the observer is assumed to represent energy flux toward the chromosphere.) The energy flux measured toward the corona, $j_{\text{E}+}$, is assumed

to be the energy flux through an area above the reconnection point and the energy flux measured moving toward the chromosphere, j_{E-} , is assumed to be through an area below the reconnection point. Within one scale height of the atmosphere, the energy flux is then assumed go to zero. It is within these volumes (marked as V_+ and V_- in Figure 6.1) that the explosive event plasma deposits its energy through collisions with the ambient plasma.

The energy density released into these volumes is proportional to the divergence of the energy flux of the event, i.e.,

$$\frac{d\varepsilon_{\pm}}{dt} = -\nabla \cdot j_{E\pm} \quad [\text{ergs cm}^{-3} \text{ s}^{-1}], \quad (6.2)$$

where $\frac{d\varepsilon_+}{dt}$ corresponds to the divergence of j_{E+} and is the heating rate in the volume above the reconnection point and $\frac{d\varepsilon_-}{dt}$ corresponds to j_{E-} and is the heating rate in the volume below the reconnection point. By assuming that the energy flux goes to zero over the scale height of the atmosphere, the total energy released in the volume element above or below the event over the event's lifetime, t_E , is

$$\begin{aligned} E_{\pm} &= \frac{d\varepsilon_{\pm}}{dt} V_{\pm} t_E \\ &= \frac{j_{E\pm}}{H_0} V_{\pm} t_E \\ &= j_{E\pm} \Sigma t_E, \end{aligned} \quad (6.3)$$

where Σ (the area of the pixel) is assumed to be the area of the event (or cross-sectional area of the coronal loop). The average energy released toward the corona or chromosphere per event is then

$$\overline{E_{\pm}} = \frac{1}{N_0} \sum_i^{N_0} j_{E\pm i} \Sigma_i t_{Ei}, \quad (6.4)$$

where the sum is taken over all events.

Combining Equations (6.1), (5.7), and (6.4), the global energy flux can be written as

$$j_{\text{global}\pm} = \sum_i^{N_0} j_{E\pm i} \frac{\Sigma_i}{A_{\text{slit}}} \frac{t_{Ei}}{\tau}, \quad (6.5)$$

which is simply the sum of the measured energy fluxes weighted by a spatial “filling factor” and a temporal “duty cycle”. (To find the average total energy release by the explosive event plasma, the specific energy release rate, $j_{\text{specific}} = |j_{E+}| + |j_{E-}|$ can be substituted into Equation (6.5).) The uncertainty in the global energy flux is due to the uncertainty in the energy flux of each event (derived from the uncertainty in the VDEM function and velocity array), as well as the uncertainty in the event area ($\frac{1}{2}\Sigma_i$) and lifetime ($\frac{1}{2}t_{Ei}$) resulting from the spatial and temporal resolution of the spectrometer.

Table 6.1 summarizes the global energy flux contribution derived from the events observed in the four spectral lines. The average global energy flux contribution toward the corona (toward the observer) is $3.6 \times 10^4 \text{ ergs cm}^{-2} \text{ s}^{-1}$ and the global energy flux contribution toward the chromosphere (away from the observer) is $4.4 \times 10^4 \text{ ergs cm}^{-2} \text{ s}^{-1}$. Both values imply that the global energy flux associated with explosive events is too small to be significant in atmospheric heating. The energy flux away from the observer is clearly dominant in the C III and N IV lines, while the magnitude of the terms are approximately equal in the O VI and Ne VIII events. The average total energy flux released into the

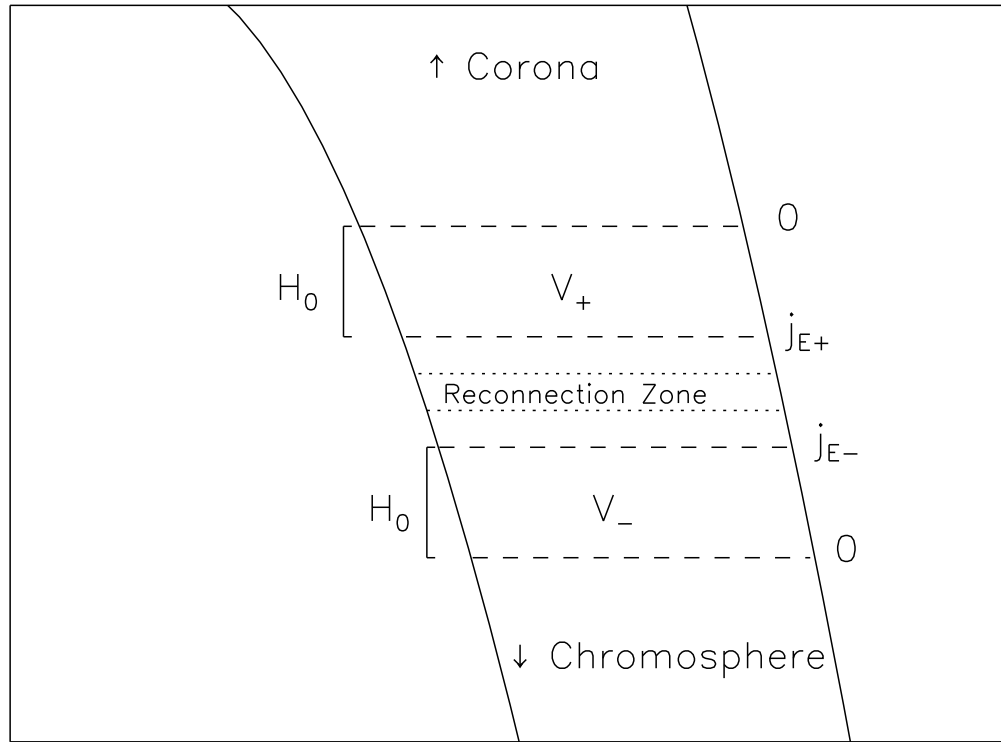


Figure 6.1: This simple model is assumed to represent the energy flows in the solar atmosphere associated with explosive events. The event plasma is driven away from the reconnection site either toward the corona or chromosphere. The plasma then deposits its energy through collisions with the ambient plasma in the volumes marked V_+ and V_- .

Table 6.1: These values are the global energy flux contribution toward the corona and toward the chromosphere, as well as the total energy flux associated with the explosive events.

	C III ($10^{4.8}$ K)	N IV ($10^{5.15}$ K)	O VI ($10^{5.45}$ K)	Ne VIII ($10^{5.9}$ K)
$j_{\text{global}+}$	$(4.46 \pm 0.08) \times 10^4$	$(1.64 \pm 0.04) \times 10^4$	$(7.9 \pm 0.1) \times 10^4$	$(2.67 \pm 0.05) \times 10^3$
$j_{\text{global}-}$	$(-8.6 \pm 0.1) \times 10^4$	$(-3.63 \pm 0.07) \times 10^4$	$(-4.96 \pm 0.07) \times 10^4$	$(-2.54 \pm 0.04) \times 10^3$
$j_{\text{global}T}$	$(1.30 \pm 0.02) \times 10^5$	$(5.3 \pm 0.1) \times 10^4$	$(1.29 \pm 0.02) \times 10^5$	$(5.20 \pm 0.08) \times 10^3$

solar atmosphere, $j_{\text{global}T}$, found by substituting the specific energy release rate into Equation (6.5), is $7.9 \times 10^4 \text{ ergs cm}^{-2} \text{ s}^{-1}$. These quantities are shown as a function of the peak temperature of each ion's emissivity function in Figure 6.2. These values will be compared with previous results in Section 6.3.

6.2 The Global Distribution Functions

The global contribution of explosive events to the solar atmosphere calculated in the previous section implies that explosive events, themselves, are not energetically significant in the solar atmosphere. However, the distribution of events as a function of energy released either toward the corona or toward the chromosphere, $\frac{dN}{dE_{\pm}}$, (events $\text{erg}^{-1} \text{ s}^{-1}$), provides information about the possible energetic significance of smaller, undetectable events. By assuming the explosive event distributions continue to the lower, undetectable energies, important nanoflare requirements, such as the typical energy of a nanoflare and the number required to heat the solar atmosphere, can be derived. In this section, the method of determining these distributions and deriving the required energy and number of nanoflares will be illustrated with the events observed in the C III spectral line. The distributions of events will then be shown both as a function of energy released toward the corona and toward the chromosphere for each spectral line observed.

To illustrate the method of deriving the distribution, consider the energy released toward the corona [cf. Equation (6.3)] by the events observed in the C III 977 Å spectral line. To find the distribution of events as a function of this coronal energy release, a histogram is generated that describes the number of events with energy released between $\log E_+$ and $\log E_+ + \delta$, where δ is the size of the histogram bins. For the dissertation, this bin size is always 0.1. To find the number of events occurring globally with an energy in the range of each bin, the number of observed events in each bin is then multiplied by the solar surface

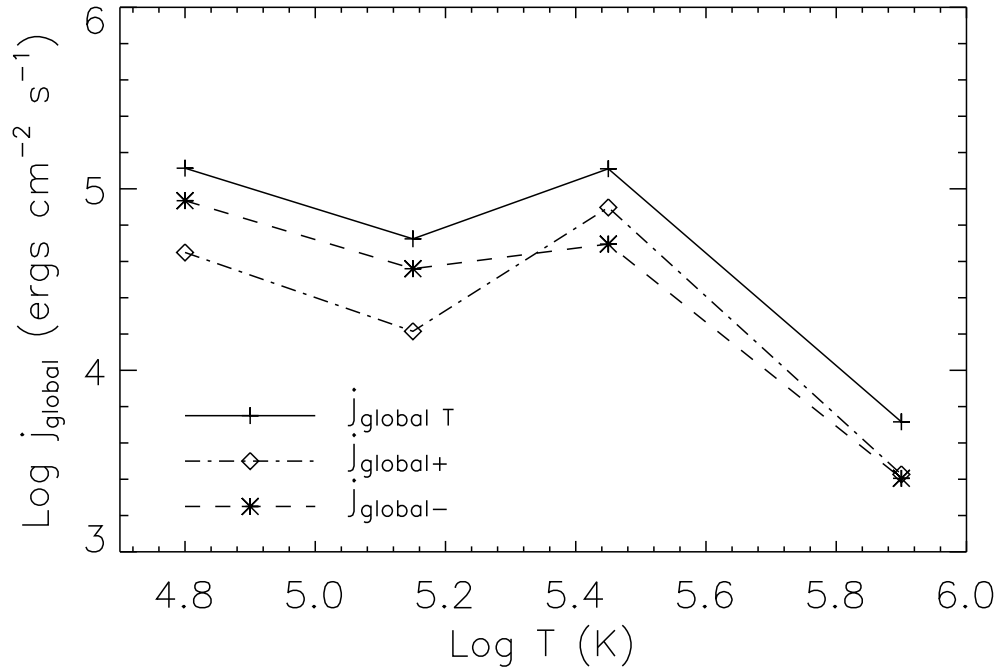


Figure 6.2: The magnitudes of the global energy flux toward the observer and away from the observer, as well as the total global energy flux, are shown as a function of the peak temperature of each ion's emissivity function. The uncertainty associated with each point is given in Table 6.1.

area and divided by the observation time, area of the slit and width of the bin, i.e.,

$$\frac{dN}{dE_+} = \frac{A_{\text{sun}}}{A_{\text{slit}} \tau \Delta E_+} N(E_+), \quad (6.6)$$

where $\Delta E_+ = 10^{\log E_+ + \delta} - 10^{\log E_+}$. The resulting C III distribution is shown in Figure 6.3. The uncertainty in the distribution at each point comes from both uncertainty in the number of events in each bin and the uncertainty in the energy associated with each event. The distribution of the number of events in each bin is assumed to follow Poisson statistics, so the uncertainty will then be the square root of the number of events in each bin. The uncertainty in the energy is derived from the uncertainty in the energy flux, event area, and event lifetime.

If the distribution shown in Figure 6.3 followed a power-law curve, i.e., $\frac{dN}{dE_+} = A E_+^{-\alpha}$, then plotting it on a logarithm scale should result in a straight line with slope $-\alpha$ and y-intercept of $\log A$, i.e.,

$$\log \frac{dN}{dE_+} = \log A - \alpha \log E_+. \quad (6.7)$$

Yet, the curve shown in Figure 6.4 does not immediately appear to be a first degree polynomial. The shape of the curve at high energies (above $\log E_+ \sim 22.5$) appears linear, but

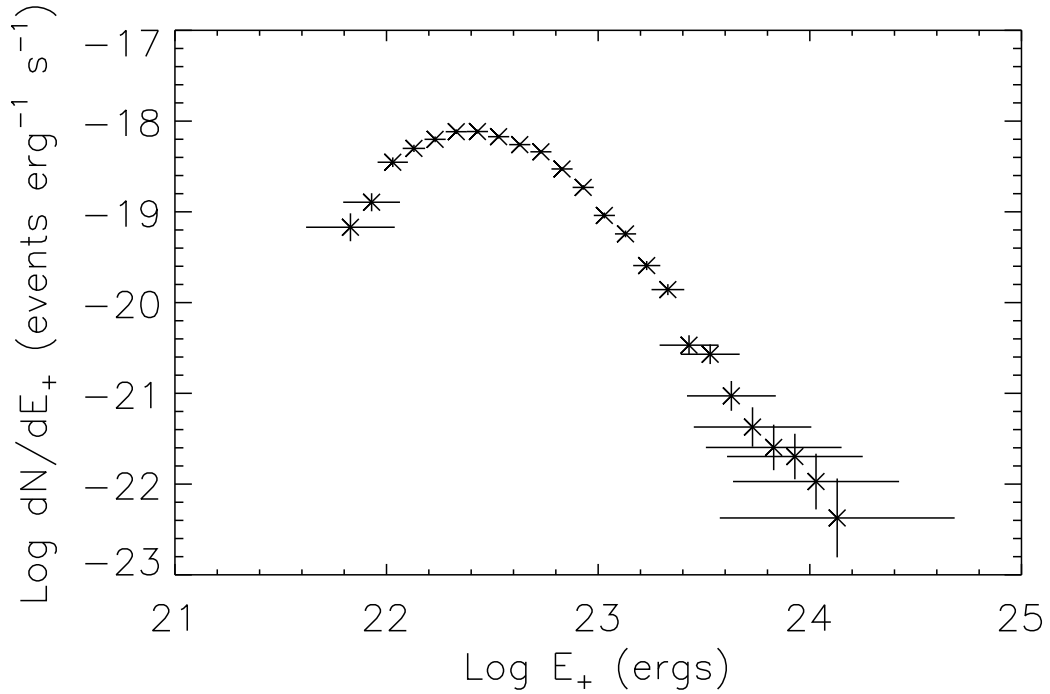


Figure 6.3: The distribution of events observed in the C III spectral line as a function of their energy released toward the corona.

at low energies, the curve levels off and begins decreasing. The reason for the deviation from a power-law at low energies, however, can be explained as a result of the inability to detect events below a certain energy. The lower energy limit at which events become undetectable is difficult to define, but it is related to both instrument sensitivity and selection criteria. The line profiles are selected as explosive events because they exhibit excess broadening or skewness. This definition does not lend itself to determining an implied energy cutoff; thus, the energy cutoff has been determined empirically for each distribution. For each distribution, an initial slope is found considering only the high energy points. Then, a single additional point at the immediate lower energy to those points considered is included to determine its influence on the fit. The energy at which fit deteriorated with the addition of the next point in the distribution is considered the cutoff value. Using this method the cutoff value for the C III distribution was found to be $\log E_+ = 22.7$. Considering only the points above this cutoff value, the slope is 2.8 ± 0.2 and the y-intercept is $\log A = 45.1 \pm 0.2$. This fit is applicable for the range of energies from the cutoff energy, $\log E_+ = 22.7$, to the maximum energy of an event, $\log E_+ \sim 24.2$. The uncertainty in the slope and y-intercept is derived from both the uncertainty in the points of the distribution and how well the points fit a straight line. The resulting fit is shown in Figure 6.4.

After establishing the fit parameters, it is possible to find the required nanoflare energy and the implied birthrate of events at that energy. The total power required to heat the

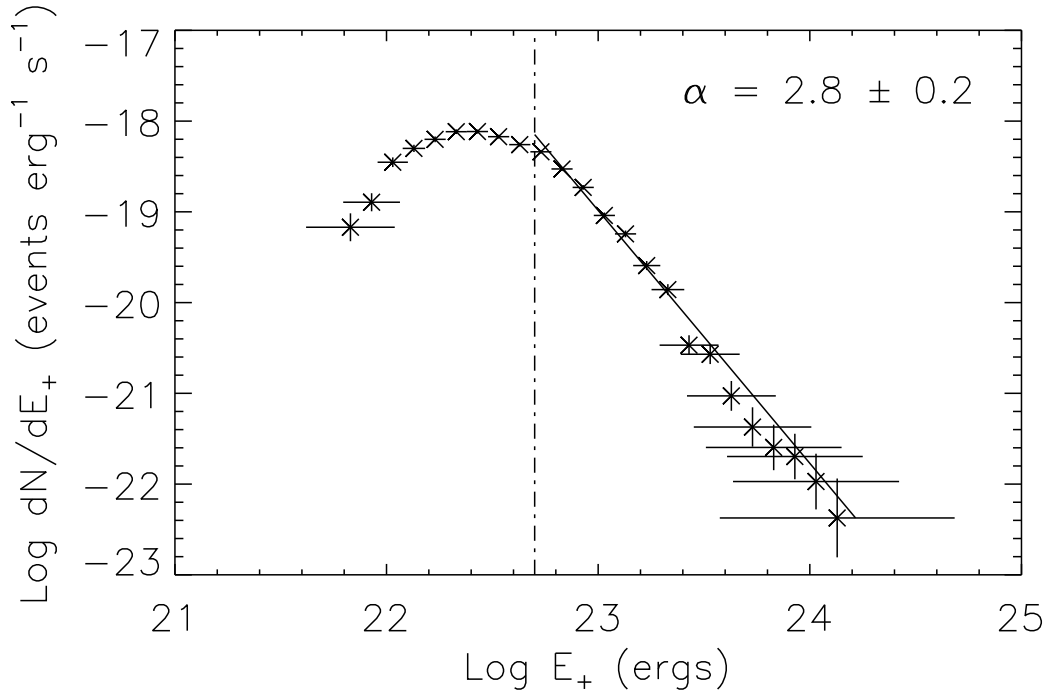


Figure 6.4: The cutoff value for this distribution of events was found by fitting the high energy points, then adding a single low energy point until the fit deteriorated. The cutoff value determined for the above distribution was $\log E_+ = 22.7$.

corona by nanoflares is found by integrating the distribution, i.e.,

$$\begin{aligned}
 P_T &= \int_{E_{\min+}}^{E_{\max+}} \frac{dN}{dE_+} E_+ dE_+ \\
 &= A \int_{E_{\min+}}^{E_{\max+}} E_+^{-\alpha+1} dE_+ \\
 &= \frac{A}{-\alpha+2} \left[E_{\max+}^{-\alpha+2} - E_{\min+}^{-\alpha+2} \right] \\
 &\approx \frac{A}{\alpha-2} E_{\min+}^{-\alpha+2}.
 \end{aligned} \tag{6.8}$$

The last approximation is made because the index of the distribution is greater than 2 and the minimum energy is much less than the maximum energy. Substituting the total power required to heat the corona (3×10^{28} ergs s^{-1}) and solving for $E_{\min+}$, the required nanoflare energy implied the C III distribution to heat the corona is $10^{21.3}$ ergs. (This value was also evaluated for the events observed in the other spectral lines. The results are given in the following sections.) For this energy to be realized by explosive events, the distribution found here must be extrapolated downward by over an order of magnitude.

Table 6.2: The power law index and coefficient, A , for the fits to the distribution of events as a function of their energy released toward the corona observed in each ion, as well as the applicable range and the nanoflare energy and number implied by each distribution.

	C III	N IV	O VI	Ne VIII
α	2.8 ± 0.1	2.8 ± 0.1	3.3 ± 0.4	2.8 ± 0.5
$\log A$	45.1 ± 0.1	46.2 ± 0.1	57.7 ± 0.4	45.5 ± 0.5
Applicable Range (ergs)	$10^{22.7} - 10^{24.2}$	$10^{23.8} - 10^{25.1}$	$10^{23.1} - 10^{24.3}$	$10^{22.8} - 10^{24.1}$
Nanoflare Energy (ergs)	$10^{21.3}$	$10^{21.8}$	$10^{22.3}$	$10^{20.1}$
R_n (events s^{-1})	$10^{6.6}$	$10^{6.7}$	$10^{5.9}$	$10^{9.0}$

The number of nanoflares, R_n (events s^{-1}), required to heat the corona can then be found from

$$\begin{aligned}
 \int dN &= \int_{E_{\min+}}^{E_{\max+}} A E_+^{-\alpha} dE_+ \\
 R_n &= \frac{A}{\alpha - 1} E_{\min+}^{-\alpha+1}.
 \end{aligned} \tag{6.9}$$

This number evaluated from the C III events is $10^{6.6}$ events s^{-1} .

6.2.1 Distribution of Events as a Function of Energy Released Toward the Corona

The distributions of energy released toward the corona was found for the remaining three spectral lines. These distributions are shown in Figure 6.5. A composite of all the distributions of energy release toward the corona is shown in Figure 6.6.

The results of fitting the distributions shown in Figure 6.5 are given for each spectral line in Table 6.2. The values of the index, α , for the coronal distribution of each spectral line are remarkably similar. The weighted average of the index of these distributions is 2.9 ± 0.1 . The minimum value of the applicable range is simply the empirically chosen cutoff value, while the maximum value is the approximate maximum energy of the events observed. These events are observed in a range of energies from $10^{22.7}$ ergs to $10^{25.1}$ ergs. The implied nanoflare energy is between $10^{20.1}$ and $10^{22.3}$, while the number of nanoflares required to heat the corona is between $10^{5.9}$ and $10^{9.0}$ events s^{-1} .

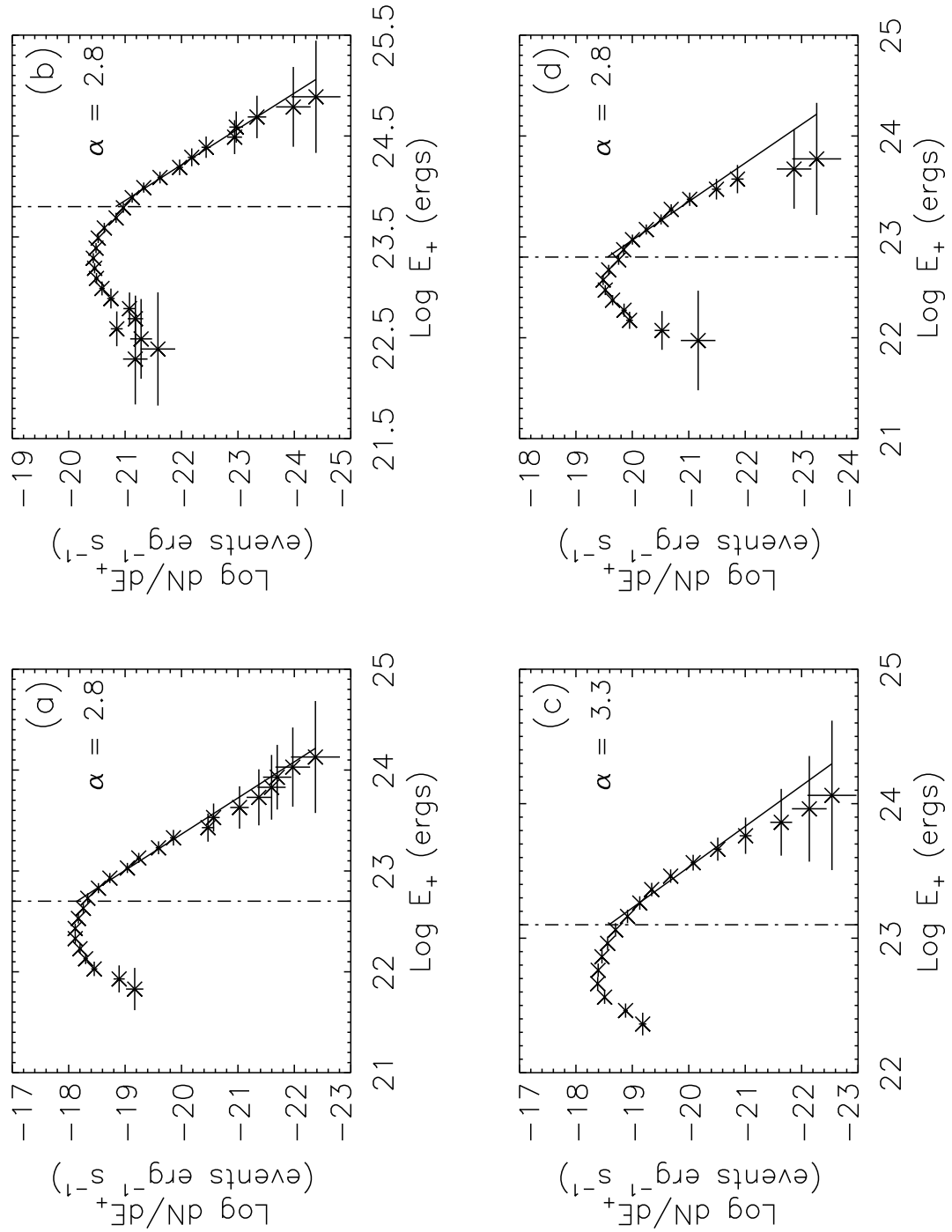


Figure 6.5: Distributions of events observed in the C III line (a), N IV line (b), O VI line (c), and Ne VIII line (d) as a function of their energy released toward the corona. The results of the fits of these distributions are given in Table 6.2. A composite plot of the fits is shown in Figure 6.6.

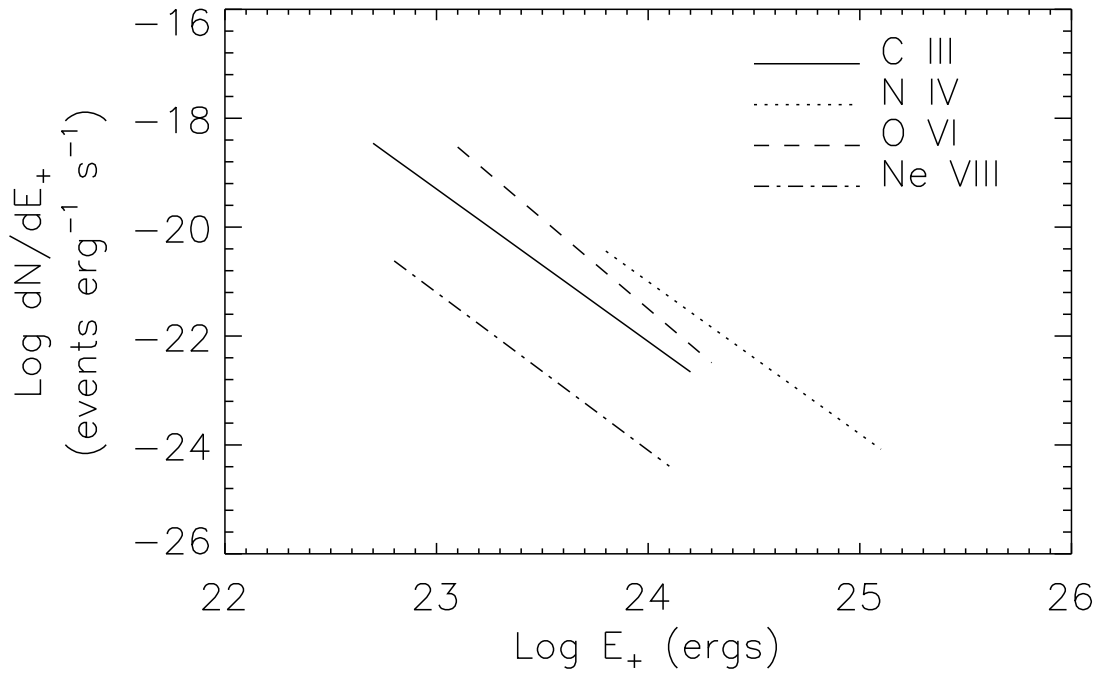


Figure 6.6: A composite of the distribution of energy released toward the corona by the observed events [cf. Figure 6.5].

6.2.2 Distribution of Events as a Function of Energy Released Toward the Chromosphere

The distributions of the energy released toward the chromosphere for the events observed in the C III, N IV, O VI and Ne VIII lines are shown in Figure 6.7. A composite of all the fits is shown in Figure 6.8.

The results of the fits to the distributions in Figure 6.7 are summarized in Table 6.3. The weighted average of the index of these distributions is 2.9 ± 0.1 . The range of energies with approximately this index is $10^{22.7} - 10^{25.3}$ ergs. The nanoflare energies predicted by these distributions range between $10^{19.9}$ ergs and $10^{21.4}$ ergs. The number of these nanoflares required to provide the energy to heat the chromosphere (2×10^{29} ergs s^{-1}) is between $10^{7.6}$ and $10^{9.5}$ events s^{-1} .

6.3 Discussion of the Global Energetics of Explosive Events

The measured contribution of explosive events to the global energy flux released toward the corona ($\sim 3.6 \times 10^4$ ergs $cm^{-2} s^{-1}$) and to the global energy flux released toward the chromosphere ($\sim 4.4 \times 10^4$ ergs $cm^{-2} s^{-1}$), implies that the events themselves are not significant to the energy balance in the solar atmosphere. The values reported here are approximately 10 and 100 times smaller than the values needed to heat the corona or chromosphere, 3×10^5 ergs $cm^{-2} s^{-1}$ and 4×10^6 ergs $cm^{-2} s^{-1}$, respectively. The physical

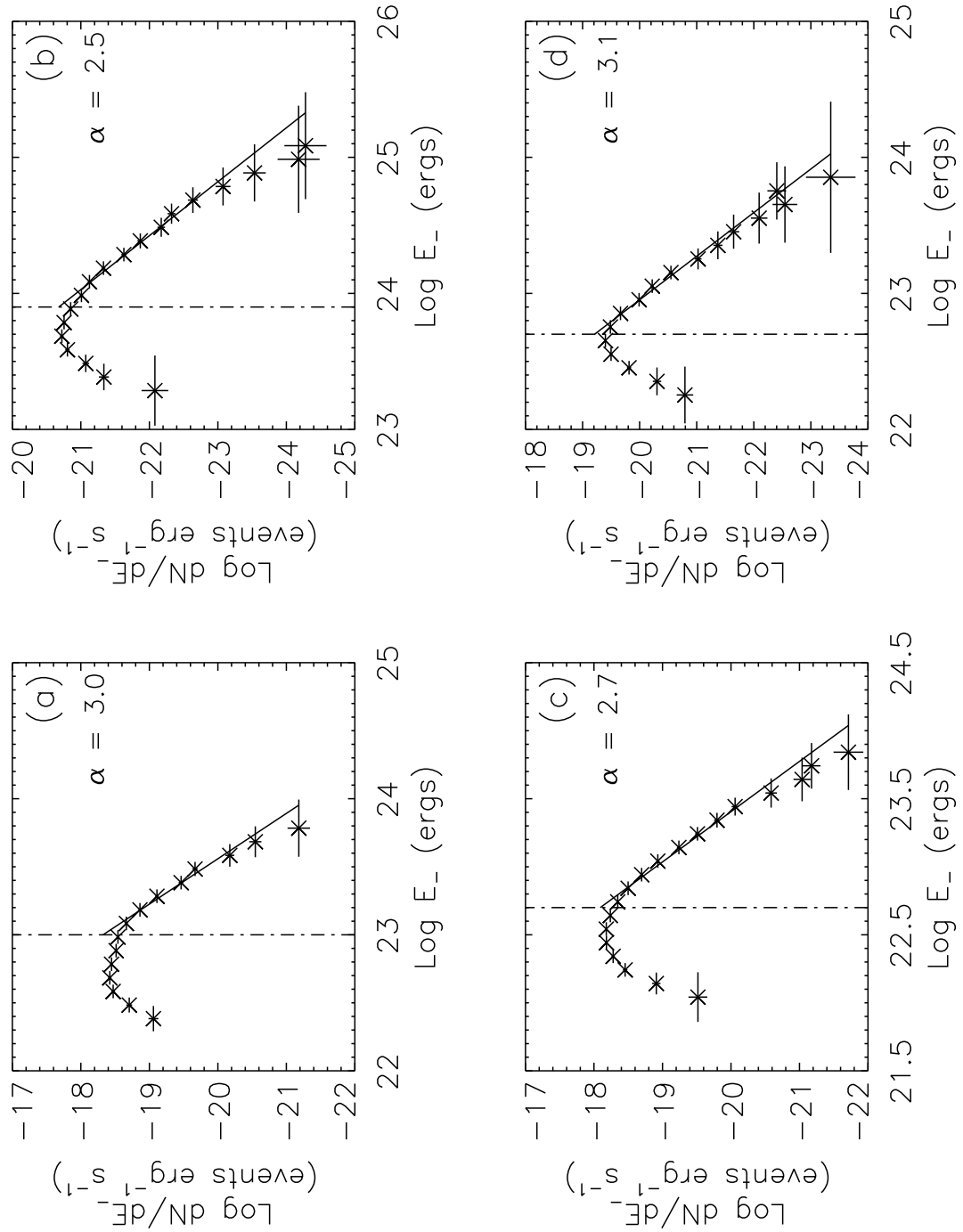


Figure 6.7: Distributions of the events observed in the C III line (a), N IV line (b), O VI line (c), and Ne VIII line (d) as a function of their energy released toward the chromosphere. The results of the fits of these distributions are given in Table 6.3. A composite plot of these fits is shown in Figure 6.8.

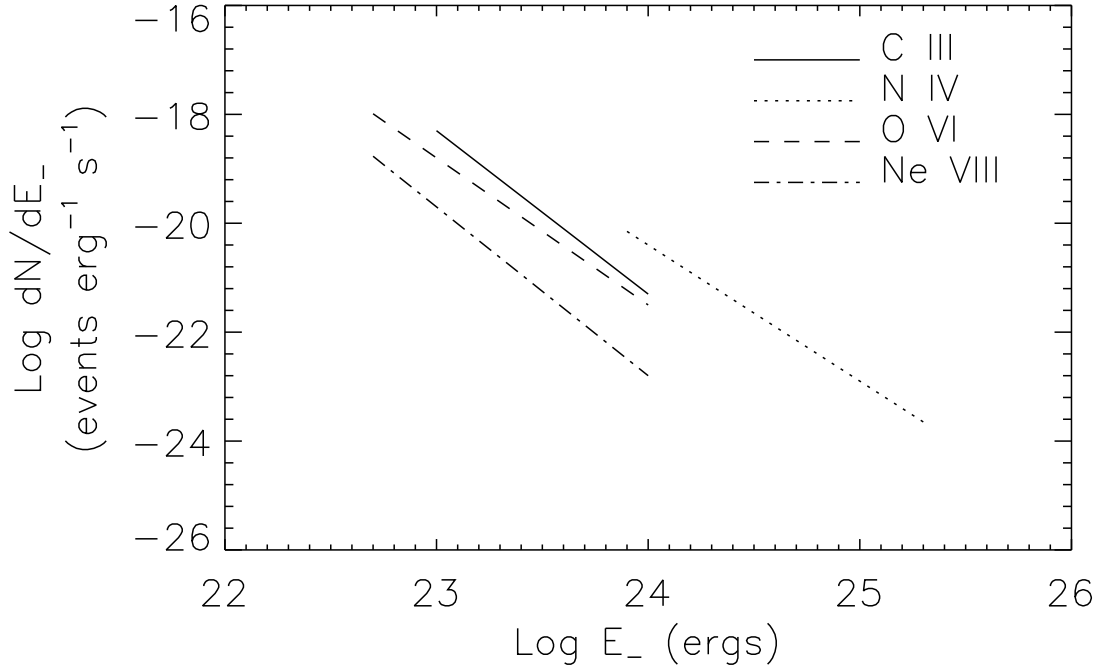


Figure 6.8: A composite of the distributions of the number of events as a function of energy released toward the chromosphere [cf. Figure 6.7].

Table 6.3: The power law index and coefficient, A , for the fits to the distribution of events observed in each ion as a function of their energy released toward the chromosphere, as well as the applicable range and the nanoflare energy and number implied by each distribution.

	C III	N IV	O VI	Ne VIII
α	(3.0 ± 0.2)	(2.5 ± 0.3)	(2.7 ± 0.2)	(3.1 ± 0.2)
$\log_{10} A$	(50.7 ± 0.2)	(39.6 ± 0.3)	(43.3 ± 0.2)	(51.6 ± 0.2)
Applicable Range	$10^{23.0} - 10^{24.0}$	$10^{23.9} - 10^{25.3}$	$10^{22.7} - 10^{24.0}$	$10^{22.7} - 10^{24.0}$
Nanoflare Energy	$10^{21.4}$	$10^{20.3}$	$10^{20.1}$	$10^{19.9}$
R_n (events s^{-1})	$10^{7.6}$	$10^{9.0}$	$10^{9.0}$	$10^{9.5}$

viability of these values is dependent on the geometric model described in Section 6.1. In the model, it was assumed that the energy would be deposited in a volume element with a depth of one scale height and the cross-sectional area equal to the event area. Most HRTS observations of explosive events were made in the low to middle transition region, for example in the resonance lines of C IV at 1,548 and 1,555 Å, which are formed at a temperature of about 10^5 K. These events appear to be associated with the magnetic network (e.g., Porter & Dere 1991). Though the energy given here is not necessarily deposited in the corona or chromosphere, it is assumed to be released in a large coronal structure which is magnetically connected to the corona and chromosphere.

The energy flux of explosive events characterized in this dissertation has been only the energy flux associated with accelerated (and radiating) particles. Of course, the reconnection process associated with explosive events could drive other processes, such as Alfvén waves. In Section 6.2, the energy released into the volume element toward the corona during, for instance, the O VI events, was established to be $\sim 10^{24}$ ergs. The volume element (ΣH_0) for the O VI plasma was $\sim 10^{23}$ cm³. The energy density was therefore approximately 10 ergs cm⁻³. This same energy released perpendicular to the field lines would drive Alfvén waves. The energy would be propagated upward at the Alfvén speed (for instance, ~ 100 km s⁻¹), resulting in an additional energy flux of 10^6 ergs cm⁻² s⁻¹. This energy flux is an order of magnitude greater than the average energy flux of the plasma for the O VI events [cf. Table 5.8]. The realization of this additional energy flux, however, is highly dependent upon establishing a physically realizable model of explosive event reconnection, including how efficiently the energy is released both parallel and perpendicular to the field lines.

In trying to understand the energetic implications of explosive events, it is important to appreciate that they also require energy to sustain them. At a pressure of 10^{15} cm⁻³ K, maintaining the plasma during an average event against radiative losses, $n_e n_H P(T)$ [cf. Equation (1.11)], requires an energy deposition rate of 0.09 ergs cm⁻³ s⁻¹ for C III events, 0.03 ergs cm⁻³ s⁻¹ for N IV events, 0.007 ergs cm⁻³ s⁻¹ for O VI events, and 2×10^{-4} ergs cm⁻³ s⁻¹ for Ne VIII events. The radiative cooling time of the event plasmas [cf. Equation (2.4)] are ~ 2 s for C III, ~ 7 s for N IV, ~ 30 s for O VI, and $\sim 1,300$ s for Ne VIII. The fast cooling times for the C III, N IV, and O VI events imply energy must be continually supplied to sustain radiation during the events. Thus, the energy supplied by the reconnection event must provide not only the enthalpy that may heat the corona and chromosphere, but also a substantial amount of energy to power the radiation from the explosive event.

The distributions of events as a function of energy toward the observer follow a power-law curve with an average index of 2.9 ± 0.1 . These distributions span a range of energies from $10^{22.7}$ to $10^{25.1}$ ergs. These distributions predict an average nanoflare energy of approximately $10^{21.9}$ ergs, an order of magnitude less than the applicable range. The average global birthrate of the nanoflares is predicted to be $10^{8.4}$ events s⁻¹. The distributions of events as a function of energy away from the observer have an average index of 2.9 ± 0.1 valid for the energy range of $10^{22.7}$ to $10^{25.3}$ ergs. The average nanoflare energy implied by this distribution is $10^{20.8}$ ergs, two orders of magnitude less than the minimum cutoff of the distribution. The global birthrate predicted by the average distribution is $10^{9.1}$ events s⁻¹.

Throughout this study, several (potentially drastic) assumptions have been made that could affect the slope of these distributions. These assumptions include the filling factor, lifetime, and area of explosive events, as well as the event selection criteria. The possible effects of these assumptions will be discussed briefly here.

As discussed in Section 5.4, the filling factor measured here was dependent upon an assumed density and scale height of the emitting plasma. It is quite possible that the scale height or density was underestimated, resulting in a relatively high ($\sim 25\%$ compared to $\sim 10\%$ or less) filling factor. If, in fact, the density or scale height of the event plasma was systematically higher in all event plasmas, the energy associated with the events (and hence the energy associated with the distribution of events) would be reduced. The distribution would be shifted to lower energies, resulting in lower estimated nanoflare energies and larger numbers of required nanoflares. However, the slope of the distribution would not be affected by this systematic error. The slope would only be influenced if the density or scale height of the events was dependent on the energy of the events (for instance, if large energy flux events were associated with a larger density than small energy flux events or vice versa). This possible influence is difficult to assess due to the lack of reliable information on the density or volume of the explosive event plasma, but it is possible to address whether an energy dependent density or scale height would increase or decrease the slope of the distribution. For instance, if larger energy flux events were associated with larger density, the total energy released toward the corona or chromosphere by these events would be reduced. [This is due to the filling factor's dependence on $\frac{1}{n^2}$, resulting in the energy flux (and hence energy of the events) being proportional to $\frac{1}{n}$.] Therefore, the largest energy flux events would be shifted to lower energies while the small energy flux events would remain unchanged. This would steepen the distribution and hence increase the slope. If instead the density of the smaller flux energy events were larger than the density of the larger energy flux events, the smaller events would be shifted to lower energies, while the larger energy events would remain unchanged. The distribution would flatten, and the slope would therefore decrease. [Because the energy flux is also inversely proportional to the scale height, the same type of behavior of the slope would be expected if the scale height were energy dependent, i.e., a larger scale height for larger events would increase the slope, while a larger scale height for smaller events would decrease the slope.]

The energy of each individual event also depends on its lifetime and area [Equation (6.3)]. In this study, the lifetime of all events was assumed to be the exposure time of the spectra (48 s for the C III events, 120 s for the N IV events, 36 s for the O VI events, and 120 s for the Ne VIII events) and the area was assumed to be the (pixel length)². These definitions of lifetime and area differ from those employed in the HRTS analysis where profiles that occurred in adjacent pixels in the same spectra or the same pixels in consecutive spectra were grouped into a single event. If the assumptions made here about event area and lifetime are systematically wrong, e.g., the lifetime of all the events were $\frac{1}{2}$ the exposure time, the distribution of events as a function of energy would be shifted in a way similar to the shift associated with an underestimation of density or volume. But, again, it would not change the slope of the distribution. If, however, the lifetime or the area of the events was dependent upon the energy, e.g., if events with larger energy fluxes lasted longer or were over larger areas than the events with smaller energy fluxes, the slope of the distribution may drastically be affected. Because the energy of the events is directly proportional to both the lifetime and area of the events, larger areas or lifetimes associated with larger energy flux events would flatten the distribution and reduce the slope. It is then necessary to consider the possible influence of grouping the profiles and to evaluate whether the assumption that each profile represents a single event is valid.

The two C III spectra shown in Figure 6.9 demonstrate the potential problems with grouping adjacent profiles into a single event. All the profiles in spectrum (a) between spatial pixels 7 and 14 were chosen as event profiles, as well as all the profiles between spatial pixels

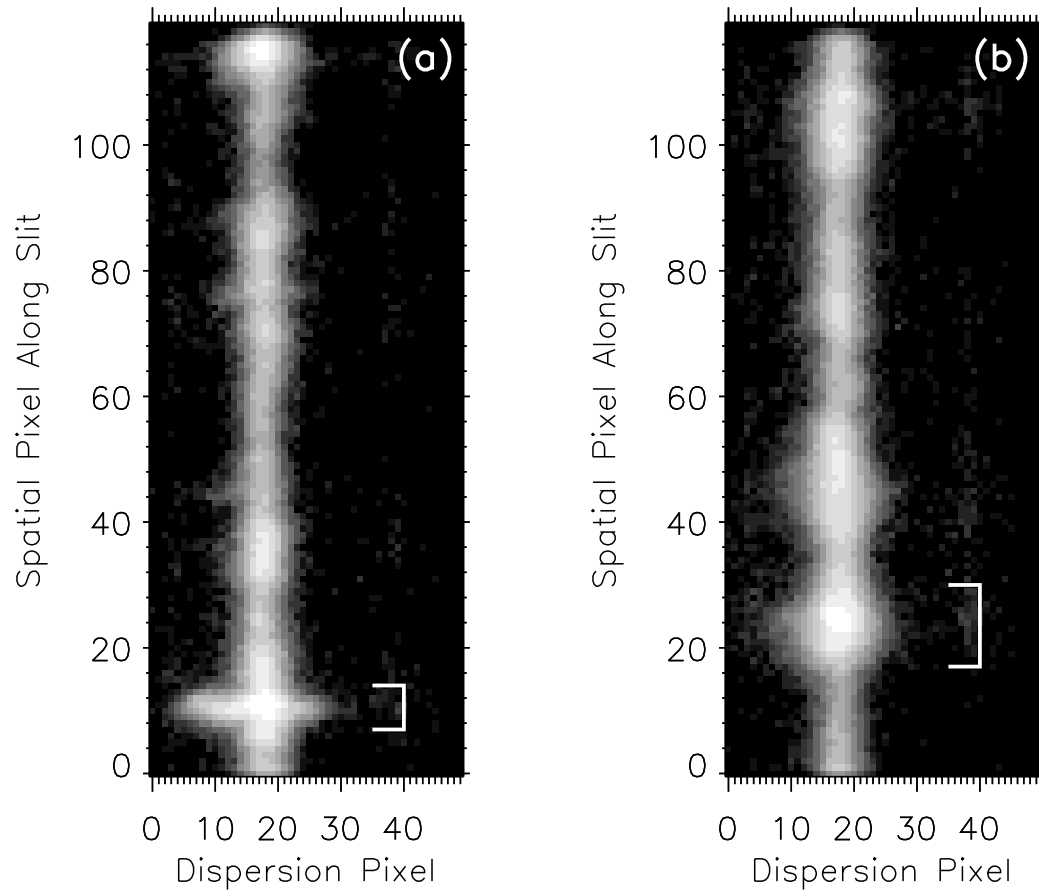


Figure 6.9: These two C III spectra show different groups of profiles selected as events. The profiles in spectrum (a) show similar shifts and velocity distributions, while the profiles in spectrum (b) are not convincingly similar.

17 and 30 in spectrum (b). Each of the profiles in spectrum (a) represent a large event with very obvious excess emission in the blue wing of the spectral line. The line profiles from pixel 7 to 14 have similar shapes and result in similar velocity distributions and measurements of energy flux. It would be defensible, then, to group these 8 profiles together and consider them to be a single event representative of a $8'' \times 8''$ area. It is not as easy to find similar characteristics in the profiles highlighted in spectrum (b). Even though they appear in adjacent pixels, it is not immediately obvious that they are representative of a single event. The line profiles associated with these pixels are not convincingly similar (or dissimilar). Each shows small amounts of excess emission in the wings of the profile, yet there is no characteristic emission that group them into a single event. With no other evidence to support the supposition that they are magnetically connected (such as a magnetogram with a neutral line running along this area or a high resolution image of the area), there is no convincing argument that these profiles all represent observations of a single event, or 10 separate events, or any other possible grouping.

In fact, it is suspect that any profiles should be grouped together, even ones with similar line profile shapes. The filling factor of the atmosphere is generally 10% or less (and even though it is found to be larger in this study, it is still consistently less than unity). If the volume observed by a single pixel is only partially filled with emitting material, how is it intrinsically connected to volume elements thousands of kilometers away? Unless the reconnection event fills the volume, it is difficult to assume that these profiles are magnetically connected. Furthermore, events are observed to occur along magnetic neutral lines in the same location over time, so different reconnection events could be occurring in spatially adjacent (yet magnetically separate) locations. To fully address the true size and lifetime of explosive events, it is necessary to have high resolution, high cadence images of the solar transition region, as well as information on the local magnetic field motions and the high quality spectral data. Until then, the effect of the area and lifetime of events on the distribution of events as a function of energy can not be addressed.

Finally, the selection method implemented in this study [cf. Section 4.4] may have an effect on the distribution of events as a function of energy. The cutoff values for the width and skewness of the profiles were selected as where the number of events dominated the number of non-events [cf. Figures 4.8 and 4.9]. This implies that some event profiles were not selected as events and some profiles that were within the acceptable non-event distribution were selected as events. If the ignored events (or the non-events mistakenly selected) have markedly different energy distributions than established here, their inclusion (or exclusion) would then affect the slope of the distribution.

A more comprehensive analysis of how these selection criteria influence the events is warranted. For instance, the distribution of events can be found for all the profiles in a single bin of the width histogram [cf. Figures 4.8]. This distribution can then be weighted by the percentage of profiles in that bin that qualifies as an event. The weighted distributions from all the bins can then be added and the total distribution can be evaluated. Such an analysis is planned for an upcoming paper.

The energy distributions found in the analysis of these explosive events imply that for nanoflares to be associated with the energy release responsible for solar atmospheric heating, an individual nanoflare must release approximately 10^{21} ergs into the solar atmosphere and approximately 10^9 new nanoflares must occur globally every second. For these results to be considered accurate, the energy distributions derived here must be representative of the energy distribution of nanoflares. The hypothesis that the nanoflare distribution is accurately represented by the explosive event distribution is supported by the similarity in

magnitude of the event energies. Explosive events range in energies from $10^{22.7} - 10^{25.3}$ ergs and the predicted nanoflare energy is 10^{21} ergs, within two orders of magnitude. Recall, however, that the event distributions found here show that the energy distribution of events is a broken power-law between this explosive event energy range (with a power-law index of ~ 2.9) and the solar flare energy range $\sim 10^{29} - 10^{32}$ ergs (with a power-law index of 1.8 – Dennis 1985). Hence, even though the energy range of explosive events is quite similar to the predicted energy range of nanoflares, the energy distribution of events, which has already been found to be inconsistent in different energy ranges, may not extend to the nanoflare energies. To further develop this distribution to smaller energies, higher spatial and spectral resolution data is needed.

CHAPTER 7

SUMMARY AND CONCLUSIONS

This dissertation has addressed the energetics of explosive events in the solar transition region. Explosive events are observed as extremely broadened or skewed spectral lines and are thought to be the bi-directional jet produced by magnetic reconnection. Previous knowledge of explosive event characteristics was derived almost solely from the HRTS instrument. Though this instrument had adequate spatial and spectral resolution, the amount of data was insufficient for a statistical study of explosive events. The previous measurements of the energy associated with explosive events relied on using the characteristic velocities of the plasma (mainly derived from the width of the spectral line) and hence were not true measurements of the energy flux (which is proportional to the third moment of the velocity).

The energy flux of a dynamic plasma can only truly be measured from the bulk velocity distribution. Assuming the plasma is constrained to move along a single direction, the energy flux in that direction can be separated into four components: the kinetic energy flux (associated with the bulk velocity of the plasma), the thermal enthalpy flux (the advection of the thermal energy of the plasma), the nonthermal enthalpy flux (the advection of the microturbulence in the plasma), and the “high-energy” component (associated with the skewed tail of the distribution). If the moments of the velocity are taken over all velocity space, then the energy flux thus found would represent the net energy flux through the volume element. If the moments are taken only over positive or negative velocities, the energy flux would be a measure of the energy flux toward or away from the observer. The specific energy release rate can also be measured as the total magnitude of the energy flux both toward and away from the observer.

To find the energy flux, the first through third moments of the velocity distribution parallel to the direction of motion must be known, as well as the temperature, density, filling factor, and width of the velocity distribution perpendicular to the direction of motion. Assuming the direction of motion is along the line-of-sight, the bulk velocities observed as Doppler shifts in the event line profiles can be characterized using the Velocity Differential Emission Measure. The normalized moments of this function, along with assumptions about the plasma temperature, density, and scale height, provide the information necessary to make accurate energy flux measurements. This method of finding the energy flux was found to be robust given some data restrictions such as a large number of counts defining the line profiles, observations taken at or near disk center, and high cadence observations.

These data requirements were met by the Solar Ultraviolet Measurements of Emitted Radiation (SUMER) telescope and spectrometer. Two data sets containing a total of four spectral lines were selected from the SUMER data archives. The wavelengths associated with the high-cadence spectra were found by fitting reference lines in long exposures observations of the wavelength range. The four spectral lines utilized were the C III 977 Å line (formed at $10^{4.8}$ K), the N IV 765 Å line (formed at $10^{5.15}$ K), the O VI 1032 Å line (formed at $10^{5.45}$ K), and the Ne VIII 770 Å line (formed at $10^{5.9}$ K). These spectral lines are formed over a temperature range that spans the transition region.

The spectra in these data sets contained between 17,000 and 45,000 line profiles, yet

only a fraction qualified as explosive events profiles. To select the event profiles from the general sample, the width and skewness of each profile were measured and compared to cutoff values derived from the distribution of widths and skewnesses of all line profiles [cf. Section 4.4]. If either the width or skewness of a profile were larger than the established cutoff values, the profile was selected as an event.

Each profile selected as an event was deconvolved with a kernel function to find the corresponding VDEM function. The moments of the VDEM function were then used to find the energy flux associated with the event plasma [cf. Section 5.3]. The characteristics of the energy flux of the observed events were assumed to be representative of the global distribution of explosive events; thus the global contribution of energy flux to the corona and chromosphere due to explosive events was found [cf. Section 6.1]. The distribution of events as a function of either energy released toward the corona or toward the chromosphere was also derived [cf. Section 6.2].

The major results of this dissertation are summarized below.

- The global birthrate and steady-state number of explosive events were found to be between 2×10^3 and 4×10^4 events s^{-1} and 2×10^5 and 2×10^6 events, one to two orders of magnitude greater than previously reported values. Though a fraction of this difference is thought to be due to differences in different analysis technique (grouping several profiles into a single event compared to treating each profile individually), the dominant reason for this increase is due to improved event selection criteria.
- The characteristics of the event profiles were also updated. It was found that $\sim 88\%$ of the events observed in the (high resolution) C III and O VI spectral lines with statistically significant skewness had dominant blue wings. This blue-wing dominance is much more pronounced in these data sets than in the HRTS data where only 60% of the profiles were reported to have blue-wing asymmetry.
- The energy flux of the events was dominated by the thermal enthalpy flows. The nonthermal enthalpy flows and skewed energy flux were also significant, while the kinetic energy flux associated with the bulk velocity of the plasma was the least significant.
- The average energy flux contribution to the solar atmosphere predicted by the characteristics of these sample events was 3.6×10^4 ergs $\text{cm}^{-2} \text{s}^{-1}$ toward the corona and 4.4×10^4 ergs $\text{cm}^{-2} \text{s}^{-1}$ toward the chromosphere. Though these values are slightly larger than the values previously found from Brueckner and Bartoe (1983) and Cook et al. (1988), they do not suggest that explosive events are significant in providing the energy requirements for heating the solar atmosphere.
- The ion-averaged distribution of events as a function of the energy released toward the observer is a power-law function with a slope of 2.9 ± 0.1 . The energy range over which this distribution is valid is $10^{22.7}$ to $10^{25.1}$. The implied energy of nanoflares is approximately $10^{21.9}$ ergs and global birthrate is $10^{8.4}$ events s^{-1} . The average distribution of events as a function of the energy released away from the observer is a power-law function with a slope of 2.9 ± 0.1 . The energy range over which this distribution is valid is $10^{22.7}$ to $10^{25.3}$. The implied energy of nanoflares is approximately $10^{20.8}$ ergs and global birthrate is $10^{8.3}$ events s^{-1} . If the distribution found here is representative of smaller, undetectable releases of energy ($\sim 10^{20.8} - 10^{21.9}$ ergs),

then enough energy would be released by these nanoflares to account for coronal and chromospheric heating.

* * * * *

Much improvement can be made over the current knowledge of reconnection events and their role in the global atmosphere. First and foremost, a physically realizable model of the acceleration process needs to be developed. The improved event characteristics provided here (such as dominance of the blue wing asymmetry) should establish criteria for a physically realistic model. Also, higher spatial, spectral, and temporal resolution images are needed with better count statistics to extrapolate the distribution of events to smaller energies.

To understand the differences in energy flux as a function of temperature, comparisons of the energy flux of multiple lines formed simultaneously at different temperatures in the solar atmosphere can be made. This type of comparison of the N IV and Ne VIII data will be made in a future paper. Assuming a plane-parallel geometry, comparing two or more measurements of energy flux would provide the divergences of the energy flux in the regions between the line formation locations. However, a correct interpretation of such an analysis depends crucially on the true geometry of the solar “transition region” plasma. Images from *SOHO* reveal that transition region plasma does not really constitute a “transition region” at all (in the sense of an interface between cool chromospheric and hot coronal plasmas as in a one-dimensional model), but rather exhibits complex geometries more suggestive of magnetically isolated structures (e.g., the “magnetic junkyard” scenario originally proposed by Dowdy, Rabin, & Moore 1986). Priest (1998) has strongly cautioned against the use of *any* one-dimensional model to describe the EUV emitting plasma regions. In the case where spectral lines are formed in different structures, differences between energy fluxes revealed by these spectral lines provide not so much the divergence of the energy flux within a single structure, but rather the spatial distribution of energy input to the different structures in the region.

In summary, this dissertation finds that although explosive events themselves do not release sufficient amounts of energy to heat the solar atmosphere, they do provide valuable information on the distribution of events as a function of energy. The distribution found here suggests smaller, undetectable nanoflares may be responsible for solar atmospheric heating.

APPENDIX

Simulating Line Profiles

The shape and magnitude of a spectral line profile emitted by a plasma depends upon the temperature and density of the plasma, the emissivity function associated with the spectral line in question, and the bulk velocity distribution of the plasma along the line-of-sight. This appendix will illustrate the process of simulating an O IV 790 Å line profile assuming the emitting plasma has a uniform temperature of $10^{5.2}$ K and an electron density of $10^{9.8}$ cm $^{-3}$.

Consider the equation of the intensity (photons cm $^{-2}$ s $^{-1}$ Å $^{-1}$),

$$I(\lambda) = \frac{\Sigma\gamma}{4\pi D^2} \int n_e^2 G(T) \frac{ds}{dv_{\text{los}}} K(\lambda, v_{\text{los}}) dv_{\text{los}} \quad (\text{A.1})$$

[restated from Equations (3.17) and (3.18)], where Σ is the area under observation, D is the sun-satellite distance, n_e is the electron density, $G(T)$ is the emissivity function (ergs cm 3 s $^{-1}$) associated with the spectral line in question, s is the path length in the solar atmosphere, v_{los} is the line-of-sight velocity, and $K(\lambda, v_{\text{los}})$ ((cm s $^{-1}$) $^{-1}$) is the kernel function. This function describes the emission from each volume element as a function of its line-of-sight velocity. It is assumed to be simply a thermally broadened Gaussian function centered on the line-of-sight velocity in question. Assuming that the emitting plasma has uniform temperature and density, the intensity becomes

$$I(\lambda) = \frac{n_e^2 G(T) \Sigma \gamma}{4\pi D^2} \int \frac{ds}{dv_{\text{los}}} K(\lambda, v_{\text{los}}) dv_{\text{los}}, \quad (\text{A.2})$$

where $\frac{ds}{dv_{\text{los}}}$ represents the percentage of fluid moving with a given line-of-sight velocity, and hence, (in a constant density plasma) is the bulk velocity distribution along the line-of-sight. For instance, consider the bulk velocity distribution shown in Figure A.1 (a). In this simple distribution, 70% of the volume elements are moving at -10 km s $^{-1}$, while 30% of the volume elements are moving with a bulk velocity of 40 km s $^{-1}$. (The assumed bin size is 1 km s $^{-1}$.)

In the absence of temperature or density gradients, all volume elements are equally likely to emit a photon. In the above example, 70% of the photons will be emitted by the plasma with a bulk velocity of -10 km s $^{-1}$, while 30% of the photons will be emitted by the volume elements with a bulk velocity of 40 km s $^{-1}$. The definition of the size of a volume element is arbitrary, thus it is intuitive to divide the plasma into the number of volume elements as required by the number of counts. For instance, to simulate a line profile defined by 10,000 counts, the emitting plasma is assumed to contain 10,000 volume elements with each volume element emitting a single photon. Such a line profile based on the bulk velocity distribution shown in Figure A.1 (a), would have 7,000 photons emitted by the plasma traveling with a bulk velocity of -10 km s $^{-1}$, and 3,000 photons emitted by the plasma traveling with bulk velocity of 40 km s $^{-1}$.

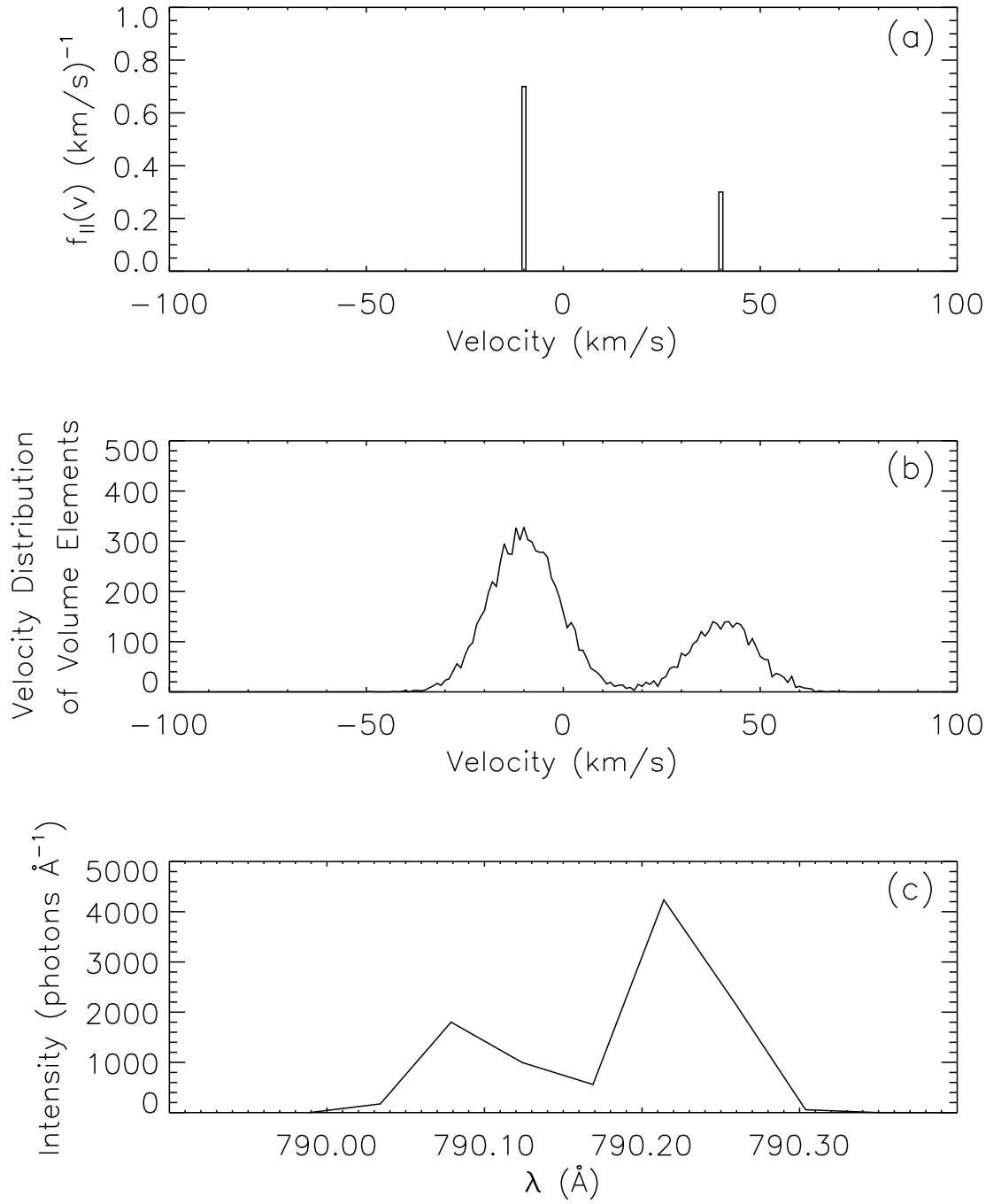


Figure A.1: A simple bulk velocity distribution is shown in (a) and the corresponding velocity distribution of 10,000 volume elements shown in (b). The resulting intensity from this distribution of volume elements is shown as a function of wavelength in (c).

The volume elements associated with a given bulk velocity will still be distributed in a thermal Gaussian distribution about that bulk velocity. To simulate the statistical fluctuations associating with the thermal distribution (related to the kernel function in Equation (A.2)), the IDL program “RANDOMN.PRO” was used. This program generates pseudo-random numbers based on a Gaussian probability distribution with a mean of zero and standard deviation of 1, i.e.

$$P \sim e^{-\frac{z^2}{2}}, \quad (\text{A.3})$$

where $z = \frac{v - v_{\text{bulk}}}{v_{\text{th}}}$. The value of z is returned by the program, and then used to find the value of the velocity, v , associated with a given volume element. The thermal velocity for the O IV ion is 9 km s^{-1} . The distribution of the 10,000 volume elements based on the assumed bulk velocity distribution is shown in Figure A.1 (b).

After determining the exact velocity for each volume element emitting a photon, the last step is to find the wavelength associated with each velocity. If the volume element is moving toward (away from) the observer, the emitted wavelength will be blueshifted (redshifted). The wavelength, λ , is found using the Doppler shift formula, $\frac{v}{c} = \frac{\lambda_0 - \lambda}{\lambda_0}$. Finally, to find the intensity of photons as a function of wavelength, a histogram is compiled from the wavelength of each photon. The bin size of the histogram should be comparable to that of a spectrometer (45 mÅ for the SUMER spectrometer). The intensity of the O IV line resulting from the assumed bulk velocity distribution is shown Figure A.1 (c). The units of this intensity can be changed to units of flux by multiplying by $\frac{n_e^2 G(T) \Sigma \gamma}{4\pi D^2}$.

REFERENCES

- Antonucci, E., Gabriel, A.H., Acton, L.W., Culhane, J.L., Doyle, J.G., Leibacher, J.W., Machado, M.E., Orwig, L.E., & Rapley, C.G. 1982, *Solar Physics*, 78, 107
- Barrett, R.K. 1995, *Inverse Problems in Helioseismology*, Doctoral Dissertation, University of Glasgow
- Brekke, P., Hassler, D.M., & Wilhelm, K. 1997, *Solar Physics*, 175, 349
- Browning, P.K. 1991, *Plasma Physics and Controlled Fusion*, 33, 539
- Brueckner, G.E. & Bartoe, J.-D.F. 1983, *Astrophysical Journal*, 272, 329
- Chae, J., Schöhle, U., & Lemaire, P. 1998, *Astrophysical Journal*, 505, 957
- Chae, J., Wang, H., Lee, C.-Y., Goode, P.R., & Schöhle, U. 1998, *Astrophysical Journal*, 497, L109
- Chae, J., Yun, H.S., & Poland, A.I. 1998, *Astrophysical Journal Supplement Series*, 114, 151
- Cook, J.W., Lund, P.A., Bartoe, J.-D.F., Brueckner, G.E., Dere, K.P., & Socker, D.G. 1988, in *Cool Stars, Stellar Systems, and the Sun*, edited J.L. Linsky and R.E. Stencel, (Berlin:Springer), 150
- Cox, D.P. & Tucker, W.H. 1969, *Astrophysical Journal*, 157, 1157
- Curdt, W., Feldman, U., Laming, J.M., Wilhelm, K., Schöhle, U., & Lemaire, P. 1997, *Astronomy and Astrophysics Supplement Series*, 126, 281
- Dennis, B. 1985, *Solar Physics*, 100, 465
- Dere, K.P. 1994, *Advanced Space Research*, 14, (4)13
- Dere, K.P., Bartoe, J.-D.F., & Brueckner, G.E. 1984, *Astrophysical Journal*, 281, 870
- Dere, K.P., Bartoe, J.-D.F., & Brueckner, G.E. 1986, *Astrophysical Journal*, 310, 456
- Dere, K.P., Bartoe, J.-D.F., & Brueckner, G.E. 1989, *Solar Physics*, 123, 41
- Dere, K.P., Bartoe, J.-D.F., Brueckner, G.E., Ewing, J., & Lund, P. 1991, *Journal of Geophysical Research*, 96, 9399

- Doschek, G.A., Feldman, U., Laming, J.M., Warren, H.P., Schühle, U., & Wilhelm, K. 1998, *Astrophysical Journal*, 507, 991
- Dowdy, J.F., Rabin, D., & Moore, R.L. 1986, *Solar Physics*, 105, 35
- Emslie, A.G. & Noyes, R.W. 1978, *Solar Physics*, 57, 373
- Feldman, U., Behring, W.E., Curdt, W., Schühle, U., Wilhelm, K., Lemaire, P., & Moran, T.M. 1997, *Astrophysical Journal Supplement Series*, 113, 195
- Golub, G.H., Heath, M., & Wahba, G. 1979, *Technometrics*, 21, 215
- Hollweg, J.V. 1991, *Mechanisms of Chromospheric and Coronal Heating*, (Springer-Verlag: Berlin), 423
- Huba, J.D. 1994, *NRL Plasma Formulary*, Naval Research Laboratory, Washington, D.C., 33
- Hudson, H.S. 1991, *Solar Physics*, 133, 357
- Innes, D.E., Inhester, B., Axford, W.I., & Wilhelm, K. 1997, *Nature*, 386, 811
- Karpen, J. 1998, private communication
- Karpen, J.T., Antiochos, S.K., DeVore, C.R., & Golub, L. 1998, *Astrophysical Journal*, 495, 491
- Krall, N.A. & Trivelpiece, A.W. 1986, *Principles of Plasma Physics*, (San Francisco Press: San Francisco), 83
- Krucker, S. & Benz, A.O. 1998, *Astrophysical Journal*, 501, L213
- Landini, M. & Monsignori Fossi, B.C. 1990, *Astronomy and Astrophysics Supplement Series*, 82, 229
- Lemaire, P., Wilhelm, K., Curdt, W., Schühle, U., Marsch, E., Poland, A.I., Jordan, S.D., Thomas, R.J., Hassler, D.M., Vial, J.-C., Kühne, M., Huber, M.C.E., Siegmund, O.H.W., Gabriel, A., Timothy, J.G., & Grewing, M. 1997, *Solar Physics*, 170, 105
- Lin, R.P., Schwartz, R.A., Kane, S.R., Pelling, R.M., & Hurley, K.C. 1984, *Astrophysical Journal*, 283, 421
- Livi, S.H.B., Wang, J., & Martin, S.F. 1985, *Australian Journal of Physics*, 38, 855
- Mariska, J.T. 1992, *The Solar Transition Region*, (Cambridge University Press: Cambridge)
- Narain, U. & Ulmschneider, P. 1990, *Space Science Reviews*, 54, 377

- Newton, E.K. 1996, *The Velocity Differential Emission Measure (VDEM) as a Diagnostic of Solar Atmospheric Response to Flare Heating*, Doctoral Dissertation, University of Alabama in Huntsville
- Newton, E.K., Emslie, A.G., & Mariska, J.T. 1995, *Astrophysical Journal*, 447, 915
- Newton, E.K., Emslie, A.G., & Mariska, J.T. 1996 *Astrophysical Journal*, 459, 804
- Parker, E.N. 1972, *Astrophysical Journal*, 174, 499
- Parker, E.N. 1979, *Cosmical Magnetic Fields*, (Oxford: Clarendon Press), 359
- Parker, E.N. 1988, *Astrophysical Journal*, 330, 474
- Petschek, H.E. 1964, *Symposium on Solar Flares*, NASA, SP-5
- Porter, J.G. & Dere, K.P. 1991, *Astrophysical Journal*, 370, 775
- Porter, J.G., Fontenla, J.M., & Simnett, G.M. 1995, *Astrophysical Journal*, 438, 472
- Porter, J.G., Moore, R.L., Reichman, E.J., Engvold, O., & Harvey, K.L. 1987, *Astrophysical Journal*, 323, 380
- Porter, J.G., Toomre, J., & Gebbie, K.B. 1984, *Astrophysical Journal*, 283, 879
- Priest, E.R. 1982, *Solar Flare Magnetohydrodynamics*, (Dordrecht: Reidel), 206
- Priest, E.R. 1985, *Reports of Progress in Physics*, 48, 955
- Priest, E.R. 1998, invited presentation at U.K. National Astronomy Meeting, St. Andrews, March
- Tandberg-Hanssen, E. & Emslie, A.G. 1988, *The Physics of Solar Flares*, (Cambridge University Press: Cambridge), 136
- Tsubaki, T. 1988, *Solar and Stellar Coronal Structure and Dynamics*, 9th Sacramento Peak Summer Workshop, NSO, Sunspot, New Mexico, 140
- Ulmschneider, P. 1970, *Astronomy & Astrophysics*, 4, 144
- van Ballegooijen, A.A. 1986, *Astrophysical Journal*, 311, 1001
- Whitaker, W.A. 1963, *Astrophysical Journal*, 137, 914
- Wilhelm, K., Curdt, W., Marsch, E., Schühle, U., Lemaire, P., Gabriel, A., Vial, J.-C., Grewing, M., Huber, M.C.E., Jordan, S.D., Poland, A.I., Thomas, R.J., Kühne, M., Timothy, J.G., Hassler, D.M., & Siegmund, O.H.W. 1995, *Solar Physics*, 162, 189

- Wilhelm, K., Lemaire, P., Curdt, W., Schühle, U., Marsch, E., Poland, A.I., Jordan, S.D., Thomas, R.J., Hassler, D.M., Huber, M.C.E., Vial, J.-C., Kühne, M., Siegmund, O.H.W., Gabriel, A., Timothy, J.G., Grewing, M., Feldman, U., Hollandt, J., & Brekke, P. 1997, *Solar Physics*, 170, 75
- Winebarger, A.R., Emslie, A.G., Mariska, J.T., & Warren, H.W. 1999, *Astrophysical Journal*, 526, 471
- Withbroe, G.L. & Noyes, R.B. 1977 *Annual Review of Astronomy and Astrophysics* 15, 363
- Zirker, J.B. 1993, *Solar Physics*, 148, 43